

# 博士論文

Copper-oxide-based semiconducting nanostructures  
for electrochemical solar water splitting and  
glucose sensing

(太陽光による電気化学水分解とグルコース検知のための  
酸化銅系半導体ナノ構造)

李 昌黎

## Abstract

The photoelectrochemical (PEC) water splitting using sunlight offers a sustainable means to produce hydrogen without relying on any fossil fuels.  $\text{Cu}_2\text{O}$  is one of the most promising photocathode materials with respect to cost, abundance, light absorption, and energy band position, although the application of  $\text{Cu}_2\text{O}$  is limited because of a negative onset potential and self-reduction in electrolyte under illumination. A new and low-cost fabrication method was introduced to synthesize  $\text{Cu}_2\text{O}$  microcrystalline films with high photoactivity. The two-step fabrication method consists of the synthesis of  $\text{Cu}/\text{Cu}(\text{OH})_2$  nanowires and their subsequent transformation into  $\text{Cu}_2\text{O}$  at  $500^\circ\text{C}$  under a vacuum. The growth of the  $\text{Cu}_2\text{O}$  microcrystalline film was driven by the outward diffusion of Cu ions from the Cu substrate via Cu vacancies to the oxide surface and reacts with the oxygen from the gas phase. By controlling the annealing time, the photoactivity and stability of the films can be tuned. Photoelectrochemical evaluation of the  $\text{Cu}_2\text{O}$  films performed under chopped simulated AM 1.5G illumination reveals that the sample annealed at  $500^\circ\text{C}$  for 2 h exhibited the highest photocurrent of  $4.07 \text{ mA}/\text{cm}^2$  at 0 V/RHE.

Although the obtained  $\text{Cu}_2\text{O}$  film exhibits a high photoactivity, the  $\text{Cu}_2\text{O}$  surface layer was reduced to Cu and lost its activity quickly during the stability test. To preclude the self-reduction and increase the photovoltage of the  $\text{Cu}_2\text{O}$  photocathode in solar water splitting, we introduce a  $\text{Ga}_2\text{O}_3$  thin layer as a buffer layer between the  $\text{Cu}_2\text{O}$  sunlight absorber layer and the  $\text{TiO}_2$  protective layer. This buffer layer decreases the conduction band discontinuity at the  $\text{Cu}_2\text{O}$ /buffer layer interface and thus increases the photovoltage of the structure, thus shifting the onset potential positively and improving the efficiency. The  $\text{TiO}_2$  protective layer inhibits the  $\text{Cu}_2\text{O}$  self-reduction efficiently and the  $\text{TiO}_2$ /electrolyte interface is favorable for electron transport due to the narrow depletion

region at  $\text{TiO}_2$  surface. The fabricated  $\text{Pt/TiO}_2/\text{Ga}_2\text{O}_3/\text{Cu}_2\text{O}$  structure achieves a large shift of the onset potential toward positive values and a stable photocurrent over at least two hours. The observed onset potential of 1.02 V vs. RHE and the relatively large photocurrent generated at low applied biases demonstrate the potential of this structure for developing superior photoelectrodes for use in high-efficiency tandem cells.

The detection of glucose in analytical applications such as clinical diagnostics, food processing and environment protection has been the subject of much attention by analytical researchers in recent years. Among the metal-oxide materials used for glucose sensing, CuO is a promising candidate toward high performance glucose sensor both in enzymatic and non-enzymatic glucose sensing because of its high isoelectric point (IEP) and good electrochemical activity. The CuO nanoporous structure with a high crystal quality is synthesized by annealing the  $\text{Cu/Cu(OH)}_2$  nanowires at  $500^\circ\text{C}$  under a  $\text{O}_2/\text{Ar}$  atmosphere. The presence of  $\text{O}_2$  during the annealing results in the formation of CuO at the outer surface of the oxide layer and the CuO porosity is enhanced by using nanowires as the starting material for the growth of the outer layer. The obtained  $\text{Cu/Cu}_2\text{O/CuO}$  structure is used as an efficient electrode for glucose sensing and exhibits good sensitivity both in enzymatic and non-enzymatic glucose sensing schemes. The high surface area of nanoporous layer and the enhanced electron transfer facilitated by a Schottky barrier at the  $\text{Cu/Cu}_2\text{O}$  interface are likely responsible for the high performance glucose sensing.

Considering that the surface area plays a great role in the electrooxidation of glucose, a CuO nanowire/microflower structure with a high electrochemically active surface area is synthesized by annealing the previously grown  $\text{Cu(OH)}_2$  nanowires/CuO flowers. The obtained CuO nanowire/microflower structure exhibits a high sensitivity of 1943  $\mu\text{A}/\text{mM}/\text{cm}^2$ , a wide linear range up to 4 mM and a low detection limit of 4  $\mu\text{M}$  in a non-

enzymatic glucose sensing scheme. With the help of a second consecutive growth of CuO nanowires on the microflowers, the sensitivity of the obtained CuO nanowire/microflower/nanowire structure further increase to 2424  $\mu\text{A}/\text{mM}/\text{cm}^2$ , benefiting from an increased density of electrochemically active sites. A performance comparison between the CuO nanowire/microflower/nanowire, CuO nanowire/microflower, CuO nanowire and  $\text{Cu}_x\text{O}$  film electrode was systematically conducted to demonstrate the significant role of surface area in the electrocatalysis of glucose. Moreover, the fabricated electrode presents a good selectivity towards interference species (ascorbic acid, uric acid and chloride anions), indicating great potential of the proposed electrode for applications in electrochemical devices. The main advantage of the presented structure is to provide a structure with well controlled interfaces using simple and low-cost fabrication techniques, without resorting on materials in the form of powders. Thus, the reported CuO nanowire/microflower/nanowire structure, which is fabricated directly from a Cu foil, provides a simple and economic way towards high performance CuO glucose sensors.



## Acknowledgements

I would like to express my sincere gratitude to people that conducive to my growth, broaden my horizons and inspired me during my Ph.D. study.

First of all, I give my deepest gratitude to my advisor Professor Jean-Jacques Delaunay for giving me the opportunity to study in his group. The group has a great and stimulating academic atmosphere that encourages innovations. I benefited a lot from his immense knowledge, valuable comments, constant encouragement and helpful guidance.

Many thanks to the jury of my Ph.D. defense, Professor Kazunari Domen, Professor Shigeo Maruyama, Professor Hitoshi Tabata and Associate Professor Junho Choi. Their constructive comments and suggestions have made significant improvements to this thesis.

I would like to extend my sincere gratitude to Professor Kazunari Domen for allowing me to use the facilities in his lab and give me helpful suggestions. I am deeply grateful to Assistant Professor Takashi Hisatomi for his constructive suggestions, valuable comments and constant help during the experiments. I also would like to express my gratitude to Mr. Osamu Watanabe for his kind help in the experiment. Also special thanks to Dr. Hiroyasu Yamahara and Dr. Dali Sun for the assistance of PLD and guidance of bio-sensing.

I wish to extend my gratitude to all of the members in Delaunay lab including Yalun, Ahmadi, Yaerim, Li-Chung, Changqing, Hassan, Mario, Yutaka, Yusuke, Takahiro, Xin, Shichen, Jinghua, Yuya and Syazwan for their countless help in experiment and life. The life would be harder without the helpful discussions, encouragement and friendship. Many thanks to Dr. Yanbo Li and Dr Miao Zhong for their valuable discussion and guidance at the early period.

I gratefully acknowledge the CSC program for the financial support (201206230077) during the three years study.

Lastly and most importantly, I would like to thank my family and friends for their great understanding and support.

## Contents

<b>1. Introduction</b>	1
1.1. Copper oxide overview	1
1.2. Solar energy	3
1.3. Photoelectrochemical water splitting	5
1.4. Cu <sub>2</sub> O-based photocathodes for water splitting	12
1.5. Research objectives of Cu <sub>2</sub> O-based photocathodes	16
1.6. Glucose sensing	16
1.7. Nanostructure-based CuO for non-enzymatic glucose sensing	20
1.8. Research objectives of CuO-based glucose sensors	21
References	23
<b>2. Fabrication of photoactive Cu<sub>2</sub>O films for photoelectrochemical cells</b>	28
2.1. Introduction	29
2.2. General experimental section	30
2.2.1. Photoelectrochemical and electrochemical impedance measurements	30
2.2.2. Structural characterization	31
2.3. Cu <sub>2</sub> O microcrystalline film formed at 500°C from Cu(OH) <sub>2</sub> nanowires	31
2.3.1. Fabrication of Cu(OH) <sub>2</sub> nanowires and Cu <sub>2</sub> O microcrystalline films	31
2.3.2. Morphology of the structures	32
2.3.3. XRD and Raman Characterization	35
2.3.4. Optical properties	39
2.3.5. Photoelectrochemical measurements	40
2.3.6. Electrochemical impedance	43
2.3.7. Discussion	46
2.4. Conclusions	47
References	48
<b>3. Fabrication of buried p-n junction on Cu<sub>2</sub>O for stable solar water splitting</b>	52
3.1. Introduction	53
3.2. Experimental section	57
3.2.1. Preparation of TiO <sub>2</sub> /ZnO/Cu <sub>2</sub> O and TiO <sub>2</sub> /Ga <sub>2</sub> O <sub>3</sub> /Cu <sub>2</sub> O structures	57
3.2.2. Co-catalyst deposition	58
3.2.3. PEC measurements	59
3.2.4. Structural characterization	59
3.3. Characterization of the TiO <sub>2</sub> /Ga <sub>2</sub> O <sub>3</sub> /Cu <sub>2</sub> O structures	60
3.4. PEC properties of Pt/TiO <sub>2</sub> /Ga <sub>2</sub> O <sub>3</sub> /Cu <sub>2</sub> O photocathodes	66

3.4.1.	Pt/Ga <sub>2</sub> O <sub>3</sub> /Cu <sub>2</sub> O structures .....	66
3.4.2.	Pt/TiO <sub>2</sub> /Ga <sub>2</sub> O <sub>3</sub> /Cu <sub>2</sub> O structures .....	68
3.5.	PEC properties of Pt/TiO <sub>2</sub> /ZnO/Cu <sub>2</sub> O photocathodes.....	81
3.6.	Band alignment of heterojunction .....	84
3.7.	Conclusions.....	89
	References.....	90
<b>4.</b>	<b>Nanoporous CuO layer modified Cu electrode for glucose sensing.....</b>	<b>94</b>
4.1.	Introduction.....	95
4.2.	Experimental section .....	96
4.2.1.	Fabrication of Cu(OH) <sub>2</sub> nanowires and Cu/Cu <sub>2</sub> O/CuO structures.....	96
4.2.2.	Electrochemical measurements .....	97
4.2.3.	Structural characterization .....	97
4.3.	Results and discussion.....	98
4.3.1.	Characterization of the Cu/Cu <sub>2</sub> O/CuO structures .....	98
4.3.2.	Enzymatic glucose sensing .....	101
4.3.3.	Non-enzymatic glucose sensing .....	105
4.3.4.	Selectivity .....	106
4.3.5.	Analysis.....	108
4.4.	Conclusions.....	110
	References.....	112
<b>5.</b>	<b>Fabrication of CuO nanostructures on Cu electrode for high performance glucose sensing.....</b>	<b>116</b>
5.1.	Introduction.....	117
5.2.	Experimental section .....	118
5.2.1.	Fabrication of the Cu <sub>x</sub> O film, the CuO nanowire and the CuO nanowire/microflower structure.....	118
5.2.2.	Electrochemical measurements .....	119
5.2.3.	Structural characterization .....	120
5.3.	Results and discussion.....	120
5.3.1.	Characterization of the CuO nano/microstructures .....	120
5.3.2.	Non-enzymatic glucose sensing performance of Cu <sub>x</sub> O film, CuO nanowire and CuO nanowire/microflower electrodes.....	124
5.3.3.	Construction of CuO nanowire/microflower/nanowire structure for higher performance glucose sensing .....	128
5.4.	Selectivity.....	134
5.5.	Conclusions.....	136

References .....	137
<b>6. Conclusions and outlooks .....</b>	<b>140</b>
6.1. Conclusions.....	140
6.2. Outlooks .....	142
<b>Appendix A. Supporting Information to Chapter 2 .....</b>	<b>147</b>

# 1. Introduction

## 1.1. Copper oxide overview

Copper oxide ( $\text{Cu}_2\text{O}$  and  $\text{CuO}$ ) have been attracting much attention in the fabrication of energy conversion devices, electrochemical sensors and optoelectronic devices owing to their unique physical and chemical properties. These materials show a promising potential in fundamental scientific research and practical applications because of their earth-abundant, non-toxic, easy to synthesize and low-cost. Copper oxide can be fabricated from abundant elements using scalable processing techniques such as electrodeposition,<sup>1-6</sup> hydrothermal method<sup>7-14</sup> and thermal oxidation of Cu foils.<sup>15-20</sup> Thermal oxidation is a widely used method of producing high quality  $\text{Cu}_2\text{O}$  and  $\text{CuO}$  due to its simplicity. By controlling the oxidation temperature and  $\text{O}_2$  pressure carefully,  $\text{Cu}_2\text{O}$  and  $\text{CuO}/\text{Cu}_2\text{O}$  bilayer structure can be prepared on Cu foils and be used as substrate for high performance solar cells, photoelectrochemical cells and sensors.

$\text{Cu}_2\text{O}$  (cuprous oxide) is a naturally p-type conducting semiconductor material and is the oldest material of semiconductor electronics.<sup>21</sup> It crystallizes in a simple cubic structure. The unit cell of  $\text{Cu}_2\text{O}$  contains four copper atoms and two oxygen atoms. The oxygen atoms are tetrahedrally coordinated by copper atoms as nearest neighbor and copper atoms are linearly coordinated by two neighboring oxygen atoms.<sup>22-23</sup> With a bandgap of 2 eV  $\text{Cu}_2\text{O}$  is a promising p-type absorber layer for solar cells. The theoretical efficiency of  $\text{Cu}_2\text{O}$  solar cells is about 20% under AM1 solar illumination.<sup>24</sup> However, the current experimental data for  $\text{Cu}_2\text{O}$ -based heterojunction solar cells is about 6%.<sup>25-26</sup> Thus, for the  $\text{Cu}_2\text{O}$ -based solar cells and photocathodes for solar water splitting, there is still a lot of room for improvement.

$\text{CuO}$  (cupric oxide) is believed to be intrinsically p-type semiconductor with a narrow

**Table 1.1.** Structural parameters of Cu<sub>2</sub>O and CuO.<sup>22, 27</sup>

	Cu <sub>2</sub> O	CuO
Crystal structure	Cubic $a = 4.2696 \text{ \AA}$ $\alpha = \beta = \gamma = 90^\circ$	Monoclinic $a = 4.6837 \text{ \AA}$ , $b = 3.4226 \text{ \AA}$ , $c = 5.1288 \text{ \AA}$ , $\alpha = 90^\circ$ , $\beta = 99.54^\circ$ , $\gamma = 90^\circ$
Band gap	1.9-2.5 eV	1.21-1.55 eV
Density	6.00 g/cm <sup>-3</sup>	6.31 g/cm <sup>-3</sup>
Melting point	1232 °C	1326 °C
Dielectric constant	7.5	18.1
Hole effective mass	0.58 $m_0$	0.24 $m_0$

band gap of 1.2-1.5 eV.<sup>27</sup> The crystal structure of CuO is monoclinic with C2/c symmetry. The copper atom is coordinated by four oxygen atoms in an approximately square planar configuration.<sup>28</sup> The structural parameters of Cu<sub>2</sub>O and CuO are listed in table 1.1.<sup>22, 27</sup> CuO is a promising material for the fabrication of bio-sensors,<sup>29</sup> gas sensors,<sup>30</sup> photodetectors,<sup>31</sup> field emission devices,<sup>32</sup> photocatalysts<sup>33</sup> and lithium-ion batteries.<sup>34</sup> The development of nanotechnology accelerated the construction of CuO nanostructures with different shapes and dimensions for higher surface area and improved catalytic kinetics.

Although Cu<sub>2</sub>O and CuO have different properties, both oxides are attracted considerable interest in the field of photovoltaics and catalysts, because of their narrow band gap and high catalytic activity.<sup>24-26, 33, 35</sup> The copper oxide nano/micro structures have been demonstrated to possess properties useful for applications in photoelectrochemical hydrogen production and bio-sensing.<sup>36-38</sup> Thus, the size and morphology control of copper oxide during synthesis is crucial for the development of high performance devices. Solution method is a facile way to design nano/micro

structures on low-cost copper foils<sup>39</sup> and the as-prepared structures can be converted to nanostructured Cu<sub>2</sub>O or CuO through a thermal annealing process according to the phase diagram of copper oxide growth.<sup>15-20</sup> So this method is introduced in this work to synthesize Cu<sub>2</sub>O film with high photoactivity for solar energy conversion and CuO nano/micro structures with high surface area for glucose sensing.

## **1.2. Solar energy**

In recent years, the rapid expansion of modern industry and global population has accelerated the consumption of energy. In 2012, worldwide primary energy consumption was  $5.6 \times 10^{20}$  J, which is equivalent to an average power use of 17.8 terawatts (TW).<sup>40</sup> The Energy Information Administration estimates that more than 80% of the energy was obtained from fossil fuels such as petroleum, oil, natural gas. The world energy consumption is projected to increase because of the economic growth of the developing country. What's more, the over use of fossil fuels also raises serious environmental concerns. If the combustion is complete, the carbon and sulfur present in the fossil fuels are burned to carbon dioxide and sulfur dioxide. The gas emissions from fossil fuels cannot be consumed by natural processes completely and thus become environmentally hazardous and enhance global warming. To protect the environment and climate, saving fossil fuels and decelerating fuel consumption has become urgent matter for all countries.<sup>41</sup>

Renewable energy such as wind power, hydropower, solar energy, biomass, biofuel and geothermal energy have been used to replace conventional fossil fuels due to its sustainability, indigenous, low pollution, and inexhaustibility. Compared to other clean and renewable energy sources, solar energy is by far the most promising energy source



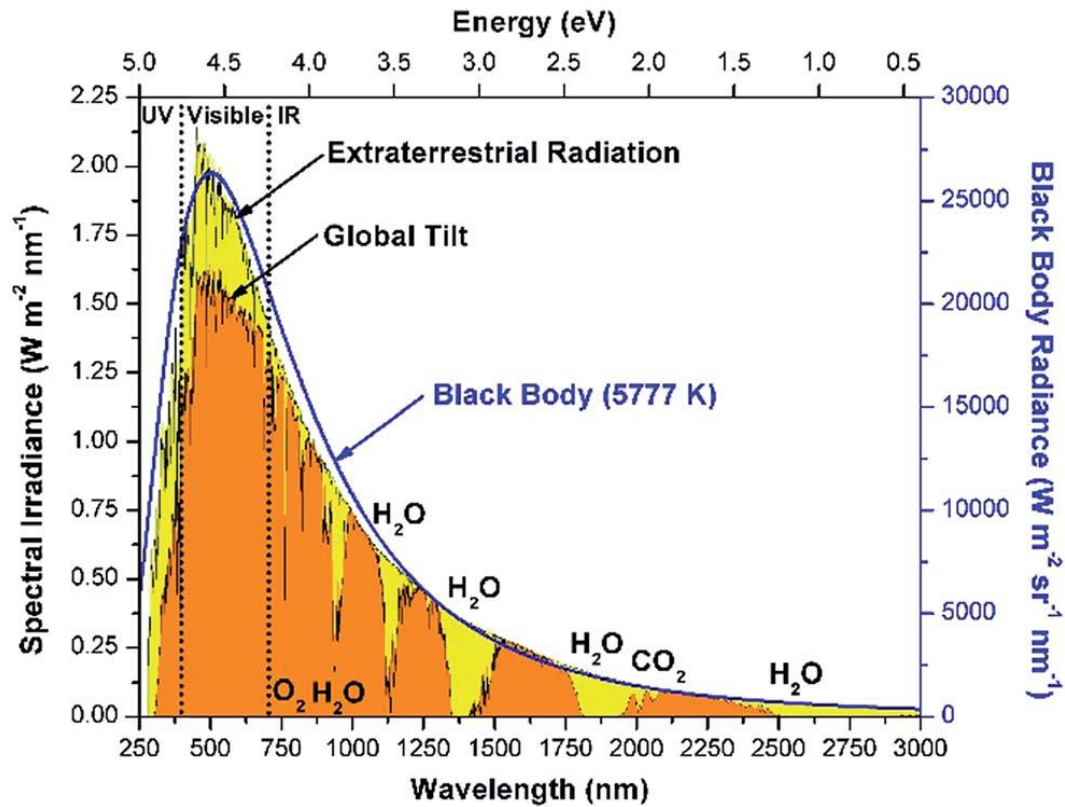


**Figure 1.1.** Solar irradiance spectra above atmosphere and at surface of earth.

Reproduced with permission from Ref. 42.

because of the huge power radiated on the surface of earth from the sun. The spectral distribution of solar radiation is shown in Figure 1.1.<sup>42</sup> The spectrum of the sunlight radiation is close to that of a black body with a temperature of about 5777 K.<sup>43</sup> According to Planck's relation ( $E = h\nu$ ), the photon's energy is proportional to its frequency ( $\nu$ ). In terms of energy, sunlight reached at earth's surface is about 52-55% in the infrared region (above 700 nm), 42-43% in the visible region (400-700 nm) and around 3-5% in the ultraviolet range (below 400 nm).<sup>42</sup> The amount of solar energy radiated on the surface of the planet in one year is about twice as much as will ever be obtained from all of the earth's fossil fuels.<sup>44</sup> Thus, solar energy plays a great role in the replacement of conventional fossil fuels to enable a more sustainable world. To harness the solar energy, photovoltaic systems, concentrated solar power and solar water heating have been

introduced to convert the sunlight into energy. To overcome the challenge of the intermittent nature of solar radiation, storing solar energy in the form of electricity and chemical fuels is critical to maximize the use of the solar energy.

In view of this, solar water splitting has been considered as a promising and practical method for hydrogen production in recent years due to its low cost, low energy consumption and environmentally friendly.<sup>45-46</sup> The solar fuels from the solar energy is suitable for storage, transportation and consumption. The combination of conventional photovoltaic (PV) technology and water splitting electrolyzers is an obvious way to convert solar energy to hydrogen. However, it is estimated that the cost of hydrogen production ( $\$10 \text{ kg}^{-1}$ ) from silicon PV and a PEM electrolyzer is still higher than the price of hydrogen (ca.  $\$1 \text{ kg}^{-1}$ ) produced through the steam reforming of fossil methane.<sup>47-48</sup> Thus, photoelectrochemical (PEC) device provides a promising way to form direct semiconductor/water junction and thus offer a more straightforward, cost-effective and convenient way to solar water splitting.<sup>48</sup>

### **1.3. Photoelectrochemical water splitting**

In general, a PEC cell consists of three components, working photoelectrode, counter electrode and electrolyte. A common method is to use photoactive semiconductors as working electrode to produce photo-excited electron-hole pairs and one or both of the electrodes can be a semiconductor. In this system, the oxidation of water (oxygen evolution) occurs at the photoanode, reduction of protons (hydrogen production) occurs at the photocathode under sunlight illumination with an assistance of small external bias.<sup>49</sup> When a semiconductor is immersed in electrolyte, there will be a charge transfer across the semiconductor/electrolyte junction to maintain the electrostatic equilibrium.

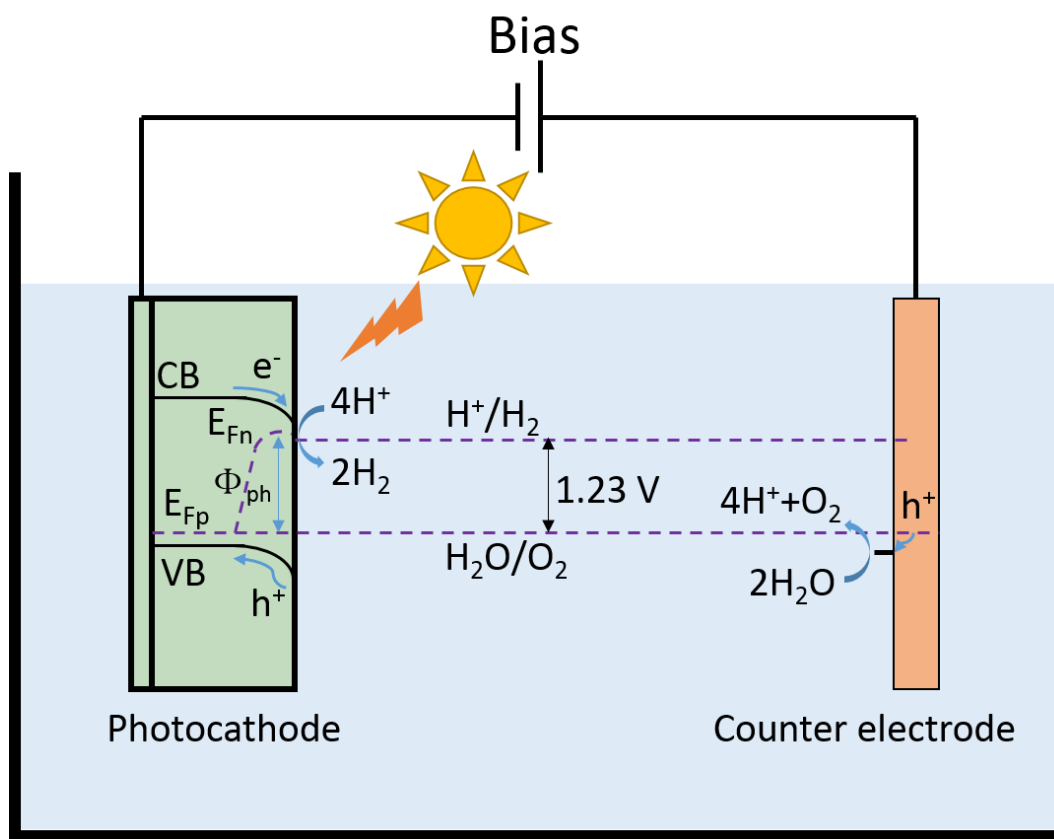
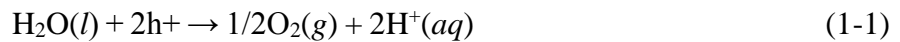


**Figure 1.2.** Principle of operation of PEC cell based on bias-assisted p-type semiconductor.

When the electronic equilibrium is reached, the Fermi level of the electrons in the semiconductor and redox potential of electrolyte are aligned at the interface of semiconductor/electrolyte junction, which lead to an upward band bending in a p-type semiconductor for p-type semiconductor/electrolyte junction and a downward band bending in a n-type semiconductor for n-type semiconductor/electrolyte junction. The schematic for a p-type photocathode is shown in Figure 1.2. In the dark, The charge transfer produces a space-charge layer on the p-type semiconductor side and a compact (Helmholtz) layer followed by the diffuse (Gony-Chapman) layer are formed on the electrolyte side.<sup>46</sup> Under illumination, the photogenerated electron-hole pairs are separated by the space-charge field and the electrons travel to the semiconductor-

electrolyte interface for reduction reaction, while the holes travel to the counter electrode for water oxidation reaction. What's more, a photovoltage is generated during the illumination because of the splitting of initial Fermi level into two separate quasi-Fermi levels for electron ( $E_{Fn}$ ) and holes ( $E_{Fp}$ ). The maximum achievable photovoltage is determined by the degree of the band bending. Therefore, to get a semiconductor/electrolyte junction with high photovoltage, the conduction band of the p-type semiconductor must be close to formal redox potential of electrolyte to enable a large degree of band bending. In the system illustrated in Figure 1.2, three processes are involved to convert and store solar energy efficiently. First, sunlight must be absorbed to produce electron-hole pairs in the semiconductor. Second, the photogenerated electrons and holes must be separated in space-charge layer and diffuse to the interface for reaction. In this process, recombination should be inhibited to avoid energy loss. Third, the photogenerated electrons must be collected by the catalyst sites and participate in the reduction reaction energetically and kinetically.

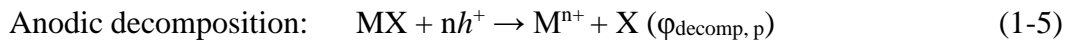
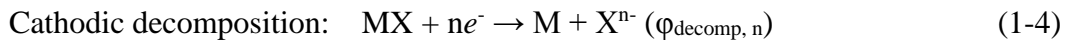
The change of Gibbs free energy for the splitting of  $H_2O$  into  $H_2$  and  $1/2 O_2$  under standard conditions is  $\Delta G^0 = 237.2 \text{ kJ/mol}$ . Based on Nernst equation, this corresponds to the standard reversible potential  $\Delta E^0$  of 1.23 V. Thus, the photo energies larger than 1.23 eV ( $\lambda < 1000 \text{ nm}$ ) is needed to drive the water splitting reaction with sunlight.<sup>50</sup> The equations for oxygen evolution (OER) and hydrogen evolution reaction (HER) are listed below:



The overall water splitting process must generate four electron-hole pairs for the

production of two hydrogen molecules and one oxygen molecule. To drive this reaction, the conduction band position of the semiconductor needs to be more negative than the reduction level of water  $E^\circ(\text{H}^+/\text{H}_2)$  while the valence band position needs to be more positive than the oxidation level of water  $E^\circ(\text{O}_2/\text{H}_2\text{O})$ .

To choose a semiconductor for efficient solar water splitting, many requirements should be considered. For example, the semiconductor should possess the properties of highly stable, low-cost, narrow band gap, efficient interfacial charge transfer and having a conduction band-edge energy and valence band-edge energy that straddles the reduction and oxidation levels of water. First, the semiconductor should be stable in aqueous solution. It is reported that the thermodynamics of cathodic reduction of semiconductors by electrons and anodic oxidation by holes are related to the free energy of electrons and holes in illuminated semiconductor electrodes,<sup>51</sup> as presented in Figure 1.3. The inadequate energy correlation between band edges and Fermi energies of electrode reactions lead to an easily corrode of some materials in aqueous solution such as silicon, cadmium sulfide and cuprous oxide. The photodecomposition of a semiconductor (MX) can be represented by following reactions:<sup>51-52</sup>



where  $n$  is the number of electrons or holes; and  $\varphi_{\text{decomp}, n}$  and  $\varphi_{\text{decomp}, p}$  are the free energy change at the cathode and anode, respectively. In the case of standard hydrogen electrode,  $E_{\text{decomp}, n}$  and  $E_{\text{decomp}, p}$  is the cathodic decomposition potential and anodic decomposition potential, respectively. The criteria for the stability of photoelectrode against photocorrosion should fulfill  $E(\text{H}^+/\text{H}_2) > E_{\text{decomp}, n}$  and  $E(\text{O}_2/\text{H}_2\text{O}) < E_{\text{decomp}, p}$ .<sup>51-53</sup>

The decomposition of unstable semiconductors can be inhibited by redox reactions

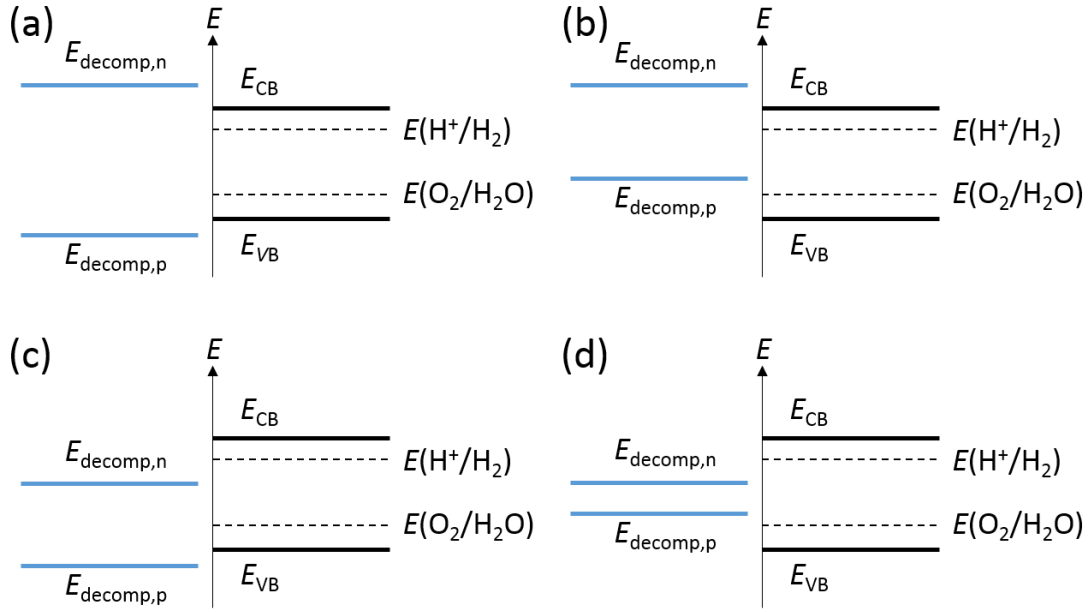


**Figure 1.3.** Typical correlations between energy band positions and decomposition potentials, controlling thermodynamic stability against photodecomposition. (a) Stable, (b) anodic decomposition, (c) cathodic decomposition, (d) unstable. (Data adapted from ref. 51 and 52).

with suitable position of the redox potential and rapid reaction rate.<sup>51</sup> In water splitting reaction, the redox potential is fixed. Thus, using a stable semiconductor over layer to stabilize the unstable electrode is a promising way to prevent the decomposition. Second, the band gap of material should be as small as possible to absorb a large portion of the sunlight. However, considering the energy needed for overall water splitting (1.23 eV) and the overpotential for both oxygen evolution and hydrogen reduction, the energy required for photoelectrolysis at a semiconductor electrode is therefore frequently reported as 1.6-2.4 eV.<sup>50</sup> Third, the conduction band of the semiconductor should be more negative to the hydrogen evolution and the valence band should be more positive to the oxygen evolution level to provide a large photovoltage under the illumination for efficient water splitting. Figure 1.4 shows the band positions of several semiconductor candidates

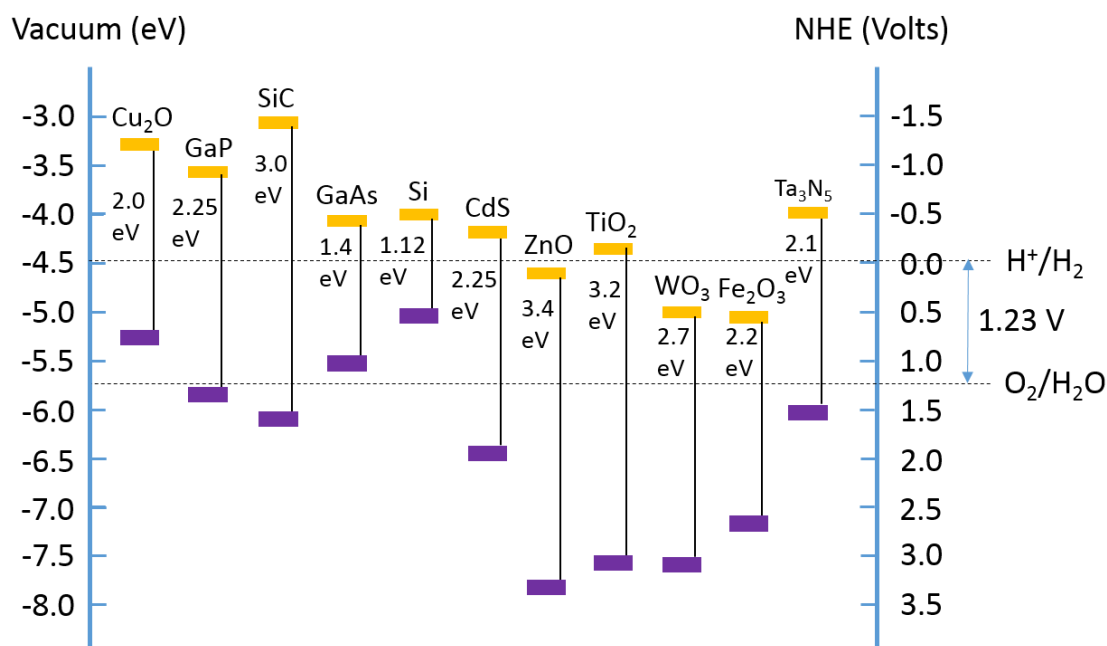


**Figure 1.4.** Energy band diagram of several semiconductors in contact with aqueous electrolyte at pH 1, together with the redox potentials of water splitting. (Data adapted from ref. 46)

for solar water splitting in contact with aqueous electrolyte at pH 1.

Since the pioneering work of A. Fujishima on the TiO<sub>2</sub> photoanode for water splitting,<sup>54</sup> metal oxides have been extensively investigated as photoanodes or photocathodes for water splitting because of the low cost and better stability in aqueous environments compared to other semiconductors. Figure 1.5 shows the theoretical photocurrent densities for several semiconductor under one-sun illumination.<sup>55</sup> TiO<sub>2</sub> has been the favoured light absorber to split water into hydrogen and oxygen, however, only a small UV fraction of sunlight (3-5 %) can be utilized by this material, thus exhibited a low conversion efficacy because of the large band gap (3.0-3.2 eV).<sup>54, 56-57</sup> Tungsten trioxide (WO<sub>3</sub>) possess a smaller bandgap of between 2.4-2.8 eV, makes it possible to absorb visible light within solar spectrum. However, WO<sub>3</sub> still has a low light energy conversion efficiency due to the reduction potential of the electrons in WO<sub>3</sub> is low, which

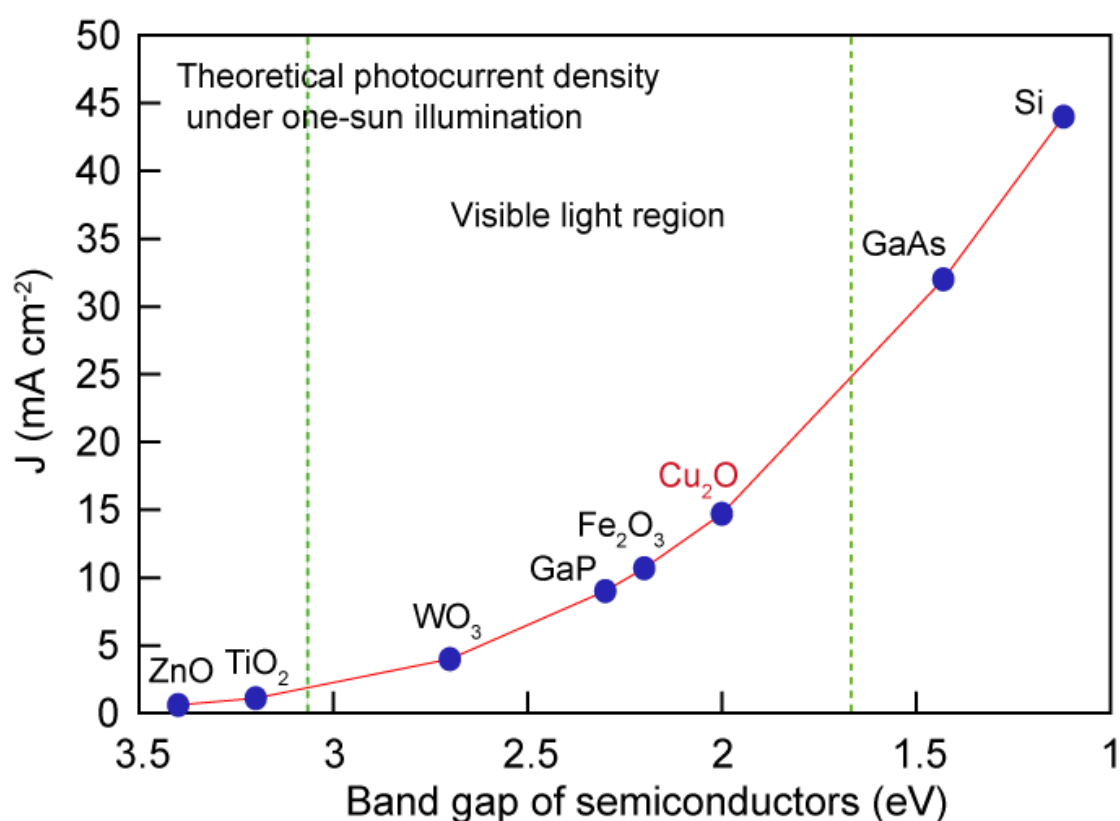


**Figure 1.5.** Theoretical photocurrent densities several semiconductors under one-sun illumination. The theoretical value is calculated by integrating photon flux at different cut-off energies based the AM 1.5G solar spectrum and assuming that all incident photons above the material band gap contribute to the photocurrent. (Data adapted from ref. 55).

is related to the positive conduction band position.<sup>58-59</sup> Hematite ( $\text{Fe}_2\text{O}_3$ ) is also a well-known and most widely used photoelectrode because of its cheap, stable and good sunlight absorption. Although tremendous studies have been conducted on this material, there are many challenges to employ this material for PEC water splitting. The flat band potential of hematite is too positive for hydrogen reduction and need a large overpotential for water oxidation. What's more, the material possesses a relatively low absorption coefficient and poor majority carrier conductivity.<sup>49</sup> The drawbacks and limitations inhibits the further improvement of light conversion efficiency for hematite. For the



photocathode, Si<sup>60</sup> and InP<sup>61</sup> have been reported to produce high photocurrent densities and with large photovoltages (> 500 mV), however, the poor stability and high cost are the main drawbacks for this two materials.

Cuprous oxide (Cu<sub>2</sub>O) is a promising candidate for PEC water splitting because of the direct energy bandgap of 2.0 eV makes it a good light absorber for solar energy conversion. According to the theoretical calculation presented in Figure 1.4 and report in literature,<sup>62</sup> a theoretical photocurrent of -14.7 mA/cm<sup>2</sup> and a light-to-hydrogen conversion efficiency of 18 % based on the AM 1.5G solar spectrum. The energy band positions of Cu<sub>2</sub>O is appropriate for the water reduction reaction<sup>63</sup> but the high valence band edge makes it ineffective for oxygen evolution.<sup>51</sup> The main limitation for the application of Cu<sub>2</sub>O as a photocathode for water splitting is the instability in aqueous solutions because the redox potentials for the oxidation and reduction of Cu<sub>2</sub>O lie within the bandgap of Cu<sub>2</sub>O.<sup>62</sup> It means Cu<sub>2</sub>O can be reduced to Cu easily under a photocathodic condition in aqueous solution. The stabilization of Cu<sub>2</sub>O can be achieved by coating n-type semiconductors on the Cu<sub>2</sub>O surface to generate a built-in field facilitating the transport of minority carriers to semiconductor/electrolyte interface and obtain a more stable operation.<sup>62</sup>

#### **1.4. Cu<sub>2</sub>O-based photocathodes for water splitting**

The attempt to stabilize Cu<sub>2</sub>O photoelectrode dates back to 2002, using TiO<sub>2</sub> as a protective layer.<sup>64</sup> However, the proposed TiO<sub>2</sub>/Cu<sub>2</sub>O structure exhibited a low photoactivity and the stability of this photocathode was not investigated in this work. Recently, Paracchino et al reported a highly active Cu<sub>2</sub>O-based photocathode for solar water splitting.<sup>62</sup> The issue of Cu<sub>2</sub>O instability in aqueous solution under illumination is

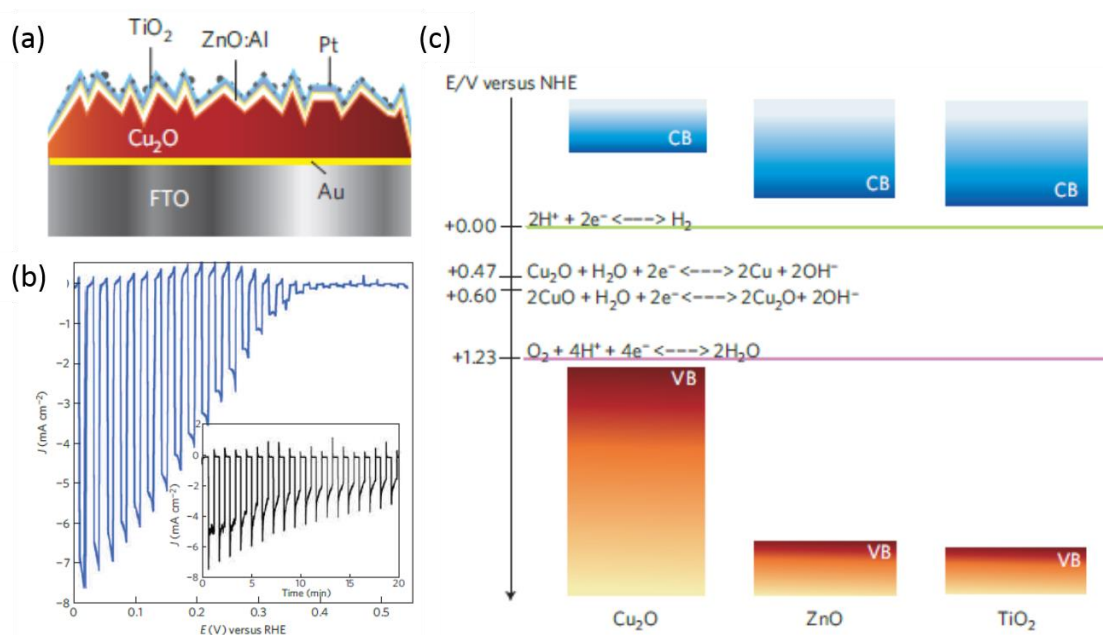


**Figure 1.6.** (a) Schematic representation of the TiO<sub>2</sub>/AZO/Cu<sub>2</sub>O electrode structure. (b) Current-potential characteristics of the as-prepared Cu<sub>2</sub>O/5×(4nm ZnO/0.17 nm Al<sub>2</sub>O<sub>3</sub>)/11nm TiO<sub>2</sub>/Pt electrode. The insets show the respective photocurrent transients for the electrodes held at 0V versus RHE in chopped light illumination with N<sub>2</sub> purging. (c) Overview of the energy band positions for the semiconductors of the multilayer photocathode and redox levels of the involved chemical reactions. CB, conduction band; VB, valence band. Reproduced with permission from Ref. 62.

addressed by depositing Al-doped ZnO (AZO) and TiO<sub>2</sub> on the electrode surface by atomic layer deposition (ALD). The local electrostatic field formed at the Cu<sub>2</sub>O/ZnO p-n junction could assist in extracting photogenerated electrons from Cu<sub>2</sub>O to the semiconductor/electrolyte interface and improve the stability. The as-deposited Cu<sub>2</sub>O/5×(4 nm ZnO/0.17 nm Al<sub>2</sub>O<sub>3</sub>)/11 nm TiO<sub>2</sub>/Pt electrode showed photocurrents of up to 7.6 mA/cm<sup>2</sup> at a potential of 0 V vs RHE at pH of 4.9. The electrodes shows a better stability compared to bare Cu<sub>2</sub>O (only 20% reduction in photocurrent after 20 min of irradiation) and remained active after 1 h of testing. The schematic representation, PEC

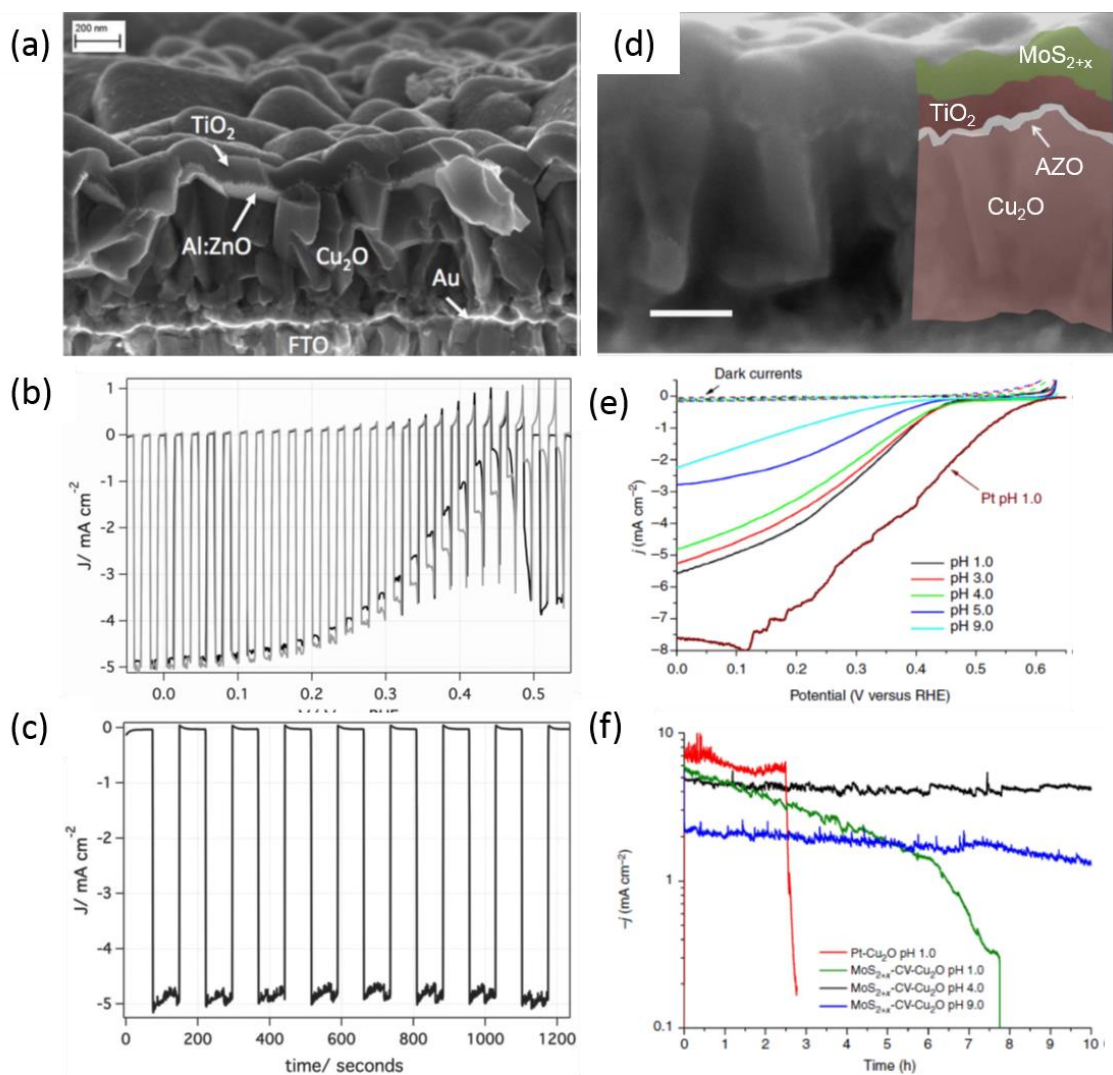


**Figure 1.7.** (a) Cross-sectional SEM micrograph of the  $\text{TiO}_2$ (100 nm)/ $\text{AZO}$ (20 nm)/ $\text{Cu}_2\text{O}$  photocathode with as-deposited ALD layers. (b) Current–voltage characteristics in pH 5.0 phosphate–sulfate electrolyte of a composite photocathode with  $\text{RuOx}$  catalyst. (c) Chronoamperometric stability measurement of the photocathode biased at 0 V/RHE in pH 5.0 phosphate–sulfate electrolyte under light chopping. (d) Cross-sectional SEM image of the  $\text{MoS}_{2+x}$ (100 nm)/ $\text{TiO}_2$ (100 nm)/ $\text{AZO}$ (20 nm)/ $\text{Cu}_2\text{O}$  photocathode. Scale bar, 200 nm. (e-f) Current–potential and stability test (0 V vs RHE) curves at different pH values for a  $\text{MoS}_{2+x}$ -CV- $\text{Cu}_2\text{O}$  photocathode. Reproduced with permission from Ref. 65 and 67.

performance and energy band alignment of this electrode are presented in Figure 1.6. The decay of the photocurrent may can be explained by the reduction of  $\text{TiO}_2$  layer and the irreversible loss of Pt from the electrode surface.<sup>62, 65</sup> To overcome this drawback, a thin film RuOx catalyst (40 nm) was deposited on  $\text{TiO}_2$ (100 nm)/AZO(20 nm)/ $\text{Cu}_2\text{O}$  electrode to improve the stability. The  $\text{RuO}_2$ -catalyzed photoelectrodes exhibit much improved stability versus platinum nanoparticles, with 94% stability after 8 h of light-chopping stability test. The photocurrent of close to  $5 \text{ mA/cm}^2$  is obtained with this electrode at 0 V vs RHE, as shown in Figure 1.7 a-c. Earth-abundant catalyst, such as amorphous molybdenum sulfide, has been proved to be highly active and versatile catalyst for the hydrogen evolution reaction.<sup>66</sup> In view of this, Morales-Guio *et al* combine  $\text{MoS}_{2+x}$  and  $\text{Cu}_2\text{O}$ -based photocathode to promote the PEC performance,<sup>67</sup> as presented in Figure 1.7 d-f. The efficient extraction of excited electrons by the conformal catalyst film leads to photocurrents of up to  $5.7 \text{ mA/cm}^2$  at 0 V vs RHE (pH 1.0) under simulated AM 1.5 solar illumination. Stable current densities of  $-4$  and  $-2 \text{ mA/cm}^2$  were obtained at 0 V vs RHE at pH 4 and 9 for 10 h, respectively, as shown in Figure 1.7f.

Although the stability of  $\text{Cu}_2\text{O}$  photoelectrode has been improved by modifying the protective layer and co-catalyst, the photovoltage extracted from the protected  $\text{Cu}_2\text{O}$  photoelectrodes is still low. This is limited by the difference between the Fermi level of  $\text{Cu}_2\text{O}$  and the hydrogen evolution level. Thus, the photovoltage measured on  $\text{TiO}_2/\text{ZnO}/\text{Cu}_2\text{O}$  structure was below 0.6 V.<sup>62, 65, 67</sup> To improve the photovoltage, we need to shift the band edge positions of  $\text{Cu}_2\text{O}$  positively, which can be achieved by forming a p-n junction on  $\text{Cu}_2\text{O}$ . For this purpose, the n-type semiconductor deposited on  $\text{Cu}_2\text{O}$  must be have a negative conduction band because the maximum achievable photovoltage is defined by the difference between the  $\text{Cu}_2\text{O}$  Fermi level and n-type semiconductor

Fermi level.<sup>68</sup> Dai *et al* reported that the introduction of a ZnS buffer layer between the Cu<sub>2</sub>O and TiO<sub>2</sub> can shift the onset potential cathodically to some extent (0.72 V vs. RHE) by increasing the photovoltage at multilayer/electrolyte junctions.<sup>68</sup> Therefore, it is suggesting that there is still much room for improvement of photovoltage by forming a better energy band alignment across the multilayers.

### **1.5. Research objectives of Cu<sub>2</sub>O-based photocathodes**

The motivation of this part in thesis is to achieve highly efficient PEC water splitting on Cu<sub>2</sub>O-based photocathode through rational material synthesis and design. Particularly, this part focuses on developing a strategy of forming better energy band alignment on Cu<sub>2</sub>O to overcome challenges of instability and low photovoltage in water splitting. The major drawback of Cu<sub>2</sub>O, i.e. the self-reduction under photocathodic condition, is tackled by coating a protective layer (TiO<sub>2</sub>). Another challenge of this material is the low photovoltage observed in water splitting. By forming a buried p-n junction on Cu<sub>2</sub>O and choosing the buffer layer rationally, the energy loss in terms of applied voltage is reduced by improving the photovoltage of the structure. The following strategies have been tried in this part to achieve a high performance Cu<sub>2</sub>O-based photocathode: (1) Synthesize Cu<sub>2</sub>O microcrystalline film with high photoactivity through annealing a Cu(OH)<sub>2</sub> nanowire/Cu precursor. (2) Deposit n-type buffer layer and protective layer on Cu<sub>2</sub>O to improve the stability and photovoltage.

### **1.6. Glucose sensing**

The development of electrochemical glucose sensor has attracted much attention due to its importance in the field of clinical, food, and environmental applications.<sup>69-73</sup> Since

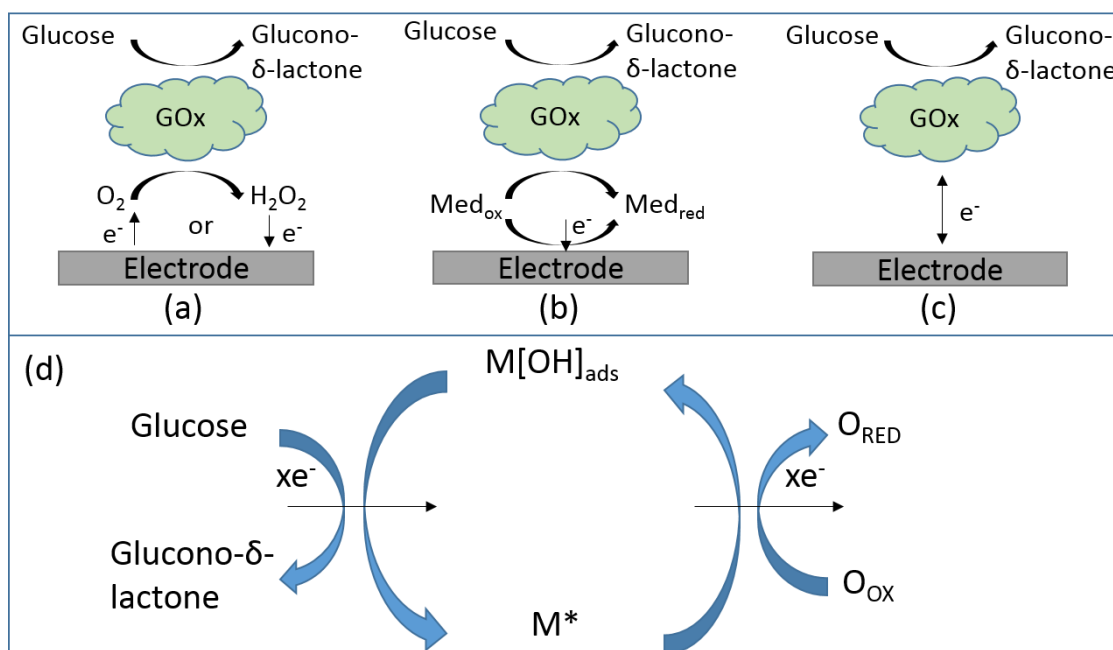
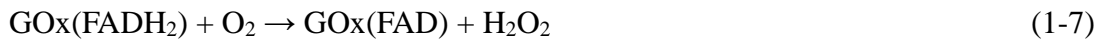
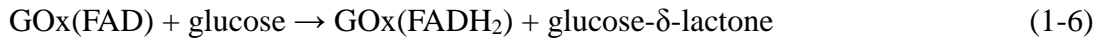


**Figure 1.8.** Three generations of amperometric enzyme glucose sensors based on the use of natural oxygen cofactor (a), artificial redox mediators (b), or direct electron transfer between GOx and electrode (c). (d) is the schematic diagram of non-enzymatic glucose sensor model.  $M^*$  is the reductive metal adsorption site and  $M[OH]_{ads}$  is the oxidative adsorbed hydroxide radical. (Data adapted from ref. 70 and 76).

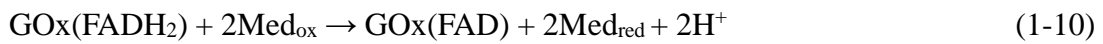
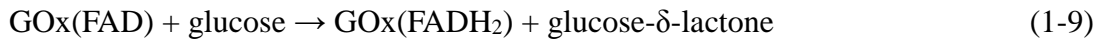
the first enzyme device introduced by Clark and Lyons in 1962,<sup>74</sup> the efforts to develop highly sensitive, cost-effective and reliable glucose sensors has been the subject of concern for decades. In 1967, Updike and Hicks constructed the first glucose oxidase (GOx) based glucose sensor and tested glucose concentration in biological solutions.<sup>75</sup> The development of amperometric glucose sensors can be summarized into three generations.<sup>69-73</sup>

First generation glucose sensors rely on the use of natural oxygen as a mediator between the GOx and electrode, as shown in Figure 1.8a. GOx reduces oxygen into hydrogen peroxide in the presence of glucose. The glucose concentration is proportional to the reduction rate of oxygen and thus can be determined by measuring the increment

of the hydrogen peroxide concentration or decrement of oxygen concentration.<sup>71-73</sup> The biocatalytic reaction involves reduction of the flavin adenine dinucleotide (FAD) in the GOx by reacting with glucose to generate the reduced form of the enzyme (FADH<sub>2</sub>). The FADH<sub>2</sub> can be oxidized by molecular oxygen to regenerate FAD:<sup>70</sup>



The accuracy of GOx based glucose sensors suffers from oxygen dependence or interference by redox-active species.<sup>71</sup> Figure 1.8b represents the second generation glucose sensor that employ artificial electron mediators to overcome oxygen limitation under low pressure of oxygen in the first generation glucose sensors. The mediators such as ferro/ferricyanide, ferrocene, hydroquinone and various redox organic dyes facilitate the electron transfer by shuttling electrons between the electrode and enzyme rapidly.<sup>70</sup>



Where Med<sub>ox</sub> and Med<sub>red</sub> are the oxidized and reduced forms of the electron mediator.

To eliminate the mediator and decrease the applied potential in glucose sensing, the third generation glucose sensors is introduced, as shown in Figure 1. 8c. In this case, electrons are transferred from the enzyme to the electrode directly when the active redox sites and electrode were electrically wired. The effect of possible interferences can be eliminated in this sensing mode. The successful realization of direct electron transfer between enzyme and electrode has a big challenge due to the spatial separation of the donor-acceptor pair. Although extensive efforts has been made on this kind of glucose sensors,

only a few reports provide the level of proof for such mediatorless detection.<sup>70</sup> Thus, further investigations and improvements in the direct charge transport between enzyme and electrodes are desired.

For the enzyme-based glucose sensors, the activity of enzyme is affected by the temperature, humidity, pH and toxic chemicals. What's more, the complicated immobilization procedure of the enzymes on electrode increase the complexity and decrease the reproducibility. In this respect, non-enzymatic glucose sensor is a promising alternative. Instead of use of fragile and relatively difficult enzyme, non-enzymatic glucose sensors enables the electro-oxidation of glucose on electrode directly. Metals (e.g. Pt, Au), alloys (e.g. PtRu, PtPb), metal oxide (e.g. NiO, CuO, RuO<sub>2</sub>) and carbon nanotube/metal(oxide) composites *etc* have been employed as non-enzymatic electrocatalysts.<sup>76</sup> It is widely accepted that the catalytic process of non-enzymatic glucose sensing involves the hydrogen abstraction occurs simultaneously to the adsorption of the organic species. Burke proposed the “incipient hydrous oxide adatom mediator ” (IHOAM) model to discuss the importance of hydrous oxide premonolayer formation on the electrocatalytic process.<sup>77</sup> It is found that the “active” surface metal atoms undergo a premonolayer oxidation step to form incipient hydrous oxide layer that mediate the oxidation of the adsorbed species. The process is illustrated in Figure 1.8d.<sup>76</sup> The oxidative adsorbed hydroxide radical ( $M[OH]_{ads}$ ) is formed by the chemisorption of hydroxyl ions to the reductive metal adsorption site ( $M^*$ ) and is proposed to be the catalytic mediator for the glucose oxidation.<sup>72</sup> Considering the importance of hydroxyl ions in the reactions, the increase in the hydroxyl ions concentration will promotes the formation of the oxidative adsorbed hydroxide radical and thus an alkaline environment is beneficial to the non-enzymatic glucose sensing.<sup>72,76</sup>



### 1.7. Nanostructure-based CuO for non-enzymatic glucose sensing

The emergence of nanotechnology has opened new horizons for the application of nanomaterials in electrochemical biosensors. Owing to the higher surface area and improved glucose oxidation kinetics such nanomaterials can be used for effective electrodes for glucose sensing. A variety of metal-based non-enzymatic glucose sensors with different nanostructures have been fabricated with the goal of improving the sensitivity and selectivity of the electrodes. For example, Pt nanoporous material,<sup>78</sup> Au nanowire array,<sup>79</sup> Pt-Pb<sup>80</sup> and Pt-Ir<sup>81</sup> porous electrode *etc* have been reported for the construction of non-enzymatic glucose sensing. However, these materials are high cost, show inadequate sensitivity and selectivity, and undergo poisoning from many species (intermediates, chloride anions *etc.*). To fabricate highly sensitive, low-cost, and fast non-enzymatic glucose sensors, metal oxide such as NiO, CuO, RuO<sub>2</sub> and metal oxide-carbon nanotube composites have been extensively explored as electrocatalysts for glucose sensing in alkaline medium.<sup>73,76</sup> Compared to other metal oxide, CuO is a promising material for heterogeneous catalysis due to its environment friendly, earth-abundant, simple production process and good electrochemical and catalytic properties. CuO has been widely reported as electrodes for non-enzymatic glucose oxidation with high sensitivity and good stability. Many kinds of CuO nanostructures such as nanowires,<sup>82</sup> nanobelts<sup>83</sup> nanorods,<sup>84</sup> nanoplatelets,<sup>85</sup> nanofibers,<sup>86</sup> nanourchins<sup>87</sup>, flowers,<sup>88</sup> and nanospheres<sup>89</sup> have been produced as efficient glucose sensors, benefiting from the improved electrochemically active surface area and enhanced electron transfer ability achieved on the low-dimensional structures. Other multi-dimensional structure such as sandwich-structured CuO (nanocrystals sandwiched in between microsheets) has also

been reported to achieve excellent sensitivity due to the highly accessible surface area and large channel-type porosity.<sup>90</sup> Furthermore, strenuous efforts have been made to combine CuO nanostructures with SWCNTs,<sup>91</sup> MWCNTS<sup>92</sup> and graphene<sup>93</sup> to increase the electroactive surface area as well as improve the conductivity for glucose electro-oxidation. However, the fabrication of most of the nanostructures are complicated and time-consuming. Additionally, most of the nanostructures are prepared by solution processes and the obtained products are in the form of dispersed powders and need to be transferred onto special substrates (e.g., glassy carbon/Au/Pt coated substrate), thus increasing fabrication cost and complexity.<sup>86-90</sup> To avoid the high cost and many limited conditions, it would be important to develop simple method to fabricate CuO nano/micro structures on Cu foil for high performance glucose detection.

### **1.8. Research objectives of CuO-based glucose sensors**

To overcome the limitations of non-enzymatic glucose sensors in terms of cost, simplicity, rapidity and reproducibility, simple approach is needed for the design and development of electrocatalysts based on metal oxide nanostructures. The object of this part is to synthesize CuO nanostructures on a Cu foil directly for electrochemical non-enzymatic glucose sensing with high sensitivity, fast response time and low detection limit. A Cu/Cu<sub>2</sub>O/CuO structure is prepared by annealing Cu/Cu(OH)<sub>2</sub> nanowires precursor under a controlled conditions to enable a good contact between CuO layer and Cu substrate for electron transport. A rational combination of CuO nanowire and microflower on Cu foil is applied to construct high performance CuO-based glucose sensor. The significant role of electrochemically active surface area in glucose oxidation is also investigated systematically by introducing different CuO nano/micro structures on

Cu substrate for glucose sensing.

## References

- [1] de Jongh, P. E.; Vanmaekelbergh, D.; Kelly, J. J. *J. Electrochem. Soc.* **2000**, *147*, 486-489.
- [2] de Jongh, P. E.; Vanmaekelbergh, D.; Kelly, J. J. *Chem. Commun.* **1999**, 1069-1070.
- [3] Paracchino, A.; Brauer, J. C.; Moser, J.-E.; Thimsen E.; Graetzel, M. *J. Phys. Chem. C* **2012**, *116*, 7341-7350.
- [4] Hu, C. C.; Nian, J. N.; Teng, H. *Sol. Energy Mater. Sol. Cells* **2008**, *92*, 1071-1076.
- [5] Nakaoka K.; Ueyama J.; Ogura K. *J. Electrochem. Soc.* **2004**, *151*, C661-C665
- [6] Kothari, H. M.; Kulp, E. A.; Boonsalee, S.; Nikiforov, M. P.; Bohannan, E. W.; Poizot, P.; Nakanishi, S.; Switzer, J. A. *Chem. Mater.* **2004**, *16*, 4232-4244.
- [7] Neupane, M. P.; Kim, Y. K.; Park, I. S.; Kim, K. A.; Lee, M. H.; Bae, T. S. *Surf. Interface. Anal.* **2009**, *41*, 259-263.
- [8] Outokesh, M.; Hosseinpour, M.; Ahmadi, S. J.; Mousavand, T.; Sadjadi, S.; Soltanian, W. *Ind. Eng. Chem. Res.* **2011**, *50*, 3540-3554.
- [9] Gao, X.; Bao, J.; Pan, G.; Zhu, H.; Huang, P.; Wu, F.; Song, G. *J. Phys. Chem. B* **2004**, *108*, 5547-5551.
- [10] Yang, C.; Su, X.; Xiao, F.; Jian, J.; Wang, J. *Sensor Actuat B: Chem.* **2011**, *158*, 299-303.
- [11] Yu, H. G.; Yu, J. G.; Liu, S. W.; Mann, S. *Chem. Mater.* **2007**, *19*, 4327-4334.
- [12] Ai, Z. H.; Zhang, L. zhi.; Lee S. C.; Ho W. K. *J. Phys. Chem. C*, **2009**, *113*, 20896-20902
- [13] Zhang, Y.; Deng, B.; Zhang, T. R.; Gao D. M.; Xu A. W. *J. Phys. Chem. C* **2010**, *114*, 5073-5079.
- [14] Zheng, Z. K.; Huang, B. B.; Wang, Z. Y.; Guo, M.; Qin, X. Y.; Zhang, X. Y.; Wang P.; Dai Y. *J. Phys. Chem. C*, **2009**, *113*, 14448-14453.
- [15] Peterson, N. L.; Wiley, C. L. *J. Phys. Chem. Solids* **1984**, *45*, 281-294.
- [16] Mrowec, S.; Stokłosa, A. *Oxid. Met.* **1971**, *3*, 291-311.
- [17] Sohn, J. S.; Song, S. H.; Nam, D. W.; Cho, I. T.; Cho, E. S.; Lee J. H.; Kwon H. I. *Semicond. Sci. Technol.* **2013**, *28*, 015005.
- [18] Haugrud, R. *J. Electrochem. Soc.* **2002**, *149*, B14-B21.
- [19] Li, J.; Vizkelethy, G.; Revesz, P.; Mayer, J. W.; Tu, K. N. *J. Appl. Phys.* **1991**, *69*, 1020.
- [20] Zhu, Y.; Mimura, K.; Isshiki, M. *Mater. Trans.* **2002**, *43*, 2173-2176.
- [21] Brattain, W. H. *Rev. Mod. Phys.* **1951**, *23*, 203.
- [22] Meyer, B. K.; Polity, A.; Reppin, D.; Becker, M.; Hering, P.; Klar, P. J.; Sander, T.;

- Reindl, C.; Benz, J.; Eickhoff, M.; Heiliger, C.; Heinemann, M.; Bläsing, J.; Krost, A.; Shokovets, S.; Müller, C.; Ronning, C. *Phys. Stat. Sol. (b)* **2012**, *249*, 1487-1509.
- [23] Korzhavyi, P. A.; Johansson, B. Literature review on the properties of cuprous oxide Cu<sub>2</sub>O and the process of copper oxidation, Swedish Nuclear Fuel and Waste Management Company, 2011.
- [24] Olsen, L. C.; Bohara, R. C.; Urie, M. W. *Appl. Phys. Lett.* **1979**, *34*, 47.
- [25] Minami, T.; Nishi, Y.; Miyata, T. *Appl. Phys. Express* **2015**, *8*, 022301.
- [26] Minami, T.; Nishi, Y.; Miyata, T. *Appl. Phys. Express* **2013**, *6*, 044101.
- [27] Zhang, Q.; Zhang, K.; Xu, D.; Yang, G.; Huang, H.; Nie, F.; Liu, C.; Yang, S. *Prog. Mater. Sci.* **2014**, *60*, 208–337.
- [28] Forsyth, J. B.; Hull, S. *J. Phys.: Condens. Matter* **1991**, *3*, 5257.
- [29] Ahmad, R.; Vaseem, M.; Tripathy, N.; Hahn Y. B. *Anal. Chem.* **2013**, *85*, 10448-10454.
- [30] Zhang, J. T.; Liu, J. F.; Peng, Q.; Wang, X.; Li, Y. D. *Chem. Mater.* **2006**, *18*, 867-871.
- [31] Wang, S. B.; Hsiao, C. H.; Chang, S. J.; Lam, K. T.; Wen, K. H.; Hung, S. C.; Young, S. J.; Huang B. R. *Sensors Actuat A: Phys.* **2011**, *171*, 207–211.
- [32] Hsieh, C. T.; Chen, J. M.; Lin, H. H.; Shih, H. C. *Appl. Phys. Lett.* **2003**, *83*, 3383.
- [33] Bandara, J.; Udawatta, C. P. K.; Rajapakse, C. S. K.; *Photochem. Photobiol. Sci.* **2005**, *4*, 857-861.
- [34] Xiang, J. Y.; Tu, J. P.; Zhang, L.; Zhou, Y.; Wang, X. L.; Shi, S. J. *J. Power Sources* **2010**, *195*, 313–319.
- [35] Yang, L. X.; Luo, S. L.; Li, Y.; Xiao, Y.; Kang, Q.; Cai, Q. Y. *Environ. Sci. Technol.* **2010**, *44*, 7641–7646.
- [36] Lin, C. Y.; Lai, Y. H.; Mersch, D.; Reisner, E. *Chem. Sci.* **2012**, *3*, 3482-3487.
- [37] Zhang, Z. H.; Dua, R.; Zhang, L. B.; Zhu, H. B.; Zhang, H. N.; Wang, P. *ACS Nano* **2013**, *7*, 1709–1717.
- [38] Cherevko, S.; Chung, C. H. *Talanta* **2010**, *80*, 1371-1377.
- [39] Chen, X. H.; Kong, L. H.; Dong, D.; Yang, G. B.; Yu, L. G.; Chen, J. M.; Zhang, P. Y. *J. Phys. Chem. C* **2009**, *113*, 5396–5401.
- [40] "2014 Key World Energy Statistics".  
<http://www.iea.org/publications/freepublications/>. IEA. 2014.
- [41] Bilgen, S. *Renew. Sust. Energ. Rev.* **2014**, *38*, 890-902.
- [42] Herron, J. A.; Kim, J. Y.; Upadhye, A. A.; Huber, G. W.; Maravelias, C. T. *Energy Environ. Sci.* **2015**, *8*, 126-157.
- [43] Appleton, E. V. *Nature* **1945**, *156*, 534-535.

- [44] "Exergy Flow Charts - GCEP". stanford.edu.
- [45] Lewis, N. S.; Nocera, D. G. *PNAS* **2006**, *103*, 15729-15735.
- [46] Grätzel, M. *Nature* **2011**, *414*, 338-344.
- [47] Kelly, N. A.; Gibson, T. L.; Ouwerkerk, D. B. *Int. J. Hydrogen Energy* **2008**, *33*, 2747-2764.
- [48] Sivula, K. *J. Phys. Chem. Lett.* **2015**, *6*, 975-976.
- [49] Sivula, K.; Le Formal, F.; Grätzel, M. *ChemSusChem* **2011**, *4*, 432 – 449.
- [50] Walter, M. G.; Warren, E. L.; McKone, J. R.; Boettcher, S. W.; Mi, Q. X.; Santori, E. A.; Lewis, N. S. *Chem. Rev.* **2010**, *110*, 6446-6473.
- [51] Gerischer, H. *J. Electroanal. Chem.* **1977**, *82*, 133-143.
- [52] Li, Z. S.; Luo, W. J.; Zhang, M. L. Feng J. Y.; Zou Z. G. *Energy Environ. Sci.* **2013**, *6*, 347-370.
- [53] Bard, A. J.; Wrighton, M. S. *J. Electrochem. Soc.* **1977**, *124*, 1706-1710.
- [54] Fujishima, A.; Honda, K. *Nature* **1972**, *238*, 37-38.
- [55] Liu, C.; Dasgupta, N. P.; Yang, P. D. *Chem. Mater.* **2014**, *26*, 415-422.
- [56] Park, J. H.; Kim, S. W.; Bard, A. J. *Nano Lett.* **2006**, *6*, 24-28.
- [57] Wang, G. M.; Wang, H. Y.; Ling, Y. C.; Tang, Y. C.; Yang, X. Y.; Fitzmorris, R. C.; Wang, C. C.; Zhang, J. Z.; Li, Y. *Nano Lett.*, **2011**, *11*, 3026-3033.
- [58] Su, J. Z.; Feng, X. J.; Sloppy, J. D.; Guo, L. J.; Grimes, C. A. *Nano Lett.* **2011**, *11*, 203-208.
- [59] Biswas, S. K.; Baeg, J. O. *Int. J. Hydrogen Energy* **2013**, *38*, 3177-3188.
- [60] Seger, B.; Pedersen, T.; Laursen, A. B.; Vesborg, P. C. K.; Hansen, O.; Chorkendorff, I. *J. Am. Chem. Soc.* **2013**, *135*, 1057-1064.
- [61] Lee, M. H.; Takei, K.; Zhang, J. J.; Kapadia, R.; Zheng, M.; Chen, Y. Z.; Nah, J. H.; Matthews, T. S.; Chueh, Y. L.; Ager, J. W.; Javey, A. *Angew. Chem. Int. Ed.* **2012**, *51*, 10760-10764.
- [62] Paracchino, A.; Laporte, V.; Sivula, K.; Grätzel, M.; Thimsen, E. *Nat. Mater.* **2011**, *10*, 456-461.
- [63] Caballero-Briones, F.; Artés, J. M.; Díez-Pérez, I.; Gorostiza, P.; Sanz, F. *J. Phys. Chem. C* **2009**, *113*, 1028- 1036.
- [64] Siripala, W.; Ivanovskaya, A.; Jaramillo, T. F.; Baeck, S. H.; McFarland, E. W. *Sol. Energy Mater. Sol. Cells* **2003**, *77*, 229-237.
- [65] Tilley, S. D.; Schreier, M.; Azevedo, J.; Stefik, M.; Grätzel, M. *Adv. Funct. Mater.* **2014**, *24*, 303-311.
- [66] Morales-Guio, C. G.; Hu, X. L. *Acc. Chem. Res.* **2014**, *47*, 2671-2681.
- [67] Morales-Guio, C. G.; Tilley, S. D.; Vrubel, H.; Grätzel, M.; Hu, X. l. *Nat. Commun.*

**2014**, *5*, 3059

- [68] Dai, P. C.; Li, W.; Xie, J.; He, Y. M.; Thorne, J.; McMahon, G.; Zhan, J. H.; Wang, D. W. *Angew. Chem.-Int. Edit.* **2014**, *53*, 13493-13497.
- [69] Ronkainen, N. J.; Halsall, H. B.; Heineman, W. R. *Chem. Soc. Rev.* **2010**, *39*, 1747-1763.
- [70] Wang, J. *Chem. Rev.* **2008**, *108*, 814-825.
- [71] Park, S.; Boo, H.; Chun, T. D. *Anal. Chim. Acta.* **2006**, *556*, 46-57.
- [72] Chen, C.; Xie, Q. J.; Yang, D. W.; Xiao, H. L.; Fu, Y. C.; Tan, Y. M.; Yao, S. Z. *RSC Adv.* **2013**, *3*, 4473-4491.
- [73] Rahman, M. M.; Ahammad, A. J.; Jin, J. H.; Ahn, S. J.; Lee J. J. *Sensors* **2010**, *10*, 4855-4886.
- [74] Clark, L., Jr.; Lyons, C. *Ann. NY Acad. Sci.* **1962**, *102*, 29.
- [75] Updike, S. J.; Hicks, G. P. *Nature* **1967**, *214*, 986 - 988.
- [76] Toghiani, K. E.; Compton, R. G. *Int. J. Electrochem. Sci.* **2010**, *5*, 1246-1301.
- [77] Burke, L. D. *Electrochim. Acta* **1994**, *39*, 1841-1848.
- [78] Park, S.; Chung, T. D.; Kim, H. C. *Anal. Chem.* **2003**, *75*, 3046-3049.
- [79] Cherevko, S.; Chung C. H. *Sens. Actuators, B* **2009**, *142*, 216-223.
- [80] Wang, J.; Thomas, D. F.; Chen, A. *Anal. Chem.* **2008**, *80*, 997-1004.
- [81] Holt-Hindle, P.; Nigro, S.; Asmussen, M.; Chen, A. *Electrochem. Commun.* **2008**, *10*, 1438-1441.
- [82] Zhuang, Z.; Su, X.; Yuan, H.; Sun, Q.; Xiao, D. Choi, M. M. F. *Analyst*, **2008**, *133*, 126-132.
- [83] Soejima, T.; Yagyu, H.; Kimizuka, N.; Ito, S. *RSC Adv.* **2011**, *1*, 187-190.
- [84] Li, C. L.; Su, Y.; Zhang, S. W.; Lv, X. Y.; Xia, H. L.; Wang, Y. J. *Biosens. Bioelectron.* **2010**, *26*, 903-907
- [85] Wang, J.; Zhang, W. D. *Electrochim. Acta* **2011**, *56*, 7510-7516.
- [86] Wang, W.; Zhang, L.; Tong, S.; Li, X.; Song, W. *Biosens. Bioelectron.* **2009**, *25*, 708-714.
- [87] Sun, S.; Zhang, X.; Sun, Y.; Yang, S.; Song, X.; Yang, Z. *ACS Appl. Mater. Interfaces* **2013**, *5*, 4429-4437.
- [88] Wang, X.; Hu, C. G.; Liu, H.; Du, G. J.; He, X. S.; Xi, Y. *Sens. Actuators, B* **2010**, *144*, 220-225.
- [89] Reitz, E.; Jia, W.; Gentile, M.; Wang, Y.; Lei, Y. *Electroanalysis* **2008**, *20*, 2482-2486.
- [90] Meher, S. K.; Rao, G. R.; *Nanoscale* **2013**, *5*, 2089-2099.
- [91] Jiang, L. C.; Zhang, W. D. *Biosens. Bioelectron.* **2010**, *25*, 1402-1407.

[92] Yang, J.; Jiang, L. C.; Zhang, W. D.; Gunasekaran, S. *Talanta* **2010**, 82, 25-33.

[93] Hsu, Y. W.; Hsu, T. K.; Sun, C. L.; Nien, Y. T.; Pu, N. W.; Ger, M. D. *Electrochim. Acta* **2012**, 82, 152-157.



## **2. Fabrication of photoactive Cu<sub>2</sub>O films for photoelectrochemical cells**

Large-scale and high-quality Cu<sub>2</sub>O microcrystalline films with high photoactivity are synthesized using a novel and low-cost method. The enhanced photoactivity is achieved through the formation of Cu<sub>2</sub>O microcrystalline films having well-defined crystal facets and porous structure. Cu<sub>2</sub>O microcrystalline films are fabricated by decomposing previously synthesized Cu(OH)<sub>2</sub> nanowires on a Cu foil under a vacuum. Subsequent crystal growth during the annealing process is driven by outward diffusion of Cu ions and oxidation. Crystal growth induces coalescence of the nanowires and results in the formation of Cu<sub>2</sub>O microcrystals enclosed by four {111} facets. Photoelectrochemical evaluation of the annealed samples performed under chopped simulated AM 1.5G illumination reveals that the sample annealed at 500°C for 2 h exhibited the highest photocurrent of 4.07 mA/cm<sup>2</sup> at 0 V/RHE. This large photocurrent is ascribed to a high carrier density ( $\sim 1.36 \times 10^{18} \text{ cm}^{-3}$ ) and a low carrier transfer resistance in electrolyte, as evidenced by electrochemical impedance spectroscopy. The obtained low-cost Cu<sub>2</sub>O microcrystalline film (2 h) may serve as an excellent solar absorber and carrier provider for use in photovoltaics and artificial photosynthesis.

## 2.1. Introduction

Cuprous oxide ( $\text{Cu}_2\text{O}$ ) is a well-known metal-deficit p-type semiconductor with holes as the charge carriers.<sup>1-2</sup> The direct energy bandgap of 1.9 – 2.5 eV makes it a promising material for solar energy conversion. In addition, the position of the conduction band (more negative than -0.7 V vs. RHE) provides a large driving force for proton reduction in photoelectrochemical cells.<sup>3-5</sup> Thus,  $\text{Cu}_2\text{O}$  has been used as a visible light catalyst for  $\text{H}_2$  production from water,<sup>6-10</sup> electrocatalyst for  $\text{CO}_2$  reduction,<sup>11</sup> and high open-circuit voltage solar cell in the configuration of conventional solid state<sup>12</sup> or semiconductor/liquid junctions.<sup>13</sup>

Electrodeposition<sup>3-5, 14</sup> and thermal oxidation of  $\text{Cu}$ <sup>1-2</sup> are the two most common methods for the fabrication of  $\text{Cu}_2\text{O}$  films. Several studies on  $\text{Cu}_2\text{O}$  photocathodes for water splitting prepared by electrodeposition showed that water can hardly be split by  $\text{Cu}_2\text{O}$  via a normal photocatalytic reaction<sup>3-5, 14</sup> and under some conditions the observed small photocurrent can be attributed to the reduction of oxygen in the solution.<sup>3-4</sup> The low photoactivity of those  $\text{Cu}_2\text{O}$  polycrystalline films and powder may be due to the low carrier density and inefficient charge transport, thus limiting the overall water splitting performances when  $\text{Cu}_2\text{O}$  was used in combination with other n-type materials.<sup>6, 14</sup> However, by controlling the electrodeposition parameters (e.g., temperature and pH) properly, Paracchino *et al.*<sup>5</sup> reported a high photocurrent of 2.4  $\text{mA}/\text{cm}^2$  at 0.25 V vs. RHE for a bare  $\text{Cu}_2\text{O}$  film under AM 1.5G illumination. Although part of the current originated from the reduction of  $\text{Cu}_2\text{O}$  to  $\text{Cu}$ , highly active and stable photocathodes for  $\text{H}_2$  production were obtained after coating  $\text{Cu}_2\text{O}$  by protective layers.<sup>7, 15-16</sup> Similarly, the PEC performance of the unstable  $\text{Cu}_2\text{O}$  electrodes with a high photocurrent of about 2.5  $\text{mA}/\text{cm}^2$  at 0 V vs. RHE prepared by thermal annealing of  $\text{Cu}(\text{OH})_2$  can also be optimized

by carbon coating.<sup>10</sup> Coating of the bare Cu<sub>2</sub>O with appropriate protective layers is essential for efficient and stable water splitting and the photoactivity of Cu<sub>2</sub>O is crucial for the efficiency of the Cu<sub>2</sub>O/protective layer structure.

In this chapter, A highly photoactive Cu<sub>2</sub>O microcrystalline film exhibiting a considerably large photocurrent of 4.07 mA/cm<sup>2</sup> (0 V vs. RHE) in PEC measurement under standardized AM 1.5 light illumination was obtained. Cu<sub>2</sub>O films were prepared by thermal decomposition of Cu(OH)<sub>2</sub> nanowires under a proper annealing pressure at 500 °C. The Cu<sub>2</sub>O film morphology was continuously modified with the annealing time. The Cu<sub>2</sub>O film annealed for 2 h achieved the highest photocurrent as well as the largest carrier density ( $\sim 1.36 \times 10^{18} \text{ cm}^{-3}$ ) compared to the 1, 3 and 4 h samples. The high photoactivity and robust Cu<sub>2</sub>O film may serve as an excellent substrate for light absorption and carrier provider for the application of photoelectrolysis and photovoltaics.

## **2.2. General experimental section**

### **2.2.1. Photoelectrochemical and electrochemical impedance measurements**

The photoelectrochemical performance of the Cu<sub>2</sub>O electrodes was performed in a three-electrode configuration using an Ag/AgCl reference electrode and a Pt wire counter electrode. The electrolyte was a 0.5 M Na<sub>2</sub>SO<sub>4</sub> solution with a pH of 6. The Na<sub>2</sub>SO<sub>4</sub> solution was stirred and purged with Ar gas before the measurements (for 10 min) and during the measurements. The photoresponse was measured under chopped AM 1.5G simulated sunlight corresponding to an irradiance of 100 mW/cm<sup>2</sup>. The scan rate for the linear sweep voltammetry was 10 mV/s.

The electrochemical impedance measurements of the Cu<sub>2</sub>O films were carried out under dark condition using a potentiostat (VersaSTAT 4, Princeton Applied Research)

with an AC amplitude of 10 mV and a frequency of 1 kHz. An aqueous solution of 0.01 M PBS (phosphate buffer saline, pH 7.4) was used as the electrolyte.

### **2.2.2. Structural characterization**

The morphology of the samples was characterized by using field-emission scanning electron microscope (JEOL JSM 7600FA). The X-ray diffraction (XRD) patterns were determined using a diffractometer (Miniflex II-MW, Rigaku Co. Ltd., Japan) with Cu K $\alpha$  radiation. The Raman spectra of the samples were measured with a Renishaw inVia Raman Microscope system using a 488 nm excitation light directed through a  $\times 20$  objective with 1.21 mW for top surface analysis and  $\times 100$  objective with 0.1 mW for cross-section analysis. The UV-Vis diffuse reflectance spectra were determined with a spectrophotometer (DRS, V-560, Jasco).

## **2.3. Cu<sub>2</sub>O microcrystalline film formed at 500° C from Cu(OH)<sub>2</sub> nanowires**

### **2.3.1. Fabrication of Cu(OH)<sub>2</sub> nanowires and Cu<sub>2</sub>O microcrystalline films**

The Cu(OH)<sub>2</sub> nanowires were grown on a Cu foil using a simple and scalable solution method.<sup>17</sup> A typical fabrication process was performed as follows. The Cu foil (99.96%, Nilaco) with a size of 10 $\times$ 10 mm<sup>2</sup> and a thickness of 0.2 mm was cleaned sequentially in acetone and ethanol ultrasonic bath for 10 min. The cleaned Cu foil was then immersed into a solution containing 2.67 M NaOH (97.0%, Wako) and 0.133 M (NH<sub>4</sub>)<sub>2</sub>S<sub>2</sub>O<sub>8</sub> (98.0%, Wako) for 10 min. In addition, gentle stirring of the solution at low temperature (5°C) was implemented to prevent the formation of CuO flowers on the Cu(OH)<sub>2</sub> nanowires. CuO flowers were found to grow under the conditions of inhomogeneous solution and increase in temperature near the Cu/solution interface caused by the chemical reaction. Finally, the

Cu foil with a light blue color was taken out from the solution, rinsed with deionized water, and dried in air.

The Cu<sub>2</sub>O microcrystalline films were prepared by annealing the Cu(OH)<sub>2</sub> nanowires at 500°C for different times under an Ar atmosphere. More specifically, the Cu(OH)<sub>2</sub> nanowires/Cu foil was loaded into an alumina boat and placed at the center of a quartz tube. The quartz tube was evacuated to about 36 Pa before heating and the flow rate of Ar was 50 sccm during the annealing. The working pressure during the annealing was kept at about  $2.5 \times 10^3$  Pa. The Cu(OH)<sub>2</sub> nanowires/Cu samples were annealed at 500 °C for 1, 2, 3 and 4 h to obtain Cu<sub>2</sub>O microcrystalline films with different morphologies.

### **2.3.2. Morphology of the structures**

The Cu(OH)<sub>2</sub> nanowires were prepared on a Cu foil by a wet chemical method in sodium hydroxide and ammonium solution, as reported previously.<sup>23</sup> The synthesized Cu(OH)<sub>2</sub> nanowires, shown in the Figure 2.1a, have a diameter of approximately 200 nm and a length of about 5 μm. The XRD pattern (Figure 2.1b) indicates that only Cu(OH)<sub>2</sub> and Cu peaks can be found in the Cu(OH)<sub>2</sub> nanowires/Cu structure. After annealing under an Ar atmosphere at 500 °C, the Cu(OH)<sub>2</sub> nanowires were completely transformed into Cu<sub>2</sub>O by dehydration of Cu(OH)<sub>2</sub> into CuO at about 120 °C and further removal of oxygen from CuO leading to the formation of Cu<sub>2</sub>O at higher temperature.<sup>18</sup> The sample morphology was found to continuously vary with the annealing time. The nanowires coalesced to larger crystals and the size of the crystals increased with annealing time. Figure 2.2 (a)-(d) show the SEM images of Cu<sub>2</sub>O films prepared under Ar atmosphere at 500 °C for 1, 2, 3 and 4 h, respectively. For the 1 h sample shown in Figure 2.2a, it is found that the neighboring nanowires merge into larger micro-nano aggregates (~0.5 μm)

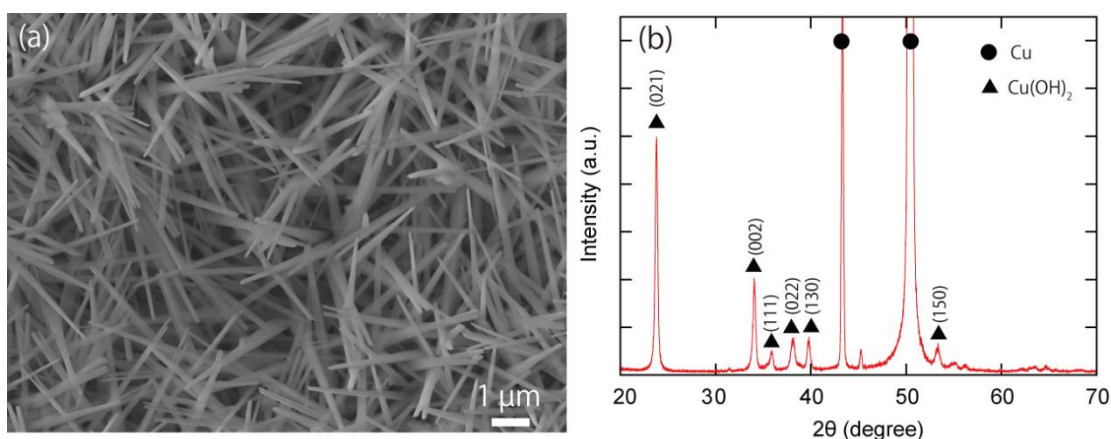


**Figure 2.1.** (a) SEM image of the  $\text{Cu}(\text{OH})_2$  nanowires on Cu substrate and (b) XRD pattern of the Cu/ $\text{Cu}(\text{OH})_2$  nanowire structures.

having their tips enclosed by four incomplete  $\{111\}$  facets. For the longer annealing time of 2 h, larger microcrystals are observed and their mean size increases to  $1.5\ \mu\text{m}$ , as shown in figure 2.2b. The inset of Figure 2.2b is evidence for the formation of some microcrystals completely covered by smooth  $\{111\}$  facets. When the annealing time is further increased to 3 h (Figure 2.2c), the size of the microcrystals was increased to  $2\ \mu\text{m}$  and most of the crystals display a four  $\{111\}$  facet tip (inset of Figure 2.2c). At the longest time (4 h, Figure 2.2d), irregular microcrystals with a size of about  $2.5\ \mu\text{m}$  were observed which indicates that a long annealing time at  $500\ ^\circ\text{C}$  degrades the regularity of the crystals to some extent. The formation of the microcrystals was presumably induced by an appropriate oxygen partial pressure during the annealing process. Indeed, the base pressure (36 Pa) in the vacuum furnace is relatively high compared to other results obtained in high-vacuum annealing systems.<sup>8-10</sup> To confirm the effect of the oxygen partial pressure, we annealed the  $\text{Cu}(\text{OH})_2$  nanowires in a high-vacuum chamber ( $\sim 10^{-5}$  Pa) at  $500\ ^\circ\text{C}$  for 3 h and found that the nanowire structure was not changed, that is, no morphology reconstruction was observed, in agreement with previous reports.<sup>8-10</sup> The mechanism of the surface reconstruction coalescence may be explained as follows. For

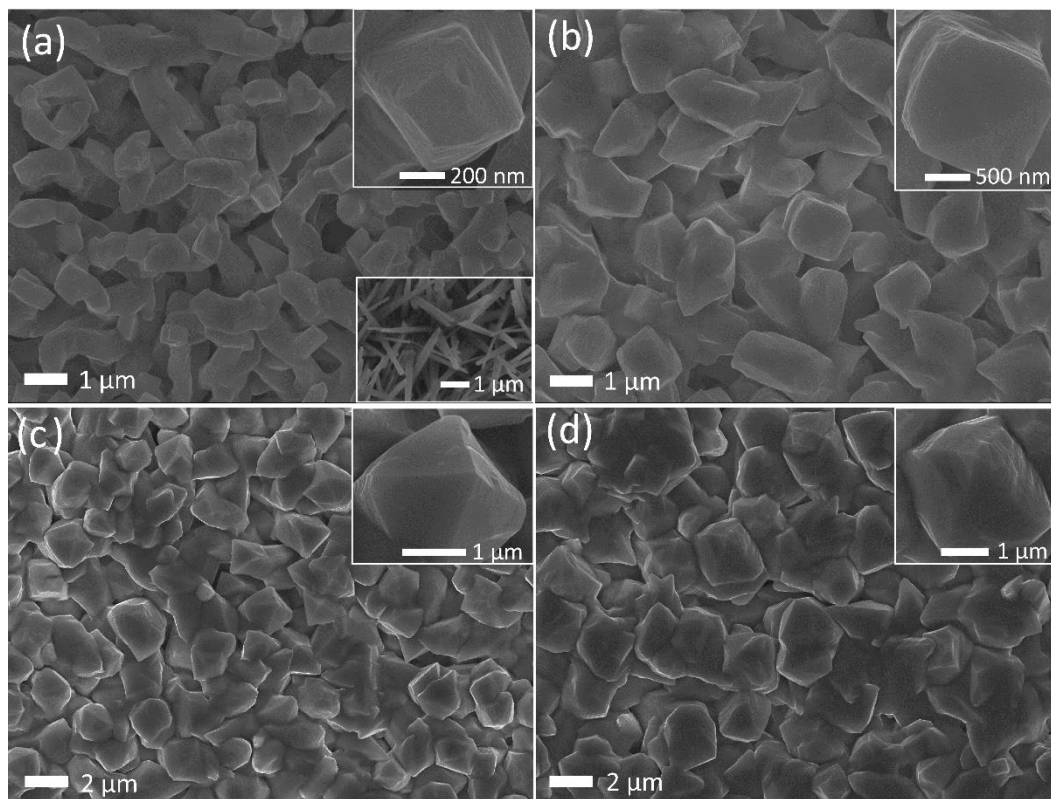


**Figure 2.2.** FE-SEM images of the  $\text{Cu}_2\text{O}$  films prepared at 500 °C with different annealing time. (a)-(d)  $\text{Cu}_2\text{O}$  microcrystalline films prepared at 500 °C for 1, 2, 3 and 4 h, respectively. The top-right insets in all images are the enlarged images of the microcrystal and the lower right inset in (a) is the  $\text{Cu}(\text{OH})_2$  nanowires before annealing.

low  $\text{O}_2$  partial pressure, the high temperature annealing ( $\sim 500$  °C) will only separate the oxygen from the lattice of  $\text{CuO}$  to form  $\text{Cu}_2\text{O}$  and the stress resulting from the phase change bend the nanowires.<sup>9-10</sup> For high  $\text{O}_2$  partial pressure, the temperature and oxygen partial pressure of this experiment is considered to be in the region of stability of  $\text{Cu}_2\text{O}$  according to the phase diagram.<sup>19</sup> Thus, besides the removal of oxygen from the lattice of  $\text{CuO}$  to form  $\text{Cu}_2\text{O}$ , the growth of the  $\text{Cu}_2\text{O}$  layer proceeds under this pressure by outward diffusion of Cu ions from the Cu substrate via Cu vacancies to the oxide/oxygen interface and react with the oxygen from the gas phase.<sup>2, 20-21</sup> The oxidation reaction on

the surface leads to a volume expansion of the nanowires and consequently coalescence of the nanowires. Finally, large crystals enclosed by low surface energy facets {111} are formed in order to minimize the total surface energy of the system.<sup>22</sup> The thickness of the oxide layers was estimated to be 7.5, 18.5, 28. and 37.  $\mu\text{m}$  for the annealing times of 1, 2, 3 and 4 h, respectively. In summary, subsequent growth of the  $\text{Cu}_2\text{O}$  crystals from nanowires induces oxide growth along the nanowires so that the grown crystals offer well-defined exposed crystal facets as well as clear separation between each crystal providing large surface area for chemical reaction.

### **2.3.3. XRD and Raman Characterization**

The XRD patterns of the  $\text{Cu}_2\text{O}$  microcrystalline films prepared at 500 °C for different annealing times are shown in Figure 2.3. The results suggest the coexistence of two types of  $\text{Cu}_2\text{O}$  phases in the films. For the 1 h annealed sample, two sets of diffraction peaks are clearly seen and the diffraction peaks are well indexed to the peaks of the cubic structure  $\text{Cu}_2\text{O}$ -I (indicated by dashed line, space group Pn-3m, lattice constant 4.2600 Å, ICDD PDF card No. 1010941) and the  $\text{Cu}_2\text{O}$ -II (indicated by solid line, space group Pn-3m, lattice constant 4.2685 Å, ICDD PDF card No. 9007497). As the annealing time increases, the intensity of the  $\text{Cu}_2\text{O}$ -I peaks decreases and simultaneously the intensity of  $\text{Cu}_2\text{O}$ -II peaks increases. For an annealing time of 4 h and judging from the XRD pattern, the sample was completely transformed into the  $\text{Cu}_2\text{O}$ -II phase. The change of the intensity of Cu peaks may be explained by the outward diffusion of Cu ions from the Cu foil to the oxide layer. Cu ions outward diffusion should be supported by the gradient of Cu vacancies between the oxide/oxygen interface (high concentration) and Cu/oxide interface (low concentration).<sup>2, 20-21</sup> In addition to the outward lattice diffusion of Cu ions



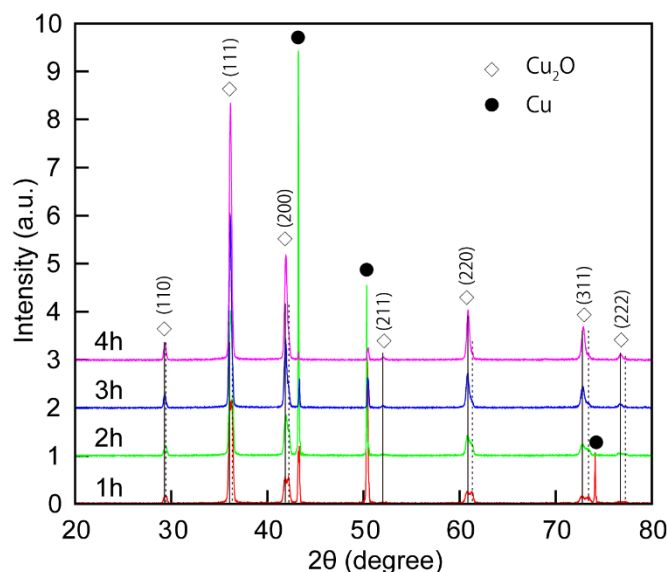


**Figure 2.3.** XRD patterns of the  $\text{Cu}_2\text{O}$  samples obtained by annealing the  $\text{Cu}(\text{OH})_2$  nanowires at  $500^\circ\text{C}$  for 1, 2, 3 and 4 h. The two phases of  $\text{Cu}_2\text{O}$  are indexed using the ICDD PDF cards No. 9007497 and No. 1010941 and indicated by solid line and dashed line, respectively.

under high temperature (above  $800\text{--}900^\circ\text{C}$ ), grain-boundary diffusion becomes relevant at low annealing temperature ( $500^\circ\text{C}$ ).<sup>23-24</sup> Thus, diffusion through lattice may account for the continuous increase in the  $\text{Cu}_2\text{O}$  oxide layer,<sup>24</sup> whereas Cu ions via grain-boundary diffusion may accumulate and form Cu grains embedded in the oxide layer as detected by XRD. When the annealing time increases from 1 to 2 h, the increase in the Cu peaks may due to the continuous migration of Cu ions through  $\text{Cu}_2\text{O}$  grain-boundary and thus more Cu grains accumulated in the  $\text{Cu}_2\text{O}$  layer. With further increase in the annealing time (3 and 4 h), the thickness of the oxide layer increases further and the grain boundary diffusion should become limited by long range transport, so that the intensity of the  $\text{Cu}_2\text{O}$  peaks increases and the intensity of Cu peaks decreases.

The phase transformation was further confirmed by Raman spectroscopy. The crystal structure of  $\text{Cu}_2\text{O}$  is a cubic lattice with six atoms in the primitive unit cell and belongs

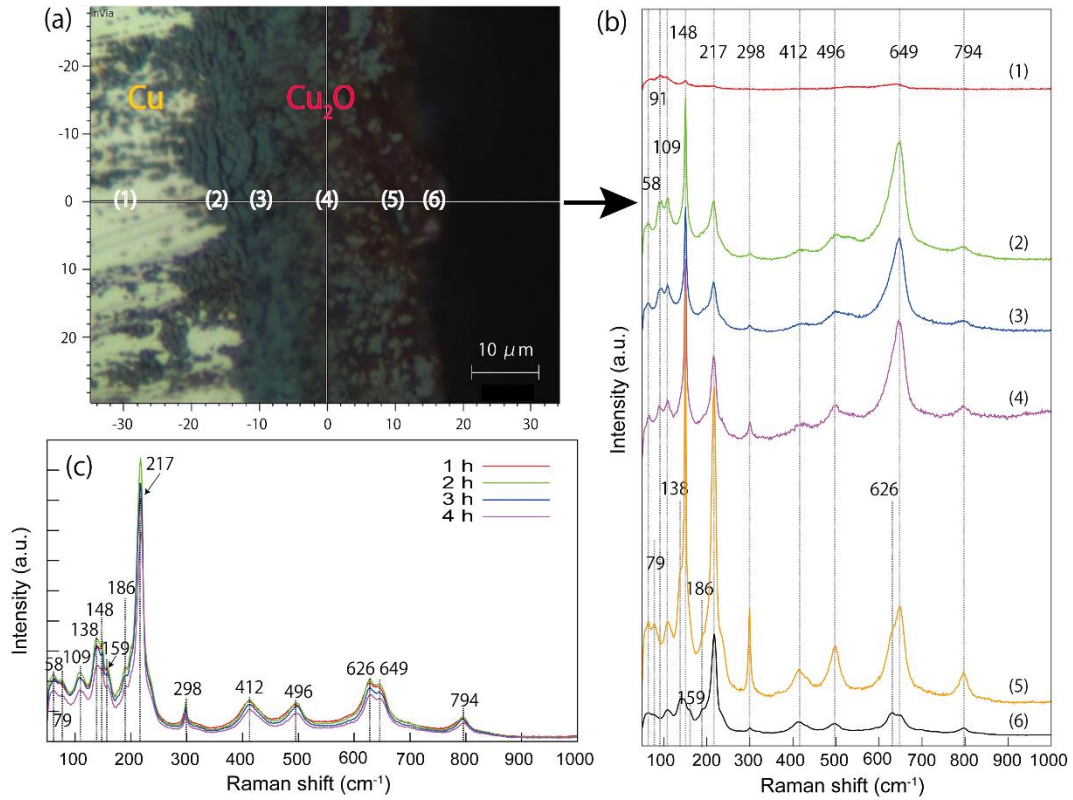


**Figure 2.4.** (a) Optical microscope image of the cross-section of  $\text{Cu}_2\text{O}$  prepared at  $500^\circ\text{C}$  for 3 h. The different positions along the central axis line of the cross-section is marked by symbol (1), (2), (3), (4), (5) and (6), respectively. The Raman spectra taken at these positions are presented in (b). (c) shows the Raman spectra taken from the top surfaces of the  $\text{Cu}_2\text{O}$  samples prepared for the different annealing times of 1, 2, 3 and 4 h.

to the  $\text{Pn-3m}$  space group. In perfect  $\text{Cu}_2\text{O}$  lattice, only the peaks from  ${}^3\Gamma_{25}^+$  (Raman active) and  $2 {}^3\Gamma_{15}^-$  (infrared active) can be observed. However, several Raman scattering studies reported the relaxation of the selection rules resulting from impurity in nonstoichiometric  $\text{Cu}_2\text{O}$ .<sup>25</sup> Figure 2.4c shows the Raman spectra taken from the top surface of the  $\text{Cu}_2\text{O}$  films prepared with different annealing times. The characteristic peaks can be identified as follows:<sup>25</sup> the lines at 148, 626, and  $649 \text{ cm}^{-1}$  are essentially attributed to the intrinsic  $\Gamma_{15}^-$  infrared-allowed (IR) active modes; the lines observed at

412 and 496  $\text{cm}^{-1}$  are interpreted as originating in double photons processes; the line at 217  $\text{cm}^{-1}$  corresponds to the activation of the zone edge photons both in the Raman and in the IR spectra; the line observed at 794  $\text{cm}^{-1}$  is attributed to IR active localized modes; the lines 58, 109 and 298  $\text{cm}^{-1}$  can be ascribed to  $\Gamma_{15}^-$ ,  $\Gamma_{12}^-$  and  $\Gamma_2^-$  band modes, respectively. All samples of figure 2.4c exhibit the same characteristic  $\text{Cu}_2\text{O}$  peaks indicating that all sample surfaces possess similar vibration modes within the penetration depth of the excitation laser. The apparent discrepancy between Raman scattering and XRD results is explained by the greater sensitivity of Raman spectroscopy to the sample surface when compared to XRD analysis.<sup>26-27</sup>

Investigation into the phase depth profile is further conducted by Raman spectroscopy using spot measurements on a cross-section of the 3 h annealed sample. Figure 2.4a shows an optical microscope image of the analyzed sample cross-section with an estimated oxide thickness of 28.2  $\mu\text{m}$ . Six spots marked by (1), (2), (3), (4), (5) and (6) from the Cu substrate to the  $\text{Cu}_2\text{O}$  thick film were chosen to probe phase change in the sample depth. The cross-section Raman spectra exhibit a continuous phase transformation from the outer region to the inner bulk region of  $\text{Cu}_2\text{O}$ , as shown in Figure 2.4b. In the  $\text{Cu}_2\text{O}$  region, the Raman spectrum from the outermost region (spot (6)) has the same characteristic bands as that of the top surface (Figure 2.4c). However, the Raman spectra taken from spots (2), (3) and (4) possessing the same characteristic bands are different from the spot (6) by the absence of the peak at 91  $\text{cm}^{-1}$  ( $\Gamma_{25}^-$ ) and the presence of the peaks at 79  $\text{cm}^{-1}$  (band modes), 138  $\text{cm}^{-1}$ , 159  $\text{cm}^{-1}$  (resonant modes) and 626  $\text{cm}^{-1}$ . From spot (6) to spot (5), the very strong increase in the forbidden 148, 298 and 649  $\text{cm}^{-1}$  lines and Raman-allowed features at 217 and 498  $\text{cm}^{-1}$  are similar to the changes induced by ion-implantation reported by Powell *et al.*<sup>28</sup> The change of the 217 and 498  $\text{cm}^{-1}$  is not clear

at this stage. Since no structural damage from external ion implantation is involved in our samples, the increase in 148, 298 and 649  $\text{cm}^{-1}$  peak intensities is likely caused by the relaxation of symmetry selection rules due to the formation of defects (Cu vacancies or other point defects).<sup>29-31</sup> And the existence of the defects in this region lead to a deviation from stoichiometry and a change of the lattice constant of  $\text{Cu}_2\text{O}$  compared to the  $\text{Cu}_2\text{O}$  on the surface, in agreement with the results in XRD data. In summary, by combining XRD and Raman results, we conclude that for all samples the outer layer should be ascribed to  $\text{Cu}_2\text{O}$ -II while the underneath layer to  $\text{Cu}_2\text{O}$ -I, and the thickness of  $\text{Cu}_2\text{O}$ -II increased with annealing time.

#### 2.3.4. Optical properties

The optical properties of  $\text{Cu}_2\text{O}$  films measured by UV-Vis diffuse reflectance spectra showed that the absorption intensity changes with annealing time, as presented in Figure 2.5a. The improved absorption in the region ranging from 250 to 600 nm for the 1 h annealed sample compared to the samples with larger crystals (2-4 h) may be attributed to its nanostructured morphology enhancing light trapping. In order to evaluate the band gap energy of these films,  $(F(R) \times h\nu)^2$  values for a direct band gap material<sup>14</sup> were plotted versus excitation energy where the absorption coefficient  $F(R)$  was calculated according to the Kubelka-Munk (K-M) equation:<sup>32-33</sup>

$$F(R) = \frac{(1-R)^2}{2R} \quad (2-1)$$

where  $R$  is the reflectance value of the thick  $\text{Cu}_2\text{O}$  layers. The samples annealed at 500 °C with different times have band gap energies between 1.99 and 2.02 eV, in agreement with the reported band gap energy for  $\text{Cu}_2\text{O}$ ,<sup>3, 34</sup> thus realizing efficient conversion of

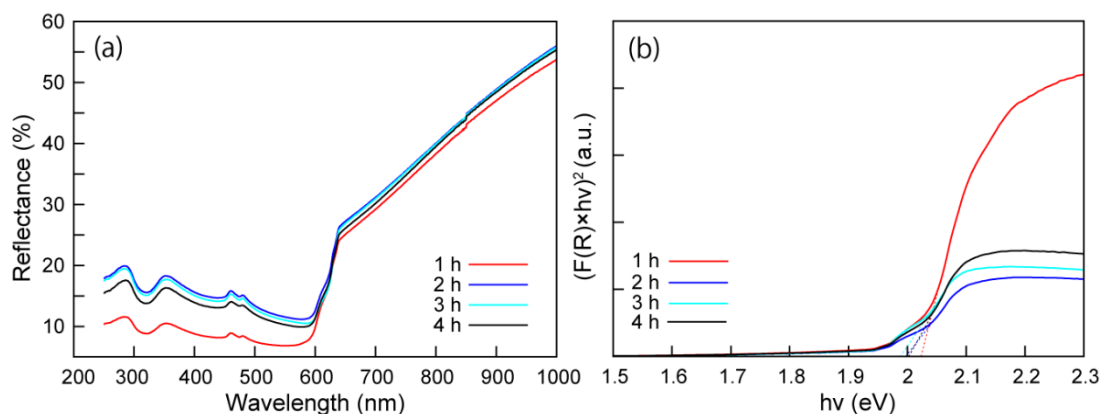


**Figure 2.5.** (a) Diffuse reflectance spectra and (b) calculated Kubelka-Munk function vs. excitation energy plots for the 1, 2, 3 and 4 h annealed samples.

solar energy into chemical energy. The K-M plots of Figure 2.5b also reveal a shoulder in the band edge absorption at 1.95 eV, indicating the presence of doping levels. This result is confirmed later by the high carrier density found in Mott-Schottky analysis.

### 2.3.5. Photoelectrochemical measurements

The photoelectrochemical (PEC) performances of the fabricated  $\text{Cu}_2\text{O}$  electrodes were evaluated in 0.5 M  $\text{Na}_2\text{SO}_4$  (pH = 6) electrolyte by linear sweep voltammetry (LSV) measurements under chopped AM 1.5G simulated sunlight at an irradiance of 100  $\text{mW}/\text{cm}^2$ . A Pt wire and an Ag/AgCl electrode were used as the counter and reference electrodes, respectively. The scan rate was 10 mV/s and the on-off interval was 2 s. The PEC responses of the  $\text{Cu}_2\text{O}$  electrodes prepared with different annealing times are presented in Figure 2.6a. The photocurrent densities of -1.55, -4.07, -2.57 and -2.11  $\text{mA}/\text{cm}^2$  were obtained at 0 V/RHE for the annealing times of 1, 2, 3 and 4 h, respectively. The photocurrents increased slowly for low external applied voltage (0.6 – 0.25 V vs. RHE) and increased rapidly above 0.25 V vs. RHE (voltage sweep is from positive to negative). The best sample annealed for 2 h generated a photocurrent of -4.07  $\text{mA}/\text{cm}^2$  at

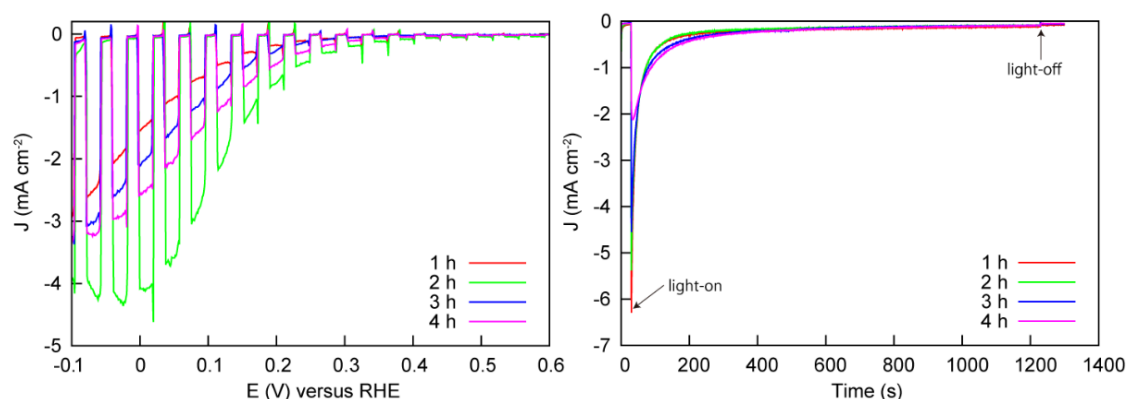


**Figure 2.6.** (a) Photoelectrochemical responses of the electrodes prepared with the samples annealed for the 1, 2, 3 and 4 h. The linear sweep voltammetry scans were conducted in 0.5 M Na<sub>2</sub>SO<sub>4</sub> electrolyte (pH = 6) under chopped AM 1.5G light illumination. (b) Current-time curve of the Cu<sub>2</sub>O electrodes (1, 2, 3 and 4 h) at 0 V vs. RHE under continuous visible light (> 420 nm) illumination of a Xe lamp equipped with a cut-off filter (HOYA; L42).

0 V vs. RHE and reached a plateau at this voltage. Above -0.1 V vs. RHE, the dark current increased due to metal oxide reduction and/or water reduction. The photocurrent of the Cu<sub>2</sub>O electrode (2 h) in our experiment was larger than the 2.5 mA/cm<sup>2</sup> at 0 V vs. RHE of Cu<sub>2</sub>O nanowires fabricated by thermal annealing of Cu(OH)<sub>2</sub> nanowires<sup>10</sup> and that of Cu<sub>2</sub>O film prepared by electrodeposition which saturated at ~2.4 mA/cm<sup>2</sup>.<sup>5</sup> Similarly to previous reports,<sup>5, 7-10</sup> a large proportion of the photocurrent is generated by the reduction of Cu<sub>2</sub>O to Cu, as confirmed by the analysis of the Cu<sub>2</sub>O electrode after water splitting shown in Figure 2.7. The XRD patterns (Figure 2.7b) show an increase in the intensity of the Cu peaks of the Cu<sub>2</sub>O electrode after the photoelectrochemical measurement compared to the original sample. The characteristic peaks of Cu<sub>2</sub>O were found to shift from the Cu<sub>2</sub>O-II (ICDD PDF card No. 9007497) to the Cu<sub>2</sub>O-I (ICDD PDF card No. 1010941), thus suggesting that part of the Cu<sub>2</sub>O-II was consumed and reduced to Cu metal. The nanoparticles formed on the surface of the electrode likely come from this Cu<sub>2</sub>O

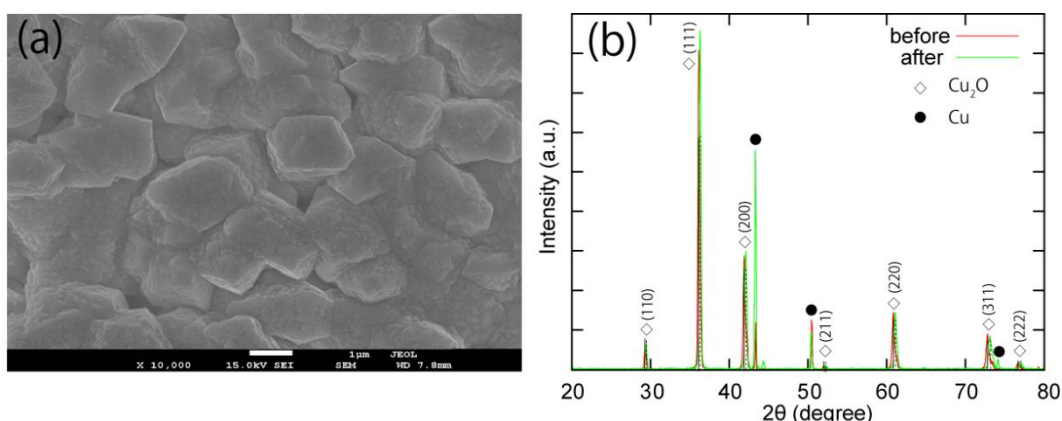


**Figure 2.7.** (a) SEM image of a bare Cu<sub>2</sub>O electrode (3 h) after PEC measurement. (b) XRD before (red line) and after (green line) PEC characterization for the bare Cu<sub>2</sub>O electrode.

reduction, as shown in Figure 2.7a. Three times LSV scans of the Cu<sub>2</sub>O samples taken under visible light ( $> 420$  nm, HOYA L42 cut-off filter) of a Xe lamp indicate an decreased photoactivity and improved stability of the Cu<sub>2</sub>O samples with the annealing time (Figure 2.8). In a stability test, the photocurrent density of the Cu<sub>2</sub>O electrodes decreased to about  $0.11 \pm 0.02$  mA/cm<sup>2</sup> after 20 min under continuous illumination (Figure 2.6b). Although the high photocurrent of the Cu<sub>2</sub>O film partially originated from the reduction of Cu<sub>2</sub>O to Cu on the oxide surface, the large amount of carriers generated under illumination can be collected for efficient water splitting if the carriers can overcome the kinetic barrier at the oxide/electrolyte interface and react with protons. This can be achieved by coating n-type materials on the Cu<sub>2</sub>O surface to generate a built-in field facilitating the transport of minority carriers into the electrolyte and obtain a more stable photocathode.<sup>7, 15-16</sup> Thus, a protective layer is necessary for this structure for stable H<sub>2</sub> production in PEC cells.

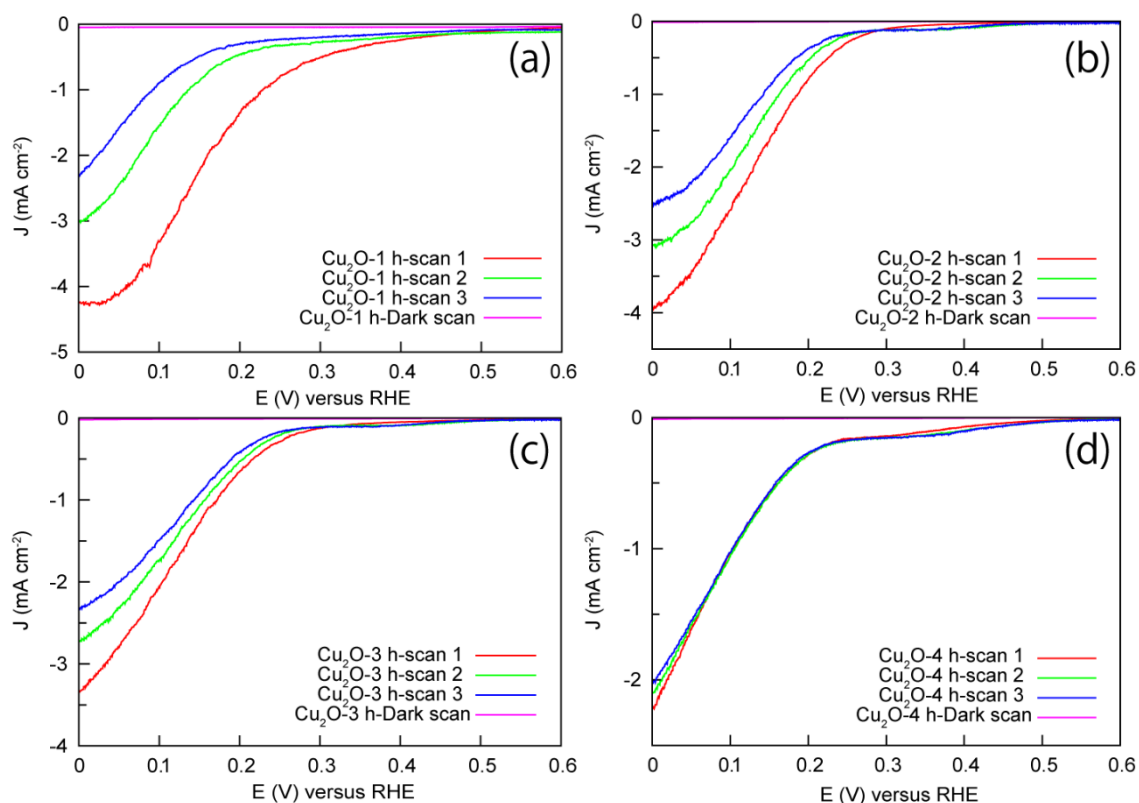


**Figure 2.8.** The linear sweep voltammetry scans of the electrodes prepared with the samples annealed for the 1, 2, 3 and 4 h. The scans conducted in 0.5 M  $\text{Na}_2\text{SO}_4$  electrolyte (pH = 6) under continuous visible light ( $> 420$  nm) illumination of a Xe lamp equipped with a cut-off filter (HOYA; L42), scan rate 20 mV/s, each sample was scanned three times under illumination.

### 2.3.6. Electrochemical impedance

To estimate the flatband potential and charge carrier density, the  $\text{Cu}_2\text{O}$  electrodes were characterized by electrochemical impedance spectroscopy. The potential sweep was performed at a fixed frequency (1 kHz) with a scan speed of 10 mV/s. The flatband potential and charge carrier density can be extracted from the  $x$ -intercept and slope of the plot between the reciprocal of the square of the capacitance per unit area,  $1/C^2$ , versus the applied voltage,  $V$ , according to the Mott-Schottky equation:<sup>35</sup>



$$\frac{1}{C^2} = \left( \frac{2}{e\epsilon\epsilon_0 N_A} \right) [V - V_{fb} - \frac{k_B T}{e}] \quad (2-2)$$

where  $e$  is the electronic charge,  $\epsilon$  is the relative permittivity of Cu<sub>2</sub>O ( $\epsilon$ :  $\sim 7.5$ ),<sup>36</sup>  $\epsilon_0$  is the permittivity of vacuum,  $k_B$  is Boltzmann's constant,  $T$  is the absolute temperature, and  $N_A$  is the carrier density. The active area of the samples were calculated by times geometric area with a roughness factor.<sup>37-38</sup> The roughness factor ( $f_r$ ) is estimated to be 3.2, 2.83, 1.75 and 1.73 for the 1 h, 2 h, 3 h and 4 h annealed sample, respectively. Thus, from the slope ( $k_{MS}$ ) of the lines, the carrier concentration ( $N_A$ ) in the samples could be estimated from the equation:<sup>38</sup>

$$N_A = \frac{2}{e\epsilon\epsilon_0 k_{MS} f_r^2} \quad (2-2)$$

Figure 2.9 shows the Mott-Schottky plot for the Cu<sub>2</sub>O electrodes taken in 0.01 M PBS electrolyte (pH = 7.4). For the Cu<sub>2</sub>O electrodes prepared with an annealing time from 1 to 4 h, the measured flatband potentials and charge carrier densities were 0.69, 0.71, 0.73, 0.78 V vs. RHE and  $4.05 \times 10^{17}$ ,  $1.36 \times 10^{18}$ ,  $5.61 \times 10^{17}$ ,  $3.92 \times 10^{17}$  cm<sup>-3</sup>, respectively. The conduction bands are positioned at -1.24, -1.23, -1.18 and -1.13 V vs. RHE, according to the above band gap energies and equation:

$$E_F - E_{VB} = k_B T \ln \frac{N_V}{N_A} \quad (2-3)$$

where  $N_A$  is the carrier density and  $N_V$  is the effective density of states in valance band which can be expressed as

$$N_V = 2 \left( \frac{2\pi m^* k_B T}{h^2} \right)^{3/2} \quad (2-4)$$

where  $m^* = 0.58 m_0$  is taken as the effective hole mass.<sup>36</sup>

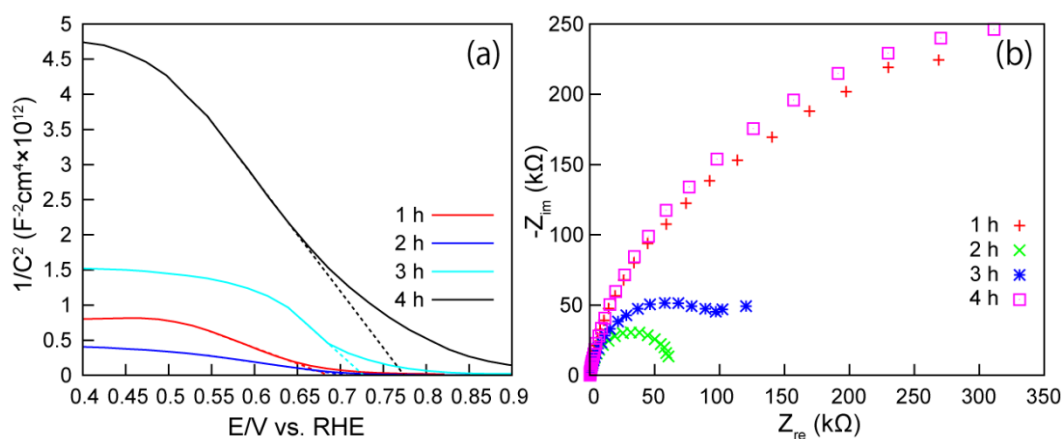


**Figure 2.9.** (a) Mott-Schottky analysis and (b) Nyquist plot taken with 0.01 M PBS solution (pH = 7.4) of the samples annealed for 1, 2, 3 and 4 h. For Mott-Schottky measurements, the electrodes were scanned with a frequency of 1 kHz in the potential range of chemical stability. The Nyquist plot measurements were carried out at 0.43 V vs. RHE by varying the frequency between 10 kHz to 1 Hz under dark condition.

The conduction band position (1 h, 2 h and 3 h) is more negative than those previously reported by Paracchino *et al.*<sup>5</sup> of -1.17 V vs. RHE and de Jongh *et al.*<sup>3</sup> of -0.7 V vs. RHE. Our relatively high conduction band may provide larger driving force for hydrogen production. The carrier density in the fabricated  $Cu_2O$  films compared well with literature values having a higher value than the  $5 \times 10^{17} cm^{-3}$  and lower value than the  $3.5 \times 10^{20} cm^{-3}$  of the  $Cu_2O$  films prepared by electrodeposition.<sup>5, 39</sup> The relatively high carrier density of the fabricated  $Cu_2O$  films may also contribute to the water splitting performance of our  $Cu_2O$  PEC cell. The Nyquist plots of figure 2.9b were used to analyze the interfacial charge transfer process of the  $Cu_2O$  electrodes with the electrolyte. The measurement was carried out in the frequency range of 10 kHz to 1 Hz at a potential of 0.43 V vs. RHE under dark condition. The diameter of the semicircle is indicative of the interfacial charge transfer resistance,  $R_{ct}$ , across the electrode/electrolyte interface.<sup>40</sup> The

2 h sample showed the lowest  $R_{ct}$  value and the resistance follows the order of  $R_{ct}$  (2 h) <  $R_{ct}$  (3 h) <  $R_{ct}$  (1 h) <  $R_{ct}$  (4 h).

### 2.3.7. Discussion

It is well known that crystal surface plays an important role in controlling catalytic activities by providing surface and energetically favorable sites (terraces, steps, kinks, and vacancies) for chemical reactions.<sup>22, 41-44</sup> In this report, the annealing time is found to increase the crystal size, thus decreasing available surface for reaction, as well as decreasing surface irregularities, thus reducing the density of active sites for reaction. The decrease in the density of active sites also lead to a decrease in Cu vacancies in the vicinity of the sample surface which can serve as acceptors and thus should reduce the surface carrier density as found in Figure 2.9a. Thus, the photocurrent decreases with the annealing time. We should note that the 1 h annealed sample is very unstable as indicated by a color change from red to shallow black within a few days and the formation of a black dot under laser illumination, which is evidence for oxidization. This fast oxidation would not allow for correct estimation of the photocurrent as the sample surface is likely transformed to CuO which has a low photocurrent. The 3 and 4 h annealed samples are far more stable, but have only fair PEC performance due to the decrease in active catalytic sites (terraces, steps, and kinks) and increase of exposed low-index crystal facets {111}.<sup>3, 44</sup> It is reported that the  $O^{2-}$ -terminated surface of  $Cu_2O$  allows  $H^+$  species to adsorb and initiate the  $Cu_2O$  reduction reaction and the  $Cu^{2+}$ -terminated surface would be more stable.<sup>45</sup> The instability of  $Cu_2O$  is attributed to predominant {211} and {311} surfaces, where the  $Cu_2O$  reduction is inevitable because of the  $O^{2-}$ -terminated surface. The {111} facets can be either  $Cu^{2+}$ -terminated or  $O^{2-}$ -terminated and thus more stable.<sup>3, 45</sup> In our experiment, with the increasing of annealing time, the improved stability can be attributed

to the decrease in exposed high-index facets and increase of low-index crystal facets  $\{111\}$ ,<sup>3, 44</sup> as shown in Figure 2.2 and 2.8. In contrast, the 2 h annealed sample has the largest photocurrent and a more stable state against surface oxidation in air compared to 1 h sample may due to the good combination between high active site density and initial formation of  $\{111\}$  facets.

## 2.4. Conclusions

In this chapter, a new and low-cost fabrication method was introduced to synthesize  $\text{Cu}_2\text{O}$  microcrystalline films with high photoactivity. The two-step fabrication method consists of the synthesis of  $\text{Cu}(\text{OH})_2$  nanowires and their subsequent transformation into  $\text{Cu}_2\text{O}$  at 500 °C under a vacuum. By controlling the annealing time, the size of the crystals can be tuned and the preferential exposed facets  $\{111\}$  can be formed. Investigation into the samples' depth crystal properties reveals that the outer and inner regions of the oxide layer were composed of two types of cubic  $\text{Cu}_2\text{O}$  with different lattice constants, as evidenced by XRD and Raman analysis. The conduction band values of -1.24, -1.23, -1.18 and -1.13 V vs. RHE and the large carrier densities of  $4.05 \times 10^{17}$ ,  $1.36 \times 10^{18}$ ,  $5.61 \times 10^{17}$ ,  $3.92 \times 10^{17} \text{ cm}^{-3}$  for the 1 to 4 h samples presumably contributed to the high photocurrents of -1.55, -4.07, -2.57 and -2.11  $\text{mA/cm}^2$  at 0 V vs. RHE under AM 1.5G illumination, respectively. The next challenge is to stabilize the bare  $\text{Cu}_2\text{O}$  electrode with appropriate protective layers as well as load proper  $\text{H}_2$  evolution catalysts on the  $\text{Cu}_2\text{O}$  surface to reduce water to hydrogen more efficiently.

## References

- [1] Peterson, N. L.; Wiley, C. L. *J. Phys. Chem. Solids* **1984**, *45*, 281–294.
- [2] Mrowec, S.; Stokłosa, A. *Oxid. Met.* **1971**, *3*, 291–311.
- [3] de Jongh, P. E.; Vanmaekelbergh, D.; Kelly, J. J. *J. Electrochem. Soc.* **2000**, *147*, 486–489.
- [4] de Jongh, P. E.; Vanmaekelbergh, D.; Kelly, J. J. *Chem. Commun.* **1999**, 1069–1070.
- [5] Paracchino, A.; Brauer, J. C.; Moser, J.-E.; Thimsen E.; Graetzel, M. *J. Phys. Chem. C* **2012**, *116*, 7341–7350.
- [6] Siripala, W.; Ivanovskaya, A.; Jaramillo T. F.; Baeck S.-H.; McFarland E. W. *Sol. Energy Mater. Sol. Cells* **2003**, *77*, 229–237.
- [7] Paracchino, A.; Laporte, V.; Sivula, K.; Grätzel, M.; Thimsen, E. *Nat. Mater.* **2011**, *10*, 456–461.
- [8] Qian, F.; Wang, G. M.; Li, Y. *Nano Lett.* **2010**, *10*, 4686–4691.
- [9] Lin, C.-Y.; Lai, Y.-H.; Merscha, D.; Reisner E. *Chem. Sci.* **2012**, *3*, 3482–3487.
- [10] Zhang, Z. H.; Dua R.; Zhang, L. B.; Zhu, H. B.; Zhang H. N.; Wang P. *ACS Nano* **2013**, *7*, 1709–1717.
- [11] Li, C. W.; Kanan, M. W. *J. Am. Chem. Soc.* **2012**, *134*, 7231–7234
- [12] Mittiga, A.; Salza, E.; Sarto, F.; Tucci, M.; Vasanthi, R. *Appl. Phys. Lett.* **2006**, *88*, 163502.

- [13] Xiang, C. X.; Kimball, G. M.; Grimm, R. L.; Brunschwig, B. S.; Atwater, H. A.; Lewis, N. S. *Energy Environ. Sci.* **2011**, *4*, 1311-1318.
- [14] Hu, C-C.; Nian, J-N.; Teng H. *Energy Mater. Sol. Cells* **2008**, *92*, 1071–1076.
- [15] Paracchino, A.; Mathews, N.; Hisatomi, T.; Stefik, M.; Tilley, S. D.; Grätzel, M. *Energy Environ. Sci.* **2012**, *5*, 8673-8681.
- [16] Tilley, S. D.; Schreier, M.; Azevedo, J.; Stefik, M.; Grätzel, M. *Adv. Funct. Mater.* **2013**, DOI: 10.1002/adfm.201301106.
- [17] Zhang, W.; Wen, X.; Yang, S.; Berta, Y.; Wang, Z. L. *Adv. Mater.* **2003**, *15*, 822–825.
- [18] Lu, C. H.; Qi, L. M.; Yang, J. H.; Zhang, D. Y.; Wu, N. Z.; Ma, J. M. *J. Phys. Chem. B* **2004**, *108*, 17825–17831
- [19] Tsiranovits, Ch.; Antonopulos, J. G.; Stoemenos, J. *Thin Solid Films* **1980**, *71*, 133.
- [20] Wagner, C.; Grunewald, K. *Z. Phys. Chem.* **1938**, *B40*, 455.
- [21] Haugrud, R. *J. Electrochem. Soc.* **2002**, *149*, B14-B21.
- [22] Quan, Z. W.; Wang, Y. X.; Fang, J. Y. *Acc. Chem. Res.* **2013**, *46*, 191–202.
- [23] Zhu, Y. F.; Mimura, K.; Isshiki, M. *Mater. Trans.* **2002**, *43*, 2173-2176
- [24] Gonçalves, A. M. B.; Campos, L. C.; Ferlauto, A. S.; Lacerda, R. G. *J. Appl. Phys.* **2009**, *106*, 034303
- [25] Reydellet, J.; Balkanski, M.; Trivich, D. *Phys. status solidi (b)* **1972**, *52*, 175–185.

- [26] Fan, F. T.; Feng, Z. C.; Li, C. *Acc. Chem. Res.* **2010**, *43*, 378–387.
- [27] Zhang, J.; Li, M. J.; Feng, Z. C.; Chen, J.; Li, C. *J. Phys. Chem. B* **2006**, *110*, 927–935.
- [28] Powell, D.; Compaan, A.; Macdonald, J. R. *Phys. Rev. B* **1975**, *12*, 20-25.
- [29] Compaan, A. *Solid State Commun.* **1975**, *16*, 293-296.
- [30] Arora, A. K.; Ramdas, A. K. *Phys. Rev. B* **1987**, *35*, 4345-4350.
- [31] Berg, R. S.; Yu, P. Y. *Phys. Rev. B* **1986**, *33*, 7349-7352.
- [32] Wilkinson, F. *J. Chem. Soc., Faraday Trans.* **1986**, *2*, 2073-2081.
- [33] Oelkrug, D.; Honnen, W.; Wilkinson, F.; Willsher, C. J. *J. Chem. Soc., Faraday Trans.* **1987**, *2*, 2081-2095.
- [34] Rakhshani, A. E. *Solid-State Electron.* **1986**, *29*, 7–17.
- [35] Cardon, F.; Gomes, W. P. *J. Phys. D: Appl. Phys.* **1978**, *11*, L63.
- [36] Hodby, J. W.; Jenkins, T. E.; Schwa, C.; Tamura, H.; Trivich, D. *J. Phys. C: Solid State Phys.* **1976**, *9*, 1429.
- [37] Formal, F. L.; Tétreault, N.; Cornuz, M.; Moehl, T.; Grätzel, M.; Sivula, K. *Chem. Sci.* **2011**, *2*, 737-743.
- [38] Li, Y. B.; Zhang, L.; Torres-Pardo, A.; González-Calbet, J. M.; Ma, Y. H.; Oleynikov, P.; Terasaki, O.; Asahina, S.; Shima, M.; Cha, D. K.; Zhao, L.; Takanabe, K.; Kubota, J.; Domen, K. *Nat. Commun.* **2013**, *4*, 2566.

- [39] Nakaoka, K.; Ueyama, J.; Ogura, K. *J. Electrochem. Soc.* **2004**, *151*, C661-C665.
- [40] Hong, S. J.; Lee, S.; Jang, J. S.; Lee, J. S. *Energy Environ. Sci.* **2011**, *4*, 1781-1787.
- [41] Shaikhutdinov, S. K.; Meyer, R.; Naschitzki, M.; Bäumer, M.; Freund, H.-J. *Catal. Lett.* **2003**, *86*, 211-219.
- [42] Strbac, S.; Adžić, R. R. *J. Electroanal. Chem.* **1996**, *403*, 169-181.
- [43] Gong, X. Q.; Selloni, A.; Dulub, O.; Jacobson, P.; Diebold, U. *J. Am. Chem. Soc.* **2008**, *130*, 370–381.
- [44] Sun, S. D.; Song, X. P.; Sun, Y. X.; Deng, D. C.; Yang, Z. M. *Catal. Sci. Technol.* **2012**, *2*, 925-930.
- [45] Sowers, K. L.; Fillinger, A. *J. Electrochem. Soc.* **2009**, *156*, F80–F85.



### **3. Fabrication of buried p-n junction on Cu<sub>2</sub>O for stable solar water splitting**

The Cu<sub>2</sub>O-based photocathode is considered as one of the most promising photocathodes for high performance water splitting with sunlight. However, the relatively negative onset potential for H<sub>2</sub> production of these photocathodes impedes further optimization of the solar-to-fuel conversion efficiency. Here, a thin Ga<sub>2</sub>O<sub>3</sub> buffer layer is introduced between the Cu<sub>2</sub>O absorber layer and the TiO<sub>2</sub> protective layer by atomic layer deposition to increase the photovoltage. For the optimized TiO<sub>2</sub> deposition temperature, the Pt/TiO<sub>2</sub>/Ga<sub>2</sub>O<sub>3</sub>/Cu<sub>2</sub>O electrode achieves a high cathodic photocurrent of -2.95 mA/cm<sup>2</sup> at 0 V vs. RHE and an extremely positive onset potential of 1.02 V vs. RHE (defined as the potential where photocathodic current reaches 20 μA/cm<sup>2</sup> under air mass 1.5 global illumination), benefiting from a buried p-n junction and a favourable band alignment. The Pt/TiO<sub>2</sub>/Ga<sub>2</sub>O<sub>3</sub>/Cu<sub>2</sub>O electrodes exhibit a stable cathodic current for 2 h under continuous illumination of a 500 W Xe lamp for TiO<sub>2</sub> deposition temperature below 180°C.

### 3.1. Introduction

In recent decades, the booming energy demand in modern industrial development has speeded up the consumption of conventional energy sources such as coal and oil; thus, the usage of clean and renewable energy sources to avoid energy shortages and serious environmental concerns associated with fossil fuel combustion have gained extensive attention. Hydrogen is considered to be an environmentally friendly fuel, and the photoelectrochemical (PEC) water splitting system provides a promising process to produce hydrogen from water by sustainable solar energy at the semiconductor/electrolyte interface.<sup>1-9</sup> Although considerable research into solar water splitting has been developed within the past decade, the construction of stable and efficient photoelectrodes to achieve a solar-to-hydrogen (STH) conversion efficiency of more than 10% required for practical applications is still challenging.<sup>10-15</sup> In this view, the use of a single photoanode in tandem with a single photocathode to achieve a more efficient PEC system without the need for external voltage is strongly desired. However, the STH conversion efficiency of this kind of tandem cell is still not high (below 0.5%),<sup>16-21</sup> which can be mainly attributed to the small photovoltages, resulting in large external voltage to drive the water splitting reaction on the electrodes. Therefore, developing highly active photoelectrodes working with small applied voltage for efficient PEC water splitting is desired.

One of the materials of choice is  $\text{Cu}_2\text{O}$ , a p-type semiconductor with a direct band gap of 2.0 eV, which can function as a photocathode that enables effective utilization of solar photons. The theoretical maximum STH conversion efficiency of 18.1% and the corresponding photocurrent of  $-14.7 \text{ mA/cm}^2$  based on the air

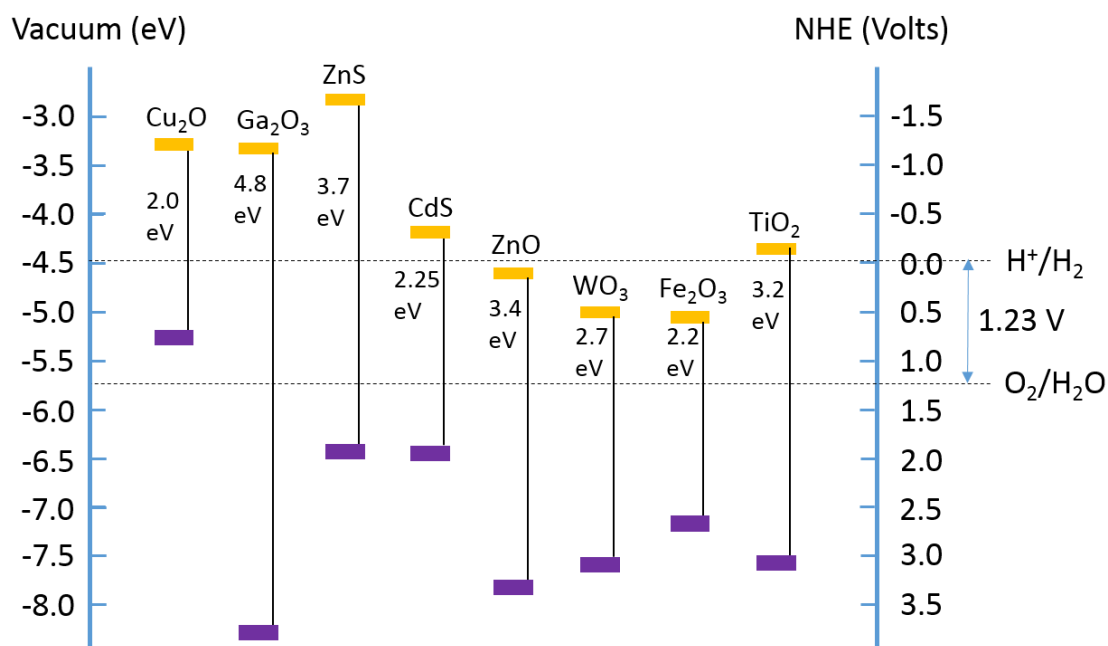


**Figure 3.1.** Band energies (in flat-band condition) of n-type semiconductors with respect to Cu<sub>2</sub>O.

mass 1.5 global (AM 1.5G) spectrum make it a very promising semiconductor for hydrogen production.<sup>9</sup> However, the Cu<sub>2</sub>O can be easily reduced into Cu in solution under illumination and bias, which limits the use of this material in photocatalytic water splitting. To address this problem, a suitable protective layer with favorable energy band position on bare Cu<sub>2</sub>O is essential for a stable and efficient water splitting reaction instead of Cu<sub>2</sub>O self-reduction. It has been reported recently that the TiO<sub>2</sub> layer can serve as an excellent protective layer for unstable photoelectrodes as well as reducing impediment for electron transfer under PEC hydrogen evolution conditions.<sup>9, 22-26</sup> Pioneering studies have shown that the TiO<sub>2</sub>-protected Cu<sub>2</sub>O-based photocathodes exhibit a large photocurrent and enhanced stability performance when using ZnO as a buffer layer.<sup>9, 24-26</sup> However, a relatively negative onset potential (0.45-0.55 V vs. RHE) was obtained in this structure, which is related to the small photovoltage produced by the

heterojunctions. A recent work shows that the introduction of a ZnS buffer layer between the Cu<sub>2</sub>O and TiO<sub>2</sub> can shift the onset potential cathodically to some extent (0.72 V vs. RHE) by increasing the photovoltage at multilayer/electrolyte junctions.<sup>27</sup> The reported work suggests that the conduction band alignment (offset) plays a great role in the photovoltage obtained from Cu<sub>2</sub>O/buffer layer structure. Decreasing the conduction band offset between Cu<sub>2</sub>O and buffer layer can lead to a higher photovoltage by increasing the difference of Fermi level of the two materials. As shown in Figure 3.1, the Cu<sub>2</sub>O has a low electron affinity and it is difficult to find an n-type material with low conduction band offset with respect to Cu<sub>2</sub>O. The large conduction band offset formed between Cu<sub>2</sub>O and many n-type materials explained the relatively low obtained photovoltage, including ZnO (-1.0- -1.8 eV), TiO<sub>2</sub> (~-1.2 eV), CdS (~-0.7 eV) *etc.* Therefore, a rational adjustment of buffer layer is expected to increase the photovoltage further by forming a better energy band alignment across the multilayers.

Recently, Minami *et al.*<sup>28</sup> reported an enhanced conversion efficiency of Cu<sub>2</sub>O heterojunction solar cell prepared on p-type Cu<sub>2</sub>O sheets that fabricated by thermal oxidation of Cu sheets at high temperature (~1000°C). Ga<sub>2</sub>O<sub>3</sub> thin film was deposited on the Cu<sub>2</sub>O sheets by pulsed laser deposition (PLD) method as buffer layer to decrease the conduction band discontinuity and defect levels at the Ga<sub>2</sub>O<sub>3</sub>/Cu<sub>2</sub>O interface, thus, a higher conversion efficiency can be achieved. It is also reported that prepare Ga<sub>2</sub>O<sub>3</sub> buffer layer on an electrochemically deposited Cu<sub>2</sub>O layer by atomic layer deposition (ALD) technique can get a better conduction band alignment and reduce the density of Cu<sup>2+</sup>-related defects at the Ga<sub>2</sub>O<sub>3</sub>/Cu<sub>2</sub>O interface.<sup>29</sup> The obtained Cu<sub>2</sub>O-based solar cell shows an improved open circuit

voltage. Thus, it is possible to extend this  $\text{Ga}_2\text{O}_3/\text{Cu}_2\text{O}$  structure to solar water splitting field by using the highly photoactive  $\text{Cu}_2\text{O}$  microcrystalline layers fabricated in chapter 2 as sunlight absorber. Compared to  $\text{Cu}_2\text{O}$ -based solar cells, the construction of PEC water splitting device is subject to more constraints. For example, co-catalyst is usually needed to promote the catalytic reaction on the photoelectrode. What's more, considering the instability of amorphous  $\text{Ga}_2\text{O}_3$  in electrolyte, the  $\text{Ga}_2\text{O}_3/\text{Cu}_2\text{O}$  structure must be protected by an appropriate overlayer with good anti-photocorrosion property and favourable electron transfer at protective layer/electrolyte interface.

Here, we introduce a  $\text{Ga}_2\text{O}_3$  thin layer as a very suitable buffer layer between the  $\text{Cu}_2\text{O}$  layer and the  $\text{TiO}_2$  protective layer to achieve a higher photovoltage and stable photocurrent. The  $\text{Ga}_2\text{O}_3$  layer provides an approximately equal electron affinity to that of  $\text{Cu}_2\text{O}$ , thus decreasing the height of the conduction band discontinuity at the  $\text{Ga}_2\text{O}_3/\text{Cu}_2\text{O}$  interface and likely reducing the interfacial recombination.<sup>28-29</sup> The stabilization of the photocathode is realized by first coating a conformal  $\text{TiO}_2$  thin film and then depositing a thin Pt layer to promote PEC hydrogen production. A systematic investigation of the effect of  $\text{TiO}_2$  deposition temperature on the performance of the photocathode indicates that an optimized energy band alignment can be achieved at a deposition temperature of  $220^\circ\text{C}$ , at which a high photocurrent of  $-2.95 \text{ mA/cm}^2$  at 0 V vs. RHE and an extremely low onset potential of 1.02 V vs. RHE are observed. The enhanced photocathodic performance observed at low applied biases ( $-1.17 \text{ mA/cm}^2$  at 0.6 V vs. RHE) demonstrates the great potential of this structure for developing superior photoelectrodes for use in tandem cells.

## 3.2. Experimental section

### 3.2.1. Preparation of TiO<sub>2</sub>/ZnO/Cu<sub>2</sub>O and TiO<sub>2</sub>/Ga<sub>2</sub>O<sub>3</sub>/Cu<sub>2</sub>O structures

**Fabrication of Cu<sub>2</sub>O Microcrystalline Films.** The Cu<sub>2</sub>O microcrystalline film was prepared by a two-step fabrication method. This method consists of the synthesis of Cu(OH)<sub>2</sub> nanowires and their subsequent transformation into Cu<sub>2</sub>O at 500°C under a vacuum. First, a Cu foil (99.96%, Nilaco) with a size of 10×30 mm<sup>2</sup> and a thickness of 0.2 mm was cleaned in ultrasonic bath of acetone and ethanol for 10 min, sequentially. The cleaned Cu foil was then immersed into a mixed solution of 2.67 M NaOH (97.0%, Wako) and 0.133 M (NH<sub>4</sub>)<sub>2</sub>S<sub>2</sub>O<sub>8</sub> (98.0%, Wako) for 10 min. In addition, gentle stirring of the solution at a low temperature (5°C) was introduced to prevent the growth of CuO microflowers structures on the Cu(OH)<sub>2</sub> nanowires. CuO microflowers were found to grow under the conditions of inhomogeneous solution and increased temperature near the Cu/solution interface caused by the chemical reaction. Finally, the Cu foil covered by Cu(OH)<sub>2</sub> nanowires with a light blue color was taken out from the solution, rinsed with deionized water, and dried in air. To synthesize the Cu<sub>2</sub>O film, the obtained Cu(OH)<sub>2</sub> nanowires/Cu foil was loaded into an alumina boat and placed at the center of a vacuum quartz tube. The quartz tube was evacuated to about 36 Pa before heating under a flow rate of Ar of 50 sccm. The working pressure during the annealing was kept at about 2.5×10<sup>3</sup> Pa. The Cu<sub>2</sub>O microcrystalline layers were prepared by annealing the Cu(OH)<sub>2</sub> nanowire film at 500°C for 2 h.

**Atomic layer deposition of Ga<sub>2</sub>O<sub>3</sub> and TiO<sub>2</sub> thin films.** Before the deposition of the oxide films, the Cu<sub>2</sub>O film was treated by Ar plasma in a reactive ion etching

(RIE) system (SAMCO, RIE-10NRU) for 30 s at room temperature to remove the residual contaminants from the annealing and change the hydrophobic surface to a hydrophilic surface. The Ar plasma was generated under an applied RF power of 50 W, a gas flow of 50 sccm and a pressure of 25 Pa. A Ga<sub>2</sub>O<sub>3</sub> buffer layer and a TiO<sub>2</sub> protective layer were deposited on the surface of the Cu<sub>2</sub>O microcrystalline layers with an ALD system (SUGA, SAL100H). The Ga<sub>2</sub>O<sub>3</sub> layer was deposited at a substrate temperature of 150°C using tris(dimethylamido)gallium (Aldrich, 98%,  $T_{\text{precursor}} = 130^{\circ}\text{C}$ ) and H<sub>2</sub>O as Ga and O sources, respectively. TiO<sub>2</sub> was deposited using tetrakis(dimethylamido)titanium (Aldrich, 99.999%,  $T_{\text{precursor}} = 90^{\circ}\text{C}$ ) and H<sub>2</sub>O as the Ti and O precursors, respectively. The substrate temperature of TiO<sub>2</sub> deposition was varied between 120 and 260°C in order to control the quality of the deposited oxide films. For comparison, a ZnO buffer layer was also deposited on Cu<sub>2</sub>O to fabricate TiO<sub>2</sub>/ZnO/Cu<sub>2</sub>O structure by using diethylzinc (Japan Advanced Chemicals,  $T_{\text{precursor}} = \text{room temperature}$ ) as a Zn source, with a substrate temperature of 150°C. The cycle numbers for TiO<sub>2</sub>, Ga<sub>2</sub>O<sub>3</sub> and ZnO are 220, 200 and 106, respectively.

### 3.2.2. Co-catalyst deposition

Platinum nanoparticles were deposited on the surface of the protective layer/Cu<sub>2</sub>O samples by ion-beam sputtering of a Pt target to enhance the kinetics of the hydrogen evolution reaction. The chamber pressure was evacuated to  $4 \times 10^{-5}$  Pa before sputtering and, the substrate holder was at a distance of 22 cm from the Pt target. The Ar flow was adjusted to get a gas pressure of  $3 \times 10^{-2}$  Pa. The Ar ion beam had an energy of 1.5 keV and a diameter of 30 mm. The thickness of the Pt

layer was monitored with a quartz crystal monitor and a thickness of 1 nm (nominally) was obtained after sputtering.

### 3.2.3. PEC measurements

The PEC performance of the protective layer/Cu<sub>2</sub>O electrodes was performed in a three-electrode configuration using an Ag/AgCl reference electrode and a Pt wire counter electrode. The electrolyte was a 0.5 M Na<sub>2</sub>SO<sub>4</sub>-0.1 M KH<sub>2</sub>PO<sub>4</sub> solution with a pH of 4.26. The measured potential vs. Ag/AgCl was converted to RHE by Nernst's equation ( $E_{\text{RHE}} = E_{\text{Ag/AgCl}} + 0.059 \text{ pH} + 0.197$ ). The electrolyte was stirred and purged with argon gas before each measurement (for 15 min) and during measurements. The current-potential curves were measured both under 500 W Xe lamp illumination (286 mW/cm<sup>2</sup>) and AM 1.5G simulated sunlight (100 mW/cm<sup>2</sup>). The scan rate for the linear sweep voltammetry was 10 mV/s. To calculate the solar energy conversion efficiency ( $\eta$ ), the equation  $\eta = (V_{\text{app}} \times J_{\text{ph}}) / P \times 100\%$  was used, where  $V_{\text{app}}$  is the applied potential (vs. RHE),  $J_{\text{ph}}$  is the photocurrent (mA/cm<sup>2</sup>) under AM 1.5G irradiation and  $P$  is the irradiance of the AM 1.5G (100 mW/cm<sup>2</sup>). The wavelength dependence of IPCE was measured under monochromatic irradiation using the 500 W Xe lamp equipped with bandpass filters (central wavelengths of 350, 400, 450, 500, and 550 nm). The IPCE at each wavelength was calculated according to the equation  $\text{IPCE}\% = [J_{\text{ph}}(\text{mA/cm}^2) \times 1240] / [P(\text{mW/cm}^2) \times \lambda(\text{nm})] \times 100$ .

### 3.2.4. Structural characterization



The morphology of the samples was characterized with a field-emission scanning electron microscope (JEOL JSM 7600FA). The X-ray diffraction (XRD) patterns were determined using a diffractometer (SmartLab, Rigaku Co. Ltd., Japan) with Cu K $\alpha$  radiation (1.540598 Å). XPS data were collected with a PHI 5000 VersaProbe (ULVAC-PHI) using an Al K $\alpha$  X-ray source (1486.6 eV). The UV-vis diffuse reflectance spectra were measured with a spectrophotometer equipped with an integrating sphere (DRS, V-560, Jasco). The structure of the sample was also identified by scanning transmission electron microscopy (STEM) and energy dispersive X-ray spectroscopy (EDS), with a JEM-2800, JEOL. The cross section was prepared by focused ion beam using an FIB-SEM (JIB-4600F, JEOL) and subsequent milling in a NanoMill 1040, E.A. Fischione Instruments.

### **3.3. Characterization of the TiO<sub>2</sub>/Ga<sub>2</sub>O<sub>3</sub>/Cu<sub>2</sub>O structures**

Cu<sub>2</sub>O microcrystalline films were prepared on Cu foil by a two-step fabrication method, as reported previously.<sup>30</sup> The Cu(OH)<sub>2</sub> nanowires was used as a template for growth of highly photoactive Cu<sub>2</sub>O film with large surface area. Briefly, the Cu(OH)<sub>2</sub> nanowires on Cu foil was fabricated by a wet chemical process in sodium hydroxide and ammonium solution, then the Cu(OH)<sub>2</sub> nanowire/Cu foils were annealed under an Ar atmosphere at 500°C for 2 h. During the annealing, the Cu(OH)<sub>2</sub> nanowires were decomposed to CuO nanowires at about 120°C, and the subsequent oxide growth was driven by outward diffusion of Cu ions via Cu vacancies from the Cu substrate to the oxide surface and reaction with oxygen from the gas phase. The continuous diffusion of Cu ions on the surface of nanowires leads to volume expansion of the nanowires and consequently coalescence of the

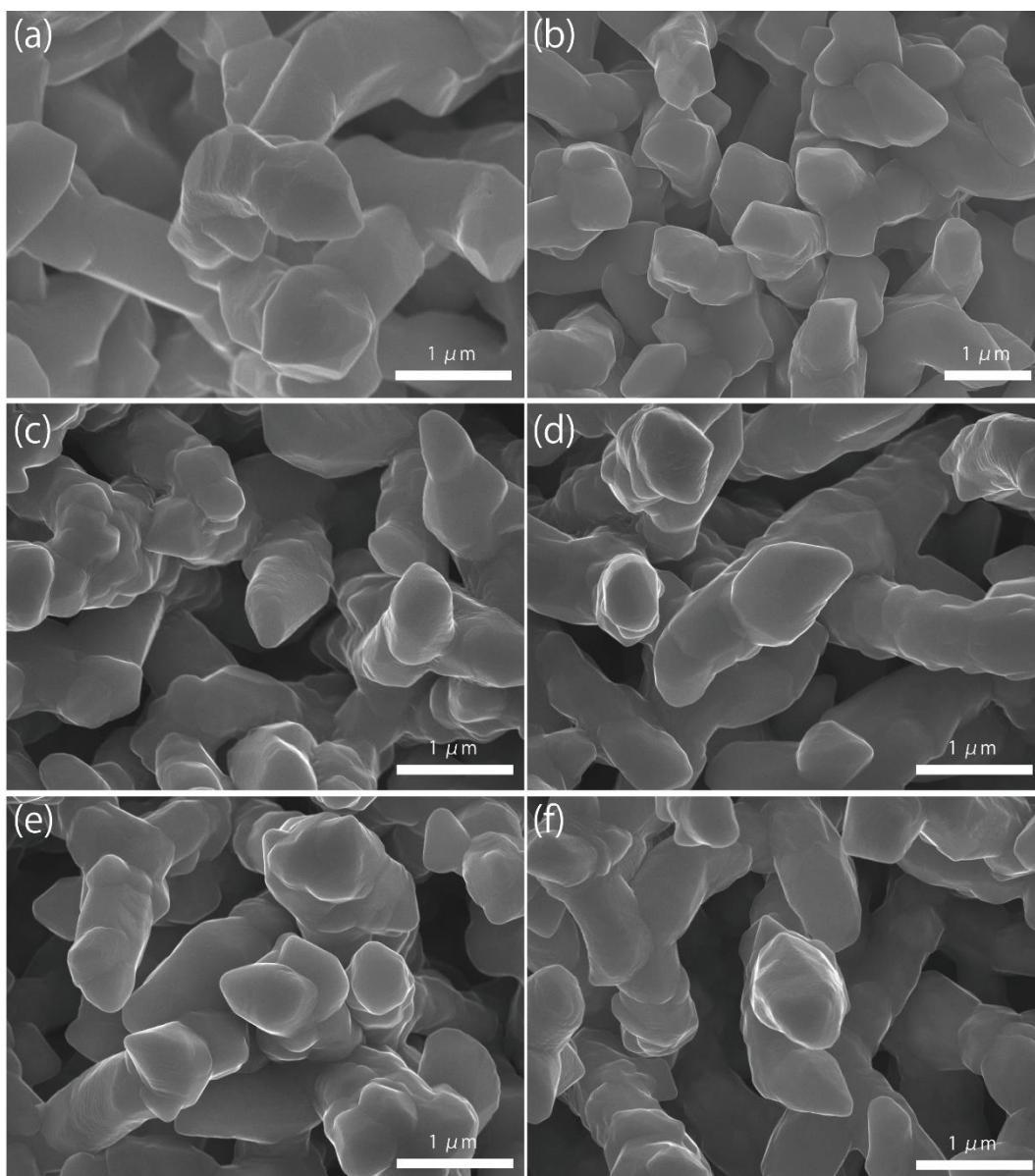


**Figure 3.2.** a) FE-SEM images of  $\text{Cu}_2\text{O}$  microcrystalline film prepared by annealing  $\text{Cu}(\text{OH})_2$  nanowires at  $500^\circ\text{C}$  for 2 h. b-f) FE-SEM images of  $\text{Cu}_2\text{O}$  microcrystalline film coated with a 20 nm  $\text{Ga}_2\text{O}_3$  buffer layer and a 15 nm  $\text{TiO}_2$  protective layer by atomic layer deposition with a  $\text{TiO}_2$  deposition temperature of 120, 150, 180, 220 and  $260^\circ\text{C}$ , respectively. The deposition temperature of  $\text{Ga}_2\text{O}_3$  thin layer was fixed at  $150^\circ\text{C}$ .

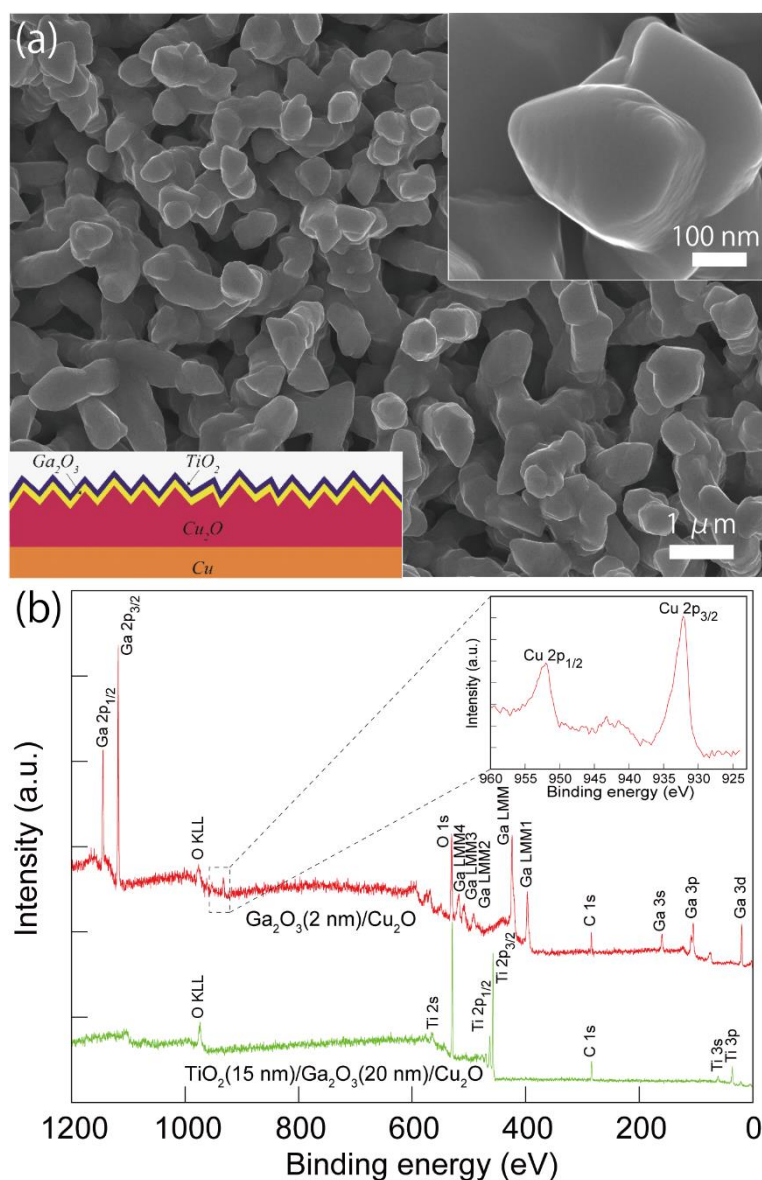


**Figure 3.3.** (a) FE-SEM images of Cu<sub>2</sub>O microcrystalline film coated with Ga<sub>2</sub>O<sub>3</sub> buffer layer and TiO<sub>2</sub> protective layer by atomic layer deposition. Lower left inset is the schematic of the multilayer structure. (b) XPS spectra of Ga<sub>2</sub>O<sub>3</sub> (2 nm)/Cu<sub>2</sub>O and TiO<sub>2</sub> (15 nm)/Ga<sub>2</sub>O<sub>3</sub> (20 nm)/Cu<sub>2</sub>O samples. Deposition temperature for Ga<sub>2</sub>O<sub>3</sub> and TiO<sub>2</sub> are 150 and 220°C, respectively. Top right inset is high resolution XPS spectrum of Cu-2p peaks of Ga<sub>2</sub>O<sub>3</sub> (2 nm)/Cu<sub>2</sub>O sample.

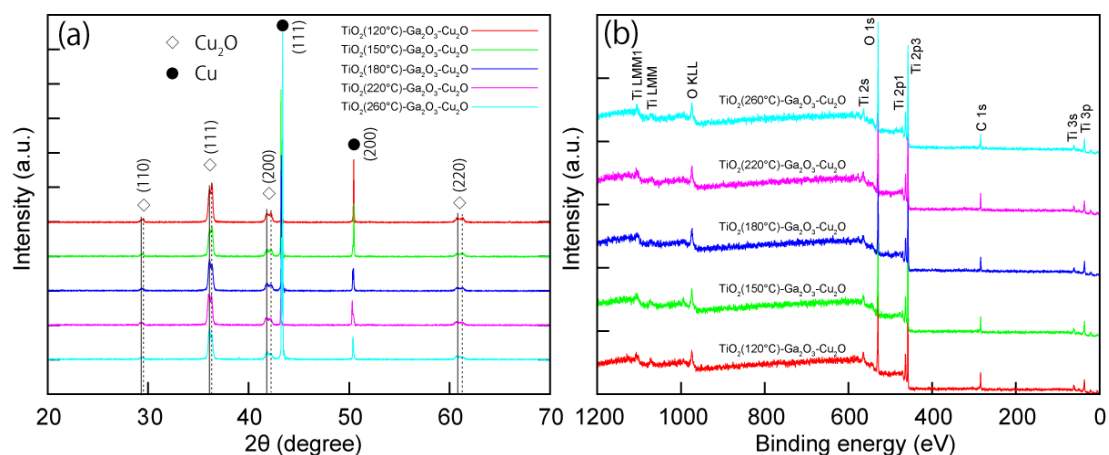


**Figure 3.4.** XRD a) and XPS spectra b) of the TiO<sub>2</sub>/Ga<sub>2</sub>O<sub>3</sub>/Cu<sub>2</sub>O samples. The deposition temperature for Ga<sub>2</sub>O<sub>3</sub> is 150°C and the TiO<sub>2</sub> deposition temperature ranges from 120 to 220°C. For the XRD data, two sets of diffraction peaks are clearly observed as the diffraction peaks are well indexed to the peaks of the cubic structure Cu<sub>2</sub>O-I (indicated by a dashed line, space group Pn-3m, lattice constant 4.2600 Å, ICDD PDF card No. 1010941) and the Cu<sub>2</sub>O-II (indicated by a solid line, space group Pn-3m, lattice constant 4.2685 Å, ICDD PDF card No. 9007497).

nanowires to form larger Cu<sub>2</sub>O crystals. The obtained Cu<sub>2</sub>O film consists of dense micro-nano aggregates with a diameter and length of ~0.6 and ~3.5 μm, respectively, as shown in Figure 3.2a. Figure 3.3a shows the top morphology of the Cu<sub>2</sub>O microcrystalline film after coating 20 nm of Ga<sub>2</sub>O<sub>3</sub>(150°C) and 15 nm of TiO<sub>2</sub>(220°C). No obvious change in the morphology of the microcrystals was found because the coating was homogeneous. XRD measurements revealed only Cu<sub>2</sub>O and Cu diffraction peaks from the TiO<sub>2</sub>(15 nm)/Ga<sub>2</sub>O<sub>3</sub>(20 nm)/Cu<sub>2</sub>O sample (Figure 3.4a). The absence of Ga<sub>2</sub>O<sub>3</sub> and TiO<sub>2</sub> signals may be due to the thin thickness and low crystallinity of the oxide layers. In order to characterize the chemical state of the overlayers, XPS was conducted on the Ga<sub>2</sub>O<sub>3</sub>/Cu<sub>2</sub>O and

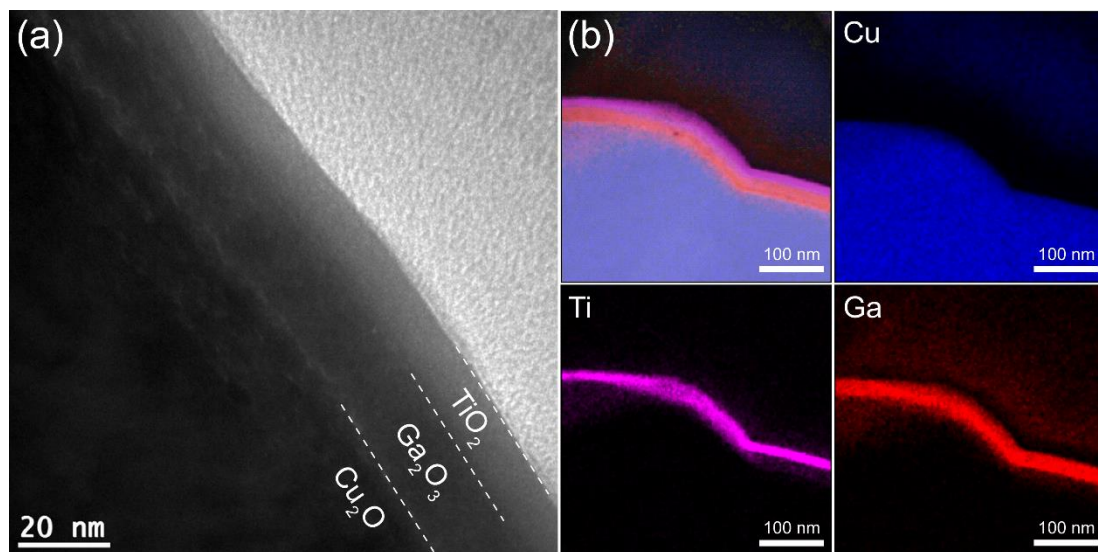


**Figure 3.5.** (a) Typical cross-section TEM image of  $\text{TiO}_2$  (15 nm)/ $\text{Ga}_2\text{O}_3$  (20 nm)/ $\text{Cu}_2\text{O}$  structure. (b) STEM-EDX mapping results of structure. Deposition temperature for  $\text{Ga}_2\text{O}_3$  and  $\text{TiO}_2$  are 150 and 220°C, respectively.

$\text{TiO}_2/\text{Ga}_2\text{O}_3/\text{Cu}_2\text{O}$  samples. With a very thin layer of  $\text{Ga}_2\text{O}_3$  (2 nm) on  $\text{Cu}_2\text{O}$ , the XPS spectrum showed the Ga 2p (1118.0 and 1144.9 eV) and O 1s (530.4 eV) peaks for  $\text{Ga}_2\text{O}_3$ , as shown in Figure 3.3b. In addition, Cu 2p peaks from the  $\text{Cu}_2\text{O}$  underlayer are also observed. The  $\text{Cu}_2\text{O}$  layer showed two main peaks at 932.2 and 952.1 eV corresponding to the  $2p_{3/2}$  and  $2p_{1/2}$  levels of  $\text{Cu}_2\text{O}$ . The shoulder peak at 933.7 eV and broad satellite peaks between 940-945 eV can be attributed to the thin CuO layer that is present on  $\text{Cu}_2\text{O}$  from natural oxidation. For the  $\text{TiO}_2/\text{Ga}_2\text{O}_3/\text{Cu}_2\text{O}$  sample, the presence of Ti peaks and the absence of Ga and Cu peaks indicate that the ALD-deposited  $\text{TiO}_2$  layer fully covered the  $\text{Ga}_2\text{O}_3$ , as indicated in Figure 3.3b and Figure 3.4b. Figure 3.5a shows a cross-section transmission electron microscopy (TEM) image of the  $\text{TiO}_2$ (220°C)/ $\text{Ga}_2\text{O}_3$ (150°C)/ $\text{Cu}_2\text{O}$  structure. It is found that both the  $\text{Ga}_2\text{O}_3$  and  $\text{TiO}_2$  layers are amorphous and the interfaces between  $\text{Ga}_2\text{O}_3/\text{Cu}_2\text{O}$  and  $\text{TiO}_2/\text{Cu}_2\text{O}$



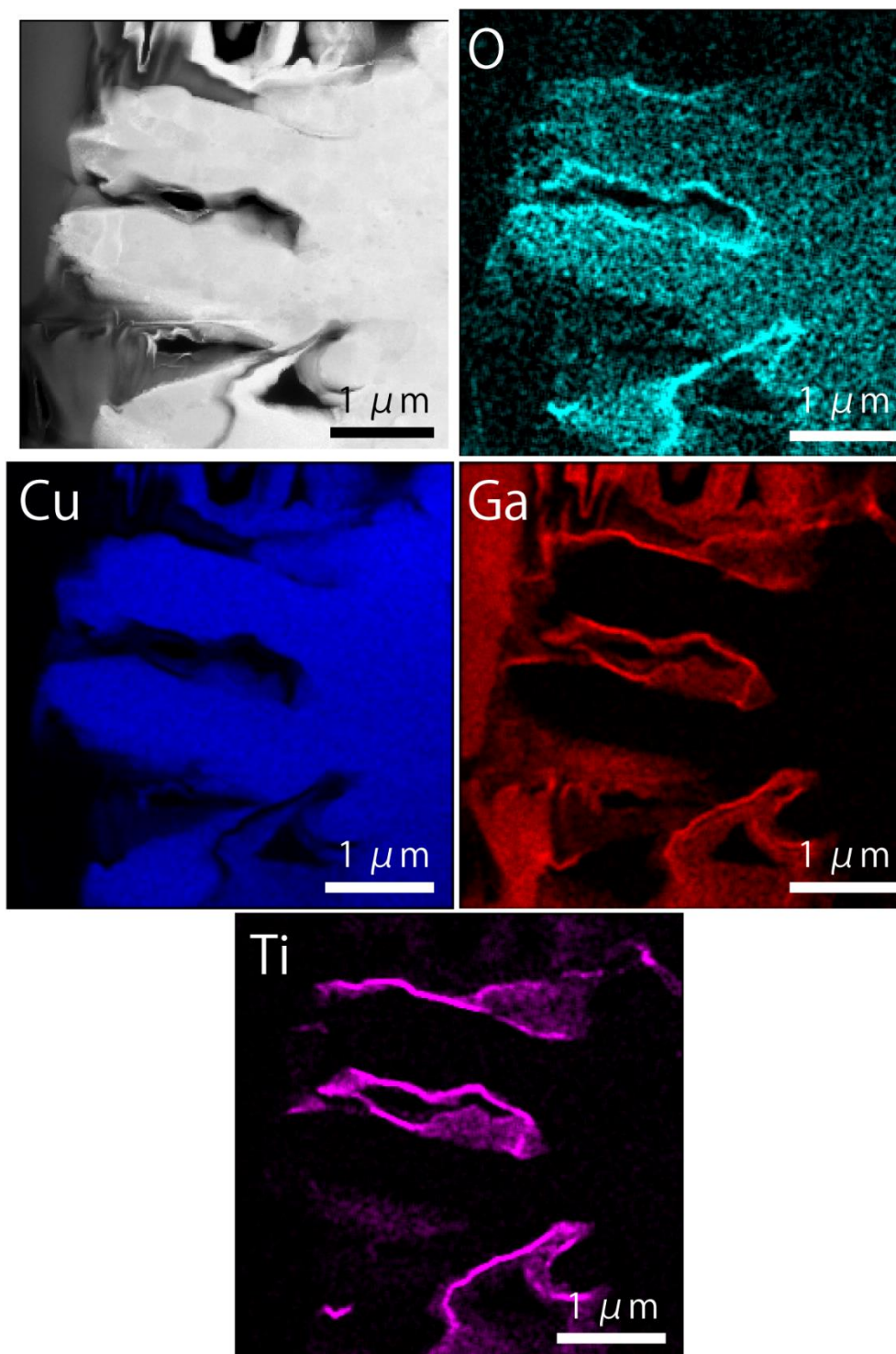


**Figure 3.6.** Large-area STEM-EDX element maps of a cross-section of the TiO<sub>2</sub>/Ga<sub>2</sub>O<sub>3</sub>/Cu<sub>2</sub>O structure. The deposition temperature for Ga<sub>2</sub>O<sub>3</sub> and TiO<sub>2</sub> are 150 and 220°C, respectively.

are of high quality. The mapping of the elements for the cross-section sample reveals a homogeneous deposition of the oxide layers, as shown in Figure 3.5b. Images of the large-area element mapping presented in Figure 3.6 also confirm the homogeneous deposition. From the TEM analysis, the thicknesses of  $\text{TiO}_2$  and  $\text{Ga}_2\text{O}_3$  are both estimated to be 15~20 nm. The uniform coating of the  $\text{TiO}_2$  overlayer enables an effective protection for the  $\text{Cu}_2\text{O}$  layer against the solution corrosion.

### **3.4. PEC properties of Pt/ $\text{TiO}_2$ / $\text{Ga}_2\text{O}_3$ / $\text{Cu}_2\text{O}$ photocathodes**

#### **3.4.1. Pt/ $\text{Ga}_2\text{O}_3$ / $\text{Cu}_2\text{O}$ structures**

In the PEC characterization, the bare  $\text{Cu}_2\text{O}$  electrode exhibited a large photocathodic current and negative onset voltage under 500 W Xe lamp illumination in argon-purged 0.5 M  $\text{Na}_2\text{SO}_4$ -0.1 M  $\text{KH}_2\text{PO}_4$  electrolyte (pH 4.26), as shown in Figure 3.7a. The  $\text{Cu}_2\text{O}$  also showed pronounced reduction and oxidation current in the dark scan, indicating an obvious corrosion of bare  $\text{Cu}_2\text{O}$  during PEC measurement. The photocurrent decreased significantly in the beginning of the stability test. The electrode almost lost its photoactivity after 20 min of continuous illumination at 0.45 V vs. RHE, as shown in Figure 3.7b. The instability of the  $\text{Cu}_2\text{O}$  electrode is consistent with the previous reports,<sup>9, 30</sup> and can be attributed to the reduction of  $\text{Cu}_2\text{O}$  to Cu under illumination and bias potential. Thus, the n-type protective layer coating is expected to improve the stability of  $\text{Cu}_2\text{O}$ . Besides, the buried junction formed between the p-type  $\text{Cu}_2\text{O}$  and the n-type oxide layer can also generate a photovoltage to shift the onset voltage positively. A thin  $\text{Ga}_2\text{O}_3$  layer (20 nm, 150 °C) was first deposited on  $\text{Cu}_2\text{O}$  to form a p-n junction due to the small conduction band offset between this two semiconductors. Under illumination, the

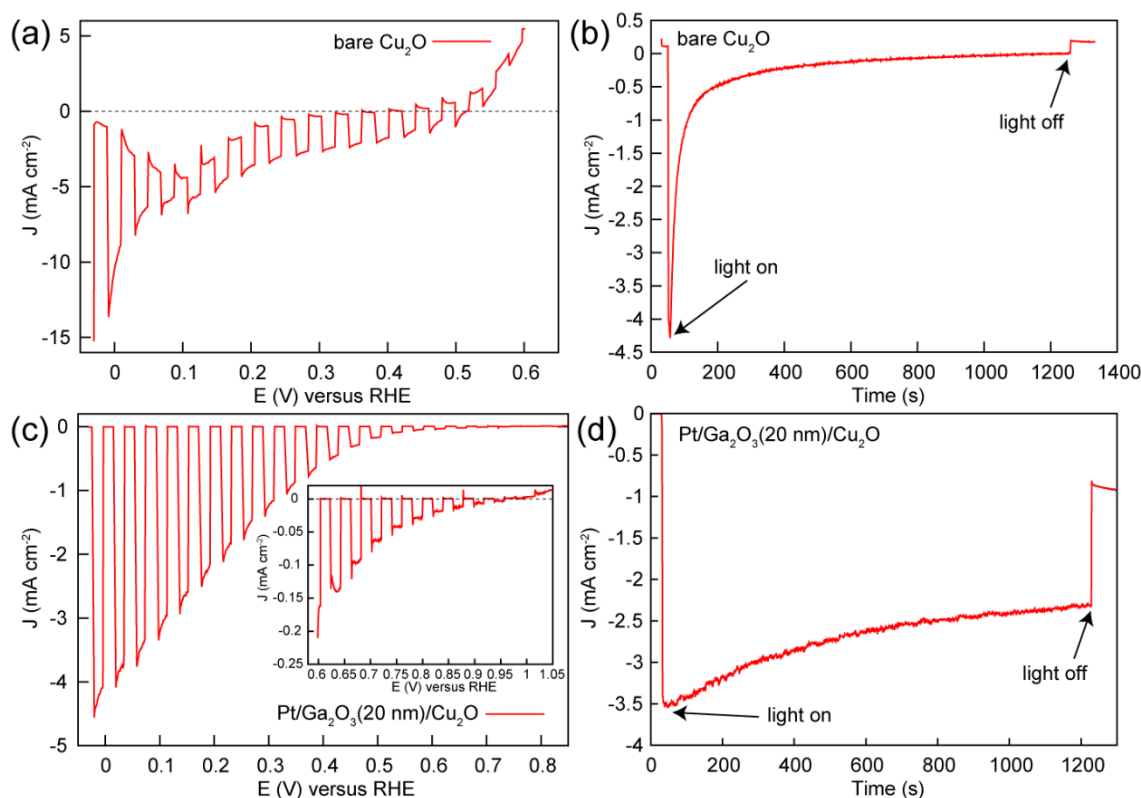


**Figure 3.7.** Current-potential curves of bare Cu<sub>2</sub>O (a) and Pt/Ga<sub>2</sub>O<sub>3</sub> (20 nm, 150°C)/Cu<sub>2</sub>O (c) electrodes. (b) and (d) are stability test of the samples. The inset in part c is the current-potential curve of Pt/Ga<sub>2</sub>O<sub>3</sub>/Cu<sub>2</sub>O electrode in positive potential range. Curves were measured in 0.5 M Na<sub>2</sub>SO<sub>4</sub>-0.1 M KH<sub>2</sub>PO<sub>4</sub> solution (pH = 4.26) under 500 W Xe lamp.

Ga<sub>2</sub>O<sub>3</sub>/Cu<sub>2</sub>O electrode produced a photocurrent of -4 mA/cm<sup>2</sup> at 0 V vs. RHE and onset potential of ~0.9 V vs. RHE with a 1 nm Pt as co-catalyst (Figure 3.7c). With a Ga<sub>2</sub>O<sub>3</sub> overlayer, the electrode showed a negligible dark current, large photocurrent and positive onset potential for water photo-reduction, indicating a successful prevention of Cu<sub>2</sub>O self-reduction by forming a favorable junction between Cu<sub>2</sub>O and Ga<sub>2</sub>O<sub>3</sub>. In this configuration, a rectifying junction was formed between Cu<sub>2</sub>O and Ga<sub>2</sub>O<sub>3</sub>, thus providing a large driving force to extract photo-generated electrons from the Cu<sub>2</sub>O. During the stability test held at 0 V vs. RHE, it is found that although the photocurrent decreased slowly with time, a



photocurrent of 1.4 mA/cm<sup>2</sup> was achieved after 20 min continuous measurement, as shown in Figure 3.7d. The stability is much improved compared to the bare Cu<sub>2</sub>O electrode, revealing an efficient electron transport and reaction during the test. The slowly decreasing of the photocurrent can be attributed to the dissolution of Ga<sub>2</sub>O<sub>3</sub> since the amorphous Ga<sub>2</sub>O<sub>3</sub> layer is unstable in electrolyte. Thus, in order to improve the long-term stability of the structure, an additional protective layer with strong anti-corrosion property and appropriate energy band position should be deposited on Ga<sub>2</sub>O<sub>3</sub> to realize a more efficient water reduction. In this work, TiO<sub>2</sub> was choose as a protective layer on Ga<sub>2</sub>O<sub>3</sub>/Cu<sub>2</sub>O structure due to the good electron transport property and appropriate conduction band (~-0.2 V vs. RHE) position for hydrogen production.<sup>22</sup>

### **3.4.2. Pt/TiO<sub>2</sub>/Ga<sub>2</sub>O<sub>3</sub>/Cu<sub>2</sub>O structures**

Figure 3.8a shows the current-potential curves for the Pt/TiO<sub>2</sub>/Ga<sub>2</sub>O<sub>3</sub>/Cu<sub>2</sub>O electrodes measured under a 500 W Xe lamp. The Ga<sub>2</sub>O<sub>3</sub> buffer layer was deposited under the same conditions (20 nm, 150°C) for all the electrodes, while the deposition temperature of TiO<sub>2</sub> was varied from 120 to 260°C to investigate the effect of TiO<sub>2</sub> quality on the performance of the electrode. The 120°C-deposited TiO<sub>2</sub> sample yielded a relatively low photocurrent and negative onset voltage. When the TiO<sub>2</sub> deposition temperature increased to 150, 180, and 220°C, the photocurrent of the electrodes increased significantly, with an enhancement factor of ~2.60, ~3.46, and ~6.30 compared to the photocurrent obtained with the 120°C-deposited electrode, respectively. Moreover, the onset voltage of the electrodes shifts positively with increasing TiO<sub>2</sub> deposition temperature, so that an extremely positive onset potential of around 1 V vs. RHE was achieved with the samples prepared at 180 and 220°C. The pronounced photocathodic current and the positive onset potential can contribute to the improvement of the overall efficiency, which will be

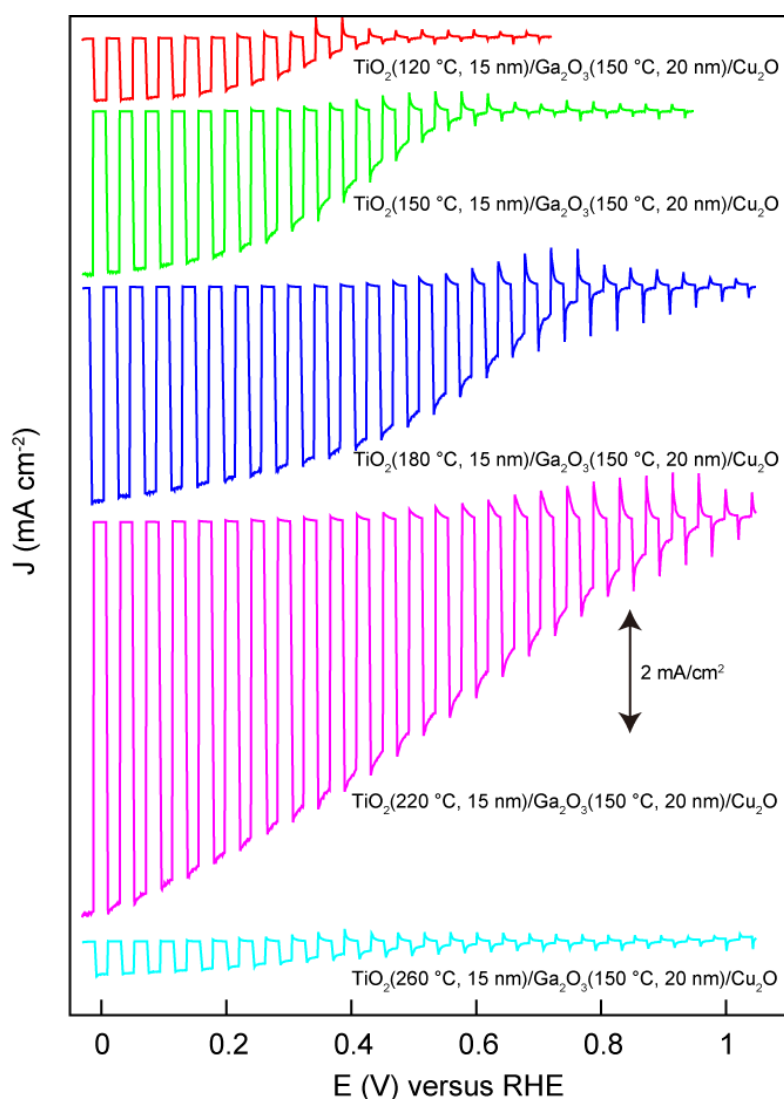


**Figure 3.8.** Current-potential curves of Pt/TiO<sub>2</sub>(15 nm)/Ga<sub>2</sub>O<sub>3</sub>(20 nm)/Cu<sub>2</sub>O samples with different TiO<sub>2</sub> deposition temperatures. Deposition temperature for Ga<sub>2</sub>O<sub>3</sub> is kept at 150°C. Curves were measured in 0.5 M Na<sub>2</sub>SO<sub>4</sub>-0.1 M KH<sub>2</sub>PO<sub>4</sub> solution (pH = 4.26) under 500 W Xe lamp.

presented and discussed later in accordance with the data obtained under AM 1.5G illumination. The enhancement in both the photocurrent and the onset potential is most likely related to improved crystallinity of TiO<sub>2</sub> and alignment of the energy bands occurring at higher TiO<sub>2</sub> deposition temperatures. When the temperature increased to 260°C, a dramatic decrease in the photocurrent was observed.

To further clarify the effect of  $\text{TiO}_2$  deposition temperature on the PEC performance of the  $\text{TiO}_2/\text{Ga}_2\text{O}_3/\text{Cu}_2\text{O}$  structure. We first investigate the  $\text{Ga}_2\text{O}_3/\text{Cu}_2\text{O}$  structure that prepared with a substrate temperature of  $150^\circ\text{C}$  and then annealed at different temperature ( $150\text{-}260^\circ\text{C}$ ) for 2 h in ALD chamber. The annealing atmosphere is the same as the condition for  $\text{TiO}_2$  deposition. Figure 3.9a show the PEC performance of the  $\text{Ga}_2\text{O}_3/\text{Cu}_2\text{O}$  electrodes with a 1 nm Pt as co-catalyst. It is found that all the electrodes exhibited the same characteristic current-potential curve, indicating that the change of  $\text{TiO}_2$  deposition temperature will not affect the  $\text{Ga}_2\text{O}_3/\text{Cu}_2\text{O}$  interface. The reflectance spectra (Figure 3.9c) for the  $\text{TiO}_2/\text{Ga}_2\text{O}_3/\text{Cu}_2\text{O}$  samples show a decrease in the absorption edge of  $\text{Cu}_2\text{O}$  with the increasing of  $\text{TiO}_2$  deposition temperature. However, the reflectance spectra for the  $\text{Ga}_2\text{O}_3/\text{Cu}_2\text{O}$  samples show a clear and similar absorption edge for  $\text{Cu}_2\text{O}$  (Figure 3.9b). Thus, we infer that the material properties of  $\text{TiO}_2$  was controlled by the  $\text{TiO}_2$  deposition temperature and then affect the photo-generated carrier conduction and junction characteristics. To get more information on the  $\text{TiO}_2$  layers deposited under different temperatures, we prepare  $\text{TiO}_2$  layers (50 nm) on ITO with a deposition temperature ranging from  $120$  to  $260^\circ\text{C}$ . The Nyquist plots of Figure 3.10a were used to analyze the interfacial charge transfer process of the  $\text{TiO}_2$  layers with the electrolyte. The measurement was carried out in the frequency range of 10 kHz to 1 Hz at a potential of 0.5 V vs. RHE under light illumination. From the diameter of the obtained semicircles, we can estimate the interfacial charge transfer resistance ( $R_{\text{ct}}$ ) across the electrode/electrolyte interface. The resistance follows the order of  $R_{\text{ct}}(220^\circ\text{C}) < R_{\text{ct}}(180^\circ\text{C}) < R_{\text{ct}}(260^\circ\text{C}) < R_{\text{ct}}(150^\circ\text{C}) < R_{\text{ct}}(120^\circ\text{C})$ . The PEC performance of  $\text{TiO}_2/\text{ITO}$  electrodes presented in Figure 3.10b also show that the photocurrent is increasing with the deposition temperature (from 120 to  $220^\circ\text{C}$ ) and decreased again when the

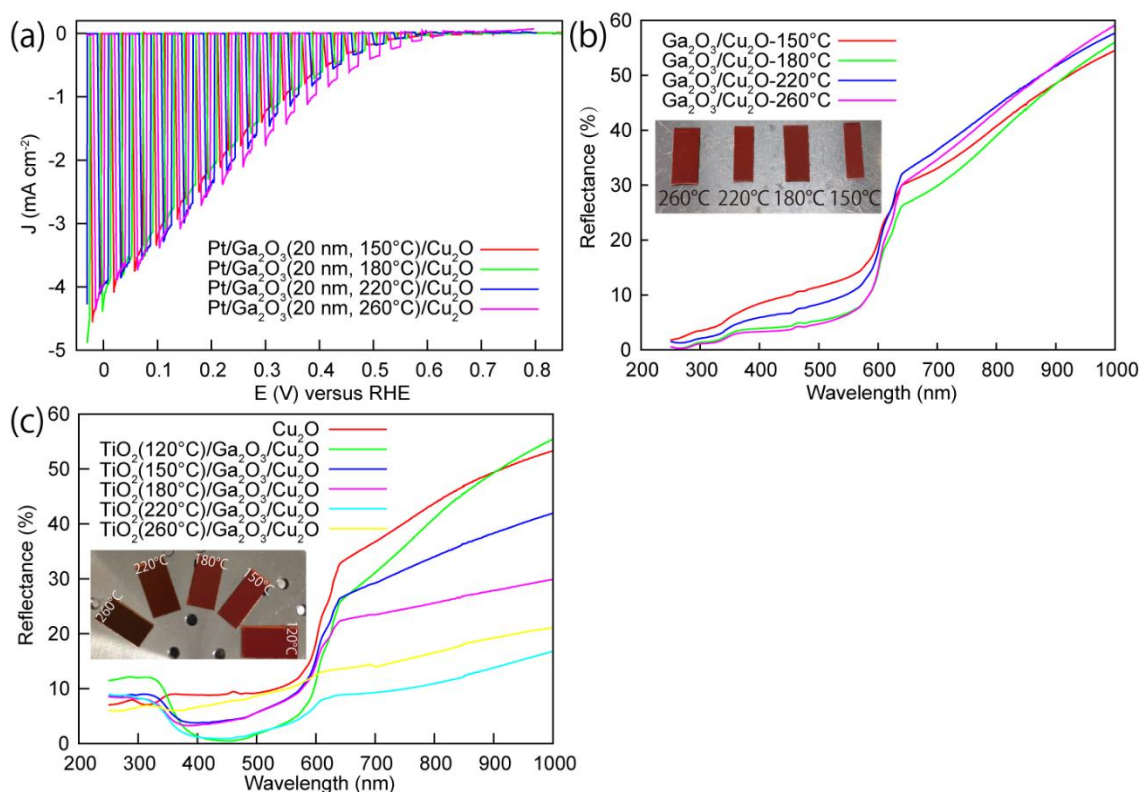


**Figure 3.9.** (a) Current-potential curves of Ga<sub>2</sub>O<sub>3</sub> (20 nm)/Cu<sub>2</sub>O electrodes annealed at different temperature. Curves were measured in 0.5 M Na<sub>2</sub>SO<sub>4</sub>-0.1 M KH<sub>2</sub>PO<sub>4</sub> solution (pH = 4.26) under 500 W Xe lamp. (b) Diffuse reflectance spectra of the Ga<sub>2</sub>O<sub>3</sub>/Cu<sub>2</sub>O samples with different annealing temperature. (c) Diffuse reflectance spectra of the Cu<sub>2</sub>O and TiO<sub>2</sub>/Ga<sub>2</sub>O<sub>3</sub>/Cu<sub>2</sub>O samples for different TiO<sub>2</sub> deposition temperatures of 120, 150, 180, 220 and 260°C. The insets in part b and c are the photographs of the Ga<sub>2</sub>O<sub>3</sub>/Cu<sub>2</sub>O and TiO<sub>2</sub>/Ga<sub>2</sub>O<sub>3</sub>/Cu<sub>2</sub>O samples.

temperature increased to 260°C. The results indicate that the charge transfer resistance of TiO<sub>2</sub> layer is decreasing with the increasing of deposition temperature and thus improved the carrier transfer conduction during the PEC measurement. When the deposition temperature increased to 260°C, the increased charge transfer resistance, decreased photocurrent and darker color of TiO<sub>2</sub> layer may can be explained by the increased density

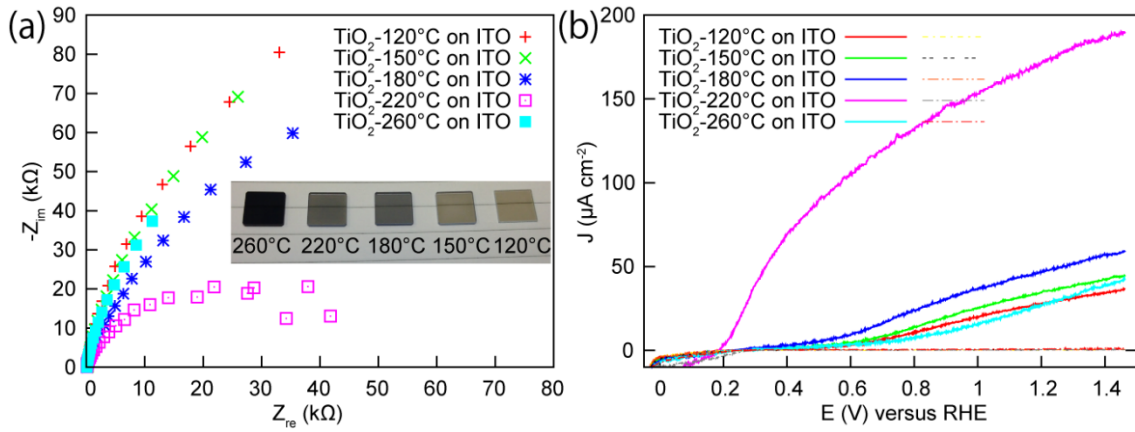


**Figure 3.10.** (a) Nyquist plot and current-potential curves of  $TiO_2$  (50 nm)/ITO electrodes for different  $TiO_2$  deposition temperatures. The inset in part a is the photograph of the  $TiO_2$ /ITO electrodes. Curves were measured in 0.1 M NaOH solution (pH = 13) under 500 W Xe lamp. The Nyquist plot measurements were carried out at 0.5 V vs. RHE by varying the frequency between 10 kHz to 1 Hz under light illumination.

of  $Ti^{3+}$  in the  $TiO_2$  layer due to the high temperature growth. In this work, the high temperature (260°C) deposited  $TiO_2$  is found to deteriorate the charge transfer conduction during the PEC measurement.

Compared to the PEC performance of  $Pt/Ga_2O_3(20\text{ nm}, 150^\circ C)/Cu_2O$  structure, the  $Pt/TiO_2(15\text{ nm}, 220^\circ C)/Ga_2O_3(20\text{ nm}, 150^\circ C)/Cu_2O$  structure exhibited a much higher photocurrent at positive potential range, indicating a better carrier transfer property of  $Pt/TiO_2(15\text{ nm}, 220^\circ C)/Ga_2O_3(20\text{ nm}, 150^\circ C)/Cu_2O$  structure. For the  $Ga_2O_3/Cu_2O$  structure, although a positive onset potential can be achieved due to the small conduction band offset between  $Ga_2O_3$  and  $Cu_2O$ , the carrier transfer from  $Ga_2O_3$  to electrolyte may be hindered by the large potential barrier at  $Ga_2O_3$ /electrolyte interface due to the conduction band pinning at around -1 V vs. RHE. The depletion layer width in  $Ga_2O_3$  can be calculated by using the equation

and data in literature<sup>31-33</sup> and the width is estimated to larger than 10 nm when the electron quasi-Fermi level ( $E_F$ ) is positioned at 0 V vs. RHE. When TiO<sub>2</sub> was used as a protective layer on Ga<sub>2</sub>O<sub>3</sub>/Cu<sub>2</sub>O structure, the potential barrier at TiO<sub>2</sub>/electrolyte interface is low because of the conduction band of TiO<sub>2</sub> is positioned at -0.1 V vs. RHE. The depletion region width of the 220°C-deposited TiO<sub>2</sub> in this experiment is about 2 nm when the electron quasi-Fermi level ( $E_F$ ) is positioned at 0 V vs. RHE, thus the electrons can tunnel through the barrier easier than that of the Ga<sub>2</sub>O<sub>3</sub> case. In summary, the TiO<sub>2</sub> layer not only served as a protective layer for the photocathode but also provide an appropriate conduction band position and short depletion layer length for electron transport, leading to an efficient PEC hydrogen reduction at positive potential region. For the TiO<sub>2</sub>/Ga<sub>2</sub>O<sub>3</sub>/Cu<sub>2</sub>O structures with different TiO<sub>2</sub> deposition temperatures, the improvement of PEC performance from 120 to 220°C may can be attributed to the decreased interfacial charge transfer resistance at the TiO<sub>2</sub>/electrolyte interface, as presented in Figure 3.10a. We calculated and compared the depletion region width of TiO<sub>2</sub> layer (biased at 0 V vs. RHE) deposited from 120 to 220°C using the same method mentioned above. It is found that the depletion layer length decreased from 4.7, 4.6, 2.7 to 2.1 nm when the deposition temperature increased from 120, 150, 180 to 220°C, respectively. The results indicate that the width of depletion region of TiO<sub>2</sub> layer in electrolyte decreasing with the increasing of deposition temperature in this work, and thus lead to a lower electron transfer resistance and a better PEC performance for the TiO<sub>2</sub>(220°C)/Ga<sub>2</sub>O<sub>3</sub>/Cu<sub>2</sub>O sample. The increasing of TiO<sub>2</sub> deposition temperature (from 120 to 220°C) may also improve

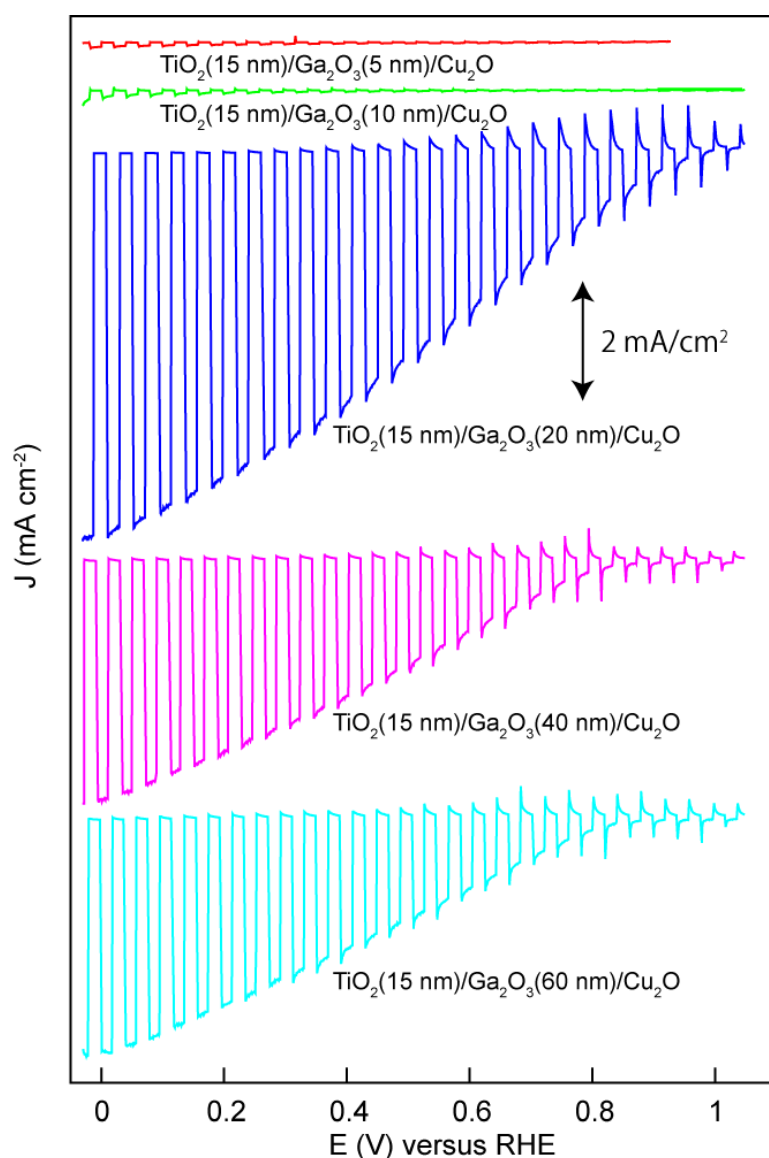


**Figure 3.11.** Current-potential curves of Pt/TiO<sub>2</sub>(220°C)/Ga<sub>2</sub>O<sub>3</sub>(150°C)/Cu<sub>2</sub>O samples with different Ga<sub>2</sub>O<sub>3</sub> thickness. Thickness for TiO<sub>2</sub> is kept at 15 nm. Curves were measured in 0.5 M Na<sub>2</sub>SO<sub>4</sub>-0.1 M KH<sub>2</sub>PO<sub>4</sub> solution (pH = 4.26) under 500 W Xe lamp.

the Ga<sub>2</sub>O<sub>3</sub>/TiO<sub>2</sub> interface and decrease the bulk resistance of TiO<sub>2</sub> and thus contribute to the enhancement of PEC performance of the photoelectrodes.

The Ga<sub>2</sub>O<sub>3</sub> buffer layers with different thickness were also investigated. The TiO<sub>2</sub> protective layer was deposited under the same conditions (15 nm, 220°C) for

all the electrodes, while the thickness of  $\text{Ga}_2\text{O}_3$  was varied from 5 to 60 nm to study the effect of buffer thickness on the performance of the electrodes. In Figure 3.11, it is found that the 5 and 10 nm buffer layer lead to a very low photocurrent (only several microamperes per square centimetre). This may can be attributed to the incomplete coverage of buffer layer on  $\text{Cu}_2\text{O}$  and the  $\text{TiO}_2$  likely contact with  $\text{Cu}_2\text{O}$ , resulting an unfavourable interface. When buffer layer thickness increased to 20 nm, the photocurrent of the electrode increased drastically, indicating a conformal coating of buffer layer and a favourable band alignment formed among the multilayers. When the thickness increased further, the photocurrent decreased correspondingly, indicating an increased resistance of buffer layer due to the incremental thickness.

To determine the stability of  $\text{Pt}/\text{TiO}_2/\text{Ga}_2\text{O}_3/\text{Cu}_2\text{O}$  photoelectrodes, the time dependency of the photocurrent was tested at 0 V vs. RHE under 500 W Xe lamp irradiation as shown in Figure 3.12a. The photocathodes fabricated with  $\text{TiO}_2$  deposition temperatures of 120, 150, and 180°C maintained a highly stable photocurrent for 2 h, during which the fluctuation in the photocurrent was caused by the formation and detachment of  $\text{H}_2$  bubbles, as presented in Figure 3.12b-c. The SEM characterization for the 180°C-deposited sample after a 2 h stability test indicates that no obvious morphology change occurred during the stability test (Figure 3.13). Furthermore, the presence of Ti and Pt peaks and the absence of Ga peaks in the XPS spectrum reveal that the photocathode is stable against corrosion in the electrolyte, as shown in Figure 3.13f. For the 220°C-deposited electrode, the sample showed a large photocurrent, but the current decreased slowly with time. After the 2 h test and a following short rest, 60% of the initial photocurrent was



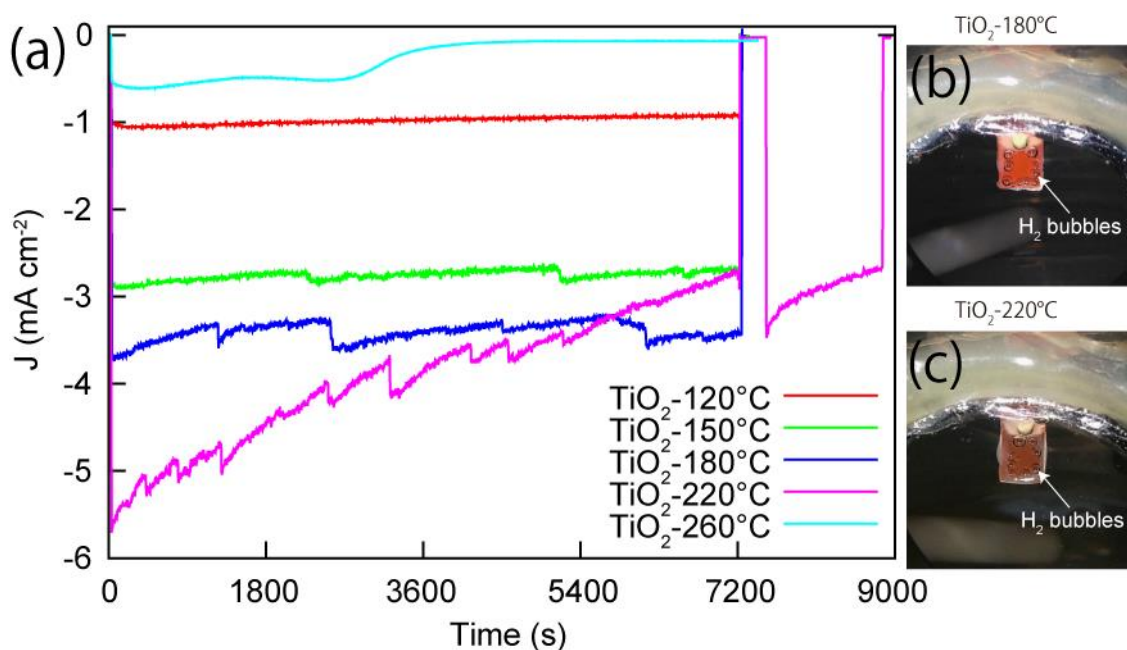


**Figure 3.12.** (a) Current-time curves (held at 0 V vs. RHE) of Pt/TiO<sub>2</sub>/Ga<sub>2</sub>O<sub>3</sub>/Cu<sub>2</sub>O samples with different TiO<sub>2</sub> deposition temperatures. Deposition temperature for Ga<sub>2</sub>O<sub>3</sub> is kept at 150°C. (b-c) H<sub>2</sub> bubbles evolving from the Pt/TiO<sub>2</sub>(180°C)/Ga<sub>2</sub>O<sub>3</sub>/Cu<sub>2</sub>O and Pt/TiO<sub>2</sub>(220°C)/Ga<sub>2</sub>O<sub>3</sub>/Cu<sub>2</sub>O samples under illumination of a Xe lamp at 0 V vs. RHE. Curves were measured in 0.5 M Na<sub>2</sub>SO<sub>4</sub>-0.1 M KH<sub>2</sub>PO<sub>4</sub> solution (pH = 4.26) under 500 W Xe lamp.

obtained. With the deposition temperature of 260°C, the photocurrent was low and could only be maintained for about 50 min, the photocathode losing its activity after one-hour stability test. The decay of the photocurrent for the electrodes prepared above 220°C may be attributed to the degradation of the TiO<sub>2</sub> layer and/or the detachment of Pt owing to H<sub>2</sub> bubble generation during the stability test.<sup>9, 24-25</sup>

The wavelength dependency of the incident photon-to-current conversion efficiency (IPCE) for Pt/TiO<sub>2</sub>/Ga<sub>2</sub>O<sub>3</sub>/Cu<sub>2</sub>O electrodes with different TiO<sub>2</sub> deposition temperatures are shown in Figure 3.14f. The 220°C-deposited sample exhibited the highest IPCE among the samples. At 0 V vs. RHE, the IPCEs for the

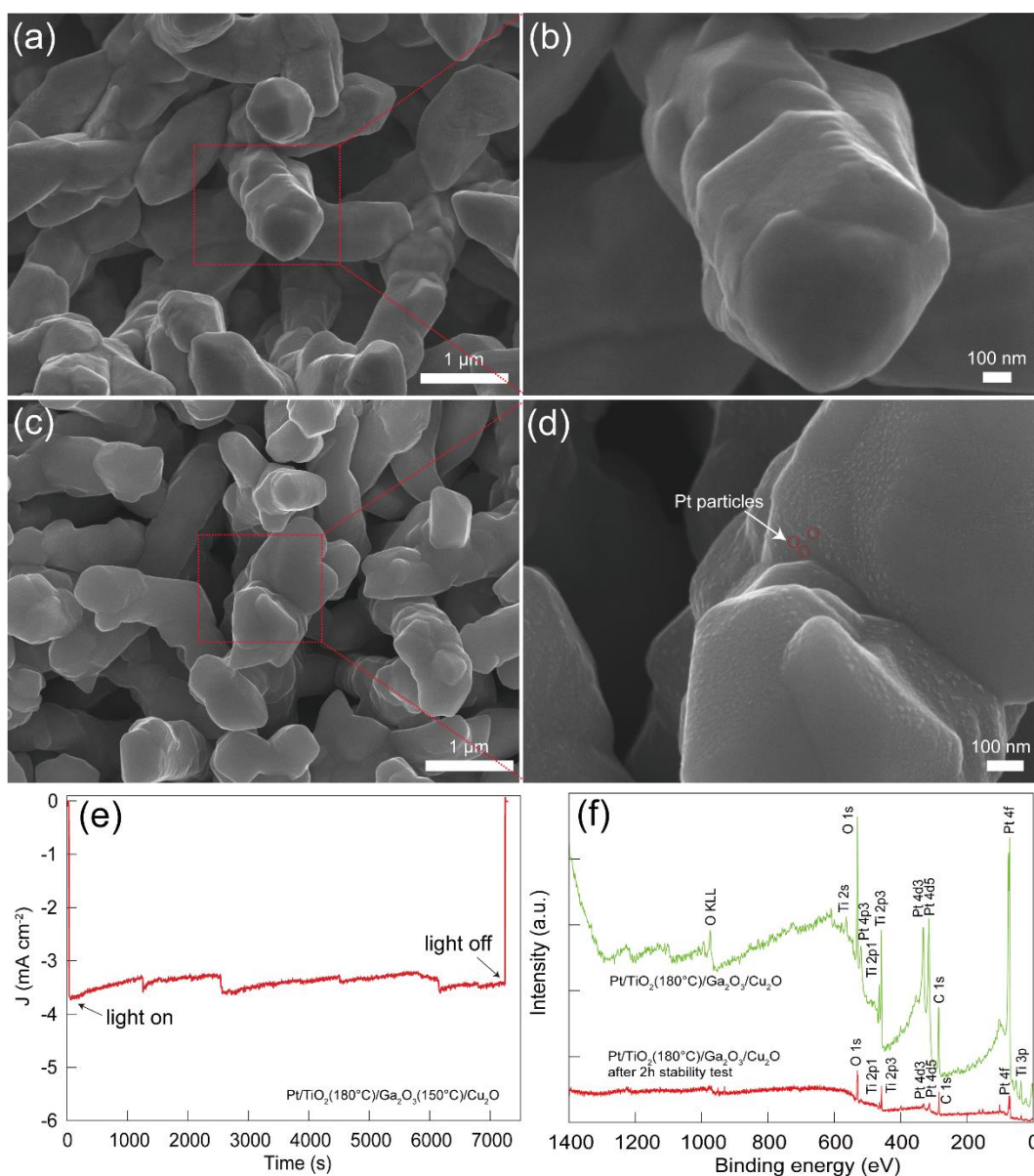


**Figure 3.13.** (a-b) FE-SEM images of the Pt/TiO<sub>2</sub> (180°C)/Ga<sub>2</sub>O<sub>3</sub> (150°C)/Cu<sub>2</sub>O electrode before stability test. (c-d) FE-SEM images of Pt/TiO<sub>2</sub> (180°C)/Ga<sub>2</sub>O<sub>3</sub> (150°C)/Cu<sub>2</sub>O electrode after 2 h stability test. (e) Stability test of the sample held at 0 V/RHE under 500 W Xe lamp for 2 h. (f) XPS measurement results of the Pt/TiO<sub>2</sub> (180°C)/Ga<sub>2</sub>O<sub>3</sub> (150°C)/Cu<sub>2</sub>O sample before and after 2 h stability test.

Pt/TiO<sub>2</sub>(220°C)/Ga<sub>2</sub>O<sub>3</sub>/Cu<sub>2</sub>O electrode were above 36% in the 350-450 nm range. The maximum IPCE achieved was 46.9% at 400 nm. By decreasing the TiO<sub>2</sub>

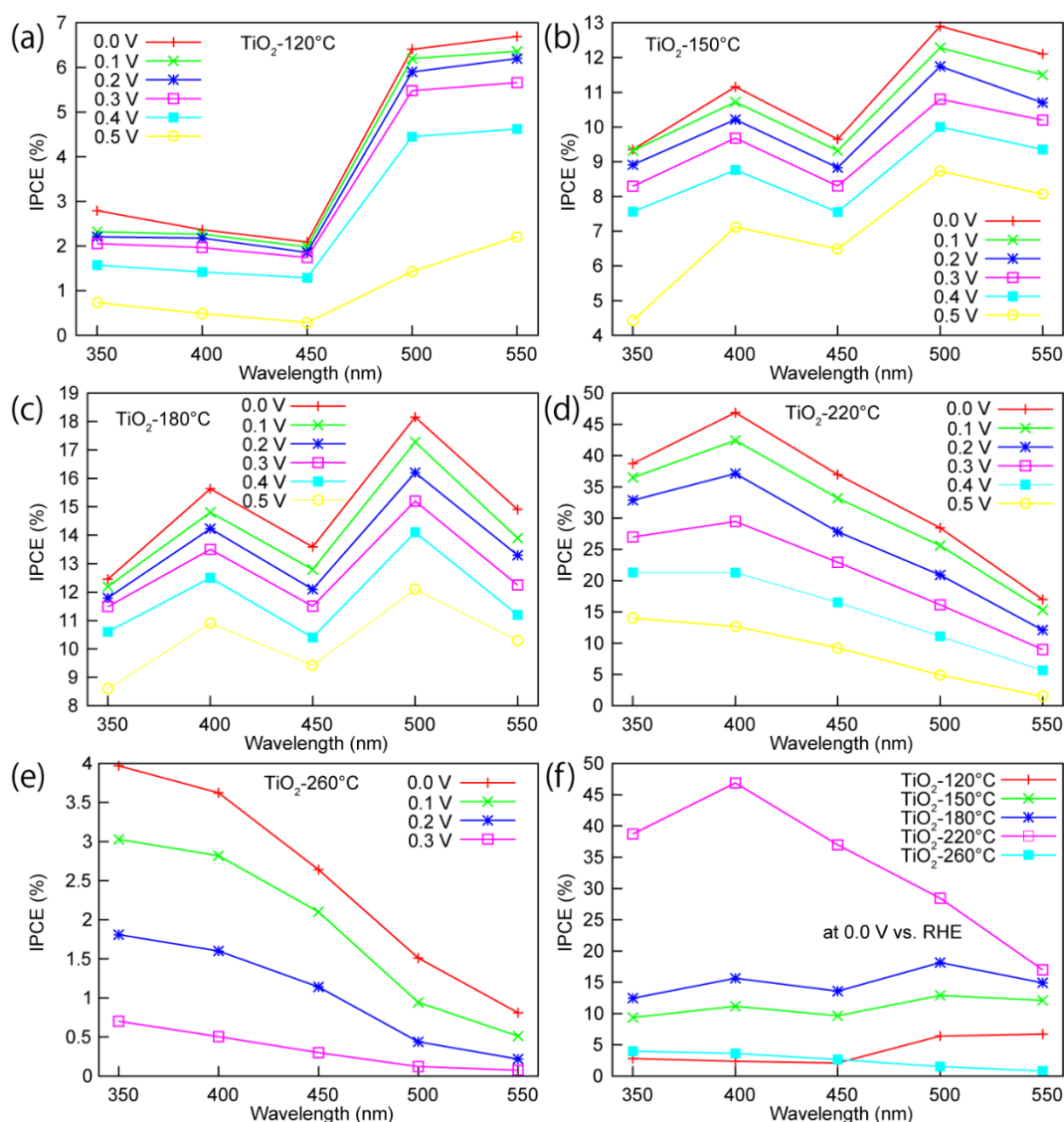


**Figure 3.14.** (a-e) Wavelength dependence of IPCE for the Pt/TiO<sub>2</sub>/Ga<sub>2</sub>O<sub>3</sub>/Cu<sub>2</sub>O electrodes with a TiO<sub>2</sub> deposition temperature of 120 a), 150 b), 180 c), 220 d) and 260°C e) at different applied potentials (vs. RHE). (f) Wavelength dependence of IPCE measured at 0 V vs. RHE for those samples.

deposition temperature, the IPCE decreased correspondingly. Notably, at wavelengths below 450 nm, the electrodes with the TiO<sub>2</sub> deposition temperature equal to or lower than 180°C showed much lower efficiency than the 220°C-deposited one. The wavelength dependence of IPCE for the electrodes was not

consistent with the absorbance spectrum of the samples (Figure 3.9c). This may be ascribed to the complexity of the transport of photocarriers through the multilayers in this structure since the improvement in the conversion efficiency is dependent on not only the absorption of the incident photons but also the transport of photocarriers to reach the surface for the chemical reaction. One possible reason for the efficiency loss with the TiO<sub>2</sub> layer prepared under low temperatures is the low crystallinity and defective interfaces at the buffer layer interface resulting in high recombination rates. In contrast to the high IPCEs for the 220°C-deposited sample, the IPCEs for the sample prepared at 260°C were very low. The low performance can be attributed to the degradation TiO<sub>2</sub> layer prepared at high temperature. The wavelength dependence of IPCE at different potentials (from 0.0 to 0.5 V vs. RHE) for the 220°C-deposited sample was also investigated (Figure 3.14d). The result indicates that even at the low applied potential of 0.5 V vs. RHE, the IPCEs are still relatively high, which is consistent with the high photocurrent at low potential presented in the current-potential curve.

The PEC water splitting properties of the photocathodes under AM 1.5G-simulated sunlight (100 mW/cm<sup>2</sup>) are also given for comparison in Figure 3.15a. The electrodes showed a large photocurrent under light and negligible current under dark conditions. The photocurrent densities of -0.54, -1.29, -1.64, and -2.95 mA/cm<sup>2</sup> were obtained at 0 V vs. RHE (the voltage is swept from negative to positive) for the TiO<sub>2</sub> deposition temperatures of 120, 150, 180, and 220°C, respectively. Interestingly, the onset potential of the Pt/TiO<sub>2</sub>(220°C)/Ga<sub>2</sub>O<sub>3</sub>/Cu<sub>2</sub>O electrode, defined as the potential at which a photocathodic current exceeds 20 μA/cm<sup>2</sup>, was 1.02 V vs. RHE. This is superior to the onset potential of 0.96, 0.94,

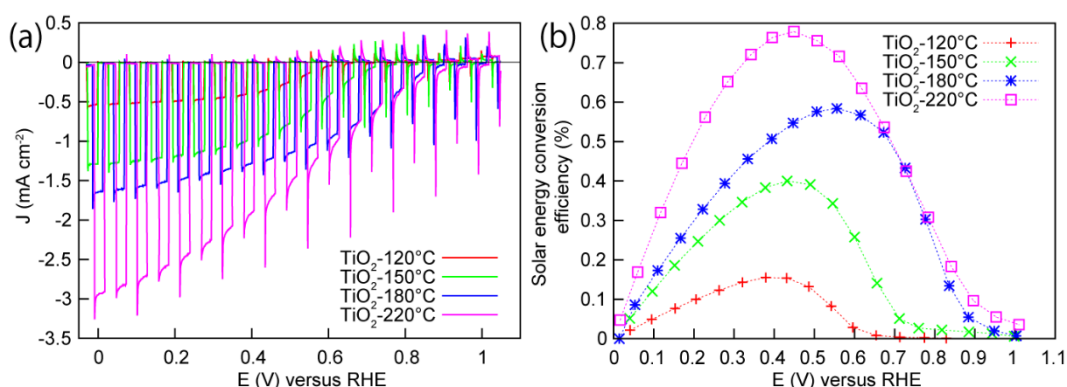


**Figure 3.15.** (a) Current-potential curves for Pt/TiO<sub>2</sub>/Ga<sub>2</sub>O<sub>3</sub>/Cu<sub>2</sub>O photocathode obtained for different TiO<sub>2</sub> deposition temperatures under AM 1.5G irradiation at 100 mW/cm<sup>2</sup>. Curves were measured in 0.5 M Na<sub>2</sub>SO<sub>4</sub>-0.1 M KH<sub>2</sub>PO<sub>4</sub> solution (pH = 4.26), and potential was swept in positive direction at rate of 10 mV/s. (b) Solar energy conversion efficiency of photocathodes calculated from current-potential curves in (a).

and 0.65 V vs. RHE obtained for 180, 150 and 120°C-deposited samples. The onset potential in this report shows a significant enhancement over the previously-reported Cu<sub>2</sub>O-based photocathodes, including the TiO<sub>2</sub>/ZnO/Cu<sub>2</sub>O (0.45-0.55 V),<sup>24-26</sup> carbon/Cu<sub>2</sub>O (0.6 V),<sup>34</sup> and TiO<sub>2</sub>/ZnS/Cu<sub>2</sub>O (0.72 V)<sup>27</sup> structures. The best electrode (220°C) shows a large photocathodic current at positive potential, i.e., -1.17 mA/cm<sup>2</sup> at 0.6 V vs. RHE, which makes it a promising candidate for tandem cell applications. The summary of the performance and stability for Cu<sub>2</sub>O-based photocathodes are presented in Table 3.1. Figure 3.15b shows the solar energy conversion efficiency of the electrodes calculated from the current-potential curves of Figure 4a. A maximum conversion efficiency of 0.16, 0.40, 0.58, and 0.78% were achieved at 0.38, 0.43, 0.56, and 0.45 V vs. RHE for the 120, 150, 180 and 220°C-deposited electrodes, respectively.

**Table 3.1.** Summary of the performance and stability for Cu<sub>2</sub>O based photocathodes.

Cu <sub>2</sub> O-based photocathodes	HER catalyst	Stability* at 0 V vs RHE	Photocurrent onset (vs RHE)	Maximum efficiency (AM 1.5 illumination)	Ref.
TiO <sub>2</sub> (180°C)/Ga <sub>2</sub> O <sub>3</sub> (150°C)/Cu <sub>2</sub> O	Pt	2 h at pH 4.26 (almost 100%)	0.96 V	0.58% at 0.56 V vs RHE	This work
TiO <sub>2</sub> (220°C)/Ga <sub>2</sub> O <sub>3</sub> (150°C)/Cu <sub>2</sub> O	Pt	2 h at pH 4.26 (60%)	1.02 V	0.78% at 0.45 V vs RHE	This work
Carbon/Cu <sub>2</sub> O	--	20 min at pH 6 (80.7%)	0.6 V	0.56% at 0.21 V vs RHE	[34]
TiO <sub>2</sub> /AZO/Cu <sub>2</sub> O	Pt	20 min at pH 5 (78%)	~0.4 V	~0.78% at 0.2 V vs RHE	[9]
TiO <sub>2</sub> (10nm, 150°C)/AZO(20nm)/Cu <sub>2</sub> O	Pt	1 h at pH 5 (almost 100%)	0.4-0.5V	~0.4% at 0.2 V vs RHE	[24]
Cu <sub>2</sub> O	NiOx	20 min (+0.26 V vs RHE) at pH 6 (72%)	0.46 V	~0.52% at 0.26 V vs RHE under LED light illumination	[35]

\* The percentage indicated in the stability column corresponds to the ratio between the photocurrent after the stability test and before the stability test.

### 3.5. PEC properties of Pt/TiO<sub>2</sub>/ZnO/Cu<sub>2</sub>O photocathodes

For comparison purposes, a ZnO buffer layer with an electron affinity much higher than Cu<sub>2</sub>O was used to fabricate a TiO<sub>2</sub>/ZnO/Cu<sub>2</sub>O photocathode. Figure 3.16a shows the top morphology of the Cu<sub>2</sub>O microcrystalline film after coating 20 nm of ZnO(150°C) and 15 nm of TiO<sub>2</sub>(120°C). No obvious change in the morphology of the microcrystals was found because the coating was homogeneous. In order to characterize the chemical state of the overlayers, XPS was conducted on the ZnO/Cu<sub>2</sub>O and TiO<sub>2</sub>/ZnO/Cu<sub>2</sub>O samples. With a very thin layer of ZnO(2 nm) on Cu<sub>2</sub>O, the XPS spectrum showed the Zn 2p<sub>3/2</sub> (1021.44 eV) and O 1s (531.2 eV) peaks for ZnO. In addition, Cu 2p peaks from the Cu<sub>2</sub>O underlayer are also observed. The Cu<sub>2</sub>O layer showed two main peaks at 931.9 and 952.2 eV corresponding to the 2p<sub>3/2</sub> and 2p<sub>1/2</sub> levels of Cu<sub>2</sub>O. The shoulder peak at 933.8



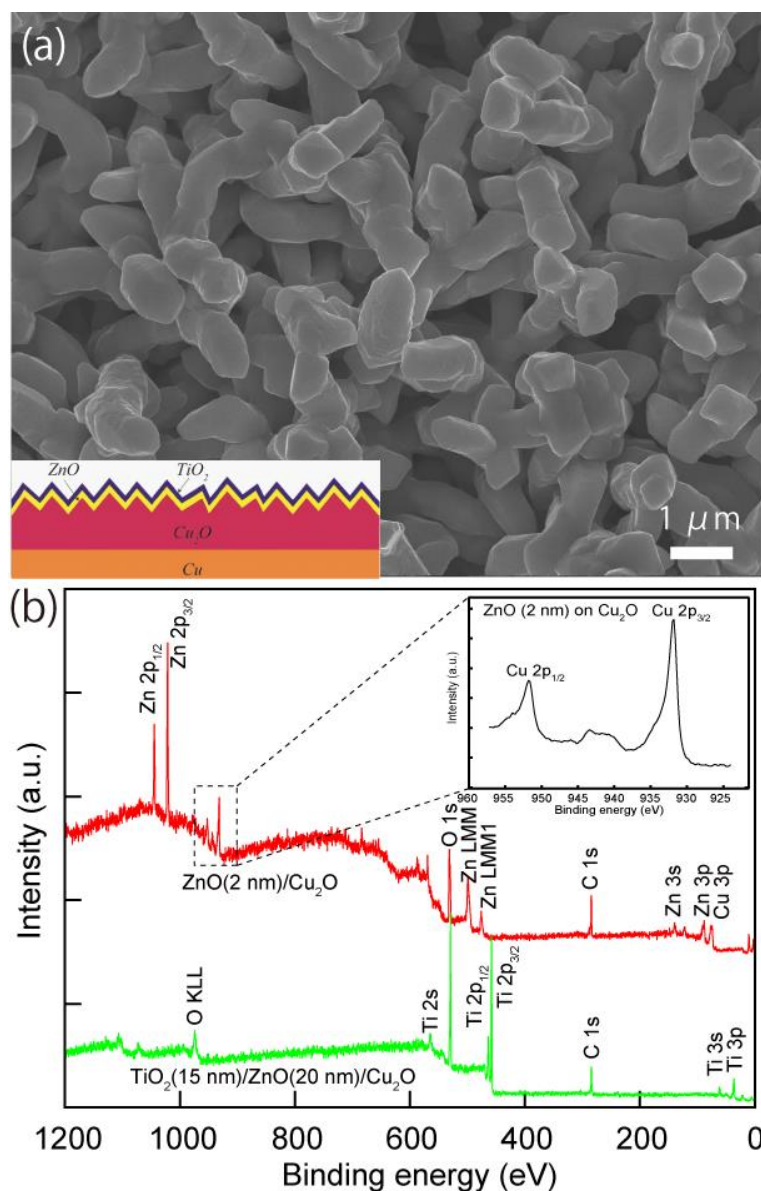


**Figure 3.16.** (a) FE-SEM images of Cu<sub>2</sub>O microcrystalline film coated with ZnO buffer layer and TiO<sub>2</sub> protective layer by atomic layer deposition. Lower left inset is the schematic of the multilayer structure. (b) XPS spectra of ZnO (2 nm)/Cu<sub>2</sub>O and TiO<sub>2</sub> (15 nm)/Ga<sub>2</sub>O<sub>3</sub> (20 nm)/Cu<sub>2</sub>O samples. Deposition temperature for ZnO and TiO<sub>2</sub> are 150 and 120°C, respectively. Top right inset is high resolution XPS spectrum of Cu-2p peaks of ZnO (2 nm)/Cu<sub>2</sub>O sample.

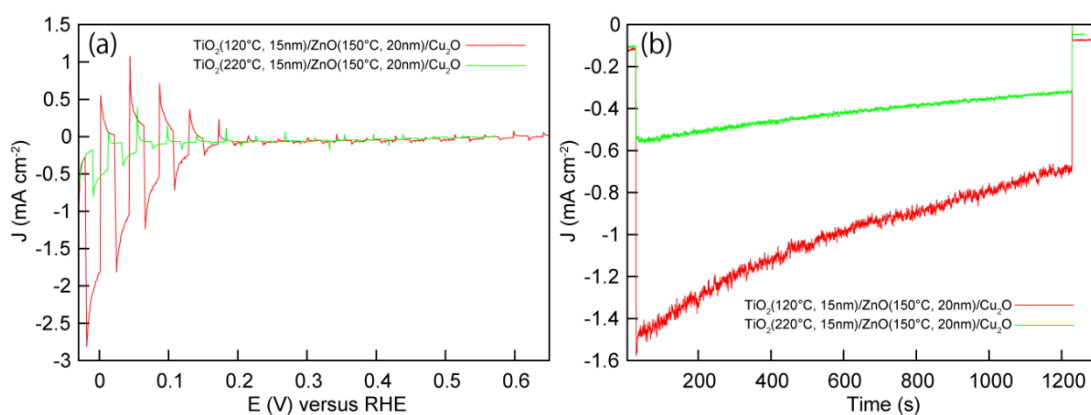


**Figure 3.17.** (a) The current-potential curves for the Pt/TiO<sub>2</sub>/ZnO/Cu<sub>2</sub>O electrodes fabricated with TiO<sub>2</sub> deposition temperatures of 120 and 220°C. The deposition temperature for ZnO was 150°C. (b) Current-time curve of the electrodes at 0 V vs. RHE under continuous light illumination. The measurements were conducted in 0.5 M Na<sub>2</sub>SO<sub>4</sub>-0.1 M KH<sub>2</sub>PO<sub>4</sub> solution (pH = 4.26) under illumination of a 500 W Xe lamp at a scan rate 10 mV/s.

eV and broad satellite peaks between 940-945 eV can be attributed to the thin CuO layer that is present on Cu<sub>2</sub>O from natural oxidation. For the TiO<sub>2</sub>/ZnO/Cu<sub>2</sub>O sample, the presence of Ti peaks and the absence of Ga and Cu peaks indicate that the ALD-deposited TiO<sub>2</sub> layer fully covered the Ga<sub>2</sub>O<sub>3</sub>, as indicated in Figure 3.16b. Figure 3.17a shows the current-potential curves for the Pt/TiO<sub>2</sub>/ZnO/Cu<sub>2</sub>O electrodes measured under a 500 W Xe lamp. The ZnO buffer layer was deposited under the same conditions (20 nm, 150°C) for all the electrodes, while the deposition temperature of TiO<sub>2</sub> was 120 and 220°C. The 120°C-deposited TiO<sub>2</sub> sample yielded a relatively low photocurrent (~1.5 mA/cm<sup>2</sup> at 0 V vs RHE) and negative onset voltage (~0.2 V vs RHE). When the TiO<sub>2</sub> deposition temperature increased to 220°C, the photocurrent of the electrodes decreased to about 0.5 mA/cm<sup>2</sup> at 0 V vs RHE. The TiO<sub>2</sub>/ZnO/Cu<sub>2</sub>O electrode prepared with a TiO<sub>2</sub> deposition temperature of 220°C shows a decreased photocurrent compared to the photocurrent



obtained with the 120°C-deposited electrode. This is may be due to the overdiffusion of ions at the buffer layer/Cu<sub>2</sub>O interface. To determine the stability of Pt/TiO<sub>2</sub>/ZnO/Cu<sub>2</sub>O photoelectrodes, the time dependency of the photocurrent was tested at 0 V vs. RHE under 500 W Xe lamp irradiation, as shown in Figure 3.17b. The photocathodes fabricated with TiO<sub>2</sub> deposition temperatures of 120 and 220°C showed a decreased photocurrent during the stability test. Small H<sub>2</sub> bubbles on the electrode edge can be found during the test. Thus, compared to the bare Cu<sub>2</sub>O electrode, this Pt/TiO<sub>2</sub>/ZnO/Cu<sub>2</sub>O electrode showed a better stability and made it possible to produce H<sub>2</sub> due to the prevention of Cu<sub>2</sub>O self-reduction. However, the production of H<sub>2</sub> is not efficient compared to the Pt/TiO<sub>2</sub>/Ga<sub>2</sub>O<sub>3</sub>/Cu<sub>2</sub>O structures, which is reflected in the low photocurrent, negative onset voltage and inadequate long-term stability. We infer that the Ga<sub>2</sub>O<sub>3</sub> buffer layer decreases the conduction band discontinuity at the Cu<sub>2</sub>O/buffer layer interface and thus increases the photovoltage of the structure, thus improving the efficiency and the stability.

### 3.6. Band alignment of heterojunction

To investigate the effect of the buffer layers on the performance of Cu<sub>2</sub>O-based photocathodes, the band alignment of the buffer layer/Cu<sub>2</sub>O interface was calculated by photoelectron spectroscopy according to the method outlined by Waldrop et al.<sup>29, 36-39</sup> X-ray photoemission spectrascopy (XPS) was applied to evaluate the conduction band discontinuity  $\Delta E_{CB}$  at Cu<sub>2</sub>O/Ga<sub>2</sub>O<sub>3</sub> heterojunction interface according to the equation:<sup>29</sup>

$$\Delta E_{CB} = (E_{Cu-2p}^{Ga_2O_3-Cu_2O} - E_{Ga-2p}^{Ga_2O_3-Cu_2O}) + (E_{Ga-2p}^{Ga_2O_3} - E_{VBM}^{Ga_2O_3}) - (E_{Cu-2p}^{Cu_2O} - E_{VBM}^{Cu_2O}) + (E_g^{Ga_2O_3} - E_g^{Cu_2O}) \quad (3.1)$$

The relative energy difference of Cu-2p<sub>3/2</sub> and Ga-2p<sub>3/2</sub> ( $E_{Cu-2p}^{Ga_2O_3-Cu_2O} - E_{Ga-2p}^{Ga_2O_3-Cu_2O}$ ), which extracted from the Ga<sub>2</sub>O<sub>3</sub>(2 nm)/Cu<sub>2</sub>O stack sample, is measured to be -185.85 eV.

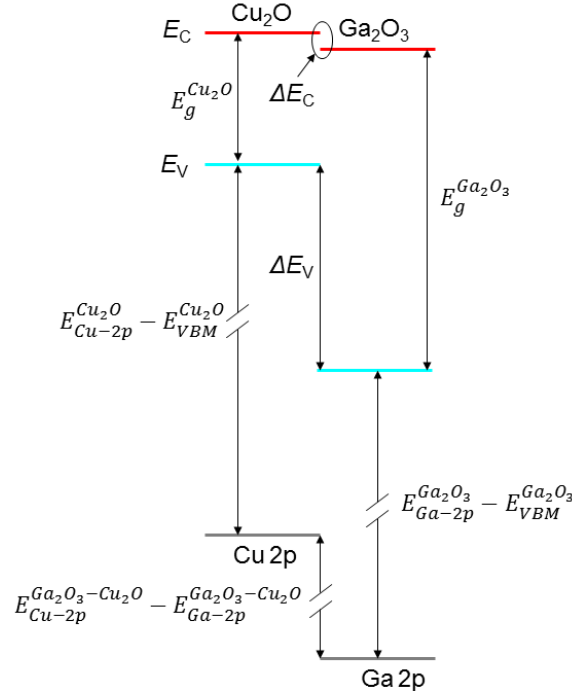


**Figure 3.18.** Schematic energy diagram of the heterojunction interface between  $\text{Cu}_2\text{O}$  and  $\text{Ga}_2\text{O}_3$

From the  $\text{Cu}_2\text{O}$  and  $\text{Ga}_2\text{O}_3$  bulk film, the binding energies of  $\text{Cu-}2p_{3/2}$  and  $\text{Ga-}2p_{3/2}$  core levels ( $E_{\text{Cu-}2p}^{\text{Cu}_2\text{O}}$  and  $E_{\text{Ga-}2p}^{\text{Ga}_2\text{O}_3}$ ) with respect to valence band edge positions of  $\text{Cu}_2\text{O}$  and  $\text{Ga}_2\text{O}_3$  are measured to be 931.95 eV and 1114.63 eV, respectively. The bandgap of the bulk  $\text{Cu}_2\text{O}$  ( $E_g^{\text{Cu}_2\text{O}}$ ) and  $\text{Ga}_2\text{O}_3$  ( $E_g^{\text{Ga}_2\text{O}_3}$ ) were 2.0 eV<sup>30</sup> and 4.8-5.18 eV.<sup>29, 40-42</sup> The extraction of the three terms in equation 3.1 is demonstrated in Figure 3.18 for  $\text{Cu}_2\text{O}$  and  $\text{Ga}_2\text{O}_3$ , where  $E_c$  is the conduction band energy,  $E_v$  is the valence band energy and  $E_g$  represents the respective bandgaps. The calculation result shows that the offset of  $E_{\text{CBM}}$  (conduction band maximum) between  $\text{Cu}_2\text{O}$  and  $\text{Ga}_2\text{O}_3$  was determined to be in the range between -0.37 and +0.01 eV (Figure 3.19), indicating the approximately equal electron affinity of the  $\text{Cu}_2\text{O}$  and  $\text{Ga}_2\text{O}_3$  layers. Thus, the introduction of the  $\text{Ga}_2\text{O}_3$  buffer layer decreases the conduction band discontinuity at the  $\text{Cu}_2\text{O}/\text{Ga}_2\text{O}_3$  interface, which is known

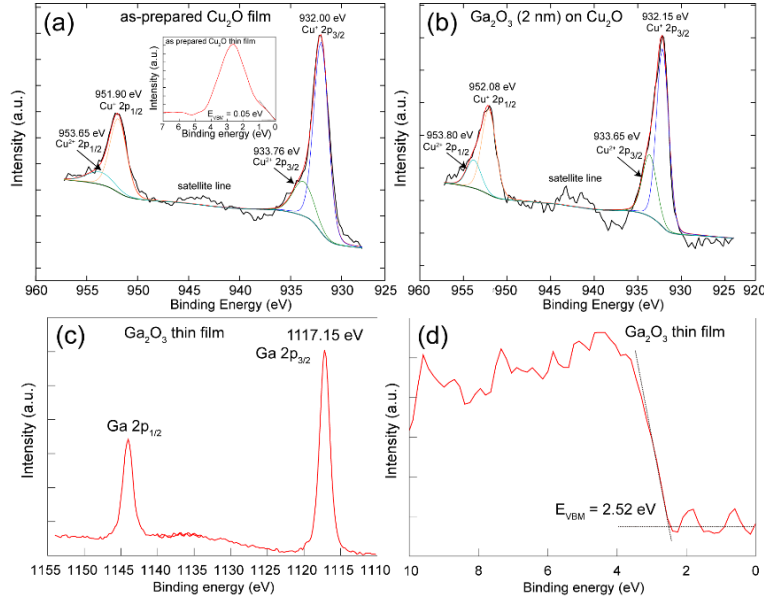


**Figure 3.19.** XPS spectra of Cu-2p core levels for as-prepared Cu<sub>2</sub>O (a) and Ga<sub>2</sub>O<sub>3</sub> (2 nm)/Cu<sub>2</sub>O multilayer sample (b). The deposition temperature for Ga<sub>2</sub>O<sub>3</sub> is 150°C. (b-d) XPS spectra of Ga<sub>2</sub>O<sub>3</sub> thin film for Ga-2p core levels and valence band. The inset in a shows the XPS spectra of Cu<sub>2</sub>O thin film for valence band.

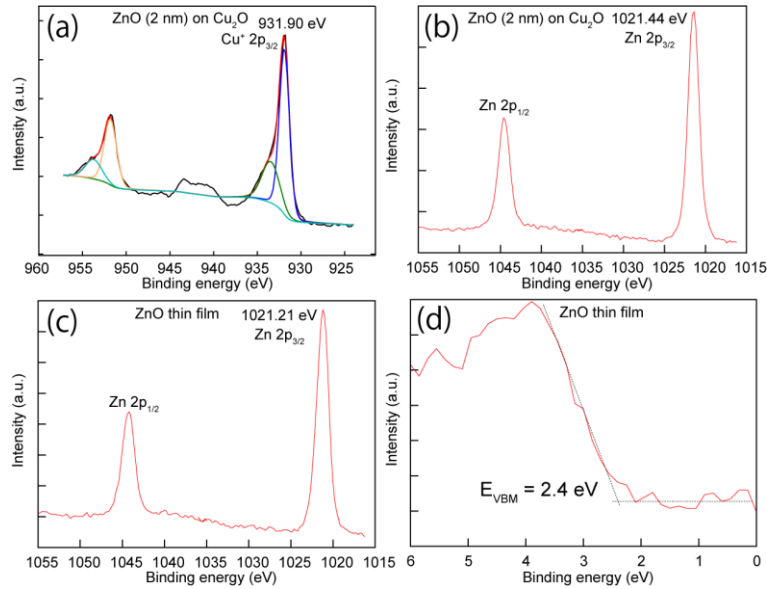


**Figure 3.20.** XPS spectra of the Cu-2p and Zn-2p core levels for the ZnO (2 nm)/Cu<sub>2</sub>O multilayer sample (a-b). The deposition temperature for ZnO is 150°C. (b-d) XPS spectra of ZnO thin film for Zn-2p core levels and valence band.

to improve the open circuit voltage and the fill factor of solar cells by reducing recombination.<sup>28-29</sup> In the PEC hydrogen evolution on Cu<sub>2</sub>O-based photocathodes, this is reflected in the cathodic shift in the onset potential of the photocurrent. In addition, the use of a Ga<sub>2</sub>O<sub>3</sub> thin layer allows to grow TiO<sub>2</sub> buffer layers at higher temperatures owing to its high thermal resistance. The reported decrease in the onset potential with the TiO<sub>2</sub> deposition temperature is ascribed to an improved Cu<sub>2</sub>O/Ga<sub>2</sub>O<sub>3</sub> and Ga<sub>2</sub>O<sub>3</sub>/TiO<sub>2</sub> interfaces formed under high temperature deposition of the TiO<sub>2</sub> layer. For comparison purposes, the ZnO buffer layer with an electron affinity much higher than Cu<sub>2</sub>O was used to fabricate a TiO<sub>2</sub>/ZnO/Cu<sub>2</sub>O photocathode. As shown in Figure 3.17a, the obtained Pt/TiO<sub>2</sub>/ZnO/Cu<sub>2</sub>O photocathodes exhibited a much more negative onset potential (lower photovoltage) than the Pt/TiO<sub>2</sub>/Ga<sub>2</sub>O<sub>3</sub>/Cu<sub>2</sub>O photocathodes, indicative of the large conduction band discontinuity between ZnO and Cu<sub>2</sub>O.<sup>9, 24</sup> To confirm this result, the same photoelectron spectroscopy method was used to characterize the band alignment between ZnO/Cu<sub>2</sub>O interface. The ZnO/Cu<sub>2</sub>O heterojunction actually possesses a large conduction band offset in the range from -1.56 to -1.42 eV (Figure 3.20), similar to previous reports.<sup>37-39</sup> In this calculation, a bandgap from 3.12 to 3.26 eV was used for ZnO.<sup>37, 39, 43-44</sup> In conclusion, the Ga<sub>2</sub>O<sub>3</sub> thin layer, owing to its high thermal resistance, worked as a suitable buffer layer to grow TiO<sub>2</sub> layers with improved quality. Figure 3.21 shows the energy band diagrams of the bare Cu<sub>2</sub>O and TiO<sub>2</sub>(15 nm, 220°C)/Ga<sub>2</sub>O<sub>3</sub>(20 nm)/Cu<sub>2</sub>O photoelectrodes under open-circuit conditions. The band position of Cu<sub>2</sub>O was calculated in Section 2.3.6. Mott-Schottky analysis of TiO<sub>2</sub>(50 nm, 220°C)/ITO electrode indicates that the conduction band and flatband potential of TiO<sub>2</sub> are -0.1 and -0.05 V vs. RHE, respectively. The band alignment between Cu<sub>2</sub>O and Ga<sub>2</sub>O<sub>3</sub> is estimated from the photoelectron spectroscopy method. For the bare Cu<sub>2</sub>O photoelectrode, the maximum

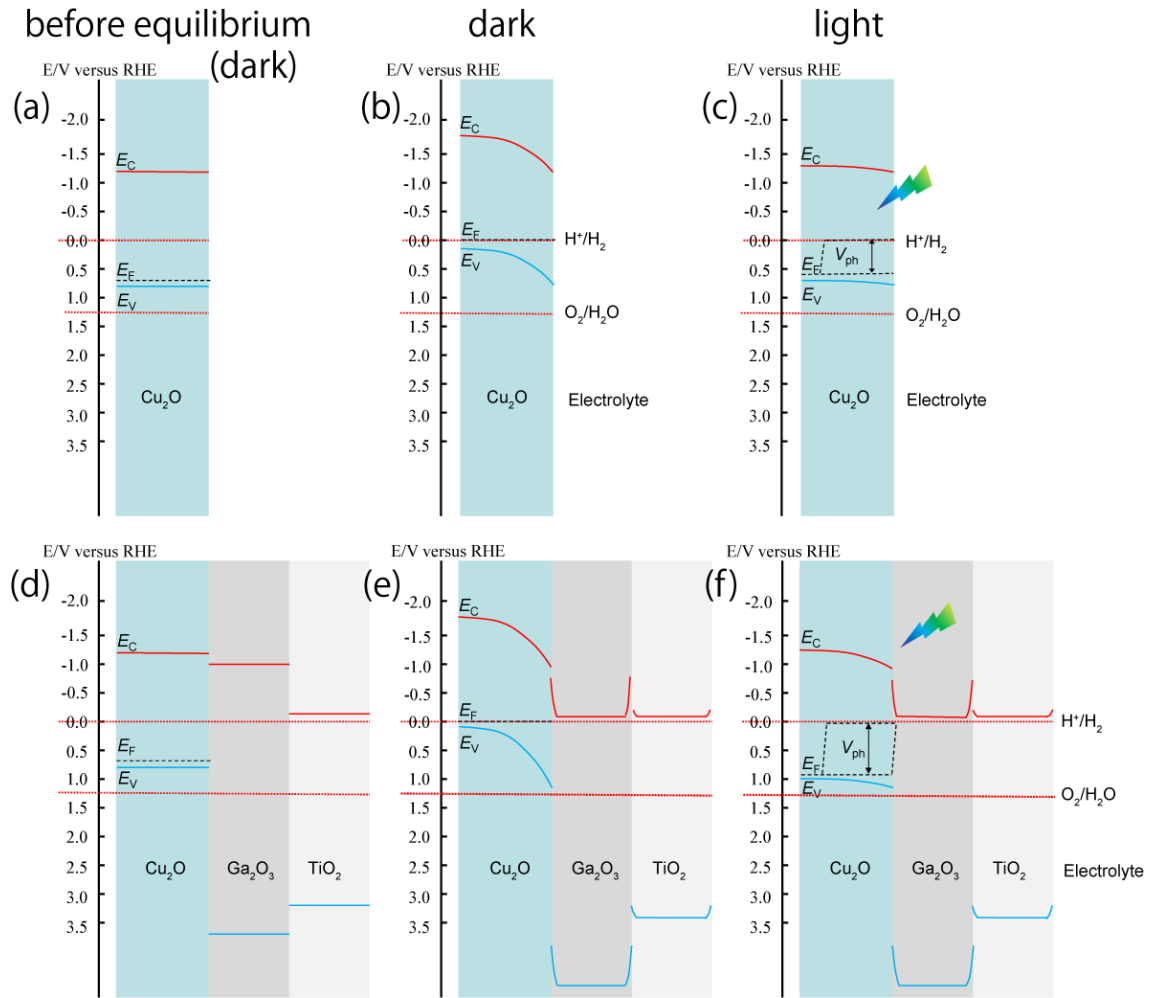


**Figure 3.21.** Schematic energy levels of the bare  $\text{Cu}_2\text{O}$  and  $\text{TiO}_2(20\text{nm})/\text{Ga}_2\text{O}_3(20\text{nm})/\text{Cu}_2\text{O}$  structure under open circuit condition: (a, d) before contacting the electrolyte solution (b, e) in the dark and in equilibrium with electrolyte solution (c, f) in the light and in quasi-equilibrium with electrolyte solution.

achievable photovoltage is determined by the difference between the flatband potential and the hydrogen evolution level. By introducing a  $\text{Ga}_2\text{O}_3$  buffer layer, the band edge positions of  $\text{Cu}_2\text{O}$  shift to positive direction because of the negative conduction band position of  $\text{Ga}_2\text{O}_3$ . In this case, the maximum achievable photovoltage is defined by the difference between the flatband potential of  $\text{Cu}_2\text{O}$  and  $\text{Ga}_2\text{O}_3$ . The  $\text{Ga}_2\text{O}_3$  exhibits a more negative flatband potential compared to  $\text{ZnO}$ , so a higher photovoltage from

TiO<sub>2</sub>/Ga<sub>2</sub>O<sub>3</sub>/Cu<sub>2</sub>O structure is obtained. Thus the obtained large energy gap between the p-type absorber and the n-type overlayers (Ga<sub>2</sub>O<sub>3</sub>) inhibits the interface recombination and provides a large driving force for the transport of photogenerated electrons in the photocathode, resulting in efficient H<sub>2</sub> reduction on the surface with the assistance of the Pt co-catalyst, as illustrated in Figure 3.21.

### 3.7. Conclusions

We have successfully deposited a Ga<sub>2</sub>O<sub>3</sub> thin film as an appropriate buffer layer for improving the performance of TiO<sub>2</sub>-coated Cu<sub>2</sub>O-based photocathodes. The Ga<sub>2</sub>O<sub>3</sub> buffer layer provided an electron affinity approximately equal to that of Cu<sub>2</sub>O, thus decreasing the conduction band discontinuity along the Cu<sub>2</sub>O/Ga<sub>2</sub>O<sub>3</sub> interface. In addition, high thermal resistance of Ga<sub>2</sub>O<sub>3</sub> allowed for ALD of TiO<sub>2</sub> at relatively high temperatures. These factors enabled suppression of the interface recombination and improvement in the photovoltage. An extremely positive onset voltage of 1.02 V vs. RHE was achieved by tuning the TiO<sub>2</sub> deposition temperature to 220°C. The photocathode produced a photocurrent of -2.95 mA/cm<sup>2</sup> at 0 V vs. RHE with a conversion efficiency of 0.78% at 0.45 V vs. RHE under AM 1.5G illumination. Moreover, the photocathodes exhibited a stable photocurrent under continuous illumination for 2 h for the deposition temperatures of TiO<sub>2</sub> ranging from 120 to 180°C, providing a promising photocathode candidate for high performance tandem cells.

## References

- [1] A. Fujishima and K. Honda, *Nature* 1972, **238**, 37.
- [2] O. Khaselev and J. A. Turner, *Science* 1998, **280**, 425.
- [3] R. Asahi, T. Morikawa, T. Ohwaki, K. Aoki and Y. Taga, *Science* 2001, **293**, 269.
- [4] Z. G. Zou, J. H. Ye, K. Sayama and H. Arakawa, *Nature* 2001, **414**, 625.
- [5] K. Maeda, T. Takata, M. Hara, N. Saito, Y. Inoue, H. Kobayashi and K. Domen, *J. Am. Chem. Soc.* 2005, **127**, 8286.
- [6] I. Cesar, A. Kay, J. A. Gonzalez Martinez and M. Grätzel, *J. Am. Chem. Soc.* 2006, **128**, 4582.
- [7] T. Hisatomi, H. Dotan, M. Stefik, K. Sivula, A. Rothschild, M. Grätzel and N. Mathews, *Adv. Mater.* 2012, **24**, 2699.
- [8] S. W. Boettcher, E. L. Warren, M. C. Putnam, E. A. Santori, D. Turner-Evans, M. D. Kelzenberg, M. G. Walter, J. R. McKone, B. S. Brunschwig, H. A. Atwater and N. S. Lewis, *J. Am. Chem. Soc.* 2011, **133**, 1216.
- [9] A. Paracchino, V. Laporte, K. Sivula, M. Grätzel and E. Thimsen, *Nat. Mater.* 2011, **10**, 456.
- [10] X. B. Chen, L. Liu, P. Y. Yu and S. S. Mao, *Science* 2011, **331**, 746.
- [11] Y. B. Li, L. Zhang, A. Torres-Pardo, J. M. González-Calbet, Y. H. Ma, P. Oleynikov, O. Terasaki, S. Asahina, M. Shima, D. K Cha, L. Zhao, K. Takanabe, J. Kubota and K. Domen, *Nat. Commun.* 2013, **4**, 2566.
- [12] Q. H Liu, J. F He, T. Yao, Z. H. Sun, W. R. Cheng, S. He, Y. Xie, Y. H. Peng, H. Cheng, Y. F. Sun, Y. Jiang, F. C. Hu, Z. Xie, W. S. Yan, Z. Y. Pan, Z. Y. Wu and S. Q. Wei, *Nat. Commun.* 2014, **5**, 5122.

- [13] M. Moriya, T. Minegishi, H. Kumagai, M. Katayama, J. Kubota and K. Domen, *J. Am. Chem. Soc.* 2013, **135**, 3733.
- [14] T. W. Kim and K. S. Choi, *Science* 2014, **343**, 990.
- [15] C. Liu, J. Y. Tang, H. M. Chen, B. Liu and P. D. Yang, *Nano Lett.* 2013, **13**, 2989.
- [16] W. B. Ingler and S. U. M. Khan, *Electrochem. Solid-State Lett.* 2006, **9**, G144.
- [17] H. L. Wang, T. Deutsch and J. A. Turner, *J. Electrochem. Soc.* 2008, **155**, F91.
- [18] S. Ida, K. Yamada, T. Matsunaga, H. Hagiwara, Y. Matsumoto and T. Ishihara, *J. Am. Chem. Soc.* 2010, **132**, 17343.
- [19] Q. X. Jia, K. Iwashina and A. Kudoa, *Proc. Natl. Acad. Sci. USA* 2012, **109**, 11564.
- [20] Q. P. Chen, J. H. Li, X. J. Li, K. Huang, B. X. Zhou and W. F. Shangguan, *ChemSusChem* 2013, **6**, 1276.
- [21] P. Bornoz, F. F. Abdi, S. D. Tilley, B. Dam, R. van de Krol, M. Graetzel and K. Sivula, *J. Phys. Chem. C* 2014, **118**, 16959.
- [22] B. Seger, T. Pedersen, A. B. Laursen, P. C. K. Vesborg, O. Hansen and I. Chorkendorff, *J. Am. Chem. Soc.* 2013, **135**, 1057.
- [23] S. Hu, M. R. Shaner, J. A. Beardslee, M. Lichterman, B. S. Brunschwig and N. S. Lewis, *Science* 2014, **344**, 1005.
- [24] A. Paracchino, N. Mathews, T. Hisatomi, M. Stefik, S. D. Tilley and M. Grätzel, *Energy Environ. Sci.* 2012, **5**, 8673.
- [25] S. D. Tilley, M. Schreier, J. Azevedo, M. Stefik and M. Grätzel, *Adv. Funct. Mater.* 2014, **24**, 303.



- [26] C. G. Morales-Guio, S. D. Tilley, H. Vrubel, M. Grätzel and X. L. Hu, *Nat. Commun.* 2013, **5**, 3059.
- [27] P. C. Dai, W. Li, J. Xie, Y. M. He, J. Thorne, G. McMahon, J. H. Zhan and D. W. Wang, *Angew. Chem.* 2014, **126**, 1.
- [28] T. Minami, Y. Nishi and T. Miyata, *Appl. Phys. Express* 2013, **6**, 044101.
- [29] Y. S. Lee, D. Chua, R. E. Brandt, S. C. Siah, J. V. Li, J. P. Mailoa, S. W. Lee, R. G. Gordon and T. Buonassisi, *Adv. Mater.* 2014, **26**, 4704.
- [30] C. L. Li, Y. B. Li and J. J. Delaunay, *ACS Appl. Mater. Interfaces* 2014, **6**, 480.
- [31] B. Seger, I. E. Castelli, P. C. K. Vesborg, K. W. Jacobsen, O. Hansen and I. Chorkendorff, *Energy Environ. Sci.* 2014, **7**, 2397.
- [32] I. A. Digdaya, L. Han, T. W. F. Buijs, M. Zeman, B. Dam, A. H. M. Smets and W. A. Smith, *Energy Environ. Sci.*, 2015, **8**, 1585.
- [33] N Suzuki, S Ohira, M Tanaka, T Sugawara, K. Nakajima, T. Shishido, *phys. stat. sol. (c)* 2007, **4**, 2310.
- [34] Z. H. Zhang, R. Dua, L. B. Zhang, H. B. Zhu, H. N. Zhang and P. Wang, *ACS Nano* 2013, **7**, 1709.
- [35] Lin, C-Y.; Lai, Y-H.; Merscha, D.; Reisner E. *Chem. Sci.* **2012**, *3*, 3482-3487.
- [36] J. R. Waldrop, R. W. Grant, S. P. Kowalczyk and E. A. Kraut, *J. Vac. Sci. Technol. A* 1985, **3**, 835.
- [37] Y. S. Lee, J. Heo, S. C. Siah, J. P. Mailoa, R. E. Brandt, S. B. Kim, R. G. Gordon and T. Buonassisi, *Energy Environ. Sci.* 2013, **6**, 2112.
- [38] L. M. Wong, S. Y. Chiam, J. Q. Huang, S. J. Wang, J. S. Pan and W. K. Chim, *J. Appl. Phys.* 2010, **108**, 033702.

- [39] Z. Q. Duan, A. Du Pasquier, Y. C. Lu, Y. Xu and E. Garfunkel, *Sol. Energy Mater. Sol. Cells* 2012, **96**, 292.
- [40] D. J. Comstock and J. W. Elam, *Chem. Mater.* 2012, **24**, 4011.
- [41] T. Oshima, K. Kaminaga, H. Mashiko, A. Mukai, K. Sasaki, T. Masui, A. Kuramata, S. Yamakoshi and A. Ohtomo, *Jpn. J. Appl. Phys.* 2013, **52**, 111102
- [42] Y. B. Li, T. Tokizono, M. Liao, M. Zhong, Y. Koide, I. Yamada and J.-J. Delaunay, *Adv. Funct. Mater.* 2010, **20**, 3972.
- [43] M. Zhong, Y. B. Li, I. Yamada and J. J. Delaunay, *Nanoscale* 2012, **4**, 1509.
- [44] S. Ren, Y. F. Bai, J. Chen, S. Z. Deng, N. S. Xu, Q. B. Wu, S. H. Yang, *Mater. Lett.* 2007, **61**, 666.

## **4. Nanoporous CuO layer modified Cu electrode for glucose sensing**

Nanoporous CuO layer on Cu foil with a thick Cu<sub>2</sub>O interlayer is synthesized via post annealing of previously fabricated Cu(OH)<sub>2</sub> nanowires at 500 °C under an oxygen flow. The formation of the thick sandwiched Cu<sub>2</sub>O layer is realized through the outward diffusion of Cu ions and subsequent oxidation. An O<sub>2</sub> pressure above the dissociation pressure of CuO is used to form a CuO layer at the outer surface of the structure, thus realizing a low cost structure having a porous and high isoelectric point layer. The Cu/Cu<sub>2</sub>O/CuO structure is used as an efficient electrode for glucose sensing. Sensitivities of 20.7  $\mu\text{A}/\text{mM}/\text{cm}^2$  at 0.8 V vs. Ag/AgCl and 1066  $\mu\text{A}/\text{mM}/\text{cm}^2$  at 0.6 V vs. Ag/AgCl are achieved in an enzymatic and non-enzymatic glucose sensing schemes, respectively. The improved electrochemical sensing ability might be attributed to the efficient electrocatalytic reaction on the high crystal quality CuO layer and the porous structure.

#### 4.1. Introduction

The detection of glucose in analytical applications such as clinical diagnostics has been the subject of much attention by analytical researchers for the past decade. The enzyme-based biosensing and enzymeless sensing are the two main electrochemical methods of glucose detection which have been widely studied.<sup>1-4</sup> The glucose oxidase (GOx)-based amperometric enzyme glucose sensors exhibit a good sensitivity and excellent selectivity but insufficient stability, because the activity of the enzymes is affected by temperature, pH, humidity and toxic chemicals.<sup>5-7</sup> The use of enzymeless glucose sensors is expected to improve the activity and stability toward electrochemical oxidation of glucose, however, most of the enzymeless sensors show low selectivity, suffering from interference responses caused by adsorbed intermediate species and chloride ions.<sup>1, 8</sup> Thus, the development of electrode materials for amperometric glucose sensor is an active research area. In addition to the widely used metallic electrodes such as Au,<sup>9-10</sup> Pt,<sup>11-13</sup> Ni,<sup>14-15</sup> Cu<sup>16-19</sup> and alloys,<sup>20-21</sup> nanostructured metal-oxides are being intensively researched for glucose sensing due to their low-cost, high specific surface area and good biological compatibility.<sup>22-34</sup> Among these metal-oxide materials, CuO is a promising candidate toward high performance glucose sensor both in enzymatic<sup>22</sup> and non-enzymatic<sup>28-34</sup> glucose sensing because of its high isoelectric point (IEP) and good electrochemical activity. However, most of the metal oxides prepared by solution processes are obtained in the form of dispersed powders and need to be transferred onto special substrates (e.g., glassy carbon/Au/Pt coated substrates),<sup>22-32</sup> thus increasing fabrication cost and complexity. In an attempt to achieve a simple and economic way towards high performance CuO glucose sensors, a structure of Cu<sub>2</sub>O/CuO thick layers fabricated directly on a Cu foil is introduced.

In this chapter, a Cu/Cu<sub>2</sub>O/CuO structure is prepared by annealing Cu/Cu(OH)<sub>2</sub> nanowires precursor under a controlled pressure and flow of O<sub>2</sub> at 500 °C. The CuO porous layer provides a large surface area for the electrochemical reaction and the sandwiched Cu<sub>2</sub>O layer may contribute to electron transfer, thus providing a suitable intermediate layer for the glucose sensing scheme. The amperometric detection of glucose exhibits a good sensitivity in enzymatic sensing (with GOx) and high performance in non-enzymatic sensing, demonstrating the potential of this structure as a facile synthesis and low-cost electrode with potential applications in glucose sensing devices.

## **4.2. Experimental section**

### **4.2.1. Fabrication of Cu(OH)<sub>2</sub> nanowires and Cu/Cu<sub>2</sub>O/CuO structures**

The Cu(OH)<sub>2</sub> nanowires on Cu substrate were fabricated by a solution process in an alkaline ammonium persulfate solution.<sup>36-37</sup> First, a Cu foil (99.96%, Nilaco) with a thickness of 0.2 mm and a size of 10×10 cm<sup>2</sup> was sonicated with acetone and ethanol for 10 min consecutively, then cleaned in distilled water; then immersed into a solution containing 2.67 M NaOH (min. 97.0%, Wako) and (NH<sub>4</sub>)<sub>2</sub>S<sub>2</sub>O<sub>8</sub> (min. 98.0%, Wako) for 10 min. During the reaction, a gentle stirring of the solution and low temperature of 5 °C were maintained to avoid the formation of CuO flowers on the top of Cu(OH)<sub>2</sub>. The CuO flowers formation at room temperature may come from inhomogeneity in solution concentration and high temperature near the Cu/solution interface. After the chemical reaction, the copper foil with a light blue color was taken out from the solution and cleaned with deionized water and dried in air.

The Cu/Cu<sub>2</sub>O/CuO structure was obtained by thermal annealing of the Cu(OH)<sub>2</sub> nanowires at 500 °C for 2 h under Ar and O<sub>2</sub> atmosphere. In detail, the Cu/Cu(OH)<sub>2</sub>

sample was loaded into a quartz boat and placed at the center of the quartz tube of a vacuum furnace. Before annealing, the quartz tube was evacuated to below 1 Pa and, then, O<sub>2</sub> (flow rate: 4 sccm) and Ar (flow rate: 50 sccm) were introduced as a reactive and a protective gas. The temperature was increased to 500 °C and kept for 2 h at a working pressure of  $2.6 \times 10^3$  Pa. After the annealing, the temperature of the quartz tube was decreased to room temperature naturally and a sample with uniform black color was obtained.

#### **4.2.2. Electrochemical measurements**

The electrochemical experiments were carried out in a standard three-electrode system using a potentiostat (VersaSTAT 4, Princeton Applied Research) at room temperature. Cyclic voltammetry (CV) measurements were performed in the potential range of 0-0.8 V vs. Ag/AgCl with a scan rate of 100 mV/s. The Ampermetric measurements were conducted by adding the desired amount of glucose consecutively at a fixed potential with the solution being stirred constantly. The electrolyte for enzymatic and non-enzymatic glucose sensing were 0.01 M PBS solution (pH 7.4) and 0.1 M NaOH solution (pH 13), respectively. For enzymatic sensing, 10 µL of glucose oxidase (GOx, 30 mg/mL, Sigma) was immobilized on the porous CuO layer surface by physical adsorption, followed by casting 10 µL of Nafion (Wako, 0.5wt %) on the surface of the fabricated electrodes to prevent the detachment of GOx during the analysis.

#### **4.2.3. Structural characterization**

The morphologies of the Cu(OH)<sub>2</sub> and CuO structures were examined with a field-emission scanning electron microscope (JEOL JSM 7600FA). X-ray diffractometer

(Miniflex II-MW, Rigaku Co. Ltd., Japan) with Cu K $\alpha$  radiation was used to identify the crystalline phase of the as-prepared samples. The Raman spectra of the samples were measured with a Renishaw inVia Raman Microscope system using a 488 nm excitation line directed through a  $\times 20$  objective with 1.2 mW for the top surface analysis and a  $\times 100$  objective with 0.1 mW for the cross-section analysis.

### 4.3. Results and discussion

#### 4.3.1. Characterization of the Cu/Cu<sub>2</sub>O/CuO structures

The Cu(OH)<sub>2</sub> nanowires were prepared by immersing a Cu foil in a mixed solution of NaOH (97.0%, Wako) and (NH<sub>4</sub>)<sub>2</sub>S<sub>2</sub>O<sub>8</sub> (98.0%, Wako) as reported elsewhere.<sup>36-37</sup> Figure 4.1a shows FE-SEM images of the as-prepared Cu(OH)<sub>2</sub> nanowires. The nanowires have a diameter of approximately 200 nm and a length of about 5  $\mu$ m. The XRD pattern of Cu/Cu(OH)<sub>2</sub> structures is shown in Figure 4.1c. The peak at 45.24 degree was assigned to NaOH, which may come from the residual chemicals attached on the surface of Cu(OH)<sub>2</sub>. All other peaks were indexed to Cu(OH)<sub>2</sub> (ICDD PDF card No. 5537) and Cu. After annealing under a mixture of Ar and O<sub>2</sub> at 500 °C for 2 h, a dense nanoporous film decorated with sparse nanowires is obtained, as shown in Figure 4.1b. The nanopores have a diameter of approximately 100-200 nm and are distributed on the whole surface. The crystalline phase of this structure was shown in Figure 4.1d. It is found that both phases, Cu<sub>2</sub>O and CuO, are detected on the Cu substrate. This indicates that the Cu(OH)<sub>2</sub> nanowires have been completely converted into copper oxides (I and II). The phase transformation was followed by Raman spectroscopy, as shown in Figure 4.2c. The Raman spectra taken from the top surface of the annealed sample consists of three peaks at 298 (A<sub>g</sub>), 346 (B<sub>1g</sub>) and 630 (B<sub>2g</sub>) cm<sup>-1</sup>, which are all indexed to CuO,<sup>38</sup> thus indicating

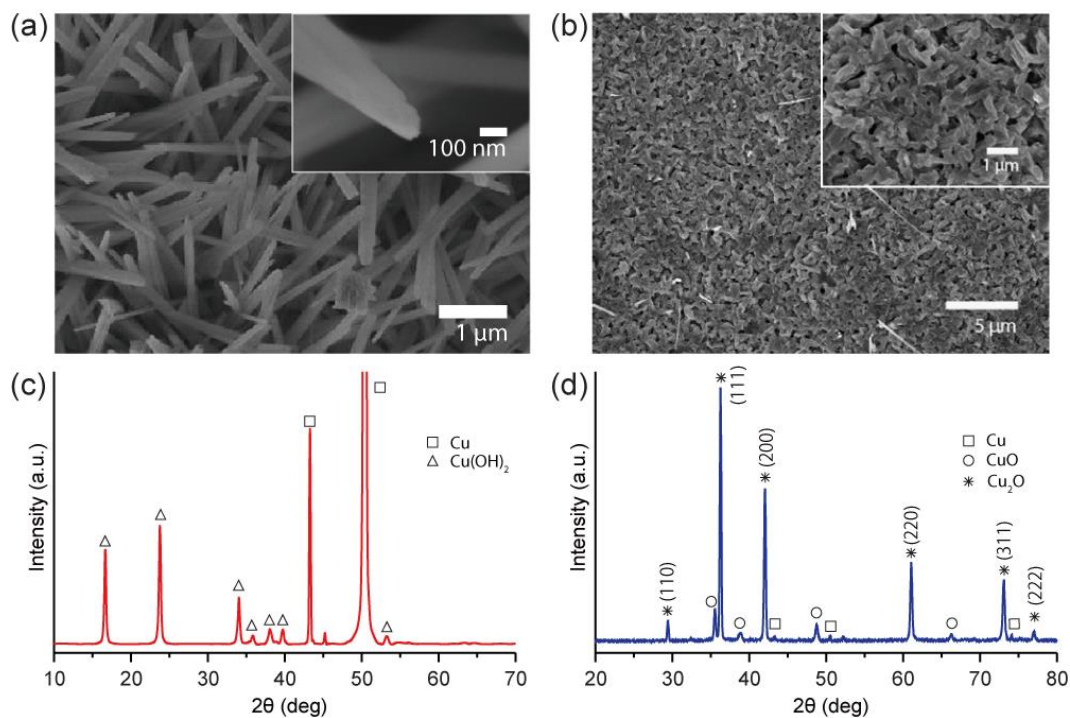


**Figure 4.1.** FE-SEM images of the morphology of the Cu(OH)<sub>2</sub> nanowires (a) and CuO porous layer (b). The top right insets in parts (a) and (b) are the enlarged images of the Cu(OH)<sub>2</sub> nanowires and CuO porous structure, respectively. (c)-(d) XRD patterns of the as-synthesized Cu/Cu(OH)<sub>2</sub> nanowires and the Cu/Cu<sub>2</sub>O/CuO structure formed upon annealing.

that the outer region of the sample was covered by a layer of CuO. What's more, Xu *et al.*<sup>38</sup> found that the Raman peaks of CuO become stronger and sharper and shift slightly to higher wavenumber as the grain size increases. In our experiment, the wavenumber of the three peaks showed a blue shift even compared to that of the CuO sample with a grain size larger than 100 nm,<sup>38</sup> indicating our CuO layer consisted of large crystal grains with an average grain size much larger than 100 nm with good crystal quality. In order to determine the crystalline phase in the inner region of the sample, a cross-section Raman spectroscopy was performed (Figure 4.2a and b). The measurement was conducted by taking Raman spectra at the spots indicated in Figure 4.2a so as to obtain information on



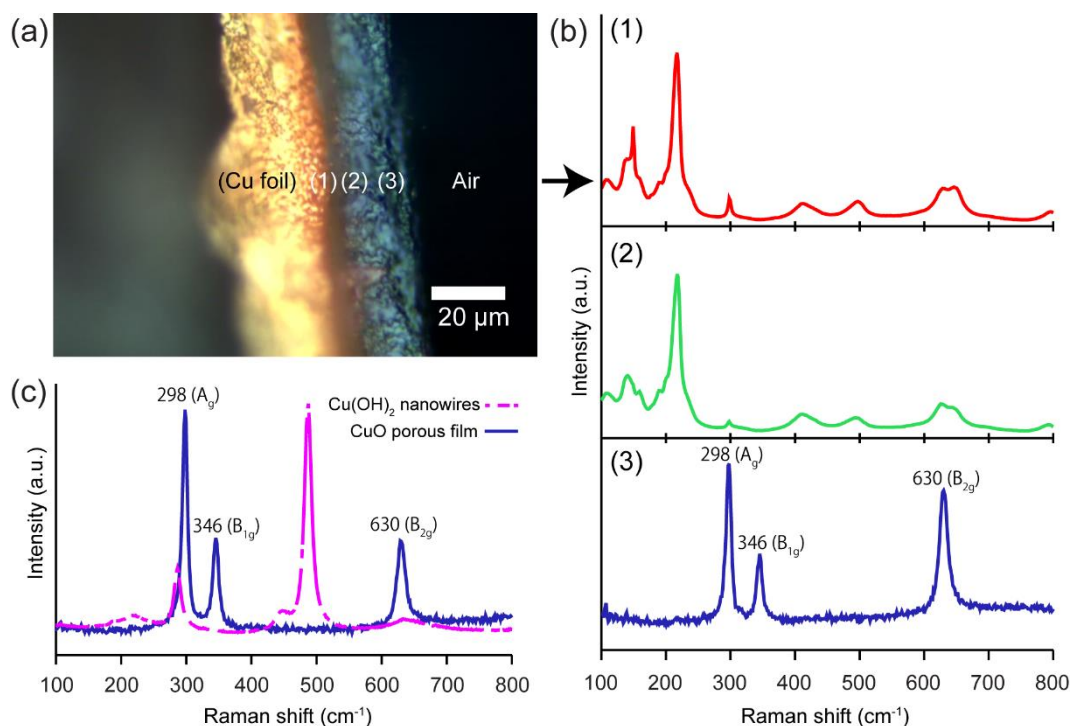


**Figure 4.2.** (a) Optical microscope image of the cross section of Cu/Cu<sub>2</sub>O/CuO structure. The different spots positioned on the cross section from Cu to CuO are marked by the symbols (1), (2) and (3), respectively. The Raman spectra taken at these spots are presented in part b. Part c shows the Raman spectra taken from the top surface of the Cu/Cu<sub>2</sub>O/CuO and Cu/Cu(OH)<sub>2</sub> samples.

the cross-section of the fabricated sample. For spots 1 and spot 2, the observed peaks at 109, 138, 148, 159, 186, 217, 298, 412, 496, 626, 649 and 794 cm<sup>-1</sup> can be ascribed to Cu<sub>2</sub>O.<sup>39</sup> Spot 3 on the outmost region exhibited the same Raman peaks that those of the Raman spectrum of the top surface. From the XRD and Raman results, we conclude that the oxide layer fabricated on the Cu foil was composed of an intermediate Cu<sub>2</sub>O thick layer and an outer CuO layer. The growth mechanism may be described as follows. The Cu(OH)<sub>2</sub> nanowires were decomposed to CuO nanowires at about 120 °C,<sup>40</sup> and the subsequent oxide growth was driven by outward diffusion of Cu ions via Cu vacancies

from the Cu substrate to the oxide layers and react with oxygen from the gas phase.<sup>41</sup> In our experiment, due to the introduction of O<sub>2</sub> during the annealing, the O<sub>2</sub> pressure is considered to be above the dissociation pressure of CuO, thus a layer of CuO is formed on the outer layer surface which separates the Cu<sub>2</sub>O from the gas atmosphere.<sup>41</sup> The Cu ions diffuse from the Cu substrate to the surface favoring the oxidation reaction which results in the volume expansion of the nanowires and consequently coalescence of the nanowires to form a nanoporous layer.

#### **4.3.2. Enzymatic glucose sensing**

The Cu/Cu<sub>2</sub>O/CuO based enzymatic glucose sensor is fabricated by surface functionalization with glucose oxidase (GOx), as shown in Figure 4.3a. The GOx dendrites formed on the CuO electrode indicates a good combination between the CuO surface and the enzyme. The efficient immobilization of GOx on CuO can be attributed to the high isoelectric point (9.5) of CuO, which provides a positive charge to attract negative charged GOx (isoelectric point: 4.7).<sup>42</sup> Figure 4.3b presents the cyclic voltammetry curves of the Cu<sub>2</sub>O/CuO/GOx electrode in PBS in the absence of glucose and presence of 0.4, 0.8, 2.0, 4.0, 6.0, 8.0, and 10 mM glucose. The five-cycle CV measurement (Figure 4.4a) of the Cu<sub>2</sub>O/CuO/GOx electrode without glucose in PBS provides evidence for repeatability during the test. With the increase in glucose concentration, the catalytic oxidation current increases accordingly in the potential range from about 0.45 to 0.8 V driven by GOx catalyzed glucose oxidation. Thus our fabricated Cu/Cu<sub>2</sub>O/CuO structure may be developed for use as a glucose sensor. In order to obtain the linear detection range, sensitivity and detection limits of the electrode, chronoamperometry is conducted by successive addition of 0.1 mM and then 1 mM

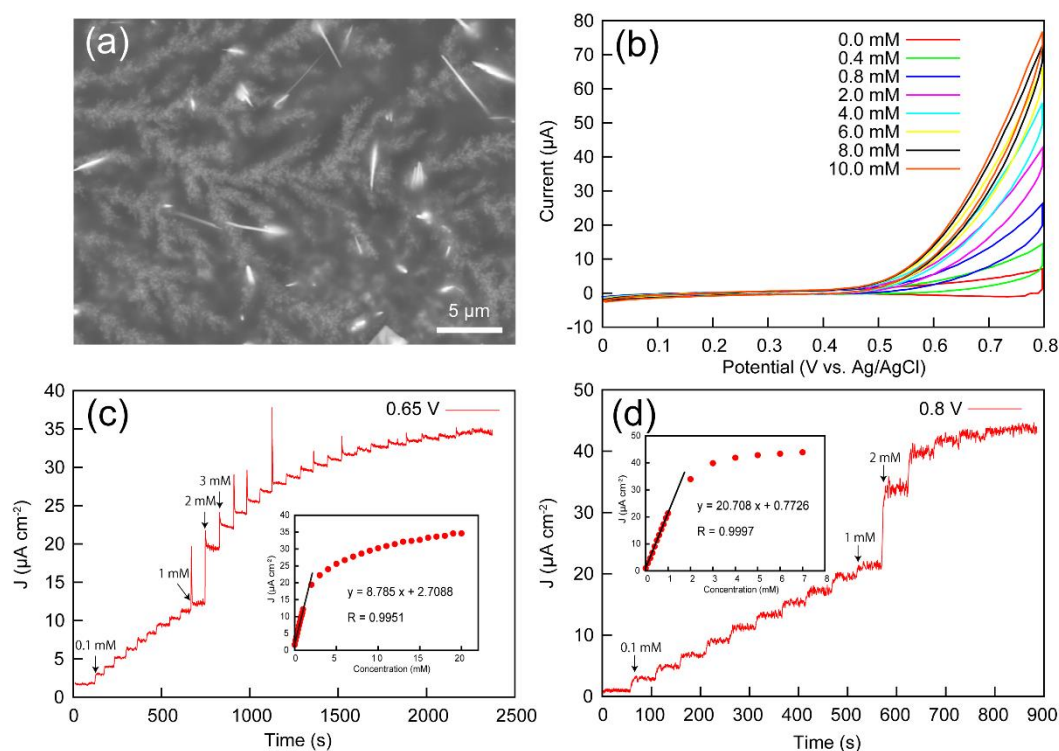


**Figure 4.3.** (a) SEM image of  $\text{Cu}_2\text{O}/\text{CuO}$  electrode after surface functionalization with GOx. (b) shows the voltammetric response of the electrode to the addition of 0.0, 0.4, 0.8, 2, 4, 6, 8, and 10 mM glucose in 0.01 M PBS (pH 7.4) at the scan rate of 100 mV/s. (c)-(d) the chronoamperometric response of the  $\text{Cu}/\text{Cu}_2\text{O}/\text{CuO}/\text{GOx}$  electrode with the potential fixed at 0.65 and 0.8 V vs. Ag/AgCl, respectively. The successive addition of 0.1 mM and then 1 mM glucose was conducted to obtain step responses. The calibration curves of the responses at 0.65 and 0.8 V are presented in the insets of part (c) and (d), respectively.

glucose into PBS every 50 s at a fixed voltage. Figure 4.3c shows the chronoamperometric result of the fabricated electrode with a potential of 0.65 V vs. Ag/AgCl. The electrode exhibits a sensitive response to the addition of glucose, indicating a good electrocatalytic performance to glucose. The response time (defined as the time for the current to reach 95% of the steady-state value) is about 8 s and the detection limit is about 5  $\mu\text{M}$  (Figure

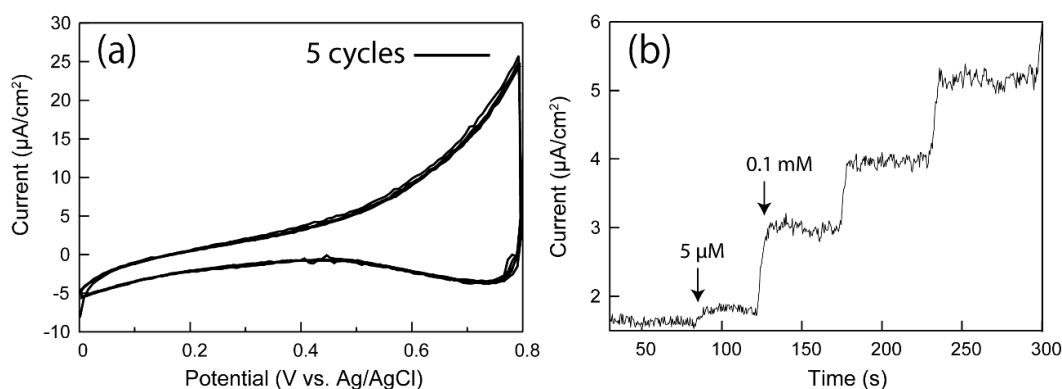


**Figure 4.4.** (a) CV sweep curves for the Cu/Cu<sub>2</sub>O/CuO/GOx electrode with five cycles in PBS at the scan rate of 100 mV/s. (b) Chronoamperometric response of the electrode for the detection of low concentration of glucose at 0.65 V vs. Ag/AgCl.

4.4b). The corresponding calibration curve of the chronoamperometric curve (0.65 V) is shown in the inset of figure 4.3c. The response current first increases rapidly with the addition of glucose solution at relatively low concentration and then reaches a plateau at a high concentration. The saturated current can be attributed to the full occupation of the active sites by reactants on the electrode surface. The electrode presents a linear range from 0.1 to 2 mM and a sensitivity of 8.8  $\mu\text{A}/\text{mM}/\text{cm}^2$ . From the CV curve (Figure 4.3b), it can be seen that the oxidation current of glucose increased with the addition of glucose solution in the whole range of 0.45 and 0.8 V and the sensitivity increases with increasing the potential. Thus a chronoamperometry at higher potential (0.8 V) is held and a higher sensitivity of 20.7  $\mu\text{A}/\text{mM}/\text{cm}^2$  is observed (Figure 4.3d). The calibration curve in the inset of Figure 4.3d shows a linear range from 0.1 to 1 mM. This Cu/Cu<sub>2</sub>O/CuO thick oxide film based electrode grown directly on Cu foils provide a low cost, facile synthesis process and relatively high sensitivity compared to other metal-oxide based enzymatic glucose sensors, as summarized in Table 4.1.

**Table 4.1.** Comparison between the performance characteristics of different enzymatic glucose sensors based on metal-oxide semiconductor.

Metal-oxide Semiconductor electrode	Fabrication Method	Sensitivity ( $\mu\text{A}/\text{cm}^2/\text{mM}$ )	Linear range (up to, mM)	LOD ( $\mu\text{M}$ )	Response time (s)	Ref.
Cu/Cu <sub>2</sub> O/CuO porous film	Grown directly from Cu foils	8.78 at 0.65 V 20.7 at 0.8 V	2 at 0.65 V 1 at 0.8 V	5	~8	This work
Flower-shape CuO nanostructures	Powder pasted onto Au film	47.19 at 0.58 V	~0.7	1.37	~5	[22]
ZnO nanorods	Grown on Si substrate	23.43 at 0.8 V	5.9	10	~7	[23]
ZnO nanorods	Powder pasted onto Au film	15.46 at 0.8 V	5.45	50	~10	[23]
ZnO nanocomb	Powder pasted onto Au film	15.33 at 0.8 V	4.5	20	~10	[24]
TiO <sub>2</sub> nanofibers	Electrospinning deposition on Pt film	9.25 at 0.6 V	4.7	10	~10	[25]
TiO <sub>2</sub> sol-gel Membrane	Grown on glassy carbon substrate	7.2 at 0.3 V	Na	70	~6	[50]

**Table 4.2.** Comparison between the performance characteristics of non-enzymatic CuO glucose sensors with different nanostructures.

Metal-oxide Semiconductor electrode	Fabrication Method	Sensitivity ( $\mu\text{A}/\text{cm}^2/\text{mM}$ )	Linear range (up to, mM)	LOD ( $\mu\text{M}$ )	Response time (s)	Ref.
Cu/Cu <sub>2</sub> O/CuO porous film	Grown directly from Cu foils	1066 at 0.6 V	2.04	2	~2	This work
CuO/TiO <sub>2</sub> nanotube arrays	Grown on Ti foils	79.79 at 0.5 V	2	1	<4	[51]
CuO nanoparticles/graphene oxide	Powder pasted onto glassy carbon substrate	262.52 at 0.7 V	2.03	0.69	Na	[29]
CuO nanorods	Powder pasted onto graphite substrate	371.43 at 0.6 V	8	4	~10	[30]
CuO flowers	Powder pasted onto graphite substrate	709.52 at 0.6 V	~2	4	~15	[8]
CuO nanoleaves	Powder pasted onto glassy carbon substrate	26.6 at 0.7 V	7.3	5	Na	[35]
CuO nanospheres	Powder pasted onto glassy carbon substrate	404.53 at 0.6 V	2.55	1	Na	[32]

#### 4.3.3. Non-enzymatic glucose sensing

The performance of non-enzymatic glucose sensing is also conducted in 0.1 M NaOH (pH 13) solution with the Cu/Cu<sub>2</sub>O/CuO electrode in the potential range of 0.0 to 1 V vs. Ag/AgCl. Figure 4.5a shows the CVs of the electrode in alkaline solution in the absence of glucose and in presence of 0.01, 0.1, 1, 5, and 10 mM glucose. It is found that there is a reduction peak at 0.62 V in the absence of glucose, which can be attributed to the reduction potential of dimeric Cu(III).<sup>19</sup> Furthermore, a broad oxidation peak appears at about 0.55 V with the addition of glucose at low concentration (inset of Figure 4.5a). Both, the oxidation and reduction peaks shift toward higher potential region with the increase in the glucose amount. A similar shift has been reported by Beden *et al.*<sup>19</sup> and may be attributed to the adsorption of glucose onto the electrode during the experiment. In the range of 0.3-0.65 V, the oxidation current of glucose increases with increasing glucose and the potential of 0.6 V is chosen for further chronoamperometric testing. Figure 4.5b shows a typical amperometric curve of the Cu/Cu<sub>2</sub>O/CuO electrode under the condition of successive addition of glucose with different concentrations. The oxidation current increased to a stable value rapidly with each drop of glucose and a saturation current is obtained for concentration larger than 10 mM. The current responses of the electrode at low concentrations of glucose is presented in figure 4.5c. The sensitivity of 1066  $\mu\text{A}/\text{mM}/\text{cm}^2$ , response time of about 2 s and detection limit of about 2  $\mu\text{M}$  can be obtained from Figure 4.5b-c. Figure 4.5d shows the calibration curve of the amperometric response and a linear detection range of 0.1 to 2.04 mM is observed. The sensitivity of the studied electrode is found to be higher than those of CuO powder (flowers and nanospheres) modified glassy carbon or graphite electrodes, as shown in Table 4.2.

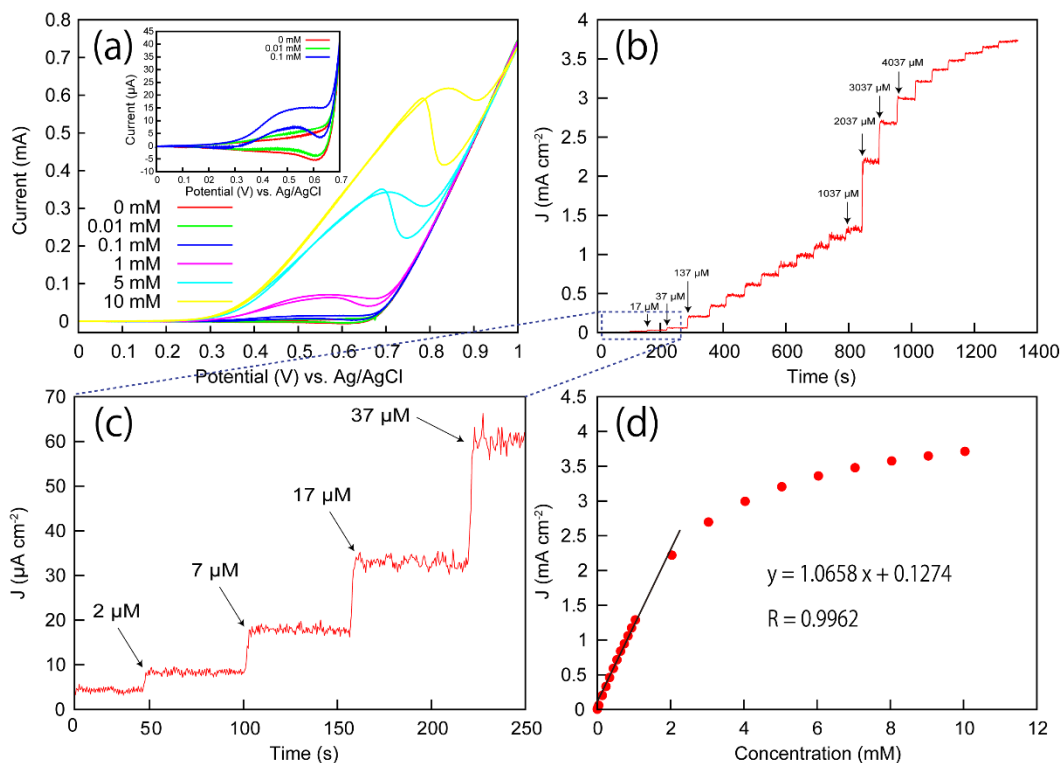


**Figure 4.5.** (a) Voltammetric response of the Cu/Cu<sub>2</sub>O/CuO electrode to the addition of 0.0, 0.01, 0.1, 1, 5, and 10 mM glucose in 0.1 M NaOH solution (pH 13) at the scan rate of 100 mV/s. The inset in part (a) shows the magnified view of the voltammetric response with 0.0, 0.01, and 0.1 mM glucose in the potential range of 0.0 to 0.7 V vs. Ag/AgCl. (b) Chronoamperometric response of the Cu/Cu<sub>2</sub>O/CuO electrode with successive additions of glucose to 0.1 M NaOH at 0.6 V vs. Ag/AgCl. The detection of low concentration glucose is presented in part (c). (d) Calibration curve of the chronoamperometric response.

#### 4.3.4. Selectivity

The selectivity of the Cu/Cu<sub>2</sub>O/CuO electrode is also studied against ascorbic acid (AA) and uric acid (UA), as interference species found with glucose in human blood serum. It was reported that the concentration of about 0.1 mM AA and UA can exist under

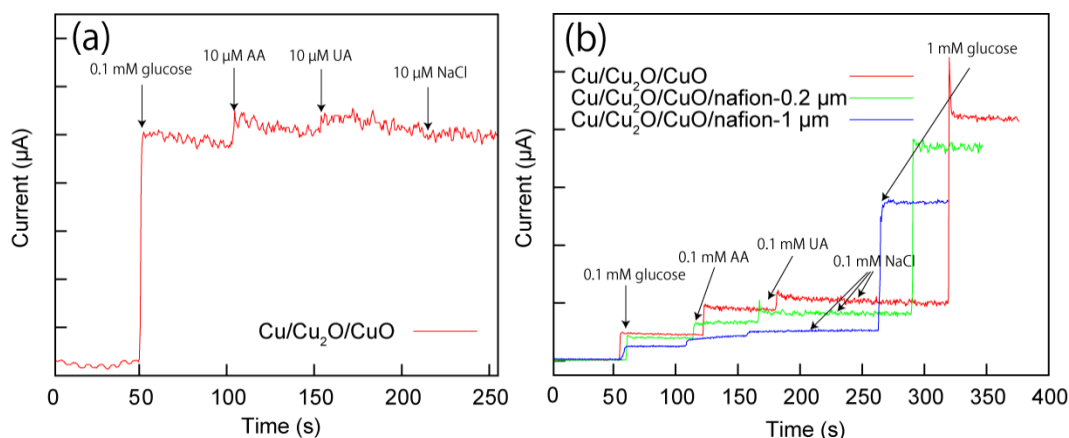


**Figure 4.6.** (a) Response (current-time) curve of the Cu/Cu<sub>2</sub>O/CuO electrode to the addition of 0.1 mM glucose, 10 μM AA, 10 μM UA, and 10 μM NaCl in 0.1 M NaOH (pH 13). (b) Responses (current-time) profiles of the Cu/Cu<sub>2</sub>O/CuO, Cu/Cu<sub>2</sub>O/CuO/Nafion (0.2 μm), and Cu/Cu<sub>2</sub>O/CuO/Nafion (1 μm) electrodes to the addition of 0.1 mM glucose, 0.1 mM AA, 0.1 mM UA, 0.1 mM NaCl, and 1 mM glucose in 0.1 M NaOH.

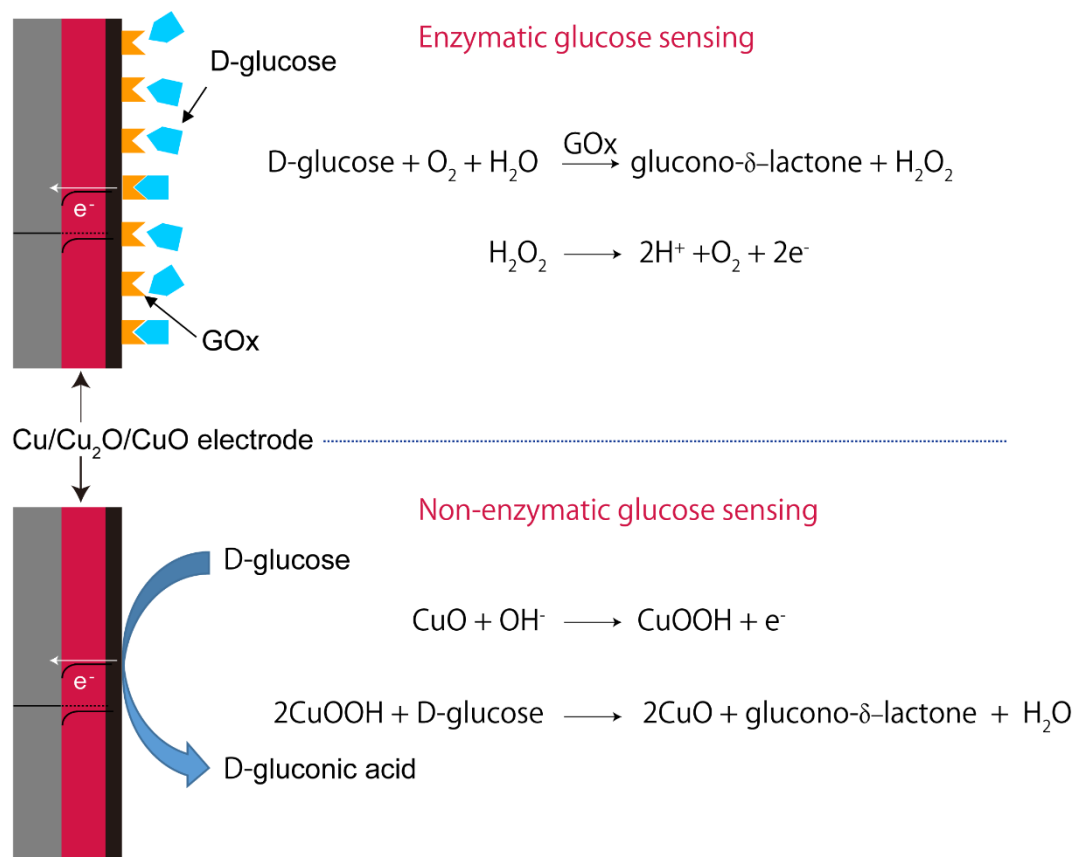
normal physiological level of glucose (3-8 mM).<sup>33</sup> The selectivity test first examined the effect of the addition of 0.1 mM glucose, 10 μM AA, and 10 μM UA in 0.1 M NaOH at 0.6 V, as shown in Figure 4.6a. A large current response to glucose and slight responses to the interference species were observed, indicating that the Cu/Cu<sub>2</sub>O/CuO electrode can be used for glucose sensing under low concentrations of AA and UA. However, when the concentration of interferences increased to 0.1 mM, a large response from the interference species was obtained. By normalizing the current density of the electrode to 100% for the 1 mM glucose, it is found that the response to the addition of 0.1 mM AA and UA is 8.8% and 5%, respectively. This may be due to the high electron transfer rate for the interference species. Nafion, a polymer with ionic properties that is extensively used to fix the electrocatalysts on the electrode, can also be used to reduce the effects of the



interference species AA and UA.<sup>43-44</sup> Thus, the Cu/Cu<sub>2</sub>O/CuO electrode modified by Nafion with different thicknesses is also investigated and the results presented in Figure 4.6b. After coating a Nafion film of  $\sim 0.2\ \mu\text{m}$  on the electrode, it is found that the response to the addition of 0.1 mM AA and UA decreased to 5.7% and 3.8 %, respectively. When the thickness of Nafion increased to about  $1\ \mu\text{m}$ , the response of AA and UA further decreased to 4.5% and 2.9%, respectively. But a significant decrease in the glucose oxidation current is also observed. So the thickness of the Nafion should be chosen carefully to maintain the glucose oxidation current and improve selectivity. The mechanism may be attributed to the negative charges of sulfonic groups of Nafion. On the negatively-charged Nafion interface, the AA and UA anions were repelled and thus the signals from interferences decreased.<sup>45-46</sup> The presence of chloride ions may also affect the glucose oxidation.<sup>32</sup> In this experiment, no response can be observed to the addition of 0.01 mM and 0.1 mM NaCl for all the electrodes, showing a good anti-interference to chloride ions.

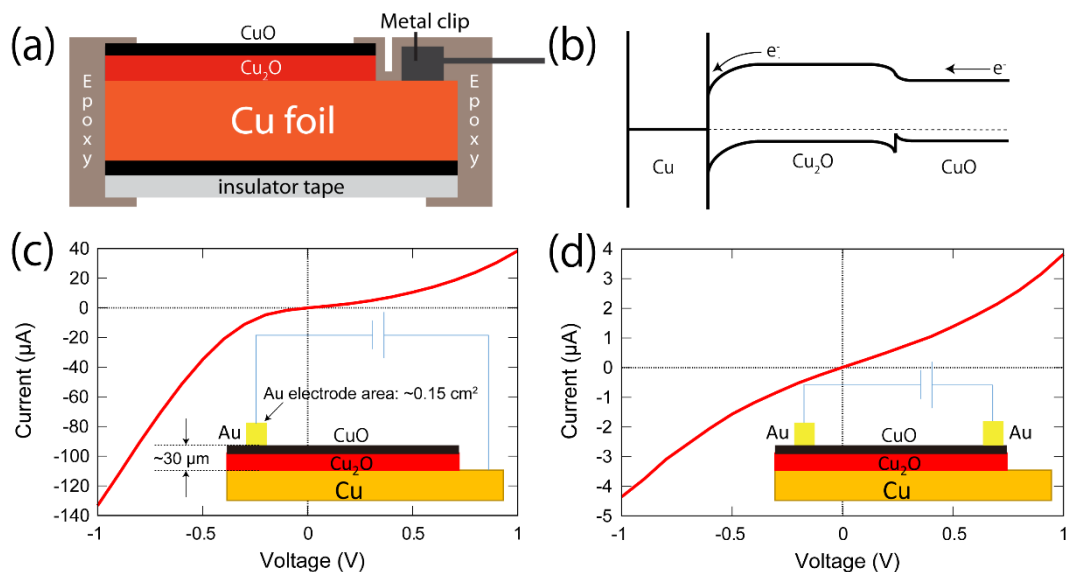
#### 4.3.5. Analysis

Figure 4.7 depicts the possible mechanism of the enzymatic and non-enzymatic glucose sensing. For the enzymatic glucose sensing, the enzyme catalyzes the oxidation of glucose to produce glucono- $\delta$ -lactone and the generated electrons transfer from the enzyme to the electrode so as to generate an amperometric signal.<sup>1, 3</sup> The signal from interference species such as AA and UA can be avoided because of the selective catalysis of glucose by GOx. For the non-enzymatic sensing, the Cu(II) and Cu(III) redox have been considered to be the essential factors in the oxidation of the glucose at the electrode surface,<sup>19, 28-29</sup> as illustrated in Figure 4.7. The CuO layer on the electrode surface is oxidized to a catalytically active Cu(III) radical. The glucose absorbs onto the electrode



**Figure 4.7.** Schematic of the possible mechanisms of the enzymatic glucose sensing on the Cu/Cu<sub>2</sub>O/CuO/GOx electrode in 0.01 M PBS (pH 7.4) and the non-enzymatic glucose sensing on the surface of the Cu/Cu<sub>2</sub>O/CuO electrode in 0.1 M NaOH (pH 13) , and the energy band diagram and charge transfer for Cu/Cu<sub>2</sub>O/CuO.

surface and oxidized to glucono- $\delta$ -lactone by the Cu(III) radical species. The enhanced performance of the Cu/Cu<sub>2</sub>O/CuO electrode compared to other powder based glucose sensors<sup>29-32</sup> and nanowires on a film glucose sensors<sup>33</sup> can be attributed to two factors. On the one hand, the high crystal quality (as evidenced by the Raman data) and large surface area of the CuO nanoporous layer obtained at high temperature (500 °C) benefits to electrocatalytic reaction on the surface. On the other hand, the existence of Cu<sub>2</sub>O beneath the CuO may also improve the current flow. Figure 4.8c-d show the I-V characteristics of the electrode in the contact configuration of Cu-CuO and CuO-CuO,



**Figure 4.8.** (a) Schematic configuration of the Cu/Cu<sub>2</sub>O/CuO electrode. (b) The possible charge transfer mechanism at the Cu/Cu<sub>2</sub>O/CuO contacts. (c)-(d) I-V characteristics of the contacts between Cu-CuO and CuO-CuO, respectively.

from which the CuO-CuO contact exhibits an Ohmic characteristic, whereas the Cu-CuO contact presents a weak rectifying effect, likely originating in the Cu/Cu<sub>2</sub>O/CuO heterojunction. A possible charge transfer mechanism in the Cu/Cu<sub>2</sub>O/CuO contacts is presented in figure 4.8b. The Schottky barrier between the Cu<sub>2</sub>O and Cu can generate a photovoltaic effect that has been used for the solar cells.<sup>47-49</sup> In this experiment, the electrons generated by the electrochemical process can be transferred from the oxide to the Cu electrode more efficiently due to the large driving force provided by the Schottky barrier at the Cu/Cu<sub>2</sub>O interface, thus the Cu<sub>2</sub>O could serve as an appropriate intermediate layer for the CuO reaction layer.

#### 4.4. Conclusions

We reported a low-cost and facile fabrication technique for preparing high crystal quality porous copper oxide thick layer on Cu foil. The fabrication method consists of the

pre-synthesis of  $\text{Cu}(\text{OH})_2$  nanowires on copper by a solution process and subsequent transformation into  $\text{Cu}_2\text{O}/\text{CuO}$  double layer via annealing under an oxygen flow. The  $\text{Cu}/\text{Cu}_2\text{O}/\text{CuO}$  structure exhibits promising performance for not only enzyme-based glucose sensing, but also non-enzymatic glucose detection. The fabricated sensor showed high sensitivity, low detection limit, and fast response in non-enzymatic sensing of glucose due to the favorable electrocatalytic reaction on crystalline  $\text{CuO}$  porous surface and improved electron transfer ability assisted by a Schottky junction between  $\text{Cu}$  and  $\text{Cu}_2\text{O}$ , thus offering a novel structure for applications in glucose sensing devices.

## References

- [1] Park S, Boo H and Chung T D 2006 *Anal. Chim. Acta.* 556 46-57
- [2] Wang J 2008 Electrochemical glucose biosensors *Chem. Rev.* 108 814-825
- [3] Rahman M M, Ahammad A J, Jin J H, Ahn S J and Lee J J 2010 *sensors* 10 4855-4886
- [4] Chen C, Xie Q J, Yang D W, Xiao H L, Fu Y C, Tan Y M and Yao S Z 2013 *RSC Adv.* 3 4473-4491
- [5] Wilson R and Turner A P F 1992 *Biosens. Bioelectron.* 7 165-185
- [6] Schügerl K, Hitzmann B, Jurgens H, Kullick T, Ulber R and Weigal B 1996 *Trends Biotechnol.* 14 21-31
- [7] Kimmel D W, LeBlanc G, Meschivitz M E and Clifffel D E 2012 *Anal. Chem.* 84 685–707
- [8] Toghill K E and Compton R G 2010 *Int. J. Electrochem. Sci.*, 5 1246-1301
- [9] Qiu H J and Huang X R 2010 *J. Electroanal. Chem.* 643 39–45
- [10] Lang X Y, Fu H Y, Hou C, Han G F, Yang P, Liu Y B and Jiang Q 2013 *Nat. Commun.* 4 2169
- [11] Vassilyev Y B, Khazova O A and Nikolaeva N N 1985 *J. Electroanal. Chem.* 196 105-125
- [12] Yuan J H, Wang K and Xia X H 2005 *Adv. Funct. Mater.* 15 803-809
- [13] Boo H, Park S, Ku B, Kim Y, Park J H, Kim H C and Chung T D 2004 *J. Am. Chem. Soc.* 126 4524-4525
- [14] Luo P F, Zhang F Z and Baldwin R P 1991 *Anal. Chim. Acta* 244 169-178
- [15] You T Y, Niwa O, Chen Z L, Hayashi K, Tomita M and Hirono S 2003 *Anal. Chem.* 75 5191-5196

- [16] Prabhu S V and Baldwin R P 1989 *Anal. Chem.* 61 852-856
- [17] Prabhu S V and Baldwin R P 1989 *Anal. Chem.* 61 2258-2263
- [18] Luo P F, Prabhu S V and Baldwin R P 1990 *Anal. Chem.* 62 752-755
- [19] Marioli J M and Kuwana T 1992 *Electrochim. Acta* 37 1187-1197
- [20] Sun Y P, Buck H and Mallouk T E 2001 *Anal. Chem.* 73 1599-1604
- [21] Wang J P, Thomas D F and Chen A C 2008 *Anal. Chem.* 80 997-1004
- [22] Umar A, Rahman M M, Al-Hajry A and Hahn Y B 2009 *Electrochem. Commun.* 11 278–281
- [23] Lei Y, Yan X Q, Zhao J, Liu X, Song Y, Luo N, Zhang Y 2011 *Colloids Surf. B* 82 168–172
- [24] Wang J X, Sun X W, Wei A, Lei Y, Cai X P, Li C M and Dong Z L 2006 *Appl. Phys. Lett.* 88 233106(1-3)
- [25] Tang H, Yan F, Tai Q D and Chan H L W *Biosens. Bioelectron.* 25, 1646–1651
- [26] Turkusic E, Kalcher K, Schachl K, Komersova A, Bartos M, Moderegger H, Svancara I and Vytras K 2001 *Anal. Lett.* 34 2633–2647
- [27] Ansari A A, Solanki P R and Malhotra B D 2008 *Appl. Phys. Lett.* 92 263901(1–3)
- [28] Sun S D, Zhang X Z, Sun Y X, Yang S C, Song X P and Yang Z M 2013 *ACS Appl. Mater. Interfaces* 5 4429–4437
- [29] Song J, Xu L, Zhou C Y, Xing R Q, Dai Q L, Liu D L and Song H W 2013 *ACS Appl. Mater. Interfaces* 5 12928–12934
- [30] Wang X, Hu C G, Liu H, Du G J, He X S and Xi Y 2010 *Sens. Actuators, B* 144 220–225

- [31] Batchelor-McAuley C, Du Y, Wildgoose G G and Compton R G 2008 *Sens. Actuators, B* 135 230–235
- [32] Reitz E, Jia W Z, Gentile M, Wang Y and Lei Y 2008 *Electroanalysis* 20 2482–2486
- [33] Zhuang Z J, Su X D, Yuan H Y, Sun Q, Xiao D and Choi M M F 2008 *Analyst* 133 126-132
- [34] Cherevko S and Chung C H 2010 The porous CuO *Talanta* 80 1371–1377
- [35] Zhao Y, Zhao J H, Li Y L, Ma D C, Hou S N, Li L Z, Hao X L and Wang Z C 2011 *Nanotechnology* 22 115604
- [36] Zhang W, Wen X, Yang S, Berta Y and Wang Z L 2003 *Adv. Mater.* 15 822–825
- [37] Li C L, Li Y B and Delaunay J J 2014 *ACS Appl. Mater. Interfaces* 6 480–486
- [38] Xu J F, Ji W, Shen Z X, Li W S, Tang S H, Ye X R, Jia D Z and Xin X Q 1999 *J. Raman Spectrosc.* 30 413–415
- [39] Reydellet J, Balkanski M and Trivich D 1972 *Phys. Status Solidi B* 52 175–185
- [40] Lu C H, Qi L M, Yang J H, Zhang D Y, Wu N Z and Ma J M 2004 *J. Phys. Chem. B* 108 17825–17831
- [41] Mrowec S and Stokłosa A 1971 *Oxid. Met.* 3 291-311
- [42] Lewis J A 2000 *J. Am. Ceram. Soc.* 83 2341–2359
- [43] Hrapovic S, Liu Y, Male K B and Luong J H T 2004 *Anal. Chem.* 76 1083–1088
- [44] Kang X H, Mai Z B, Zou X Y, Cai P X and Mo J Y 2007 *Anal. Biochem.* 363 143–150
- [45] Wang G F, Wei Y, Zhang W, Zhang X J, Fang B and Wang L 2009 *Microchim. Acta* 168 87-92
- [46] Zhao H, Zhang Y Z and Yuan Z B 2001 *Anal. Chim. Acta* 441 117-122

- [47] Assimios J A and Trivich D 1973 Photovoltaic properties and barrier heights of single-crystal and polycrystalline  $\text{Cu}_2\text{O}$ -Cu contacts *J. Appl. Phys.* 44 1687-1693
- [48] Shao F, Sun J, Gao L, Luo J Q, Liu Y Q and Yang S W 2012 *Adv. Funct. Mater.* 22 3907–3913
- [49] Yue Y M, Chen M J, Ju Y and Zhang L 2012 *Scripta Mater.* 66 81–84
- [50] Yu J H, Liu S Q and Ju H X 2003 *Biosens. Bioelectron.* 19 401–409
- [51] Luo S L, Su F, Liu C B, Li J X, Liu R H, Xiao Y, Li Y, Liu X N, Cai Q Y 2011 *Talanta* 86 157-163



## **5. Fabrication of CuO nanostructures on Cu electrode for high performance glucose sensing**

CuO nanowire/microflower structure on Cu foil is synthesized by annealing a Cu(OH)<sub>2</sub> nanowire/CuO microflower structure at 250°C in air. The nanowire/microflower structure with its large surface area leads to an efficient catalysis and charge transfer in glucose detection, achieving a high sensitivity of 1943  $\mu\text{A}/\text{mM}/\text{cm}^2$ , a wide linear range up to 4 mM and a low detection limit of 4  $\mu\text{M}$  for amperometric glucose sensing in alkaline solution. With a second consecutive growth of CuO nanowires on the microflowers, the sensitivity of the obtained CuO nanowire/microflower/nanowire structure further increase to 2424  $\mu\text{A}/\text{mM}/\text{cm}^2$ , benefiting from the increased electrochemically active sites. The enhanced electrocatalytic performance of the CuO nanowire/microflower/nanowire electrode compared to the CuO nanowire/microflower, CuO nanowire and Cu<sub>x</sub>O film electrodes provides evidence for the significant role of available surface area for electrocatalysis. The rational combination of CuO nanowire and microflower makes it a promising composite nanostructure for use in CuO based electrochemical sensors with excellent analytical properties.

## 5.1. Introduction

The development of high performance glucose sensors has attracted particular attention because of increasing needs in analysis tools for medical diagnostics and food processing over the past decade. The glucose oxidase (GOx) –based enzymatic glucose sensors have been widely studied and employed due to their good sensitivity and excellent selectivity.<sup>1-7</sup> However, the complicated and multi-step immobilization procedure of the enzymes results in a general problem of poor reproducibility, thermal instability and high cost.<sup>8-10</sup> Hence, research on non-enzymatic glucose sensors has become an active research area to further improve long term stability of the glucose sensors. Metals such as Au,<sup>11</sup> Pt,<sup>12-13</sup> Ni,<sup>14-15</sup> Cu,<sup>16</sup> and alloys<sup>17-18</sup> have been extensively studied for non-enzymatic glucose detection, but most of the materials are costly and exhibit inadequate sensitivity and selectivity. To solve these problems, CuO nanostructures, such as nanowires,<sup>19</sup> microflowers,<sup>20</sup> nanorods,<sup>21</sup> nanospheres,<sup>22</sup> and porous films<sup>23</sup> have been introduced to both increase the sensitivity to glucose and decrease the effect of interference species such as ascorbic acid and uric acid. Nonetheless, narrow linear ranges and complex fabrication methods limit the wide spread use of the CuO nanostructure based biosensors. In an attempt to obtain a non-enzymatic glucose sensor with a high sensitivity, a long-term stability and a wide linear range, we attempt to combine microscale and nanoscale CuO structures in order to enhance the electrocatalytic performance towards glucose sensing and achieve a trade-off between sensitivity and linear range.

In this report, CuO nanowires and microflowers are synthesized simultaneously on a Cu foil to realize an electrochemical glucose sensor with high surface area at a low cost. The microflowers decorated nanowires provide a large electrochemically active surface area for efficient catalysis of glucose. Furthermore, the porous structure between

nanowires and interspace among microflowers ensure efficient transport of electroactive species for sensing. A simple and low-cost solution method is used to synthesize the  $\text{Cu}(\text{OH})_2$  nanowire/ $\text{CuO}$  microflower structure, and then a dehydration process under mild annealing leads to the formation of the  $\text{CuO}$  nanowire/microflower composite structure. The fabricated electrode exhibits an improved sensitivity, a wider linear range and a good selectivity. Furthermore, a second growth of  $\text{Cu}(\text{OH})_2$  nanowires on the microflower is achieved by sputtering a Cu layer on  $\text{CuO}$  nanowire/microflower structure and transforming the Cu layer into  $\text{Cu}(\text{OH})_2$  nanowires via the same solution method. A subsequent annealing is used to convert the  $\text{Cu}(\text{OH})_2$  nanowires into  $\text{CuO}$  nanowires, so that a  $\text{CuO}$  nanowire/microflower/nanowire structure is formed. The  $\text{CuO}$  nanowire/microflower/nanowire structure used as an electrode exhibits an enhanced sensitivity for glucose compared to the  $\text{CuO}$  nanowire/microflower electrode. A comparison between electrodes having different morphologies including  $\text{CuO}$  nanowires and  $\text{Cu}_x\text{O}$  film is conducted to clarify the role of the surface area on the electrochemical activity as well as the linear range. The reported electrode consisting of a  $\text{CuO}$  nanowire and microflower composite structure on a Cu foil shows excellent performance, while having low material cost and scalable fabrication process, so the reported electrode offers great potential in electrochemical applications.

## **5.2. Experimental section**

### **5.2.1. Fabrication of the $\text{Cu}_x\text{O}$ film, the $\text{CuO}$ nanowire and the $\text{CuO}$ nanowire/microflower structure**

The  $\text{Cu}_x\text{O}$  film was obtained by annealing a Cu foil (99.96% purity and thickness of 0.2 mm, Nilaco) in a muffle furnace at 250°C for 6 h. The Cu foils were cleaned

consecutively in ultrasonic baths of acetone, ethanol and distilled water before use. In order to prepare the  $\text{Cu}(\text{OH})_2$  nanowire/ $\text{CuO}$  microflower structure, Cu foil with a size of  $10 \times 10 \text{ cm}^2$  was immersed into a solution containing 2.67 M NaOH (min. 97.0%, Wako) and  $(\text{NH}_4)_2\text{S}_2\text{O}_8$  (min. 98.0%, Wako) for 10 min at room temperature.<sup>24</sup> After the chemical reaction, the copper foil with a dark blue color was taken out from the solution, cleaned with deionized water and dried in air.  $\text{Cu}(\text{OH})_2$  nanowire structure was fabricated by the same procedure as mentioned above, the only difference being a gentle stirring of the solution and a low temperature reaction of  $5^\circ\text{C}$  maintained to avoid the formation of  $\text{CuO}$  flowers on the top of  $\text{Cu}(\text{OH})_2$ .<sup>25</sup> After reaction, a uniform  $\text{Cu}(\text{OH})_2$  nanowire layer was formed on the Cu foil with a light blue color. Both the  $\text{Cu}(\text{OH})_2$  nanowire and  $\text{Cu}(\text{OH})_2$  nanowire/ $\text{CuO}$  microflower samples were annealed in the muffle furnace at  $250^\circ\text{C}$  for 6 h to form the  $\text{CuO}$  nanowires and the  $\text{CuO}$  nanowire/ $\text{CuO}$  microflower structure on a Cu foil. To prepare the  $\text{CuO}$  nanowire/microflower/nanowire structure, a 300 nm-thick Cu layer was coated on the as-prepared  $\text{CuO}$  nanowire/microflower structure (annealed at  $250^\circ\text{C}$  for 4 h) by ion beam sputtering. Then the Cu layer coated  $\text{CuO}$  nanowire/microstructure sample was immersed into the same solution mentioned before for 10 min to convert the Cu layer into  $\text{Cu}(\text{OH})_2$  nanowire. After a 2 h annealing at  $250^\circ\text{C}$ ,  $\text{CuO}$  nanowire/microflower/nanowire with high surface area was obtained.

### 5.2.2. Electrochemical measurements

Field-emission scanning electron microscope (JEOL JSM 7600FA) was used to examine the morphologies of the  $\text{Cu}(\text{OH})_2$  and  $\text{CuO}$  nano/microstructures. The crystalline phase of the structures was identified by X-ray diffractometry (Miniflex II-MW, Rigaku Co. Ltd., Japan) with the  $\text{Cu K}\alpha$  radiation. The Raman spectra of the samples were

measured with a Renishaw inVia Raman Microscope system using a 488 nm excitation line directed through a  $\times 20$  objective under a 1.2 mW illumination for the top surface analysis and a  $\times 50$  objective under a 1.15 mW for the cross-section analysis.

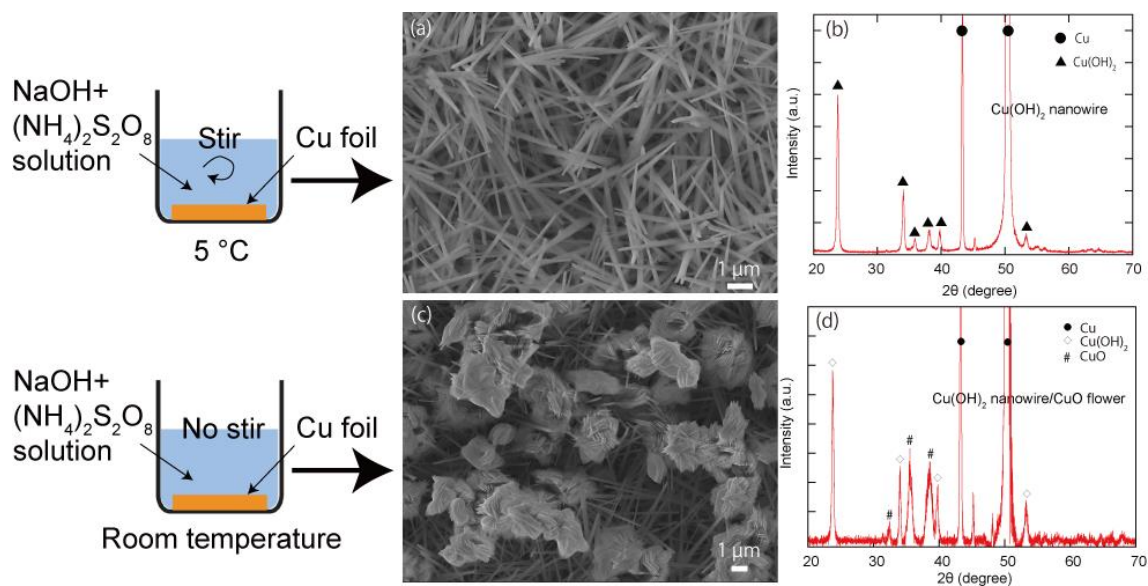
### **5.2.3. Structural characterization**

The electrochemical experiments were carried out in a standard three-electrode system using a potentiostat (VersaSTAT 4, Princeton Applied Research) at room temperature. Cyclic voltammetry (CV) measurements were performed in the potential range of 0-0.8 V vs. Ag/AgCl. The amperometric measurements were conducted by adding the desired amount of glucose consecutively at a fixed potential with the solution being stirred constantly. The electrolyte used for the non-enzymatic glucose sensing was 0.1 M NaOH solution (pH 13).

## **5.3. Results and discussion**

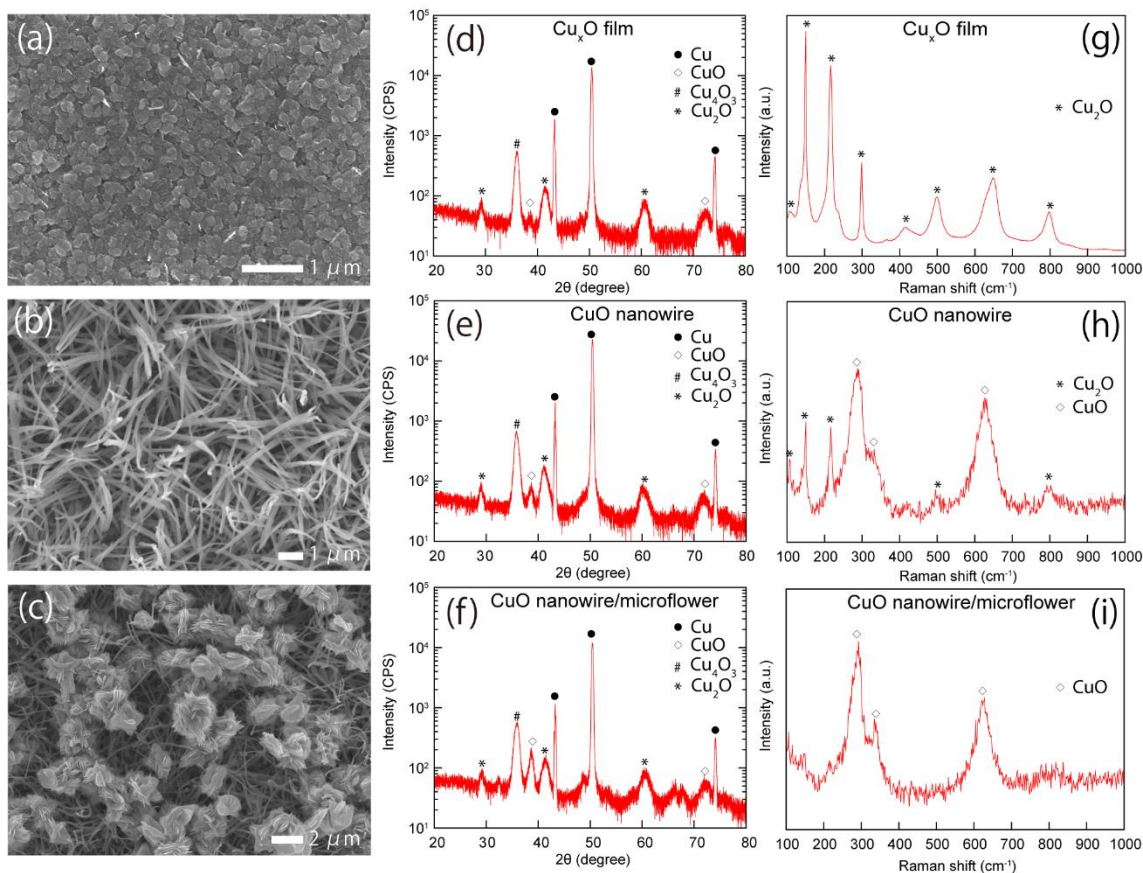
### **5.3.1. Characterization of the CuO nano/microstructures**

Figure 5.1 show the Schematic of the growth process of  $\text{Cu}(\text{OH})_2$  nanowire and  $\text{Cu}(\text{OH})_2$  nanowire/CuO microflower structure. During the fabrication of  $\text{Cu}(\text{OH})_2$  nanowire/CuO microflower structure, CuO flowers were found to grow under the conditions of inhomogeneous solution and increase in temperature near the Cu/solution interface caused by the chemical reaction. To prepare  $\text{Cu}(\text{OH})_2$  nanowire structure, gentle stirring of the solution at low temperature (5 °C) was implemented to decrease the temperature at  $\text{Cu}(\text{OH})_2$ /solution interface and prevent the formation of CuO flowers on the  $\text{Cu}(\text{OH})_2$  nanowires. The  $\text{Cu}(\text{OH})_2$  nanowires have a diameter of approximately 200 nm and a length of 5-10  $\mu\text{m}$ . The CuO microflowers covered on the surface of CuO



**Figure 5.1.** Schematic of the growth process of  $\text{Cu}(\text{OH})_2$  nanowire and  $\text{Cu}(\text{OH})_2$  nanowire/ $\text{CuO}$  microflower structure. SEM images showing the surface morphologies of the (a)  $\text{Cu}(\text{OH})_2$  nanowire and (c)  $\text{Cu}(\text{OH})_2$  nanowire/ $\text{CuO}$  microflower structure. The XRD pattern of the two structures are presented in (b) and (d).

nanowires has an average diameter of 2.5  $\mu\text{m}$ . The XRD patterns are shown in right side of Figure 5.1, it is found that only  $\text{Cu}(\text{OH})_2$  and Cu phase can be observed for the  $\text{Cu}(\text{OH})_2$  nanowire structure. For the  $\text{Cu}(\text{OH})_2$  nanowire/ $\text{CuO}$  microflower structure, CuO peaks can be found besides the  $\text{Cu}(\text{OH})_2$  signal, which can be attributed to the formation of CuO flowers on the top of  $\text{Cu}(\text{OH})_2$  nanowire structure. Figure 5.2a shows the FE-SEM image of the  $\text{Cu}_x\text{O}$  film obtained by annealing the Cu foil in the muffle furnace at 250°C for 6h. After the annealing, a nanocrystalline film composed of small grains ( $\sim 200$  nm) and decorated with sparse nanorods is obtained. The morphologies of CuO nanowires and CuO nanowire/ $\text{CuO}$  microflower structure were revealed in figure 1 (b-c). The CuO nanowires have a diameter of approximately 200 nm and a length of 5 to 10  $\mu\text{m}$ . The CuO microflowers having an average diameter of 2.5  $\mu\text{m}$  were found to cover uniformly the surface of the CuO nanowires. The microflowers consist of dense CuO nanosheets with



**Figure 5.2.** FE-SEM images showing the morphology of the  $\text{Cu}_x\text{O}$  film (a), CuO nanowires (b) and CuO nanowire/microflowers (c). (d-f) XRD patterns of the  $\text{Cu}_x\text{O}$  film, CuO nanowires and CuO nanowire/microflowers formed upon annealing. (g-i) Raman spectra of the top surface of the three structures.

thickness of about 30-50 nm. Compared to the as-prepared  $\text{Cu}(\text{OH})_2$  nanowire and  $\text{Cu}(\text{OH})_2$  nanowire/CuO microflower structure shown in Figure 5.11a-b, the CuO nanowires obtained after annealing exhibited a curved topography. This curved topography is attributed to the dehydration of  $\text{Cu}(\text{OH})_2$  into CuO during annealing, which results in stress from the phase change and consequently bending of the nanowires.

The XRD patterns of the  $\text{Cu}_x\text{O}$  film, CuO nanowires and CuO nanowire/CuO microflower structure are reported in Figure 5.2(d-f). The positions of the XRD peaks

revealed that all the three samples were composed of CuO, Cu<sub>4</sub>O<sub>3</sub> and Cu<sub>2</sub>O. For the Cu<sub>x</sub>O film sample, two weak peaks at 38.71° and 72.48° were assigned to the CuO phase (JCPDS, 00-045-0937), suggesting the formation of a thin and amorphous CuO layer on layers made of the Cu<sub>4</sub>O<sub>3</sub> (JCPDS, 01-071-6397) and Cu<sub>2</sub>O (JCPDS, 01-071-3645) phases. The CuO nanowire sample had a CuO peak at 38.71° with a stronger intensity than that of the Cu<sub>x</sub>O film, likely due to a more complete transformation of Cu(OH)<sub>2</sub> into CuO during annealing. In Figure 5.2f, the intensity of the 38.71° peak belonging to CuO further increased for the nanowire/CuO microflower structure sample, most likely due to the contribution of the CuO microflowers.

Raman spectroscopy was used to examine the surface composition of the samples due to the shorter penetration depth of this technique when compared with XRD analysis.<sup>26-</sup>  
<sup>27</sup> Figure 5.2(g-i) shows the Raman spectra taken from the top surface of the three annealed samples. For the Cu<sub>x</sub>O film sample (Figure 5.2g), all peaks can be indexed to the Cu<sub>2</sub>O vibration modes.<sup>28</sup> The CuO peaks could not be detected likely due to a too weak signal from the thin and amorphous CuO, which was hidden by strong Cu<sub>2</sub>O peaks. In Figure 5.2h, the Raman peaks of the nanowires can be indexed to CuO (293, 335 and 628 cm<sup>-1</sup>)<sup>29</sup> and Cu<sub>2</sub>O (109, 150, 496 and 795 cm<sup>-1</sup>), thus revealing that the excitation laser penetrates the porous CuO nanowire arrays and collects information from the underneath Cu<sub>2</sub>O layer. Figure 5.2i shows the Raman peaks of the CuO nanowire/microflowers structure for which only CuO (293, 335 and 628 cm<sup>-1</sup>) peaks can be detected owing to the microflower top layer. In order to clarify the crystalline phases of the sample, a cross-section analysis of the sample was performed using Raman spectroscopy (Figure 5.3). The measurement was conducted by taking Raman spectra at the spots indicated in Figure 5.3a so as to obtain information on the cross-section of the



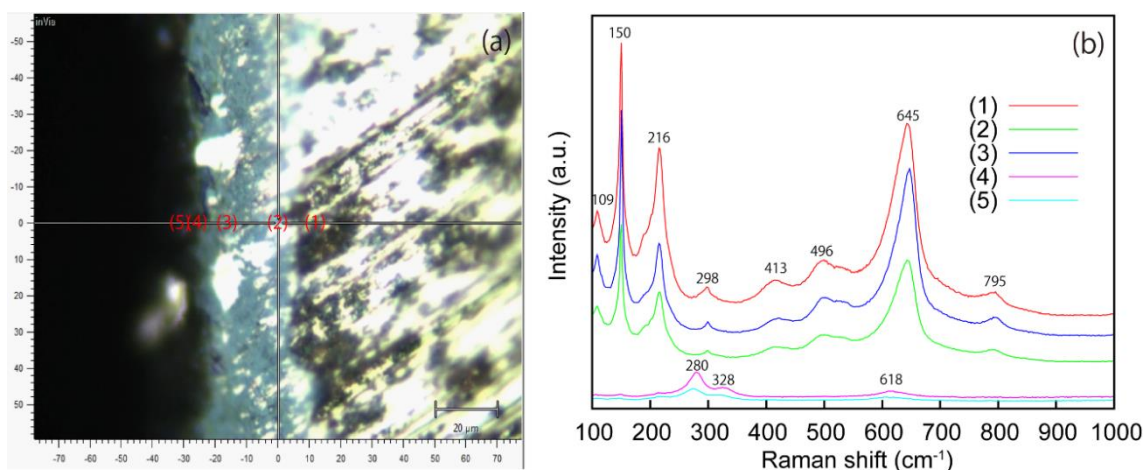


**Figure 5.3.** (a) Optical microscope image of the cross-section of CuO nanostructure/microflower structure prepared at 250 °C for 6 h. The different positions along the central axis line of the cross-section is marked by symbol (1), (2), (3), (4) and (5), respectively. The Raman spectra taken at these positions are presented in (b).

fabricated sample. For spots 1, 2 and spot 3, the observed peaks at 109, 150, 216, 298, 413, 496, 645 and 795  $\text{cm}^{-1}$  can be ascribed to  $\text{Cu}_2\text{O}$ .<sup>28</sup> Spot 4 and 5 on the region of nanowires and microflowers exhibited the same Raman peaks and all peaks can be indexed to  $\text{CuO}$ .<sup>29</sup> The result shows that  $\text{CuO}$  phase is present near the surface of the sample, whereas the region underneath the top layer is made of  $\text{Cu}_2\text{O}$ . Combining the results of the XRD and Raman analyses, we concluded that the  $\text{CuO}$  nanostructures (nanowires and microflowers) were formed on the sample porous top layer and were grown on a thick layer made of a composite layer of  $\text{Cu}_4\text{O}_3$  and  $\text{Cu}_2\text{O}$ .

### 5.3.2. Non-enzymatic glucose sensing performance of $\text{Cu}_x\text{O}$ film, $\text{CuO}$ nanowire and $\text{CuO}$ nanowire/microflower electrodes

The electrocatalytic performance of the  $\text{CuO}$  nanowire/microflower electrode towards the oxidation of glucose was examined by cyclic voltammetry (CV) in 0.1 M

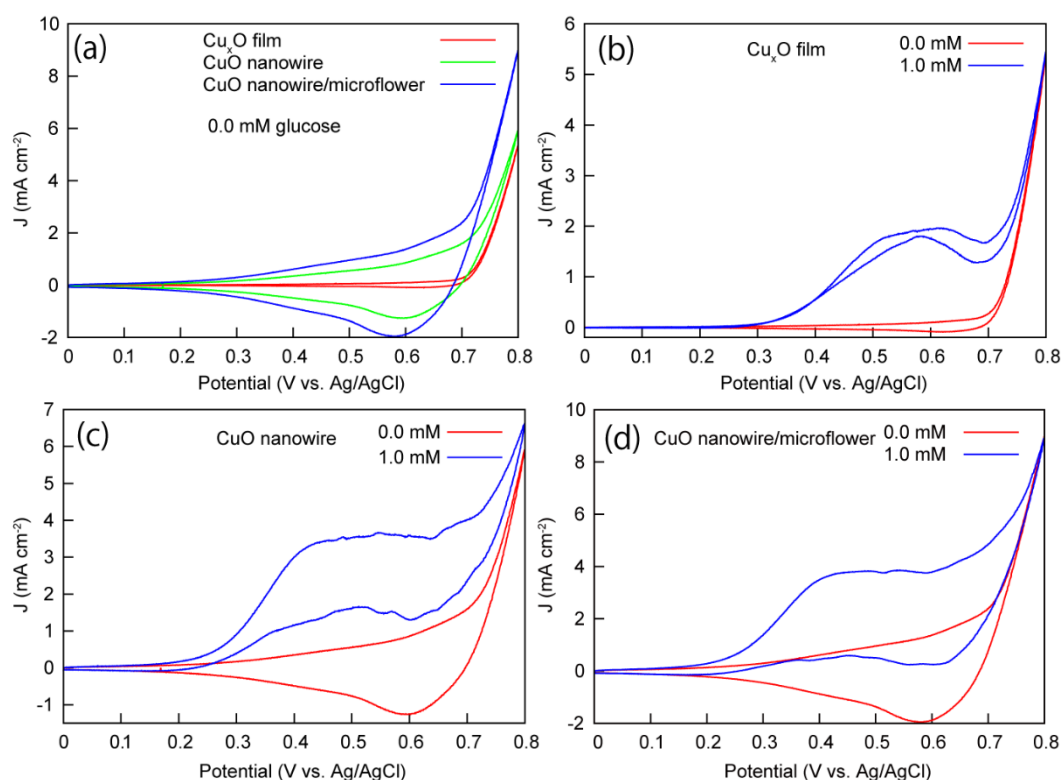


**Figure 5.4.** (a) CV sweep curves for the  $\text{Cu}_x\text{O}$  film electrode, CuO nanowire electrode and CuO nanowire/microflower electrode in 0.1 M NaOH. (b-d) CV of the  $\text{Cu}_x\text{O}$  film electrode, CuO nanowire electrode and CuO nanowire/microflower electrode in 0.1 M NaOH in the presence and absence of 1.0 mM glucose. Scan rate is 100 mV/s.

NaOH (pH 13) solution in the potential range of 0.0 to 0.8 V vs. Ag/AgCl. Moreover, the oxidation characteristics of glucose on  $\text{Cu}_x\text{O}$  film and CuO nanowire were also studied to characterize the effect of surface area on the sensitivity of glucose sensing. The comparison of the electrocatalytic activity between the CuO nanowire/microflower structure, the CuO nanowires and the  $\text{Cu}_x\text{O}$  film is presented in Figure 5.4. It is found that the electrodes with CuO nanostructures exhibited improved onset potential and significant increases in current density compared to the planar  $\text{Cu}_x\text{O}$  electrode. The CuO nanowire electrode shows a similar CV characteristic shape with that of the CuO nanowire/microflower electrode, except for a smaller current density at identical potential.

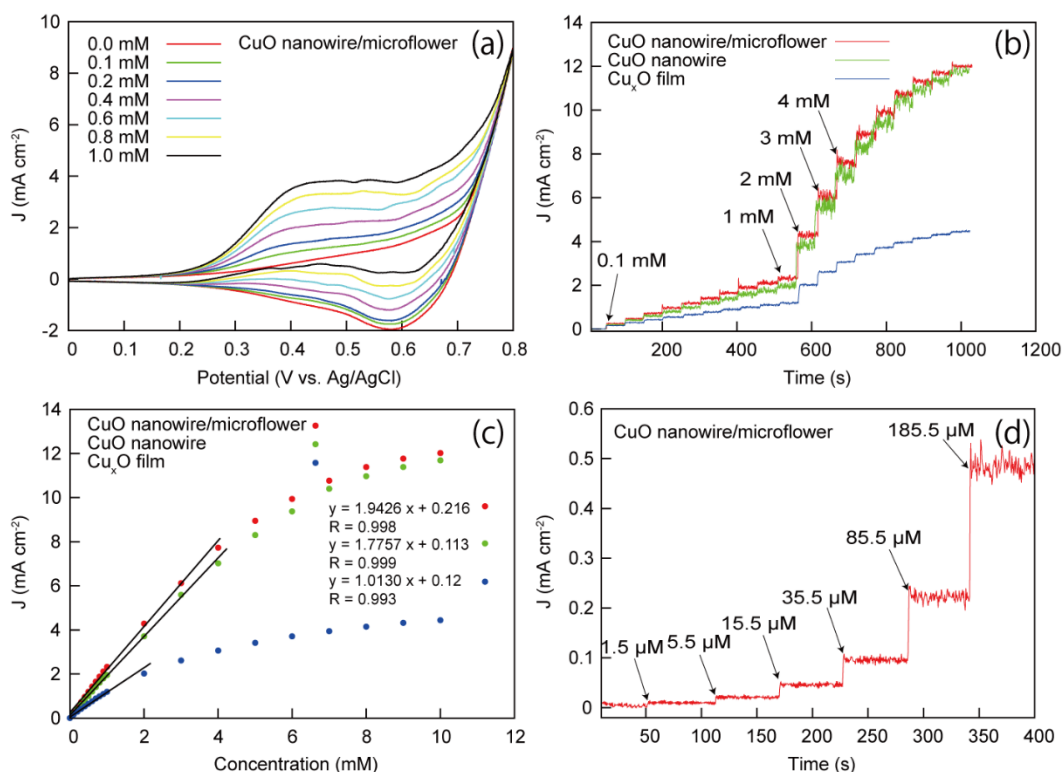


**Figure 5.5.** (a) Voltammetric response of the CuO nanowire/microflowers electrode to the addition of 0.0, 0.1, 0.2, 0.4, 0.6, 0.8 and 1.0 mM glucose in 0.1 M NaOH solution (pH 13) at the scan rate of 100 mV/s. (b) Chronoamperometric response of the Cu<sub>x</sub>O film electrode, CuO nanowire electrode and CuO nanowire/microflowers electrode with successive additions of glucose to 0.1 M NaOH at 0.5 V vs. Ag/AgCl. (c) Calibration curve of the chronoamperometric response. Response to low glucose concentrations of the CuO nanowire/microflower electrode is presented in (d).

The smaller current density is attributed to the decreased surface area of the sample. The results revealed that the nanowire/microflower structure provides a large electrochemically-active surface area, which results in a superior catalytic performance in glucose sensing. Figure 5.5a shows CV curves of the CuO nanowire/microflower electrode in alkaline solution in the absence of glucose and in the presence of 0.1, 0.2, 0.4, 0.6, 0.8, and 1.0 mM glucose. With the addition of glucose, a broad oxidation peak

from about 0.4 to 0.6 V and a reduction peak at about 0.58 V can be observed. The increased oxidation current but decreased reduction current are caused by glucose oxidation under the electrocatalysis of Cu( II ) and Cu( III ) redox.<sup>30-31</sup> The electro-oxidation current increases linearly with increasing glucose, suggesting that the measured electrode can be used in glucose sensing.

In order to obtain the sensitivity and linear detection range of the CuO nanowire/microflower electrode, chronoamperometry is conducted by successive addition of 0.1 mM and then 1 mM glucose at an interval of 50 s into a 0.1 M NaOH solution at a fixed potential of 0.5 V. The potential of 0.5 V is chosen for the chronoamperometric study because the corresponding oxidation current is high and reaches a plateau between 0.4 and 0.6 V. A typical amperometric curve of the CuO nanowire/microflower electrode is shown in Figure 5.5b, the oxidation current increased to a stable value rapidly after each drop of glucose with a response time within 2 s (the response time is defined as the time for the current to reach 95% of the steady-state value). The calibration curve of the amperometric response of this electrode is shown in Figure 5.5c from which a sensitivity of 1943  $\mu\text{A}/\text{mM}/\text{cm}^2$  is obtained with a linear range up to 4 mM. Moreover, Figure 5.5d presents the current response of the electrode at low glucose concentrations, for which a detection limit of 4  $\mu\text{M}$  was achieved ( $S/N=3$ ). For comparison purposes, the electrocatalytic performance of CuO nanowire electrode and  $\text{Cu}_x\text{O}$  film electrode toward the oxidation of glucose are reported in Figure 5.5b-c. The CuO nanowire electrode exhibited a sensitivity of 1776  $\mu\text{A}/\text{mM}/\text{cm}^2$  and a linear range up to 4.0 mM, both inferior performance when compared to the results obtained with the nanowire/microflower electrode. The  $\text{Cu}_x\text{O}$  film electrode gives a sensitivity of 1013  $\mu\text{A}/\text{mM}/\text{cm}^2$  and a linear range up to 2 mM, providing further reduced performance when

compared to the CuO electrodes with nanostructures (nanowires and nanowire/microflower). These results are evidence for a significant role of nano/micro structures in the improvement of the electrocatalytic activity in glucose sensing by providing large surface area and enhanced electron transfer ability.<sup>19-23</sup> In this report, the catalytic reaction cannot only occur on the high surface-to-volume ratio nanowires, but also react on the dense nanosheets of microflowers, leading to an efficient catalysis towards glucose oxidation. Thus, the existence of microflowers on the nanowires increases the electrochemically active surface area and thus presents an improved performance compared to the nanowire electrode and likewise much better than the planar electrode.

### **5.3.3. Construction of CuO nanowire/microflower/nanowire structure for higher performance glucose sensing**

Considering that the surface area plays a great role in the electrooxidation of glucose, a CuO nanowire/microflower/nanowire structure based on the previous fabricated CuO nanowire/microflower architecture was fabricated using the Cu(OH)<sub>2</sub> nanowire growth technique from Cu layer in NaOH and (NH<sub>4</sub>)<sub>2</sub>S<sub>2</sub>O<sub>8</sub> solution. The detailed growth process was presented in Scheme 5.6 and Figure 5.7. Figure 5.8(a-d) show the FE-SEM of the obtained CuO nanowire/microflower/nanowire structure. It is found that all the microflowers are covered by the subsequently synthesized nanowires, which possess an average length of 1.5 μm and diameter of 100 nm. The nanowires show a curved shape due to the dehydration of Cu(OH)<sub>2</sub> to CuO during the annealing. Additionally, the second process induces the growth of small nanosheets on the previously fabricated CuO nanowire and produces a rough surface of the CuO nanowires (Figure 5.8d). The XRD

pattern and Raman spectra (Figure 5.8e-f) taken from the top surface of the sample

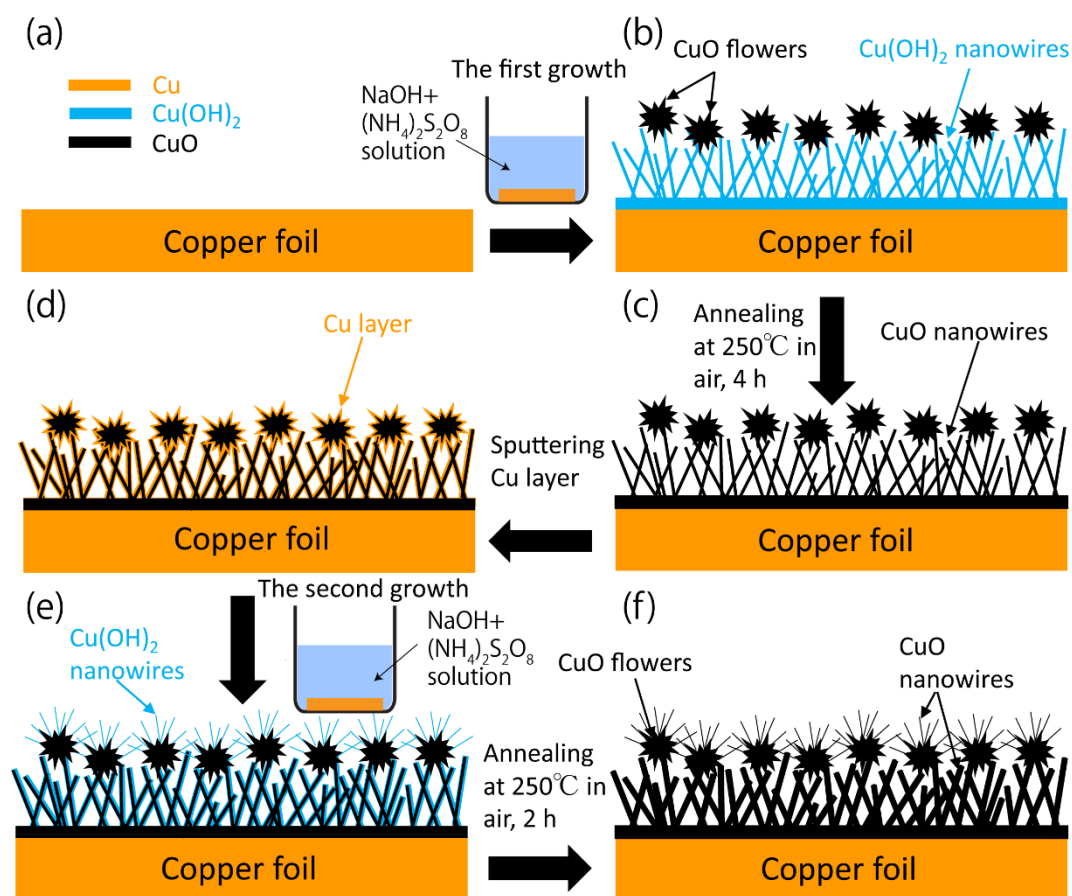


**Figure 5.6.** Schematic process for the fabrication of CuO nanowire/microflower/nanowire structure.

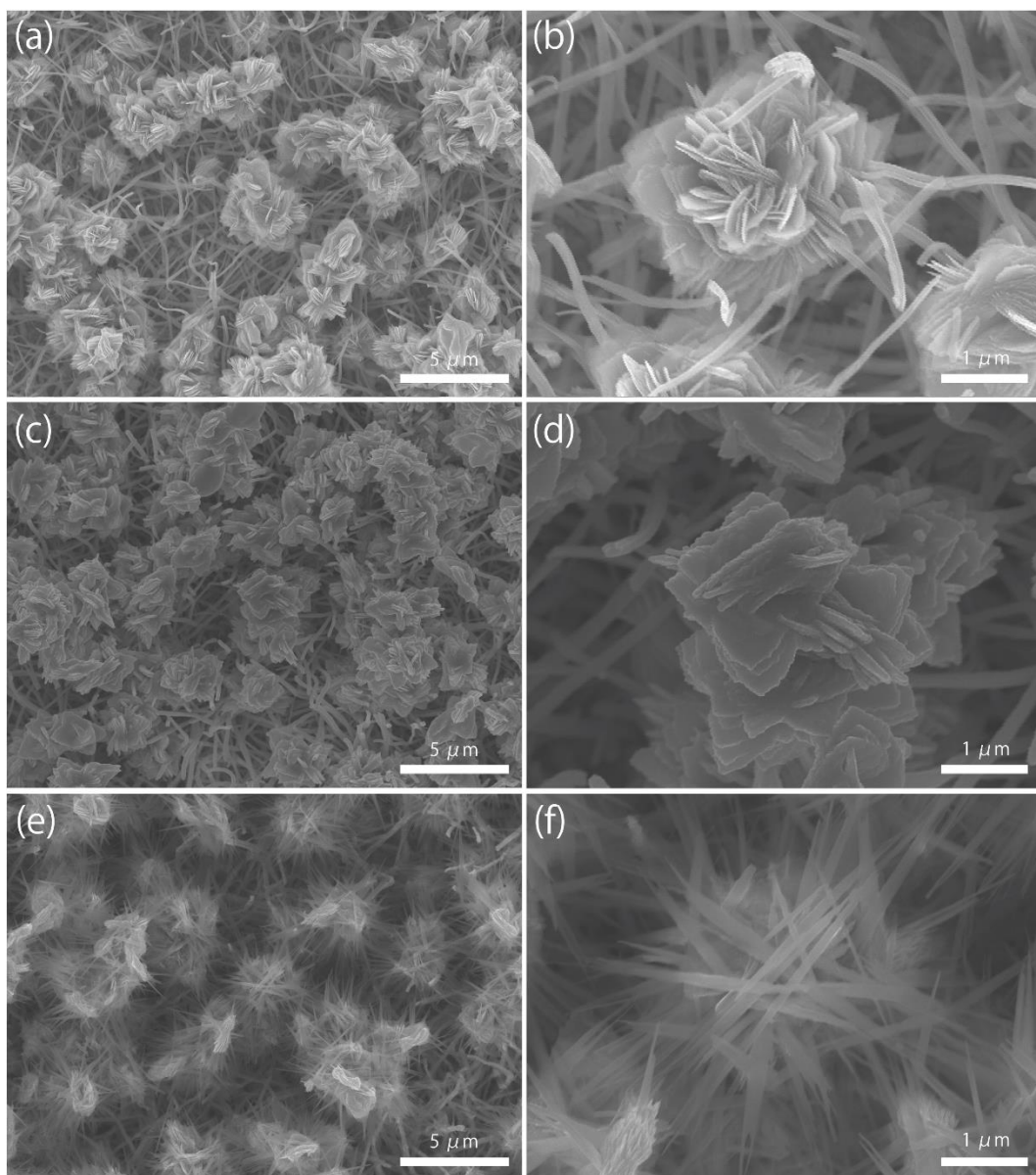


**Figure 5.7.** (a) FE-SEM images showing the morphology of the CuO nanowire/microflower (a-b), CuO nanowire/microflower deposited with a 300 nm-thick Cu layer (c-d) and CuO nanowire/microflower covered by  $\text{Cu}(\text{OH})_2$  nanowires through the second solution method process (e-f).



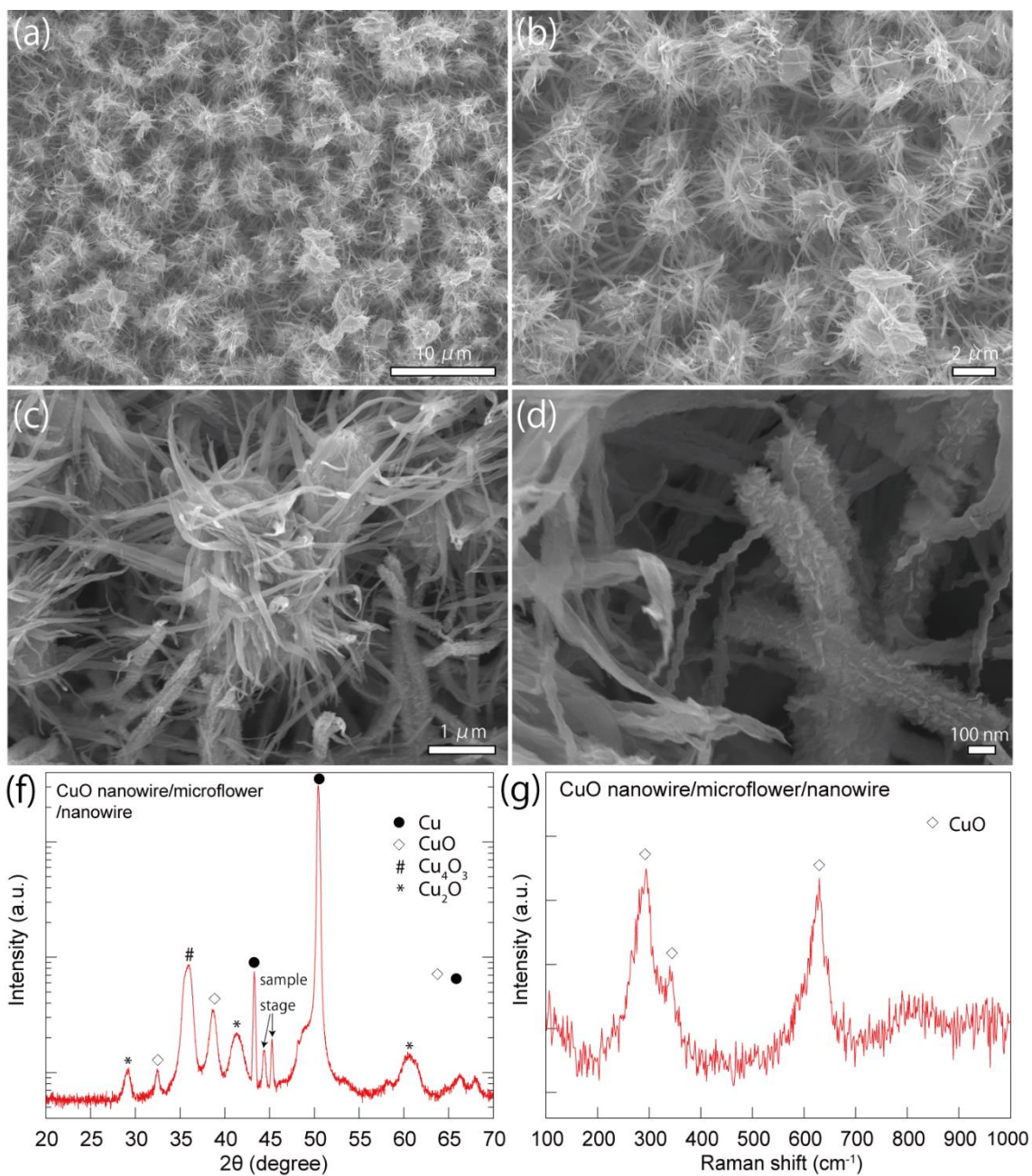


**Figure 5.8.** (a-d) FE-SEM images of the morphology of the CuO nanowire/microflower/nanowire structure. (f-g) XRD pattern and Raman spectra of the structure.



indicates that the phase of the nanostructures can be identified as CuO. The increase in the electrochemically active sites from the subsequently grown nanowires and nanosheets is expected to improve the electrooxidation ability towards glucose.

The voltammetric response of the CuO nanowire/microflower/nanowire electrode to the addition of different concentration (0.0-1.0 mM) of glucose in 0.1 M NaOH was performed to test its performance, as shown in Figure 5.9a. The CV curves show a similar characteristic feature compared to the CuO nanowire/microflower electrode, but exhibits a larger oxidation current during the scans, indicating efficient oxidation ability towards glucose. The sensitivity of 2424  $\mu\text{A}/\text{mM}/\text{cm}^2$  obtained from Figure 5.9b also demonstrates that the new growth nanostructures on CuO nanowire/microflower improve the electrocatalytic activity and electron transfer in the electrocatalytic process. The calibration curve in the inset of figure 5.9b shows a linear range up to 3 mM. The electrode also exhibits a low detection limit of 4  $\mu\text{M}$  (S/N=3). Figure 5.9c shows the CV curves of the CuO structures with different morphologies in 0.1 M NaOH. The oxidation reaction occurred during the forward scan is related to the absorption of hydroxyl on CuO to form Cu(III) radical and the reduction reactions in the backward scan is due to the reduction of Cu(III) radical.<sup>30-31</sup> Comparing the CV curves obtained for the different morphologies of the CuO structures, it is found that nanostructured electrode produces a much higher oxidation current compared to those of the planar electrode, indicating that a higher amount of hydroxyl is absorbed on nanostructured CuO ( $\text{CuO} + \text{OH}^- \rightarrow \text{CuOOH} + \text{e}^-$ ) due to the increase in the density of electrochemically active sites. Additionally, the evolution of CuO nanostructure from nanowire, nanowire/microflower to nanowire/microflower/nanowire increases the effective surface area systematically. This is also reflected in the progressively enhancement of glucose selectivity from the planar

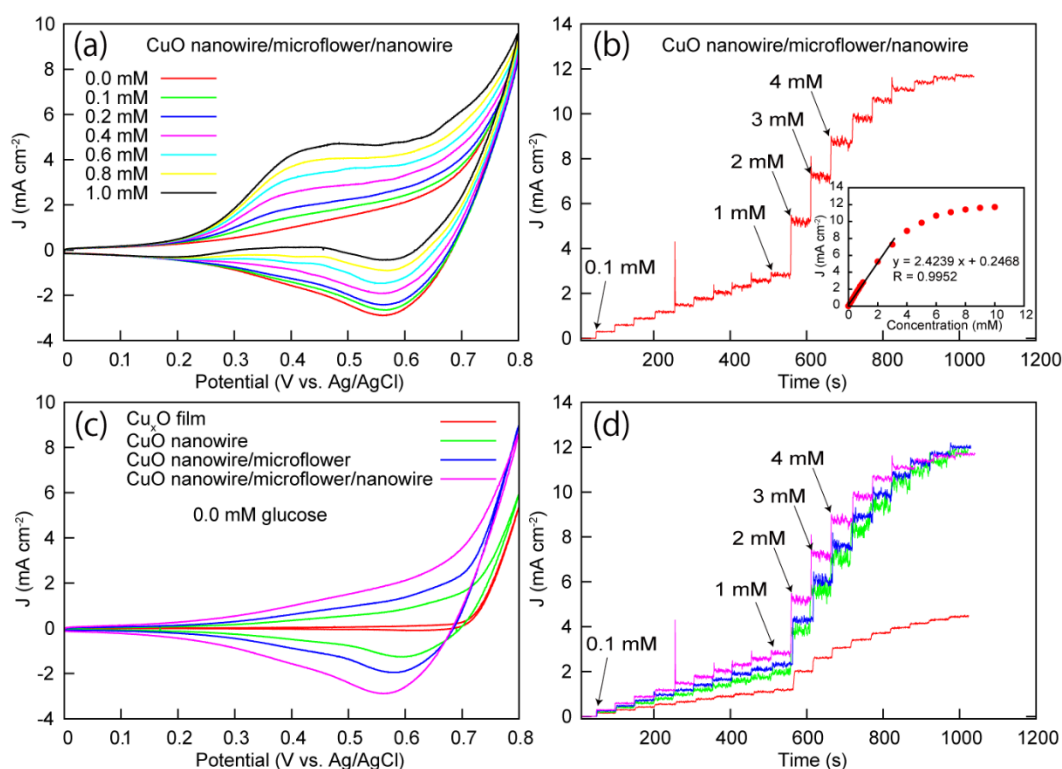


**Figure 5.9.** (a) Voltammetric response of the CuO nanowire/microflower/nanowire electrode to the addition of 0.0, 0.1, 0.2, 0.4, 0.6, 0.8 and 1.0 mM glucose in 0.1 M NaOH solution (pH 13) at the scan rate of 100 mV/s. (b) Chronoamperometric response of the CuO nanowire/microflower/nanowire electrode with successive additions of glucose to 0.1 M NaOH at 0.5 V vs. Ag/AgCl. The inset in part (b) shows the calibration curve of the chronoamperometric response. (c) CV sweep curves for the  $\text{Cu}_2\text{O}$  film electrode, CuO nanowire electrode, CuO nanowire/microflower and CuO nanowire/microflower/nanowire electrode in 0.1 M NaOH. (d) Chronoamperometric response of the four electrodes with successive additions of glucose to 0.1 M NaOH at 0.5 V vs. Ag/AgCl.

electrode to the more complex nanostructured electrodes, as seen in figure 5.9d. The sensitivity of the CuO nanowire/microflower/nanowire electrode is found to be higher than that of the  $\text{Cu}_x\text{O}$  nanorod modified Cu electrode<sup>21</sup> and other CuO powder (flowers

and nanospheres) modified glassy carbon or graphite electrodes, as shown in Table 5.1. The linear range of the reported CuO nanowire/microflower electrode is wider than the CuO nanowire (up to 2 mM)<sup>19</sup> and the porous CuO electrode (up to 2.5 mM).<sup>23</sup>

**Table 5.1.** Comparison between the performance characteristics of non-enzymatic CuO glucose sensors with different nanostructures.

Metal-oxide Semiconductor electrode	Fabrication Method	Sensitivity ( $\mu\text{A}/\text{cm}^2/\text{mM}$ )	Linear range (up to, mM)	LOD ( $\mu\text{M}$ )	Response time (s)	Ref.
<b>CuO nanowire/microflower/nanowire</b>	Grown directly from Cu foils	2424 at 0.5 V	3	4	~2	This work
<b>CuO nanowire/microflower</b>	Grown directly from Cu foils	1943 at 0.5 V	4	4	~2	This work
<b>CuO nanowire</b>	Grown directly from Cu foils	1776 at 0.5 V	4	4	~2	This work
<b>CuO-MWCNTs/TA plate</b>	Grown on Ta plate	2190 at 0.55 V	3	0.8	<2	[32]
<b>Cu<sub>2</sub>O nanorods</b>	Grown directly from Cu foils	1620 at 0.5 V	4	49	Na	[21]
<b>CuO nanoplates/TiO<sub>2</sub></b>	Electrospun on FTO glass	1321 at 0.7 V	2	0.39	<10	[33]
<b>CuO nanoparticles/graphene oxide</b>	Powder pasted onto glassy carbon substrate	262.52 at 0.7 V	2.03	0.69	Na	[31]
<b>CuO nanorods</b>	Powder pasted onto graphite substrate	371.43 at 0.6 V	8	4	~10	[20]
<b>CuO flowers</b>	Powder pasted onto graphite substrate	709.52 at 0.6 V	~2	4	~15	[20]
<b>CuO nanospheres</b>	Powder pasted onto glassy carbon substrate	404.53 at 0.6 V	2.55	1	Na	[22]
<b>Cu nanocluster/MWCNTs/GCE</b>	Grown on MWCNTs/GCE	253 at 0.65 V	3.50	0.21	5	[34]

#### 5.4. Selectivity

To investigate the effect of interference species (AA, UA and NaCl) on the CuO nanowire/microflower electrode, selectivity tests were conducted. Figure 5.10 shows the selectivity test of the nanostructured CuO electrodes conducted by adding 0.1 mM AA, 0.1 mM UA, and 1 mM glucose, in 0.1 M NaOH at 0.5 V, respectively. By normalizing

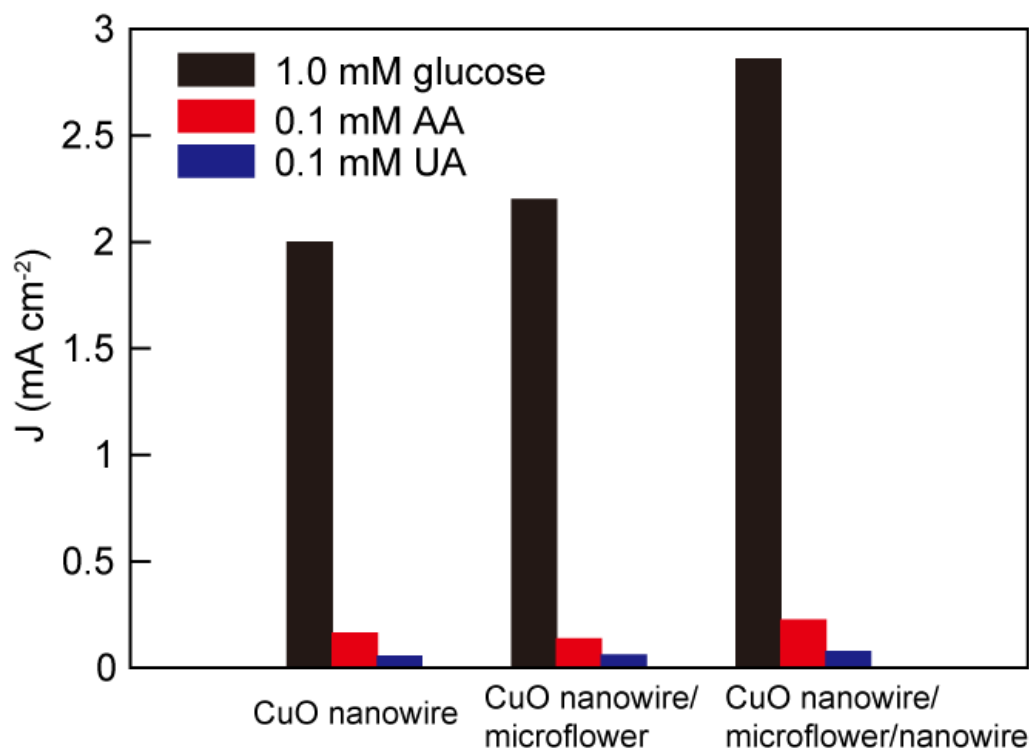


**Figure 5.10.** (a) Response of the CuO nanowire, CuO nanowire/microflower and CuO nanowire/microflower/nanowire electrode to 1.0 mM glucose, 0.1 mM ascorbic acid and 0.1 mM uric acid in 0.1 M NaOH at 0.5 V vs. Ag/AgCl .

the current density of the electrode to a value of 100% for 1 mM glucose, it is found that the response to the addition of 0.1 M AA and UA is 8.2 and 2.8%, 6.18 and 2.7%, 7.8 and 2.7% for the CuO nanowire, nanowire/microflower and nanowire/microflower/nanowire electrodes, respectively. The anti-interference ability of this electrode towards AA is better than the reported porous CuO electrode<sup>23</sup> and CuO nanosphere electrode.<sup>22</sup> The concentration of AA and UA under normal physiological level of glucose (3-8 mM) is of the order 0.1 mM,<sup>19</sup> thus AA and UA showed minor influence on the response of the fabricated CuO nanostructured electrodes, which can be said to have a good selectivity. Moreover, the electrodes show a good anti-interference ability to chloride ions because no response can be observed to the addition of 0.1 mM NaCl during the test.

## 5.5. Conclusions

The fabrication of highly sensitive amperometric glucose sensor based on CuO nanowire/microflower structure was achieved via a facile and low-cost method. The fabrication process consisted of the growth of  $\text{Cu}(\text{OH})_2$  nanowire/CuO microflower structure by a simple solution method, followed by annealing at a mild temperature ( $250^\circ\text{C}$ ) in air. Compared to the CuO nanowire- and  $\text{Cu}_x\text{O}$  film-based glucose sensors, the CuO nanowire/microflower glucose sensor showed high electrochemical activity due to the larger electrochemically active surface area. The sensitivity of the electrode was further improved by growing CuO nanowires on the microflowers to form a CuO nanowire/microflower/nanowire structure. The large-scale synthesis technique, high sensitivity, wide linear range, low detection limit and good selectivity make the CuO nanowire and microflower composite electrode a promising candidate for analytical applications.

## References

- [1] Wang J 2008 *Chem. Rev.* **108** 814-825
- [2] Rahman M M, Ahammad A J, Jin J H, Ahn S J and Lee J J 2010 *Sensors* **10** 4855-4886
- [3] Wang J X, Sun X W, Wei A, Lei Y, Cai X P, Li C M and Dong Z L 2006 *Appl. Phys. Lett.* **88** 233106(1-3)
- [4] Turkusic E, Kalcher K, Schachl K, Komersova A, Bartos M, Moderegger H, Svancara I and Vytras K 2001 *Anal. Lett.* **34** 2633-2647
- [5] Umar A, Rahman M M, Al-Hajry A and Hahn Y B 2009 *Electrochem. Commun.* **11** 278-281
- [6] Ansari A A, Solanki P R and Malhotra B D 2008 *Appl. Phys. Lett.* **92** 263901(1-3)
- [7] Tang H, Yan F, Tai Q D and Chan H L W 2010 *Biosens. Bioelectron.* **25** 1646-1651
- [8] Wilson R and Turner A. P. F. 1992 *Biosens Bioelectron.* **7** 165-185
- [9] Schügerl K, Hitzmann B, Jurgens H, Kullick T, Ulber R and Weigal B 1996 *Trends Biotechnol.* **14** 21-31
- [10] Kimmel D W, LeBlanc G, Meschievitz M E and Cliffl D E 2012 *Anal. Chem.* **84** 685-707
- [11] Lang X Y, Fu H Y, Hou C, Han G F, Yang P, Liu Y B, Jiang Q 2013 *Nat. Commun.* **4** 2169
- [12] Yuan J H, Wang K and Xia X H 2005 *Adv. Funct. Mater.* **15** 803-809
- [13] Boo H, Park S, Ku B, Kim Y, Park J H, Kim H C, Chung T D 2004 *J. Am. Chem. Soc.* **126** 4524-4525
- [14] Luo P F, Zhang F Z and Baldwin R P 1991 *Anal. Chim. Acta* **244** 169-178

- [15] You T Y, Niwa O, Chen Z L, Hayashi K, Tomita M and Hirono S 2003 *Anal. Chem.* **75** 5191-5196
- [16] Prabhu S V and Baldwin R P 1989 *Anal. Chem.* **61** 852-856
- [17] Sun Y P, Buck H and Mallouk T E 2001 *Anal. Chem.* **73** 1599-1604
- [18] Wang J P, Thomas D F and Chen A C 2008 *Anal. Chem.* **80** 997-1004
- [19] Zhuang Z J, Su X D, Yuan H Y, Sun Q, Xiao D and Choi M M F 2008 *Analyst* **133** 126-132
- [20] Wang X, Hu C G, Liu H, Du G J, He X S, Xi Y 2010 *Sens. Actuators, B* **144** 220–225
- [21] Li C L, Su Y, Zhang S W, Lv X Y, Xia H L and Wang Y J 2010 *Biosens. Bioelectron.* **2** 903–907
- [22] Reitz E, Jia W Z, Gentile M, Wang Y and Lei, Y 2008 *Electroanalysis* **20** 2482–2486
- [23] Cherevko S and Chung C H 2010 *Talanta* **3** 1371-1377
- [24] Zhang W, Wen X, Yang S, Berta Y and Wang Z L 2003 *Adv. Mater.* **15** 822–825
- [25] Li C L, Li Y B and Delaunay J J 2014 *ACS Appl. Mater. Interfaces* **6** 480–486
- [26] Fan F T, Feng Z C and Li C 2010 *UV Acc. Chem. Res.* **43** 378–387
- [27] Zhang J, Li M J, Feng Z C, Chen J and Li C 2006 *J. Phys. Chem. B* **110** 927–935
- [28] Reydellet J, Balkanski M and Trivich D 1972 *Phys. Status Solidi B* **52** 175–185
- [29] Xu J F, Ji W, Shen Z X, Li W S, Tang S H, Ye X R, Jia D Z and Xin X Q 1999 *J. Raman Spectrosc.* **30** 413–415
- [30] Marioli J M and Kuwana T 1992 *Electrochim. Acta* **37** 1187-1197
- [31] Song J, Xu L, Zhou C Y, Xing R Q, Dai Q L, Liu D L and Song H W 2013 *ACS Appl. Mater. Interfaces* **5** 12928–12934

- [32] Yang J, Jiang L C, Zhang W D and Gunasekaran S 2010 *Talanta*, **82**, 25-33
- [33] Chen J, Xu L, Xing R, Song J, Song H, Liu D and Zhou J 2012 *Electrochem. Commun.* **20** 75-78
- [34] Kang X, Mai Z, Zou X, Cai P and Mo J 2007 *Anal. Biochem.* **363** 143-150



## 6. Conclusions and outlooks

### 6.1. Conclusions

The work conducted in this thesis aimed at constructing high performance photocathode for solar-driven water splitting and electrochemical sensor for glucose sensing based on copper oxide. Under controllable annealing condition, the Cu/Cu(OH)<sub>2</sub> nanowire was used as template to synthesis highly photoactive Cu<sub>2</sub>O microcrystalline films and CuO nano/micro structures for solar water splitting and glucose sensing, respectively. The method introduced in this work opens up possibilities in developing high performance solar water splitting and glucose sensing devices that are based on earth-abundant, environmentally friendly Cu-based oxide semiconductors.

In chapter 1, the fundamentals of PEC water splitting and glucose sensing were described. The constraints of Cu<sub>2</sub>O for stable solar water splitting and CuO for high performance glucose sensing were presented in this part. Therefore this thesis introduced new approach developed to address the main limitations for copper oxide based solar water splitting and glucose sensing. As discussed in details in the following chapters.

In chapter 2, we presented a novel method to fabricate Cu<sub>2</sub>O microcrystalline film with high photoactivity for potential use in high-efficiency photocathode. By decomposing previously synthesized Cu(OH)<sub>2</sub> nanowires on a Cu foil at 500 °C under a vacuum, Cu<sub>2</sub>O nanowires are formed and the subsequent oxide growth is driven by outward diffusion of Cu ions from Cu substrate to oxide surface and react with oxygen from the gas phase. The nanowires induce the oxide layer proceeds along the nanostructure to get a reorganized microcrystalline film with well-defined crystal facets and porous structure. The morphology of Cu<sub>2</sub>O film can be continuously modified by changing the annealing time. The Cu<sub>2</sub>O film annealed for 2 h achieved the highest

photocurrent of 4.07 mA/cm<sup>2</sup> at 0 V/RHE under chopped simulated AM 1.5 illumination as well as the largest carrier density ( $\sim 1.36 \times 10^{18}$  cm<sup>-3</sup>) compared to the 1, 3 and 4 h samples. Although the high photocurrent of the Cu<sub>2</sub>O film partially originated from the reduction of Cu<sub>2</sub>O to Cu on the oxide surface, the large amount of carriers generated under illumination can be collected for efficient water splitting by coating n-type materials on the Cu<sub>2</sub>O surface to overcome the kinetic barrier at the oxide/electrolyte interface.

In chapter 3, the Cu<sub>2</sub>O photocathode was stabilized by coating overlayers with favorable band alignment relative to Cu<sub>2</sub>O, which improve the onset potential and stability of the photocathode in PEC measurement. A large shift of the onset potential toward positive values and a stable photocurrent over time are achieved by introducing a Ga<sub>2</sub>O<sub>3</sub> buffer layer between the Cu<sub>2</sub>O absorber layer and the TiO<sub>2</sub> protective layer. The conformally coated Ga<sub>2</sub>O<sub>3</sub> thin layer (20 nm), owing to its high thermal resistance, works as a suitable buffer layer to grow TiO<sub>2</sub> layers (15 nm) with improved quality. Furthermore, the Ga<sub>2</sub>O<sub>3</sub> buffer layer decreases the conduction band discontinuity at the Cu<sub>2</sub>O/Ga<sub>2</sub>O<sub>3</sub> interface, thus improving the open circuit voltage of the structure. The obtained large energy gap between the p-type absorber and the n-type overlayers inhibits the interface recombination and provides a large driving force for the transport of photogenerated electrons in the photocathode, resulting in efficient water reduction on the structure surface with the assistance of Pt co-catalyst.

In chapter 4, a Cu/Cu<sub>2</sub>O/CuO structure is prepared by annealing Cu/Cu(OH)<sub>2</sub> nanowires precursor under a controlled pressure and flow of O<sub>2</sub> at 500°C. The amperometric detection of glucose exhibits a good sensitivity in enzymatic sensing (with GOx) and high performance in non-enzymatic sensing due to the favorable electrocatalytic reaction on crystalline CuO porous surface and improved electron transfer

ability assisted by a Schottky junction between Cu and Cu<sub>2</sub>O, demonstrating the potential of this structure as a facile synthesis and low-cost electrode.

In chapter 5, a rational combination of CuO nanowire and microflower on Cu foil is applied to construct high performance CuO-based glucose sensor. The CuO nanowire/microflower structure with its large surface area leads to an efficient catalysis and charge transfer in glucose detection, achieving a high sensitivity of 1943  $\mu\text{A}/\text{mM}/\text{cm}^2$ , a wide linear range up to 4 mM and a low detection limit of 4  $\mu\text{M}$  for amperometric glucose sensing in alkaline solution. With a second consecutive growth of CuO nanowires on the microflowers, the sensitivity of the obtained CuO nanowire/microflower/nanowire structure further increase to 2424  $\mu\text{A}/\text{mM}/\text{cm}^2$ , benefiting from the increased electrochemically active sites. The electrode shows a satisfactory sensitivity, acceptable selectivity and fast response time toward non-enzymatic glucose sensing, making it a promising electrochemical sensor for glucose analysis.

## 6.2. Outlooks

Although the high photovoltage and relatively stable photocurrent on Cu<sub>2</sub>O-based photocathodes were realized by coating appropriate overlayers on Cu<sub>2</sub>O, there is still a long way before achieving solar-to-hydrogen efficiencies necessary for commercial application. Nevertheless, the study presented in this thesis provides an effective method to decrease the overpotential for Cu<sub>2</sub>O photocathode. Combining with this low overpotential, a larger photocurrent can improve the solar-to-hydrogen efficiency of this system largely. One method to enlarge the photocurrent is to improve the conductivity of overlayers by doping and thus decrease the energy loss during the reaction. The carrier density of Ga<sub>2</sub>O<sub>3</sub> likely can be increased by Zn doping to form ZnGa<sub>2</sub>O<sub>4</sub>, which may can

be achieved by depositing ZnO and Ga<sub>2</sub>O<sub>3</sub> thin layer alternatively on Cu<sub>2</sub>O through atomic layer deposition technique. To control the photoactivity of Cu<sub>2</sub>O, electrodeposition method may provide a more effective method to tune the carrier density and conductivity of Cu<sub>2</sub>O by varying the electrodeposition parameters such as deposition carrier density, pH and deposition temperature. Another way to enhance the conversion efficiency is to connect this photocathode with a highly efficient photoanode to form a dual-electrode configuration. In this configuration, the photoanode oxidizes water to oxygen and the photocathode performs water reduction directly and a bias-free overall water splitting system can be achieved. This promising configuration suggests a higher solar-to-hydrogen conversion efficiency if the band gap energies and band-edge energy levels of the photoelectrodes are chosen carefully. Stable and efficient photoanode such as WO<sub>3</sub> and BiVO<sub>4</sub> may good candidates for this promising combination due to the appropriate band-edge level and band gap (2.4-2.5 eV).<sup>1-4</sup> In addition to the photoactivity improvement, applying earth-abundant co-catalyst such as MoS<sub>x</sub><sup>5</sup> or Ni-Mo<sup>6</sup> thin film as HER catalyst on the protected Cu<sub>2</sub>O photocathode is a promising way to enhance the long-term stability both in acidic and alkaline solutions.

CuO is one of the most sensitive electrodes for non-enzymatic glucose sensors in alkaline solutions. The sensitivity achieved in this thesis is as high as mA/cm<sup>2</sup>/mM, however, the inability to function in the physiological condition makes it potentially more useful in food industry, industrial processes and fuel cell industry. To develop the non-enzymatic glucose sensor can work in pH neutral or acid conditions is important for blood glucose monitoring. Noble metal such as Pt and Au have been widely reported as non-enzymatic glucose sensors that can work in physiological condition.<sup>7</sup> Thus, the combination of this kind of metal nanoparticles with the CuO nano/micro structures may

introduce a high-performance non-enzymatic glucose sensor for blood glucose monitoring due to the synergistic effect of the noble metal and CuO. What's more, the highly accessible surface area and large roughness factor of the microflowers may improve the selectivity of electrode due to the kinetic-controlled electrochemical reactions are sensitive to the nanoscopic surface area of the electrode.<sup>8</sup>

## References

- [1] S. Ida, K. Yamada, T. Matsunaga, H. Hagiwara, Y. Matsumoto and T. Ishihara, *J. Am. Chem. Soc.*, 2010, 132, 17343.
- [2] Q. X. Jia, K. Iwashina and A. Kudo, *Proc. Natl. Acad. Sci. U. S. A.*, 2012, 109, 11564.
- [3] Q. P. Chen, J. H. Li, X. J. Li, K. Huang, B. X. Zhou and W. F. Shangguan, *ChemSusChem*, 2013, 6, 1276.
- [4] P. Borno, F. F. Abdi, S. D. Tilley, B. Dam, R. van de Krol, M. Graetzel and K. Sivula, *J. Phys. Chem. C*, 2014, 118, 16959.
- [5] C. G. Morales-Guio, S. D. Tilley, H. Vrubel, M. Grätzel and X. L. Hu, *Nat. Commun.*, 2014, 5, 3059.
- [6] Morales-Guio, C. G.; Liardet, L.; Mayer, M. T.; Tilley, S. D.; Grätzel, M.; Hu, X. *Angew. Chem., Int. Ed.* 2015, 54, 664– 667.
- [7] Toghiani, K. E.; Compton, R. G. *Int. J. Electrochem. Sci.* **2010**, 5, 1246-1301.
- [8] S Park, TD Chung, HC Kim *Anal. Chem.* **2003**, 75, 3046–3049.

## Publications

- [1] **Changli Li**, Yanbo Li and Jean-Jacques Delaunay, “A novel method to synthesize highly photoactive Cu<sub>2</sub>O microcrystalline films for use in photoelectrochemical cells,” *ACS applied materials & interfaces* 2013, *6*, 480-486
- [2] **Changli Li**, Mario Kurniawan, Dali Sun, and Hitoshi Tabata and Jean-Jacques Delaunay, “Nanoporous CuO layer modified Cu electrode for high performance enzymatic and non-enzymatic glucose sensing,” *Nanotechnology* 2015, *26*, 015503
- [3] **Changli Li**, Takashi Hisatomi, Osamu Watanabe, Mamiko Nakabayashi, Naoya Shibata, Kazunari Domen and Jean-Jacques Delaunay, “Positive onset potential and stability of Cu<sub>2</sub>O-based photocathodes in water splitting by atomic layer deposition of a Ga<sub>2</sub>O<sub>3</sub> buffer layer,” *Energy & Environmental Science* 2015, *8*, 1493-1500
- [4] **Changli Li**, Hiroyasu Yamahara, Yae-rim Lee, and Hitoshi Tabata and Jean-Jacques Delaunay, “CuO nanowire/microflower/nanowire modified Cu electrode with enhanced electrochemical performance for non-enzymatic glucose sensing” *Nanotechnology* 2015, *26*, 305503
- [5] Changqing Zhu, # **Changli Li**, # (Co-first author), Maojun Zheng and Jean-Jacques Delaunay, “Plasma-induced Oxygen Vacancies in Ultrathin Hematite Nanoflakes Promoting Photoelectrochemical Water Oxidation,” in revision.

## Appendix A. Supporting Information to Chapter 2

### Fully oxidized $\text{Cu}_2\text{O}$ film formed at $1010^\circ\text{C}$ from Cu foil

#### Fabrication and structural properties of fully oxidized $\text{Cu}_2\text{O}$ films

The  $\text{Cu}_2\text{O}$  film prepared from high temperature ( $\sim 1000^\circ\text{C}$ ) oxidization of Cu foil has been extensively studied over the past decades. In this section, the  $\text{Cu}_2\text{O}$  film was prepared by annealing a Cu foil at  $1010^\circ\text{C}$  under Ar and  $\text{O}_2$  atmosphere. More specifically, the Cu foil with a size of  $10 \times 30\text{ mm}^2$  and a thickness of  $0.2\text{ mm}$  was cleaned sequentially in acetone and ethanol ultrasonic bath for 10 min. The cleaned Cu foil was loaded into an

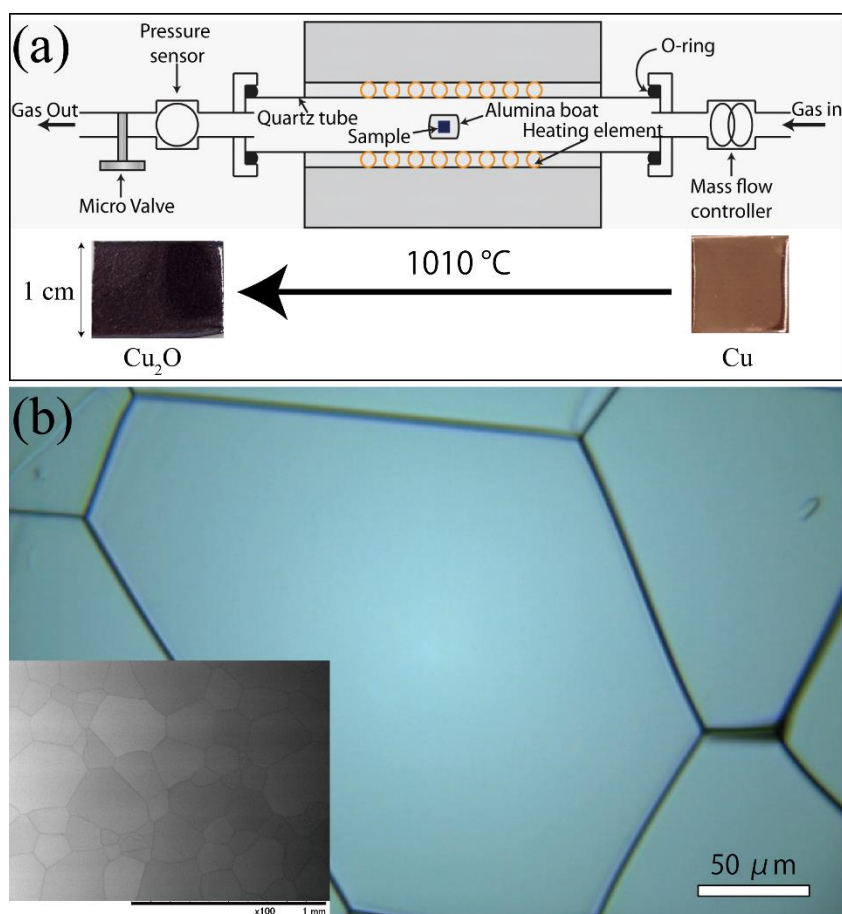


**Figure A.1.** (a) Schematic diagram of the annealing system and photographs of the Cu foil before and after annealing. (b) Optical microscope image of the  $\text{Cu}_2\text{O}$  film prepared at  $1010^\circ\text{C}$ . The inset in part b is the SEM image of the film with low magnification.



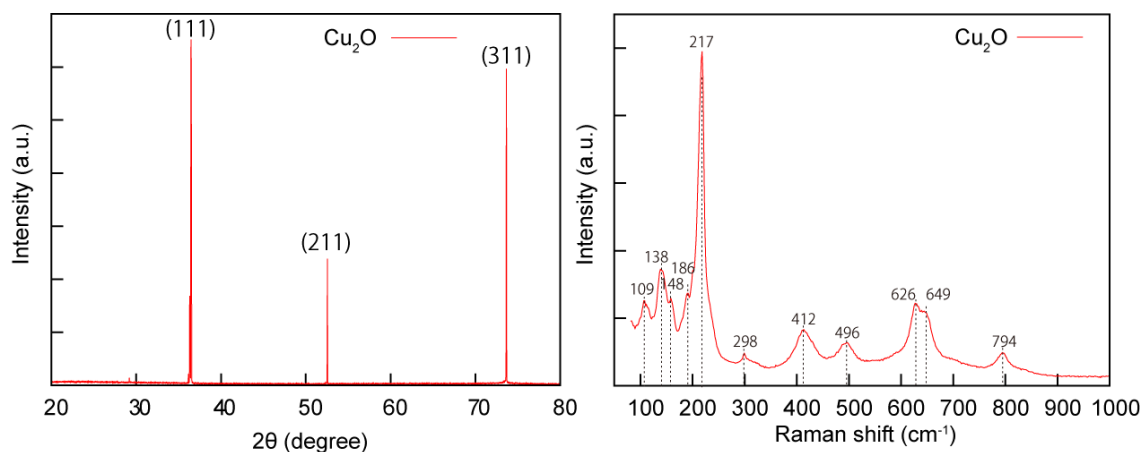


**Figure A.2.** (a) XRD pattern and (b) Raman spectra of the  $\text{Cu}_2\text{O}$  film prepared at 1010  $^{\circ}\text{C}$  for 2 h.

alumina boat and placed at the center of a quartz tube. The quartz tube was evacuated to about 36 Pa before heating, and the flow rate of Ar was 50 sccm during the heating and cooling process. When the temperature of tube increased to 1010 $^{\circ}\text{C}$ ,  $\text{O}_2$  was introduced into the tube for Cu oxidation reaction and the flow rate was 10 sccm. The temperature was kept at 1010 $^{\circ}\text{C}$  for 1 h to ensure complete oxidation of the Cu foil. After a 1 h annealing,  $\text{O}_2$  flow was stopped and the sample was annealed at 1010 $^{\circ}\text{C}$  for 1 h in Ar atmosphere. Subsequently, the temperature was lowered to room temperature naturally. The schematic diagram of the annealing system and the photographs of the Cu foil before and after annealing are presented in Figure A.1a. The resulting  $\text{Cu}_2\text{O}$  film was polycrystalline p-type semiconductor composed of grains with a size in the range from approximately 0.01 to 0.16  $\text{mm}^2$ , as shown in Figure A.1b. The XRD pattern (Figure A.2a) of the  $\text{Cu}_2\text{O}$  film indicates that all the diffraction peaks are well indexed to the peaks of cubic structure  $\text{Cu}_2\text{O}$  (space group  $\text{Pn-3m}$ , lattice constant 4.2600  $\text{\AA}$ , ICDD PDF card No. 1010941). The full width at half maximum (FWHM) of the three peaks are about 0.1 $^{\circ}$ , revealing a high crystal quality of the layer. The Raman spectra taken from the top surface of the  $\text{Cu}_2\text{O}$  film is presented in Figure A.2b. The observed peaks can be ascribed

to Cu<sub>2</sub>O.<sup>17</sup> Thus, combining the results from XRD and Raman spectra, we conclude that Cu<sub>2</sub>O layer with high quality was formed by using this high temperature annealing method and no impurity such as CuO was found.

### Optical properties

The optical properties of the Cu<sub>2</sub>O film prepared at 1010 °C was analyzed by UV-vis diffuse reflectance spectra, as shown in Figure A.3. A clear absorption edge at around 620 nm reflects a typical absorption characteristic of Cu<sub>2</sub>O. The light absorption ability of the film in visible region makes it a promising candidate for use in solar energy conversion applications. In order to evaluate the band gap energy of the film,  $(F(R) \times hv)^2$  values for a direct band gap material were plotted versus excitation energy where the absorption coefficient  $F(R)$  was calculated according to the Kubelka-Munk (K-M) equation. The samples annealed at 1010 °C have a band gap energy of 1.94 eV (Figure A.3b).

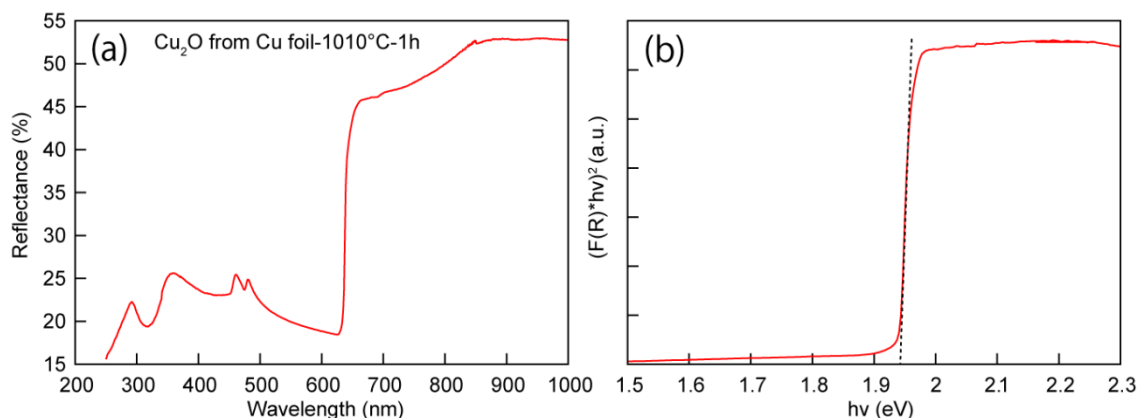


**Figure A.3.** (a) Diffuse reflectance spectra and (b) calculated Kubelka-Munk function vs excitation energy plots for the Cu<sub>2</sub>O film prepared at 1010°C.

## PEC properties

The photoelectrochemical (PEC) performances of the fabricated  $\text{Cu}_2\text{O}$  electrodes were evaluated in 0.5 M  $\text{Na}_2\text{SO}_4$  (pH = 6) electrolyte by linear sweep voltammetry (LSV) measurements under a 500 W Xe lamp with UV filter ( $\lambda > 420$  nm). A Pt wire and an Ag/AgCl electrode were used as the counter and reference electrode, respectively. The scan rate was 10 mV/s and the on-off interval was 2 s. The PEC responses of the  $\text{Cu}_2\text{O}$  electrode is presented in Figure A.4. The photocathodic current observed under illumination confirmed that the electrode was a p-type semiconductor. The onset potential of electrode was about 0.7 V vs. RHE and the photocurrent increased with the increasing of applied voltage negatively. The photocurrent densities of  $-0.27 \text{ mA/cm}^2$  was obtained at 0 V/RHE. A stability measurement of the electrode at 0 V vs. RHE was conducted to check the stability of the sample, as shown in Figure A.4b. The photocurrent density of the  $\text{Cu}_2\text{O}$  electrode decreased slowly with time under continuous illumination, indicating an unstable property of this material in contact with electrolyte under PEC measurement. This can be explained by the self-reduction of  $\text{Cu}_2\text{O}$  to Cu under illumination.

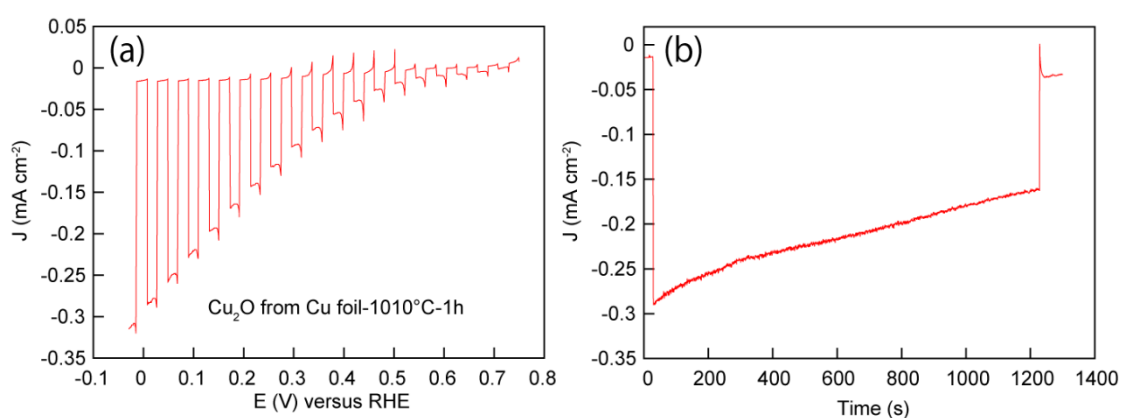


**Figure A.4.** (a) Current-potential curves and (b) current-time curves (held at 0 V vs. RHE) of the  $\text{Cu}_2\text{O}$  layer prepared at  $1010^\circ\text{C}$ . Curves were measured in 0.5 M  $\text{Na}_2\text{SO}_4$  electrolyte (pH 6) under 500 W Xe lamp with a UV filter (cut-off filter  $> 420$  nm, HOYA L42).

## Mott-Schottky analysis

To estimate the flatband potential and charge carrier density, the Cu<sub>2</sub>O electrode

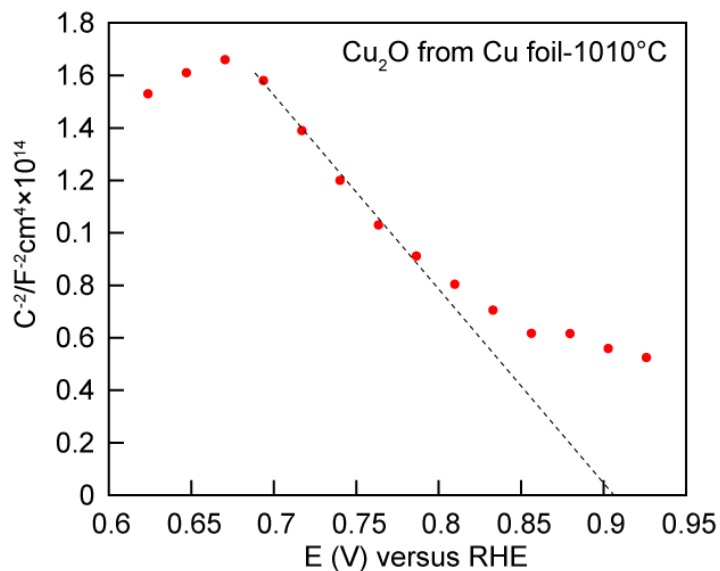


**Figure A.5.** Mott-Schottky plot for the Cu<sub>2</sub>O film prepared at 1010°C for 2 h from electrochemical impedance analysis in 0.01 M PBS solution (pH 7.4). The electrode was scanned with a frequency of 1 kHz in the potential range of chemical stability.

were characterized by electrochemical impedance spectroscopy. The potential sweep was performed at a fixed frequency (1 kHz) with a scan speed of 10 mV/s. Figure A.5 shows the Mott-Schottky plot for the Cu<sub>2</sub>O electrode taken in 0.01 M PBS electrolyte (pH = 7.4). The measured flatband potential and charge carrier density were 0.91 V vs. RHE and  $2.64 \times 10^{16} \text{ cm}^{-3}$ , respectively. The conduction bands are positioned at -0.86 V vs. RHE.

## Analysis

Cu<sub>2</sub>O film with high crystal quality was fabricated by oxidizing Cu foil at 1010 °C. The oxide film possesses a bandgap of 1.94 eV and a carrier density of  $2.64 \times 10^{16} \text{ cm}^{-3}$ . The conduction band and valence band of the film were positioned at -0.86 and 1.07 V vs. RHE, respectively. Under a PEC measurement, the electrode exhibited a low

photocurrent of  $-0.27 \text{ mA/cm}^2$  at 0 V vs. RHE, which may be attributed to the low carrier density and large film thickness ( $\sim 250 \text{ }\mu\text{m}$ ). Thus, a thinner  $\text{Cu}_2\text{O}$  layer with higher carrier density based on Cu foil may improve the photoactivity and serve as absorber layer for solar energy conversion devices.

### **$\text{Cu}_2\text{O}$ microcrystalline film formed at $500^\circ\text{C}$ from Cu foil**

#### **Fabrication and structural properties of $\text{Cu}_2\text{O}$ films**

In order to fabricate a thinner  $\text{Cu}_2\text{O}$  film on Cu foil, the annealing temperature for Cu foil was decreased to  $500^\circ\text{C}$  and the annealing time was varied from 1 to 4 h. The Cu foil with a size of  $10\times 10 \text{ mm}^2$  and a thickness of 0.2 mm was cleaned sequentially in acetone and ethanol ultrasonic bath for 10 min. The cleaned Cu foil was loaded into an alumina

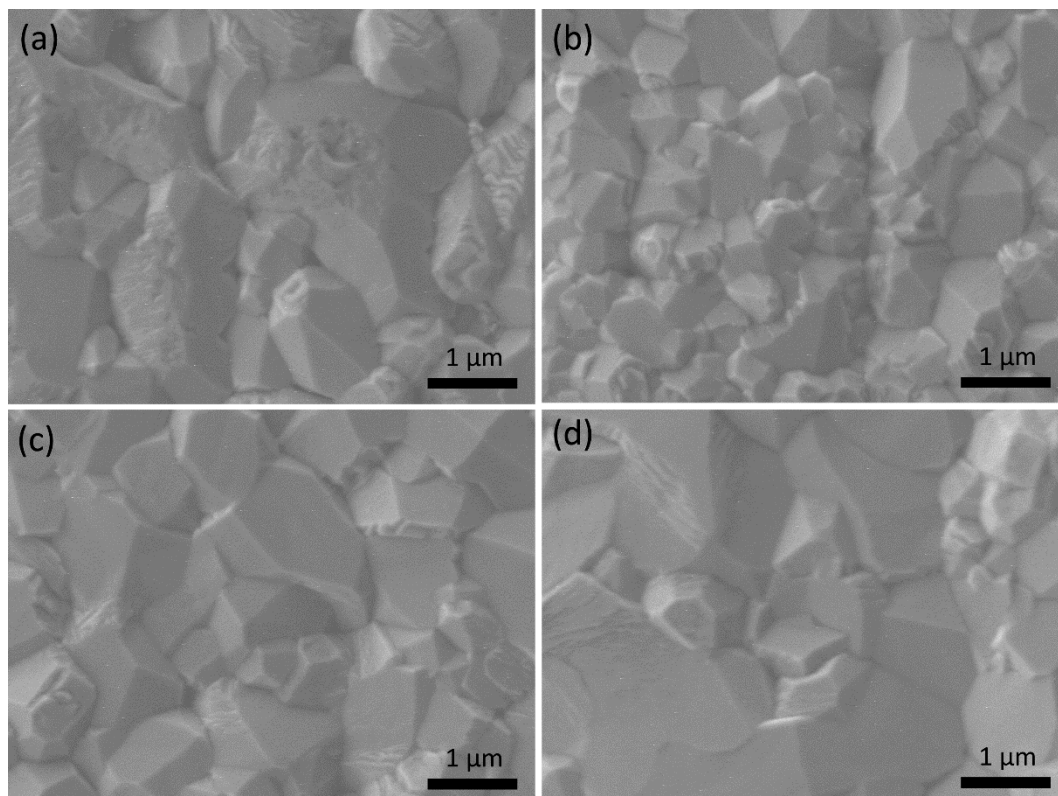


**Figure A.6.** FE-SEM images of the  $\text{Cu}_2\text{O}$  film prepared at  $500^\circ\text{C}$  from Cu foil with different annealing time. (a-d)  $\text{Cu}_2\text{O}$  film prepared at  $500^\circ\text{C}$  for 1, 2, 3 and 4 h, respectively.

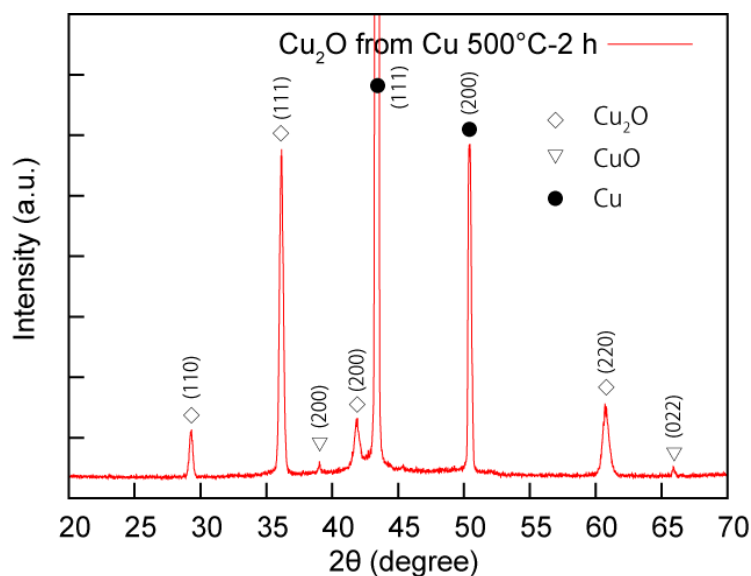


**Figure A.7.** XRD pattern of the  $\text{Cu}_2\text{O}$  film prepared at  $500^\circ\text{C}$  for 2 h.

boat and placed at the center of a quartz tube. The quartz tube was evacuated to about 36 Pa before heating, and the flow rate of Ar was 50 sccm during the heating and cooling process. The working pressure during the annealing was kept at about  $2.5 \times 10^3$  Pa. The Cu foils were annealed at  $500^\circ\text{C}$  for 1, 2, 3 and 4 h to obtain  $\text{Cu}_2\text{O}$  film with controlled PEC properties. In this experiment, only Ar was introduced into the tube as protection gas, the growth of  $\text{Cu}_2\text{O}$  proceeded through the Cu oxidation with the residual  $\text{O}_2$  in the furnace tube.

The resulting  $\text{Cu}_2\text{O}$  film shows a thickness of several tens of micrometers on the Cu substrate. Figure A.6 shows the SEM images of the  $\text{Cu}_2\text{O}$  film prepared at  $500^\circ\text{C}$  with different times. For the 1 h sample shown in Figure A.6a, it is found that the film was composed of incomplete microcrystals with a size of about 0.5-1.5  $\mu\text{m}$ . With the increasing of time, the facets of the microcrystals become more regular and flat. The XRD pattern of the  $\text{Cu}_2\text{O}$  microcrystalline film prepared at  $500^\circ\text{C}$  for 2 h is shown in Figure A.7. It is found that except for peaks from  $\text{Cu}_2\text{O}$ , two weak peaks from CuO can also be observed. Thus a very thin CuO layer may have formed on the surface of  $\text{Cu}_2\text{O}$ .

## Optical properties

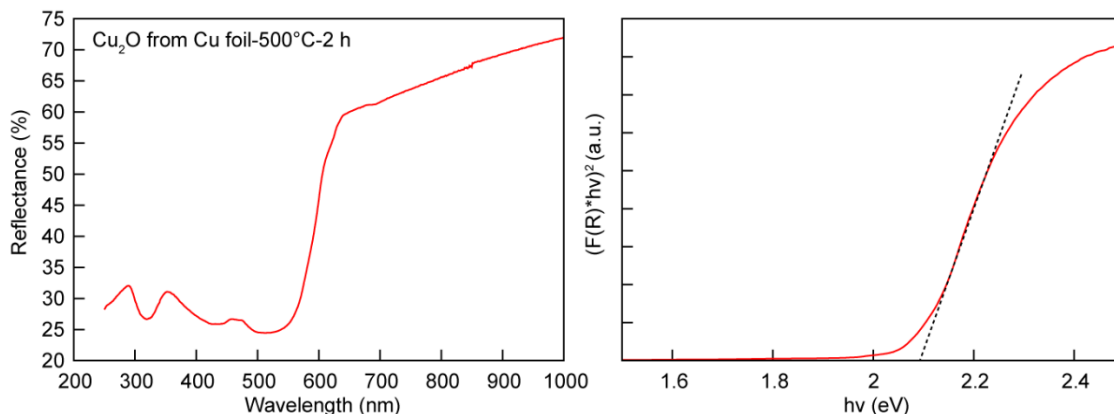


**Figure A.8.** (a) Diffuse reflectance spectra and (b) calculated Kubelka-Munk function vs excitation energy plots for the  $\text{Cu}_2\text{O}$  film prepared at  $500^\circ\text{C}$  for 2 h.

The optical properties of the  $\text{Cu}_2\text{O}$  film prepared at  $500^\circ\text{C}$  was measured by UV-vis diffuse reflectance spectra, as shown in Figure 2.8. The absorption property of the sample is similar to the  $\text{Cu}_2\text{O}$  film prepared at  $1010^\circ\text{C}$ . By using the same Kubelka-Munk (K-M) equation presented in Section 2.3.2, a band gap of 2.09 eV was obtained for the  $\text{Cu}_2\text{O}$  film prepared at  $500^\circ\text{C}$  (2 h).

## PEC properties

The PEC responses of the  $\text{Cu}_2\text{O}$  electrodes prepared with different annealing times are presented in figure A.9. The photocurrent densities of -1.9, -2.5, -2.0 and -0.5  $\text{mA}/\text{cm}^2$  were obtained at 0 V/RHE for the annealing times of 1, 2, 3 and 4 h, respectively. In the stability test, the photocurrent decreases rapidly with time and the film lose its photoactivity after 20 min test. The instability of the sample indicates that a large proportion of the photocurrent is generated from the reduction of  $\text{Cu}_2\text{O}$  to Cu.

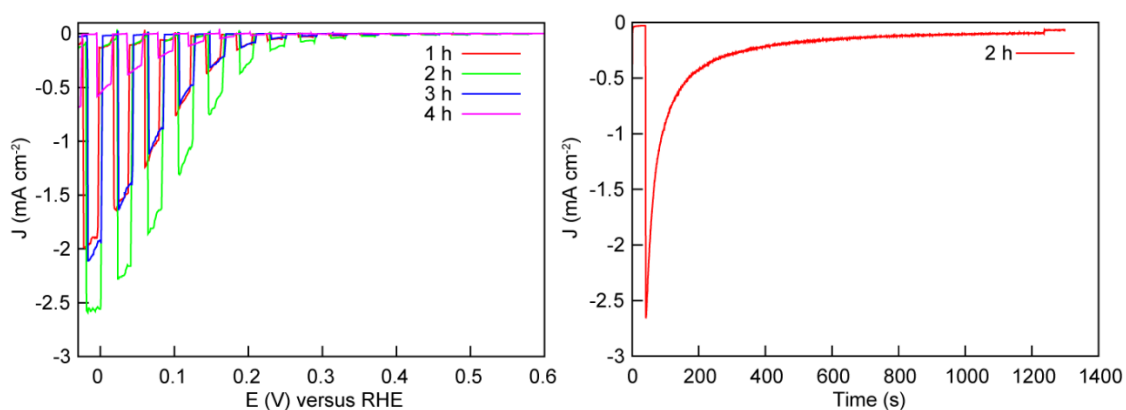


**Figure A.9.** (a) Current-potential curves of the Cu<sub>2</sub>O films prepared at 550°C for 1, 2, 3 and 4 h. (b) Current-time curves (0 V vs. RHE) of the Cu<sub>2</sub>O film prepared at 500°C for 2 h. Curves were measured in 0.5 M Na<sub>2</sub>SO<sub>4</sub> electrolyte (pH 6) under 500 W Xe lamp with a UV filter (cut-off filter >420 nm, HOYA L42).

### Mott-Schottky analysis

Figure A.10 shows the Mott-Schottky plot of the Cu<sub>2</sub>O film prepared at 500°C for 2 h. The flat band potential and carrier density were determined by the Mott-Schottky method. The flat band and carrier density for the Cu<sub>2</sub>O film were calculated to be 0.85 V vs. RHE and  $8.17 \times 10^{17}$  cm<sup>-3</sup>, respectively. Thus, combining the band gap, the position of

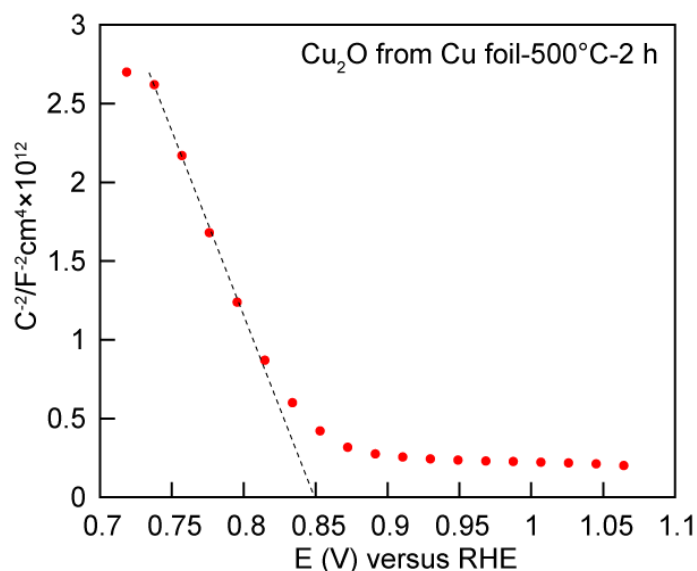


**Figure A.10.** Mott-Schottky plot for the Cu<sub>2</sub>O film prepared at 500°C for 2 h from electrochemical impedance analysis in 0.01 M PBS solution (pH 7.4). The electrode was scanned with a frequency of 1 kHz in the potential range of chemical stability.



conduction band and valence band of this film can be determined to be -1.17 and 0.92 V vs. RHE.

## Analysis

Cu<sub>2</sub>O microcrystalline films based on Cu foil were fabricated by oxidizing Cu foil at 500°C for different times. The oxide film prepared at 500°C for 2 h possesses a bandgap of 2.09 eV and a carrier density of  $8.17 \times 10^{17} \text{ cm}^{-3}$ . The conduction band and valence band of the film were positioned at -1.17 and 0.92 V vs. RHE, respectively. Under a PEC measurement, the electrode exhibited a photocurrent of -2.5 mA/cm<sup>2</sup> at 0 V vs. RHE, which is much higher than that of the Cu<sub>2</sub>O film prepared at 1010°C. The higher carrier density and thinner film thickness may account for the improved photocurrent. However, the thin CuO layer formed on the Cu<sub>2</sub>O, confirmed by XRD results, may decrease the photoactivity of the film since CuO is an unstable and low-photoactivity semiconductor with indirect band gap. Thus, avoiding the formation of CuO and nanostructuring the Cu<sub>2</sub>O surface during the Cu<sub>2</sub>O fabrication may increase the photocurrent further.